Proceedings of the

XXIV INTERNATIONAL YOUNG SCIENTISTS CONFERENCE ON APPLIED PHYSICS

ICAP 2024

May, 21-24, 2024,
Kyiv, Ukraine

Taras Shevchenko National University of Kyiv
Faculty of RadioPhysics, Electronics and Computer Systems

Organizing Committee

A. Netreba, Associate Professor – Chairman, Faculty of RadioPhysics, Electronics and Computer Systems, Taras Shevchenko National University of Kyiv

N. Bashmakova – Vice-Chairman, Faculty of RadioPhysics, Electronics and Computer Systems, Taras Shevchenko National University of Kyiv

A. Komarov, Ph.D. – Vice-Chairman, Faculty of RadioPhysics, Electronics and Computer Systems, Taras Shevchenko National University of Kyiv

O. Nechyporuk, Associate Professor – Vice-Chairman, Founder of the International Young Scientists Conference on Applied Physics

V. Moiseienko, Laboratory Head – Secretary, Faculty of RadioPhysics, Electronics and Computer Systems, Taras Shevchenko National University of Kyiv

I. Anisimov, Professor, Faculty of RadioPhysics, Electronics and Computer Systems, Taras Shevchenko National University of Kyiv

Y. Boyko, Associate Professor, Faculty of RadioPhysics, Electronics and Computer Systems, Taras Shevchenko National University of Kyiv

A. Veklich, Professor, Faculty of RadioPhysics, Electronics and Computer Systems, Taras Shevchenko National University of Kyiv

V. Vysotskiy, Professor, Faculty of RadioPhysics, Electronics and Computer Systems, Taras Shevchenko National University of Kyiv

S. Radchenko, Associate Professor, Faculty of RadioPhysics, Electronics and Computer Systems, Taras Shevchenko National University of Kyiv

S. Savenkov, Professor, Faculty of RadioPhysics, Electronics and Computer Systems, Taras Shevchenko National University of Kyiv

V. Skryshevsky, Professor, Institute of High Technologies, Taras Shevchenko National University of Kyiv

A. Karlash, Associate Professor, Faculty of RadioPhysics, Electronics and Computer Systems, Taras Shevchenko National University of Kyiv

C. Patton, Professor, USA, Colorado University

B. Hillebrands, Professor, Germany, Kaiserslautern University

M. Strikha, Professor, Faculty of RadioPhysics, Electronics and Computer Systems, Taras Shevchenko National University of Kyiv

D. Bozhko, Ph.D. Assistant Professor, USA, University of Colorado, Colorado Springs

I.Fedirchuk, Assistant, Belgium, Antwerpen University

A. Goriachko, Associate Professor, Faculty of RadioPhysics, Electronics and Computer Systems, Taras Shevchenko National University of Kyiv

M. Kononov, Associate Professor, Faculty of RadioPhysics, Electronics and Computer Systems, Taras Shevchenko National University of Kyiv

V. Ovechko, Professor, Faculty of RadioPhysics, Electronics and Computer Systems, Taras Shevchenko National University of Kyiv

S. Pogorilyi, Professor, Faculty of RadioPhysics, Electronics and Computer Systems, Taras Shevchenko National University of Kyiv

O. Nedybaliuk, Associate Professor, Faculty of RadioPhysics, Electronics and Computer Systems, Taras Shevchenko National University of Kyiv

V. Boretskij, Associate Professor, Faculty of RadioPhysics, Electronics and Computer Systems, Taras Shevchenko National University of Kyiv

O. Mokhonko – PhD Student, Faculty of RadioPhysics, Electronics and Computer Systems, Taras Shevchenko National University of Kyiv

O. Murmantsev – PhD Student, Faculty of RadioPhysics, Electronics and Computer Systems, Taras Shevchenko National University of Kyiv

D. Sliusarenko – PhD Student, Faculty of RadioPhysics, Electronics and Computer Systems, Taras Shevchenko National University of Kyiv

General information

Date	May, 21-24, 2024
Location for mails	Taras Shevchenko National University of Kyiv Volodymyrska Str. 64/13, 01601 Kyiv – Ukraine
Physical location	Faculty of RadioPhysics, Electronics and Computer Systems, Taras Shevchenko National University of Kyiv, Prospect Glushkova, 4g, Kyiv 03022, Ukraine
Organization	Taras Shevchenko National University of Kyiv, Faculty of RadioPhysics, Electronics and Computer Systems

Scientific program

The Conference contributions are accepted from the following areas:

1. Laser Physics and Optoelectronics
2. Surface Physics, Nano- and Microelectronics
3. Physics of Semiconductors and Dielectrics, Semiconductor Devices
4. Physics of Magnetism
5. Computer Technologies
6. Mathematical Problems of Applied Physics
7. Medical Physics
8. Plasma Physics
9. Radio Engineering and Communications
10. Polarimetry: Theory and Applications

Conference site

All events associated with the XXIV International Young Scientists Conference on Applied Physics will take place in on-line regime in 2024.

Time

Local time is one hour ahead of Middle European time – EEST (UTC+3).

Conference language

The language of the Conference Proceedings is English.

Presentation

The Conference program includes invited lectures and contributed papers. All reports will be lectured in oral presentation.

Invited talks: 60 minutes (including discussion)
Other talks: 20 minutes (including discussion)

Edited by O. Mokhonko, A. Komarov, Dr. O. Nechyporuk, Dr. A. Netreba.

E-mail: icap@knu.ua
ICAP web-site: http://icap.knu.ua/

PREFACE

The XXIV INTERNATIONAL YOUNG SCIENTISTS CONFERENCE ON APPLIED PHYSICS (ICAP'2024) will be held May, 21-24, 2024, in the capital of Ukraine Kyiv. The famous scientific and cultural center of Europe welcomes over 75 delegates from different Universities and Scientific Centers of 5 countries of Europe, America and Asia.

The intend of ICAP'2024 is to provide a forum where novel and relevant achievements in Applied Physics (RadioPhysics and Electronics) could be discussed, to bring together young scientists of different disciplines and foster their cooperation, to stimulate international research in the field of Applied Physics, development, fabrication and application of new physical ideas in the corresponding devices. It is too important now for Ukraine as a member of Bologna Process and as well as of European Community.

The ICAP'2024 is organized by Faculty of Radiophysics, Electronics and Computer Systems of Taras Shevchenko National University of Kyiv.

The Conference technical program is divided into nine sessions; four invited lectures and more than 70 oral contributions will be presented, discussed and argued.

We believe the ICAP'2024 will give a chance for students, postgraduate students, young professors and scientists to discuss their problems and give an impulse for the development of future research and success.

We hope the delegates will enjoy the meeting. We hope also the participants and accompanying guests will enjoy visits to local places interests.

The next XXV INTERNATIONAL YOUNG SCIENTISTS CONFERENCE ON APPLIED PHYSICS (ICAP'2025) will be held in Kyiv, in May, 2025.

We will be glad to see you next year.

Sincerely yours,
Chairman of organizing committee of ICAP 2024 Dr. A. Netreba

INVITED LECTURES

MINIATURIZED RAMAN SPECTROSCOPY AND MICROSCOPY

Yaroslav Aulin*, Konstantinos Stergiou, Sofus Boisen, Andrii Kutsyk, Yurii Pilhun, Oleksii Ilchenko
Lightnovo ApS, Blokken 11, 1., Birkerød, Denmark
** e-mail: ya@ligthnovo.com*

Raman spectroscopy provides non-destructive, label-free quantitative studies of chemical compositions at the microscale. Such capabilities come at the cost of high requirements for instrumentation. Here we present a centimeter-scale miniaturization of a Raman spectrometer using cheap non-stabilized laser diodes, densely packed optics, and non-cooled small sensors. The performance is comparable with expensive bulky research-grade Raman systems. It has excellent sensitivity, low power consumption, perfect wavenumber, intensity calibration, and 7 cm^{-1} resolution within the 400–4000 cm^{-1} spectral range using a built-in reference. We foresee that the miniaturization will allow realization of super-compact Raman spectrometers for integration in smartphones and medical devices, democratizing Raman technology.

Raman spectroscopy is a powerful tool that has a diverse range of applications, from identification of chemical hazards, explosives, and illicit drugs to biomedical applications. Such capabilities, however, come at the cost of high requirements for instrumentation, in particular thermally stabilized lasers and cooled sensors. Therefore, Raman spectroscopy and microscopy would normally need to be performed on high-end, bulky, and costly Raman instruments. The need for miniaturization of Raman instrumentation is driven by applications where the complexity and/or the bulkiness of existing devices is obstructive. Application examples in need of miniaturization include space exploration, on-site toxic substance inspection, in-vivo diagnostics of tissues, chemical identification in hardly accessible places using robots and drones, and Raman device integration into robotic arms for biomedical applications.

Fig. 1. Miniaturized handheld Lightnovo miniRaman spectrometer.

We have developed a miniaturized handheld spectrometer Lightnovo miniRaman shown in Figure 1. The optical schematics and principle of operation of miniRaman are provided in Figure 2. We use non-thermally stabilized laser diodes Laser 1- 785 nm and Laser 2 – 675 nm (for expanded spectral range). The mode hopping and drift of the laser wavelengths as well as intensity fluctuations are compensated by introduction of a reference channel with in-built polystyrene sample. The spectrometer is equipped with transmission Bragg grating and NIR coated optical elements allowing for high throughput. The Raman spectra of signal and reference channels are projected to single rows of non-cooled CMOS sensor providing high sensitivity.

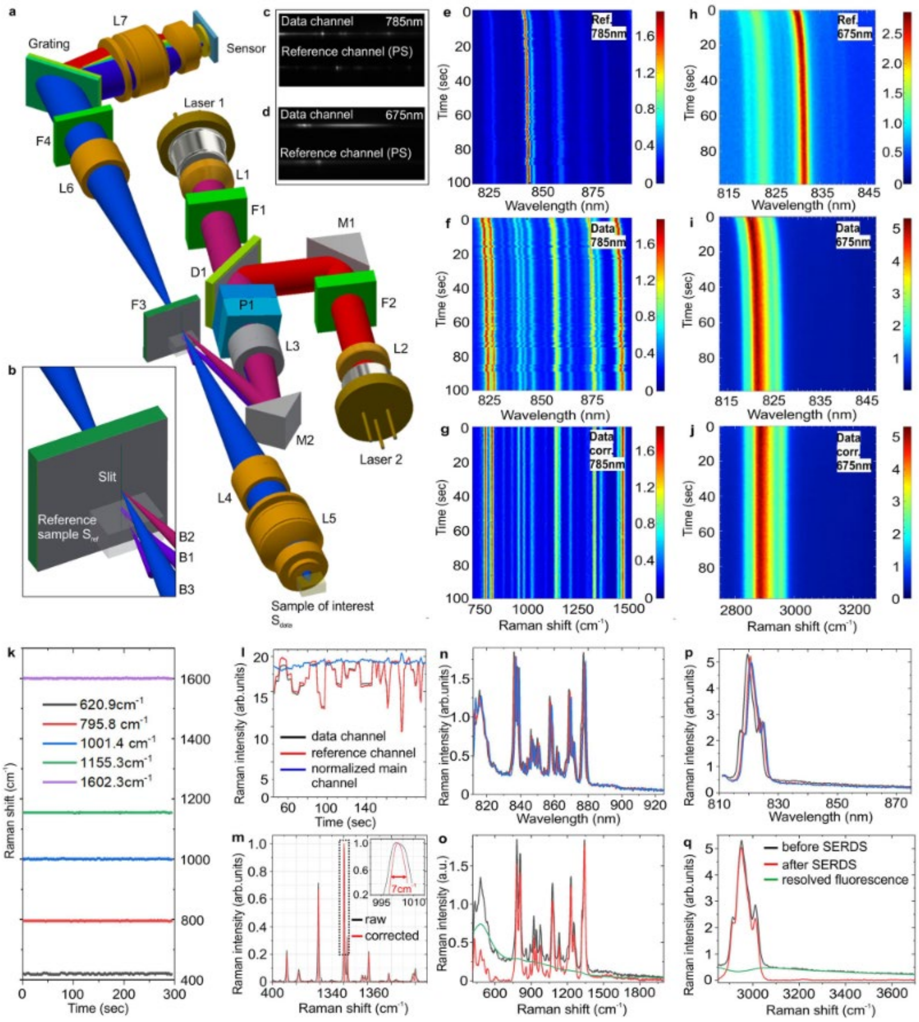

Fig. 2. Optical layout and working principle of a miniaturized Raman system [1].

Therefore, the miniaturized Raman spectrometer can collect a Raman spectrum in the range of 400–4000 cm−1 with 7 cm^{-1} resolution reaching the performance typically associated with much larger, research grade systems.

References

[1] O. Ilchenko et al., “Optics miniaturization strategy for demanding Raman spectroscopy applications”, Nature Communications, (2024)15:3049, https://doi.org/10.1038/s41467-024-47044-7

LABEL-FREE DETECTION AND ANALYSIS OF BIOMOLECULES USING SOLID-STATE NANOPORES AND NANODIELECTROPHORESIS

Sergii Pud

**University of Twente, Drienerlolaan 5, 7522NB, Enschede, The Netherlands, e-mail:* s.pud@utwente.nl

In this contribution I present two innovative non-invasive techniques for studying biomolecules in their native states: solid-state nanopores and nanodielectrophoresis. Solid-state nanopores allow for label-free detection and characterization of single molecules, while nanodielectrophoresis employs electric field interactions to trap and analyze nanoparticles at the single-entity level. Both methods aim to enhance the precision and temporal resolution of biomolecular studies without altering the molecules, facilitating deeper insights into their properties and interactions.

Introduction

The past two decades evidenced the advent of a variety of analytical methods, that enabled studying the living matter at the unprecedented single-molecule scales. These techniques revolutionized fields of biological research towards quantitative understanding of biological processes. However, most of these approaches require fluorescent labelling and chemical tethering of the molecules of interest to become precise and specific, which is time consuming and may alter the molecule under study. Only a handful of techniques are truly non-invasive and allow for studies of biomolecules in their native states, free of chemical labels. Here I am going to present two of such technologies, which I have been working on during the past 10 years: solid-state nanopores and nanodielectrophoresis

Solid-state nanopores

Solid-state nanopores[1] are known for their ability to detect and characterize single molecules in label-free fashion, by passing them from one side of a freestanding membrane to another through a tiny nanoaperture. The beautifully simple operating principle and versatility made nanopores a ubiquitous solution for single-molecule biosensing. However, molecular control and the possibility of long temporal readout for long polymer molecules is still limited in nanopores due to fast analyte transport and low signal to noise ratios. Ultimately the motion of DNA in a nanopore should be controlled thus enabling a range of biophysics studies including sequencing, probing DNA physical properties and DNA-protein interactions. The ways to control motion of a biomolecule in a nanopore are still needed to establish solid-state nanopores as a technique for studying properties of single biomolecules. I will present two of such methods methods based on dual pores using electrophoretic force to control motion of the DNA and optical forces using plasmonic nanopores to trap DNA molecule above the nanopore.

Together with colleagues we have developed a strategy based on double-barrel nanopores, that allows actively controlling the molecular transport between the nanopores. This device consists of two independently addressable nanopores that are located at the tip of a double barrel quartz nanopipette and that are separated by a gap of approximately 20 nm (Fig. 1A). We demonstrate that this double-barrel-nanopore platform is capable of actively controlling DNA transport and efficiently bridging molecules between two pores (where up to 60 % of all translocations can be bridged). DNA molecules suspended between the two apertures can be sensed with each of the nanopore individually with an enhanced temporal resolution with the possibility of complete trapping of the molecules.

Secondly, I would like to present the possibility of extending residence times of a DNA in a nanopore by optically trapping the analyte inside the nanopore by use of an inverted bowtie plasmonic nanoatenna[3]. The extreme light concentration in the nanoantenna provides high electromagnetic field gradients that can be used for optical nanotweezing and trapping of small objects (Fig. 1(b,c)). Moreover, the light transmission through this antenna allows for an alternative read-out of the trapped molecule that can complement the ionic current read-out. We demonstrate trapping of 20nm sized polystyrene beads inside an inverted plasmonic plasmonic nanoantenna and label-free readout of DNA translocations through a solid-state nanopore.

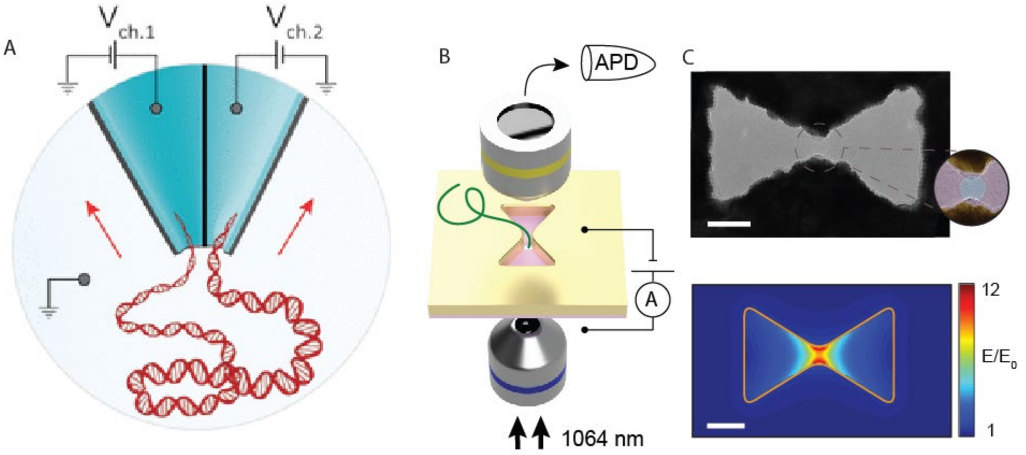

Figure 1(a) Schematic representation of the experimental setup showing a double barrel nanopore. (b) Schematic of the plasmonic nanopore experimental setup for trapping biomolecules and detection of extraordinary transmission changes. (c) TEM image of plasmonic inverted bowtie nanoantenna and optical field FDTD simulation of such an antenna.

Nanodielectrophoresis

Finally I would like to present usage of dielectrophoresis(DEP) to trap and investigate nanoparticles at the single entity level. This approach extends from the nanopore trapping into using higher order interaction with electric field. Solid-state nanopores rely on coulomb force to manipulate the object under study, but DEP is using dipole interactions. DEP is a common effect used to trap and manipulate proteins using an AC field in lab-on-a-chip applications. It causes the protein to experience a force, which is aligned with the spatial gradient of the electric field and depends on the proteins shape, size, and charge properties. Therefore by measuring the DEP force for a single protein we can learn about their physical properties. We combine interferometric scattering microscopy (iSCAT) with DEP actuation in a nanoelectrode trap to investigate the proteins and polystyrene nanoparticles in high (up to 10^7 V/cm) AC electric fields.

References

[1] Cees Dekker, “Solid-state nanopores”, Nature Nanotechnology, 2 (4), 209-215 (2007)

[2] Paolo Cadinu, Giulia Campolo, Sergii Pud, Wayne Yang, Joshua B. Edel, Cees Dekker, and Aleksandar P. Ivanov, “Double Barrel Nanopores as a New Tool for Controlling Single-Molecule Transport”, Nano Letters 2018 18 (4), 2738-2745

[3] Daniel V. Verschueren, Sergii Pud, Xin Shi, Lorenzo De Angelis, L. Kuipers, and Cees Dekker, “Label-Free Optical Detection of DNA Translocations through Plasmonic Nanopores”, ACS Nano 2019 13 (1), 61-70

LIGHT-DRIVEN ULTRAFAST MAGNETISM

Dmytro Afanasiev
Radboud University, Nijmegen, The Netherlands

For centuries, the central goal of condensed matter physics has been to understand and describe naturally occurring phenomena, both in macroscopic and microscopic terms. Over the past few decades, a new paradigm has emerged: to experimentally realize and control new states of matter that are not found in nature. In addition to answering fundamental scientific questions, the control and knowledge of potential 'exotic' phases also hold the promise of creating a new and radically different generation of functional devices.

Ultrashort pulses of light are particularly appealing in this context as they allow us to create strongly nonequilibrium transient states of matter with properties that are often not even attainable in equilibrium. Some examples include light-induced superconductivity, metal-to-insulator transitions, and light-driven Floquet engineering. In this discussion, I will explore how light can be used to control magnetism in highly interesting class of the antiferromagnets, encompassing fundamental magnetic interactions, magnetic phase transitions, and highly nonlocal spin dynamics. I will particularly focus on nonthermal methods for controlling magnetism when the photon energy of light is precisely tuned in resonance with elementary excitations, such as lattice vibrations[1], orbitals[2], or electron excitations[3], which have a direct impact on the ordered spins.

References

[1] D. Afanasiev, J.R. Hortensius, B.A. Ivanov, A. Sasani, E. Bousquet, Y.M. Blanter, R.V. Mikhaylovskiy, A.V. Kimel, A.D. Caviglia “Ultrafast control of magnetic interactions via light-driven phonons” *Nature Materials* **20,** 607–611 (2021)

[2] D. Afanasiev, J. R. Hortensius, M. Matthiesen, S. Mañas-Valero, M. Šiškins, M. Lee, E. Lesne, H. van der Zant, P. G Steeneken, B. A. Ivanov, E. Coronado, A. D. Caviglia “Controlling the anisotropy of a van der Waals antiferromagnet with light” *Science Advances* **7,** 23 (2021)

[3] J.R. Hortensius, D. Afanasiev, M. Matthiesen, R. Leenders, R. Citro, A.V. Kimel, R.V. Mikhaylovskiy, B.A. Ivanov, A.D Caviglia “Coherent spin-wave transport in an antiferromagnet” *Nature Physics* **17,** 1001 (2021)

REMOVAL OF PFAS AND PHARMACEUTICAL RESIDUES FROM WATER WITH A HYPERBOLIC VORTEX PLASMA DISCHARGE

Roman Klymenko*, Elmar C. Fuchs, W.F.L.M. (Wilfred) Hoeben***, Jakob Woisetschlägerilfred****, Luewton L.F. Agostinho*******

** Department of Electrical Engineering, Electrical Energy Systems group, Eindhoven University of Technology, Eindhoven, The Netherlands, e-mail: r.klymenko@tue.nl*

*** Wetsus, European Centre of Excellence for Sustainable Water Technology, Leeuwarden, The Netherlands, e-mail: elmarchristof.fuchs@wetsus.nl*

**** Department of Electrical Engineering, Electrical Energy Systems group, Eindhoven University of Technology, Eindhoven, The Netherlands, e-mail: w.f.l.m.hoeben@tue.nl*

***** Laser Optical Metrology Group, Institute of Thermal Turbomachinery and Machine Dynamics, Graz University of Technology, Graz, Austria, e-mail: jakob.woisetschlaeger@tugraz.at*

****** Water Technology Research Group, NHL Stenden University of Applied Sciences, Leeuwarden, The Netherlands, e-mail: luewton.agostinho@hvhl.nl*

The accumulation of micro-pollutants (per- and polyfluorinated substances (PFAS), pharmaceuticals, etc.) in wastewater and then in the environment has become a problem of growing concern. Although some compounds are easily biodegradable, many of them are hardly decomposed and pose a health hazard for both aquatic and terrestrial life. The application of gas-phase pulsed electrical discharges together with Schauberger water vortex is a promising method for the energy efficient oxidative degradation of aqueous organic pollutants. Plasma water purification includes various physical and chemical processes, many of which are independent water treatment techniques (oxidation, ultraviolet disinfection, ozonation, electrolysis, shockwave water purification etc.). The water vortex effectively mixes the water and dissolves gases from the atmosphere, including oxidants and solvated electrons formed by the plasma. The combination of these two phenomena significantly increases the efficiency of micro-pollutant degradation in water.

Per- and polyfluoroalkyl substances (PFAS)

PFAS are a group of synthetic chemicals consisting of more than 8000 compounds. These chemicals are composed of carbon chains that are either saturated or partially saturated with fluorine atoms. PFAS are highly resistant to thermal and chemical degradation, have favorable dielectric properties, and exhibit low surface energy and friction coefficient. These characteristics make PFAS versatile and durable chemicals that have been used in various applications since the1940s. All PFAS have a common chemical structure (C_nF_{2n+1}), known for its high stability due to strong C–F bonds (485 kJ mol−1 or 5 eV, respectively). PFAS can be further categorized based on the length of their carbon chains. Compounds with more than six to eight carbon segments are classified as ‘long-chain PFAS’, while those with fewer carbon segments are referred to as ‘short-chain PFAS’. The most commonly encountered PFAS in the environment are perfluorooctanoic acid and perfluorooctane sulfonate (PFOA and PFOS). Concerns about the potential impact of PFAS on human health emerged in the 1980s as their environmental distribution and bioaccumulation potential became apparent. This led to a decrease in the use of long-chain PFAS and the emergence of short-chain PFAS as substitutes, as they were believed to have lower bioaccumulation potential. When PFAS accumulates in an organism, it increases the concentration of reactive oxygen species (ROS) in the body, leading to oxidative stress. Additionally, increased cholesterol, thyroid disease, kidney & testicle cancer and pregnancy issues have been reported. Therefore, efficient and sustainable technologies being able to fully mineralize PFAS are of increasing importance in the water treatment industry. The vortex plasma treatment presented in this work is one of these technologies [1].

Pharmaceuticals

Apart from improving human and animal health, pharmaceuticals enhance livestock growth and well-being. These chemicals are designed to have a significant impact even at very low concentrations and to persist in the targeted organism for a sufficient duration to produce the desired effects. As a result, many pharmaceuticals exhibit resistance to biodegradation, leading to approximately 90%–95% being excreted unchanged after use. Conventional WWTPs have been shown to be ineffective in removing various pharmaceuticals, resulting in the discharge of these compounds into surface waters either unaltered or only partially degraded. This contamination has been observed to have ecotoxic effects and adverse health impacts on aquatic species such as fish, daphnia, and algae. There is currently limited data available on the health effects of the following, translating ecotoxicity studies from other organisms poses challenges due to the chronic nature of most health effects compared to acute toxicity. Another significant concern is the potential development of antibiotic resistance in natural bacterial populations, which can lead to increased health costs and higher rates of morbidity and mortality due to reduced effectiveness of available antibiotics [1].

Plasma treatment

Plasma technology is an advanced treatment method that can achieve a high rate of removal of various micropollutants due to its ability to initiate multiple degradation mechanisms without the need for additional chemicals, while still maintaining a moderate energy requirement. The primary mechanism of plasma chemical degradation in an aqueous environment primarily involves oxidation processes, although reduction processes and certain physical processes may also play significant roles. In gas–liquid environments, the composition typically consists of oxygen (O_2), nitrogen (N_2), and water molecules, referred to as the parent species. These parent species are the initial particles subjected to excitation and ionization by an electrical discharge. The ionization of these parent species leads to the formation of reactive particles known as primary species. Subsequent chemical reactions between the primary species and the parent species result in the creation of more stable particles called secondary reactive species. They can be categorized into two main groups: ROS and reactive nitrogen species (RNS). ROS mainly include hydroxyl radicals $^{\cdot}OH$, hydroperoxyl radicals HO_2, hydrogen peroxide H_2O_2, ozone O_3, singlet molecular oxygen $^1O_2$. On the other hand, RNS consist of NO_x and stable and transient N_2 oxyacid $H_aN_bO_c$ (Fig. 1.). These reactive species are involved in degradation reactions with organic and/or inorganic compounds, which are the target species. Additional degradation occurs due to the presence of highly reactive solvated electrons generated by the plasma discharge at the gas-liquid interface. Despite their short lifetime, their influence on degradation processes can be significant, especially noticeable in the degradation of surfactants such as PFOS and PFOA. Previous studies have shown that plasma treatment is highly effective in the destruction of bacteria, pesticides, pharmaceuticals, organic dyes, and PFAS [1].

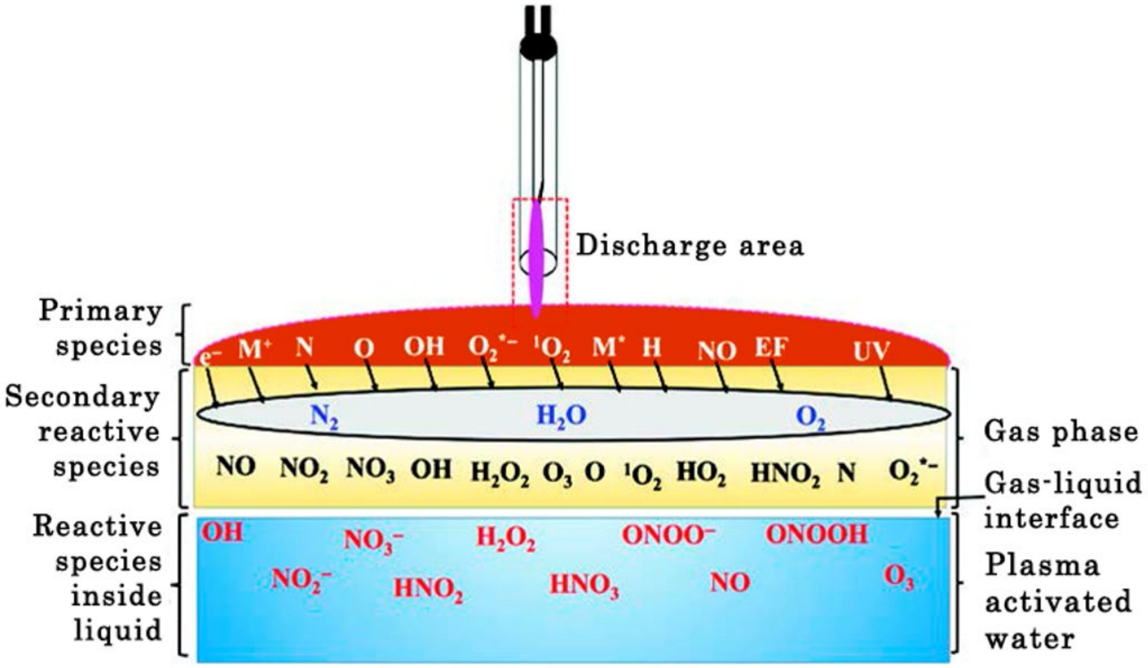

Fig. 1. Schematic diagram of the formation of active constituents in a plasma-activated medium with a conventional plasma jet [2].

Water vortex gas discharge plasma reactor combines plasma technology with a Schauberger hyperbolic vortex. As shown in [3] water vortices are very efficient aeration systems, and thus are capable of dissolving gases at very high rates. This reactor enables the in-situ production of reactive species in the gas phase for micropollutant degradation by plasma discharge and the efficient mass transfer and mixing required for distributing these reactive species into the liquid phase by the water vortex resulting into efficient degradation of micro-pollutants.

References

[1] R. Klymenko, E. de Kroon, L. L. F. Agostinho, E. C. Fuchs, J. Woisetschläger and W. F. L. M. Hoeben, “Characterization of a hyperbolic vortex plasma reactor for the removal of aqueous phase micropollutants,” J. Phys. D: Appl. Phys., vol. 57, Jan. 2024.

[2] N. K. Kaushik, B. Ghimire, Y. Li, M. Adhikari, M. Veerana, N. Kaushik, N. Jha, B. Adhikari, S. J. Lee, K. Masur, T. von Woedtke, K. D. Weltmann, E. H. Choi, “Biological and medical applications of plasma-activated media, water and solutions,” Bio. Chem., vol. 400, pp. 39-62, Jul. 2018.

[3] R. Klymenko, H., Nanninga, E. de Kroon, L. L. F. Agostinho, E. C. Fuchs, J. Woisetschläger and W. F. L. M. Hoeben, “Preparation of Free-Surface Hyperbolic Water Vortices,” J. Vis. Exp. (197), e64516, Jul. 2023.

LASER PHYSICS AND OPTOELECTRONICS

SIMPLE ANALYTICAL EXPRESSION FOR RAMAN GAIN PROFILE IN TiO_2 DOPED SINGLE-MODE SILICA FIBER

Yuliana Lazarchuk*, Georgii Felinskyi, and Iryna Serdeha
*Educational and Scientific Institute of High Technologies Taras Shevchenko National University of Kyiv, Kyiv 01601, Ukraine, *email: yuliana.lazarchuk@knu.ua*

The Raman gain profile of TiO_2 doped single-mode silica fiber is obtained in a simple analytical form using 12-mode Gaussian decomposition in the full Stokes shifted range from 20 cm^{-1} *to* 1400 cm^{-1}. *It is shown, in the practically important region of the Stokes shifted band* ($\Delta\omega \geq 4$ *THz*) *for cascade Raman lasing around the fundamental mode* G_9 929 cm^{-1}, *the gain profile can be approximated by a single Gaussian component with an accuracy of* ~0.2%.

Previously in [1,2], the spectroscopic technique of multimode decomposition of rather complex Raman gain profiles [3] was compared with alternative methods of rational approximation and it is applied to TiO_2-doped single-mode fiber based on silica glass. As a result of the comparative analysis of both approaches, it was pointed on the nature of the dominant mode G_9 929 cm^{-1} broadening in the Raman gain spectrum of this fiber. Observed line broadening should be classified by the heterogeneous mechanism since the line shape of this phonon mode is close to Gaussian. Note precisely the existence of such powerful mode in the Stokes shifted Raman gain band attracts increased attention to the nonlinear parameters research of this fiber in the light of its applications for laser technology. Here, the quantitative results of the Gaussian approximation in the vicinity of G_9 peak of the Raman gain profile we present in the simple analytical form.

Modeling theoretical background

It is known [2] the Gaussian component type is referred to the best choice for the decomposition of Raman spectra in all silica fibers because the amorphous glass is in the core material. So, the multiple Gaussian components may be written in the form:

$$g_R(\omega) = g_{R\max}\sum_{i=1}^{N} A_i \cdot \exp\left[-\frac{(\omega-\omega_{v,i})^2}{\Gamma_i^2}\right] = g_{R\max}\cdot\varphi(\omega)\,, \qquad (1)$$

where φ(ω) is the normalized Raman gain profile $g_R(\omega)$ presented as analytical function of the frequency ω; g_{Rmax} is the maximum value of the Raman gain coefficient; N – number of components; A_i and $\omega_{v,i}$ are, respectively, the amplitude and central frequency of the i-th Gaussian component, Γ_i is the dumping constant. The main task of the decomposition is to achieve the best correspondence of the forms of the factor φ(ω) to the experimental Raman gain profile.

Numerical results and discussion

Practically, the Raman gain profile $g_R(\omega)$ was decomposed on several Gaussian component by finding the optimal set of 3 × N parameters of the formula (1) using the computer procedure of nonlinear approximation according to the Levenberg-Marquardt method. Our numerical results on multimode Gaussian decomposition of Raman gain profiles in TiO_2 doped fiber using: *a*) 12 modes in the region from 20 cm^{-1} to 1400 cm^{-1}; *b*) only 1 Gaussian in the region from 870 cm^{-1} to 1010 cm^{-1}.

Table 1. *Results of the decomposition of the gain profile* $\varphi(\omega)$ *in* TiO_2 *fiber* $[g_{Rmax} = 4{,}8(W\times km)^{-1}]$ *using single-mode Gaussian decomposition.*

No mode	A_i	ω_{vi} , cm^{-1}	ω_{vi}, THz	Γ_i, cm^{-1}	Γ_i, THz
G9	1.0	929.0	27.9	45.8	1.37
Fit. error ε=0.24%					

The numerical values of the parameters resulting from the Gaussian decomposition of the profile $\varphi(\omega)$ on the Stokes shift from 870 cm^{-1} (24 THz) to 1050 cm^{-1} (30 THz) using 1 oscillatory mode are presented in the Table 1.

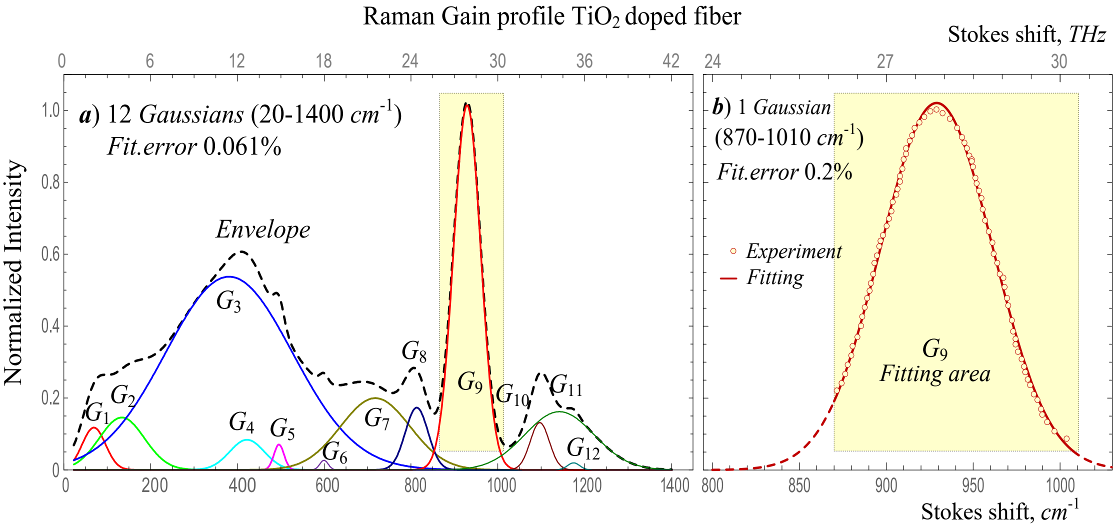

Fig. 1. Multimode Gaussian decomposition of Raman gain profiles in TiO_2 doped fiber using:
a) 12 modes in the region from 20 cm^{-1} to 1400 cm^{-1};
b) only 1 Gaussian in the region from 870 cm^{-1} to 1010 cm^{-1}.

Therefore,

$$g_{R\max}(\omega) = 4.8(W \cdot km)^{-1} \times \begin{cases} \exp[-4.8 \cdot 10^{-4}(\omega - 929)^2], & \text{where } 870\ cm^{-1} < \omega < 1010\ cm^{-1} \\ \exp[-0.53(\omega - 27.9)^2], & \text{where } 26.1\ THz < \omega < 30.3\ THz \end{cases}, \tag{2}$$

Conclusion:

In our study, we achieved highly accurate results in numerically approximating the Raman gain profile in TiO_2-doped single-mode silica fiber through the application of the spectroscopic approach using single-mode Gaussian decomposition. The advantage of utilizing a single mode for decomposition lies in its higher intensity maximum, reduced need for cascade laser converters, and enhanced efficiency of nonlinear conversion processes, ultimately enabling accurate modeling of the experimental profile of Raman amplification. Notably, we attained a fitting precision of no worse than 0.2% using this method. The simple analytical form of our modeling results holds significant advantages for the design of modern photonic devices based on fiber nonlinear optics.

References

[1] G. S. Felinskyi, V. I. Grygoruk, I. V. Serdeha, O. O. Drobakhin and M. V. Andreev, "Gaussian and Rational Approximation of Raman Gain Profile in TiO₂ Doped Silica Fiber," 2021 IEEE 26th International Seminar/Workshop on Direct and Inverse Problems of Electromagnetic and Acoustic Wave Theory (DIPED), 2021, pp. 130-133, doi: 10.1109/DIPED53165.2021.9552290

[2] Y. V. Lazarchuk, O. O. Drobakhin, V. I. Grygoruk, G. S. Felinskyi, M. V. Andreev and I. V. Serdeha, "Analytic Representation of Stokes Noise Spectrum and Raman Gain Profile in Silica Fiber," 2022 IEEE 41st International Conference on Electronics and Nanotechnology (ELNANO), 2022, pp. 213-218, doi: 10.1109/ELNANO54667.2022.9927018.

[3] I.V. Serdeha, V.I. Grygoruk, G.S. Felinskyi. Spectroscopic features of Raman gain profiles in single-mode fibers based on silica glass // Ukr. J.Phys. 2018. Vol. 63, No. 8, p. 683-700.

USING FERMAT’S PRINCIPLE TO CALCULATE FILM FORMS

Rohovtsova A.*, Ovechko V.**
** Faculty of Radiophysics, Electronics and Computer Systems Address, e-mail:* annarohovtsova.oficial@gmail.com
*** Faculty of Radiophysics, Electronics and Computer Systems, Address, e-mail:* volodymyr3395@gmail.com

Fermat's principle: light travels from one point to another along a line, along which the propagation time T will be minimal. This principle can be used to calculate film forms, which is the main task of these theses.

Variational calculus for Fermat’s principle

Statement of the problem: to formulate the differential equation of the line of light propagation in an optically inhomogeneous environment, where the speed of propagation $v(x,y,z)$depends significantly on the coordinates. According to Fermat's principle, light travels from point $A(x_0,y_0,z_0)$to point $B(x_1,y_1,z_1)$ along a line along which the propagation time T will be locally minimal. If we mark the equation of the propagation line through $y = y(x), z = z(x)$, then the formalized formulation of the problem has the form

$$T\ (y,z) = \int_{x_0}^{x_1} \frac{\sqrt{1+(y(x)')^2+(z(x)')^2}}{v(x,y,z)} dx \quad \rightarrow min$$

$$y(x_0) = y_0, z(x_0) = z_0, y(x_1) = y_1, z(x_1) = z_1$$

Example of integral elements

Let us consider three integral elements, namely the ratio $\frac{n(x,y)}{n_0}$.

1. OF=f, $n_0 f = \int_0^f n(x,y)\sqrt{1+(y')^2}dx$

$$y(x) = Ax(f-x) \rightarrow A = \frac{y}{x(f-x)};\ y'(x) = A(f-2x)$$

If $n(x,y) = \frac{n_0}{\sqrt{1+(y\prime)^2}}$, then $\int_0^f n(x,y)\sqrt{1+(y')^2}dx = n_0 f$. So, $n(x,y) = \frac{n_0}{\sqrt{1+A^2(f-2x)^2}} = \frac{n_0}{\sqrt{1+\frac{y^2}{x^2(f-x)^2}(f-2x)^2}} = \frac{n_0 x(f-x)}{\sqrt{x^2(f-x)^2+y^2(f-2x)^2}}$

$$\frac{n(x,y)}{n_0} = \frac{\frac{x}{f}(1-\frac{x}{f})}{\sqrt{(\frac{x}{f})^2(1-\frac{x}{f})^2+(\frac{y}{f})^2(1-2\frac{x}{f})^2}} = \left\{\frac{x}{f} = x; \frac{y}{f} = y\right\}$$

$$= \frac{x(f-x)}{\sqrt{x^2(f-x)^2+y^2(f-2x)^2}}$$

Consider the limiting cases. $\frac{n}{n_0}_{min} = \frac{1}{2}, \frac{n}{n_0}_{max} = \sqrt{3}$

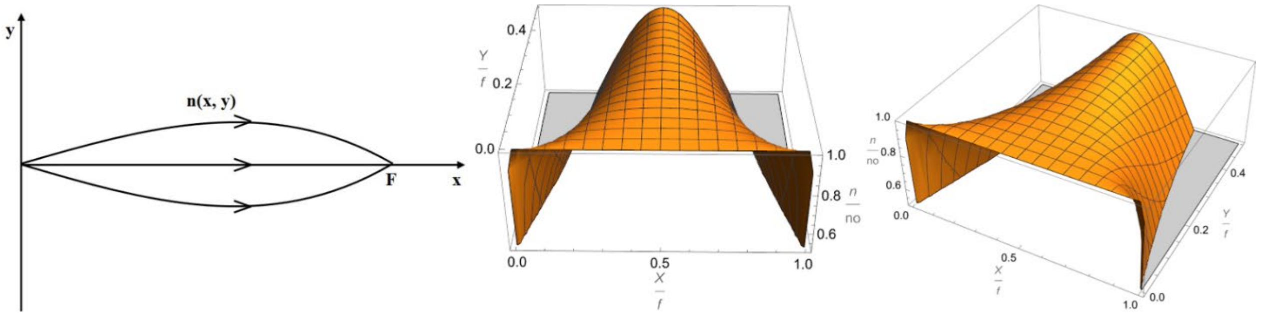

Figure 1 The movement of rays in an inhomogeneous environment

2. Integral focusing lens.

$$y(x) = A(f-x)(f+x) \to A = \frac{y}{(f^2-x^2)};\ y'(x) = -2Ax$$

If $n(x,y) = \frac{n_0}{\sqrt{1+(y')^2}}$, then $\int_0^f n(x,y)\sqrt{1+(y')^2}dx = n_0 f$.

All beams are phased and focused at point F.

$$n(x,y) = \frac{n_0}{\sqrt{1+\frac{2xy}{(f^2-x^2)}}}$$

Consider the limiting cases. $n_{min} = 1.5, n_{max} = 1.5\sqrt{2} \approx 2.13$

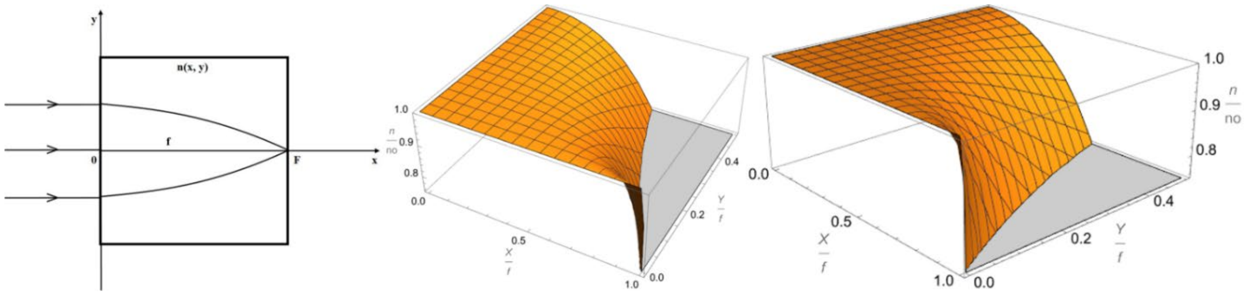

Figure 2 Integral focusing lens

3. Integral retroreflector

$$L = \int n(x,y)\sqrt{1+(y')^2}dx$$

$R_1^2 \le x^2+y^2 \le R_2^2 \to x^2+y^2 = R^2-$ ray trajectories; $2yy' = -2x, y' = -\frac{x}{\sqrt{R^2-x^2}}$

If $n(x,y) = \frac{n_0}{a\sqrt{x^2+y^2}}$, then $L = \frac{2n_0}{a}\int_0^1 \frac{dx}{\sqrt{R^2-x^2}} = \pi\frac{n_0}{a}$

The optical lengths within the range $R_1^2 \le x^2+y^2 \le R_2^2$ are the same

Consider the limiting cases. $\frac{n_0}{aR_1} = n_{max}, \frac{n_0}{aR_2} = n_{min} \to \frac{n_{max}}{n_{min}} = \frac{R_2}{R_1}$

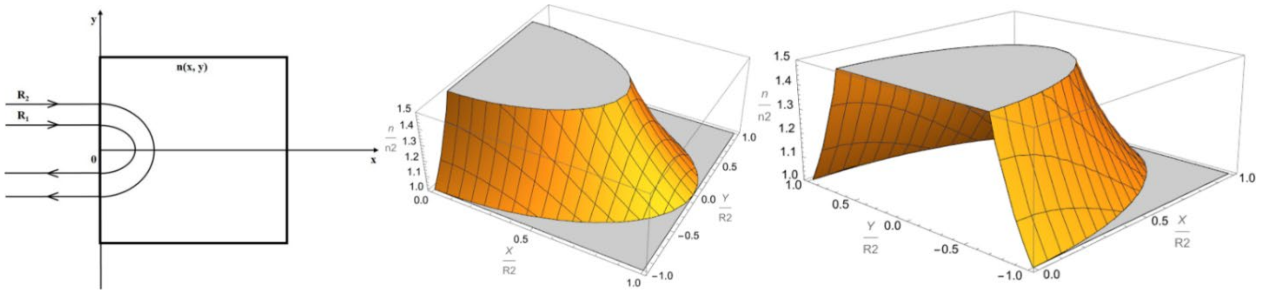

Figure 3 Integral retroreflector

Conclusions: Fermat's principle plays a significant role in optics, because it works in heterogeneous environment, which significantly expands the range of applied problems, for example, the calculation of film forms.

References

[1] Ovechko V., Mygashko V., Khrometz B. Kinoform as optical component. Proceedings of the XVII International Young Scientists Conference on Applied Physics, May, 23-27, 2017, Kyiv, Ukraine, p. 29-30.

TEMPERATURE OF SMALL PARTICLES IN OPTICAL TWEEZERS

Butakova Y.*, Negriyko A.**
** National Technical University of Ukraine "Igor Sikorsky Kyiv Polytechnic Institute", 37, Prospect Beresteiskyi, Kyiv, Ukraine, 03056, e-mail: lzbutakova@gmail.com*
*** The Institute of Physics of the National Academy of Sciences of Ukraine, 46, avenu Nauki, Kyiv, Ukraine, 03028, e-mail: amnegriyko@gmail.com*

A universal experimental scheme for holding absorbing particles in optical tweezers with a potential well on the axis of the holding beam formed from laser beams of arbitrary mode composition for measuring the temperature of small absorbing particles was developed and created. The idea of estimating the temperature of a heated semiconductor particle using recombination radiation is proposed.

Introduction

Heating of small absorbing particles held in optical tweezers is an important process that characterizes the energy exchange between micron and submicron-sized solid particles and the laser field. Estimates of the temperature of the particles in the tweezers show that it can reach thousands and even tens of thousands of Kelvin [1]. The study of the heating process for well-defined parameters of a single particle (size, shape, material) allows obtaining accurate data on the quantitative parameters of this interaction, which, in turn, can be important for the study of a number of phenomena and important applications, starting from the problems of global warming and the role atmospheric aerosols, to the use of heated particles in optical tweezers as microsurgery tools. As far as we know, the heating of small particles in laser tweezers, especially in a gas environment or in a vacuum, remains a poorly studied topic due to, in particular, the experimental difficulties associated with the small magnitude of the signal from a submicron-sized particle.

Methods of measuring the temperature of small particles

Obviously, for measuring the temperature of small solid particles in optical tweezers, direct contact methods of temperature measurement such as thermocouples or thermistors are not suitable due to the small size of the heated object and the need to maintain access to a particle of focused laser radiation. Well-known remote methods, such as pyrometers [2-3], also have limited application due to the extremely low value of the signal from micron and submicron-sized particles. Indirect estimates based on the change in motion of heated particles in the liquid have significant uncertainty.

Promising approaches to measuring the temperature of small absorbing particles in optical tweezers are remote methods based on the analysis of the spectral composition of the radiation either scattered by the particle or emitted by it. Recently, works were published in which a method based on the phenomenon of temperature dependence of forced Raman radiation by a particle in tweezers was proposed and implemented [4-5]. The method allows obtaining some data on the temperature of the particle, but has limited capabilities in terms of accuracy and measured temperature range.

Development of a method for estimating the temperature of a heated particle using the recombination radiation of a semiconductor

To develop a method for estimating the temperature of a heated particle, we suggested using the temperature dependence of the wavelength of the recombination radiation of a semiconductor during the transition of electrons from the conduction band to the valence band, when energy is released in the form of light quanta - photons with a certain energy [6].

An experimental setup based on an optical scheme with axicons and filtering of the mode composition of radiation was developed and created. This makes it possible to create an effective optical trap for solid particles. A camera with optical windows makes it possible to study the spectral composition of radiation scattered or emitted by a particle under the conditions of its retention in laser tweezers both in the atmosphere and, if desired, in a vacuum. The spectral composition of the radiation is analyzed using spectral equipment, and the signal is recorded using the method of counting the number of photons.

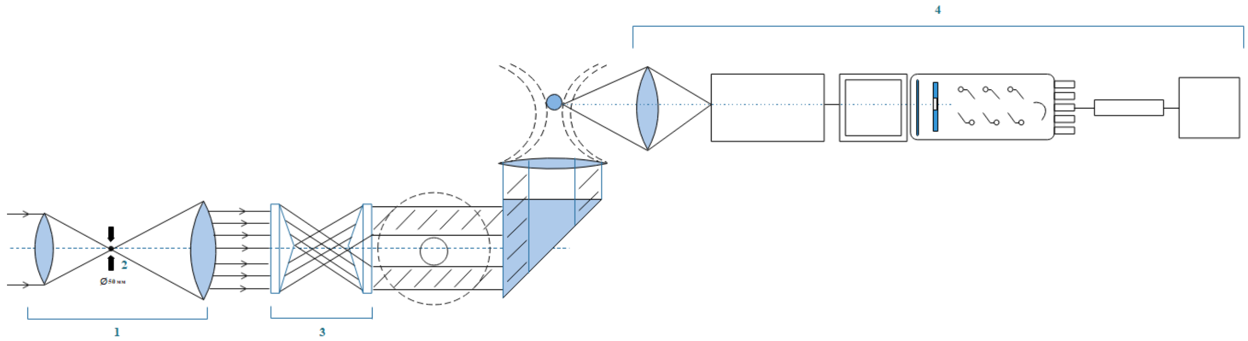

Fig. 1. Optical scheme of laser tweezers

1 – telescope; 2 – mode selector; 3 – axicon; 4 – registration scheme.

References

[1] Зеленський С., Копишинський О. Індуковане лазером теплове випромінювання конденсованих середовищ. — 2020. — С. 150. — URL: https://optics.knu.ua/wp-content/uploads/2020/04/Zelensky-Laser-induced-thermal-emission-1-3-2-1.pdf

[2] Pyrometric measurement of the temperature and size of individual combusting fuel particles / T. Joutsenoja, J. Stenberg, R. Hernberg, M. Aho // Applied Optics. — 1997. — T. 36, № 7. — DOI: 10.1364/ao.36.001525

[3]. Dongqing L. Encyclopedia of microfluidics and nanofluidics. — Spring Verlag, 2008. — C. 750 — 752. — ISBN 9780387324685.

[4] Temperature measurement of trapped, thermally sensitive single particles in an optical trap using raman spectroscopy / Y. Ai, Y. L. Pan, G. Videen, C. Wang // Applied Spectroscopy. — 2023. — DOI: 10.1177/00037028231198878.

[5] Tuschel D. Raman Thermometry // Molecular spectroscopy workbench: the 2016 collection. — 2016. — C. 33—38. — URL: https://www.spectroscopyonline.com/view/raman-thermometry.

[6] Agrawal G. P., Dutta N. K. Recombination Mechanisms in Semiconductors. — 1993. — DOI: 10.1007/978-1-4613-0481-4_3.

«GREEN» SYNTHESIS OF Ag-In-Se PARTICLES AND THEIR OPTICAL PROPERTIES

Nikolaenko A.*, Dmytruk A., Karlash A. ***

** Faculty of Radiophysics, Electronics and Computer Systems, Taras Shevchenko National University of Kyiv, Kyiv 01601, Ukraine. E-mail: asya.nikolaenko@gmail.com*

*** Institute of Physics, National Academy of Sciences of Ukraine, Kyiv 03028, Ukraine*

The green synthesis method of luminescent Ag-In-Se particles in an aqueous environment has been proposed. Absorption and luminescence spectra of the synthesized particles were investigated. The luminescence peak is at 747 nm, which corresponds to the red luminescence region. Synthesized Ag-In-Se particles were compared with Ag-In-S nanoparticles produced at Yuriy Fedkovych Chernivtsi National University.

Introduction

During the last years ternary semiconductor quantum dots of I–III–VI compounds have attracted considerable interest due to their remarkable properties, which determined a wide range of their potential applications. Silver-containing chalcogenides Ag–III–VI (III = In, Ga; VI = S, Se and Te) have found wide use in optoelectronic devices such as photocells, narrow-band optical filters or as thin films for solar cells [1]. Research is also being actively conducted using ternary particles for medical applications: magnetic resonance imaging diagnostics, optical imaging and photodynamic therapy [2].

Different synthesis methods for $AgInSe_2$ particles were described by many authors [1,2,3]. Most of proposed methods are complex and require high temperatures, long times for growth and the use of multiple stabilizers simultaneously to limit particle sizes. In this work, the green synthesis method for obtaining colloidal solutions of Ag-In-Se particles in an aqueous medium is implemented. The proposed method is ecological and avoids difficulties mentioned above. The analyses of optical absorption and luminescence were performed using SDL-2 spectrometer in a wavelength range of 350 – 800 nm.

Technology

The method of Ag-In-Se synthesis consists of dissolved in water precursor salts of silver nitrate ($AgNO_3$), indium nitrate ($In(NO_3)_3$) and selenium solution with the addition of L-cysteine stabilizer, at room temperature (18-20°C) and at normal pressure (760 mm Hg). Silver nitrate in the amount of 0.085 g is dissolved in 10 ml of distilled water, reaching 0.05 M. In a similar way, we dissolve 0.15 g of indium nitrate in 10 ml of distilled water (0.05 M). For the Se solution, we use 0.04 g of selenium powder, 0.1912 g of sodium sulfide Na_2SO_3 dissolved in 10 ml of water (0.05 M). The selenium mixture is intensively stirred at 100 °C for one hour. The main reaction mixture consists of 0.18 g of dissolved L-cysteine in 3 ml of water. After adding L-cysteine, it is important to stir the mixture until the stabilizer is completely dissolved. The mixture should be transparent without sediment in the form of cysteine powder. Alternately add 1 ml of dissolved $AgNO_3$ and $In(NO_3)_3$. At each addition of solutions, thoroughly stir the reaction mixture for a short time. Quickly and gradually add 2 ml of hot selenium solution (Na_2SeSO_3) to the resulting reaction mixture. The substance will gradually acquire a dark brown color in the upper part, and a thin transparent layer of water will form below. After adding 2 ml of selenium solution, it is important to shake the mixture until it has a uniform color - dark brown.

Fig. 1,a shows photos of as synthesized Ag-In-Se particles with a molar ratio of Ag:In:Se = 1:1:2. For comparison, similar nanoparticles of Ag-In-S, prepared by hydrothermal synthesis method [4] are shown on Fig.1,b. By exciting the synthesized Ag-In-Se sample with a 406 nm semiconductor laser, we can see intense luminescence (a pink glow), which is visually similar to the glow of the Ag-In-S sample at the same excitation wavelength. Therefore, we expect the luminescence peak of both samples at approximately the same wavelength in the near-infrared region.

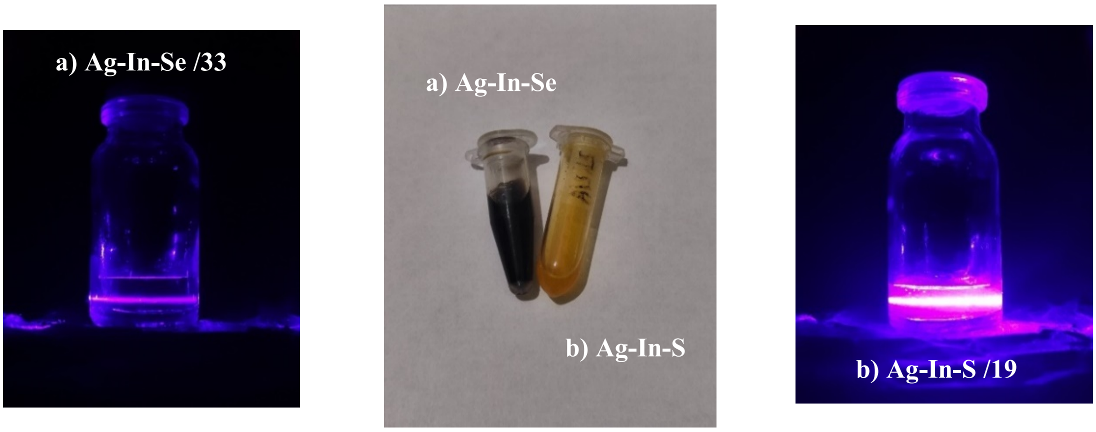

Fig.1. Ternary semiconductor particles and their visual luminescence under excitation at 406 nm: a) as synthesized Ag-In-Se diluted 33 times with water; b) Ag-In-S diluted 19 times with water

UV-vis absorption spectra of Ag-In-Se and Ag-In-S particles are presented on Fig.2,a. Strong absorption in UV range was revealed for both samples with a pronounced shoulder at 400 nm for Ag-In-S particles.

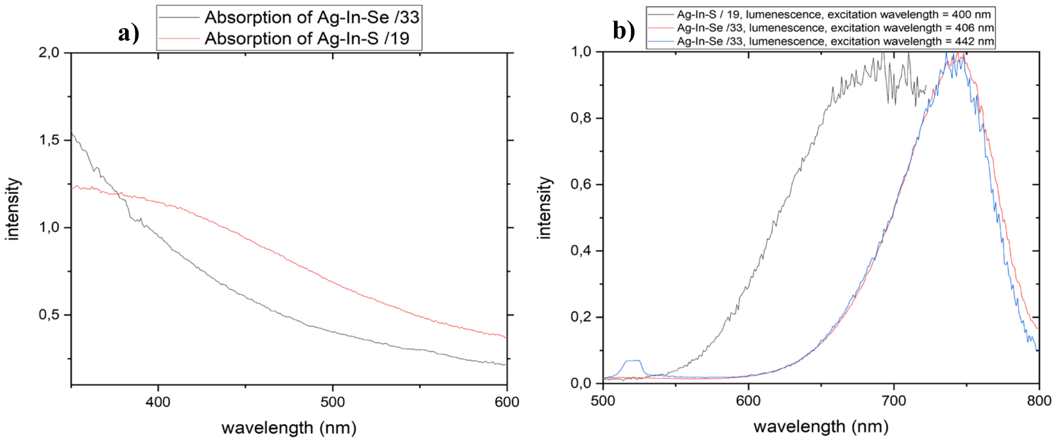

Fig.2. a) UV-vis absorption spectra of Ag-In-Se and AgInS particles: b) normalized luminescence spectra of Ag-In-Se particles excited by 408 and 442 nm and AgInS particles excited by 400 nm.

Both samples demonstrate luminescence at near-IR region. Ag-In-Se sample excited at 406 nm and 442 nm (Fig.2, b, blue and red lines) demonstrates quite intense luminescence with maximum at 747 nm. A weak peak at 520 nm can be glow of the L-cysteine stabilizer. Cysteine in combination with the remains of unbound particles gives a greenish luminescence. For comparison the luminescence spectrum of Ag-In-S particles excited by 400 nm is presented in Fig.2,b. This spectrum is wider with maximum at around 690 nm. Beside this Ag-In-S particles prepared by hydrothermal synthesis method demonstrate more intense and stable luminescence. Despite this, the synthesis method proposed by us is much simpler and more environmentally friendly, with comparable luminescent properties.

References

[1] N. Karunagaran, P. Ramasamy, Synthesis, growth and characterization of AgInSe2 single crystals. Mater. Sci. Semicond. Process. 40 (2015) 591.

[2] Dawei Deng, Lingzhi Qua and Yueging Gu, “Near-infrared broadly emissive $AgInSe_2$/ZnS quantum dots for biomedical optical imaging” from the journal: Sustain. Energy & Fuels 34 (2014) 7077.

[3] Mounir Ait Aouaj, Raquel Diaz, Fouzia Cherkaoui El Moursli, Arturo Tiburcio-Silver, Mohammed Abd-Lefdil. $AgInSe_2$ thin films prepared by electrodeposition process. International Journal of Materials Science and Applications. 4 (2015) 35.

[4] N. Doskaliuk, Y. Babyuk, A. Hotynchan, G. Okrepka and Y. Khalavka. Tuning Optical Properties of $AgInS_2$ Quantum Dots by the Change of Ag-In Stoichiometry for their Light-emitting Applications. *2020 IEEE 10th International Conference Nanomaterials: Applications & Properties (NAP)*, Sumy, Ukraine, 2020, pp. 01NP05-1-01NP05-3, doi: 10.1109/NAP51477.2020.9309659.

OPTICAL CHARACTERIZATION OF COLLOIDAL SOLUTIONS OF Ag-In-S PARTICLES

Kapshuchenko O.[1], Dmytruk A.[2], Karlash A.[1]
[1] *Faculty of Radiophysics, Electronics and Computer Systems, Taras Shevchenko National University of Kyiv, Kyiv 01601, Ukraine. E-mail: oksochkakaps@gmail.com*
[2] *Institute of Physics, National Academy of Sciences of Ukraine, Kyiv 03028, Ukraine*

In this work Ag-In-S particles made by hydrothermal method have been investigated by optical spectroscopy and dynamic light scattering. DLS experiments showed large hydrodynamic radius of particles of about 500-1500 nm. UV-vis spectroscopy demonstrates absorption spectra with a continuous band in the range of 350-600 nanometers. Luminescence spectra showed a large Stokes shift of all the samples and a blue shift of luminescence maximum with increasing of In:Ag molar ratio.

Recently, ternary I–III–VI (I = Cu, Ag; III = In, Ga, Al and VI = S, Se, Te) semiconductor quantum dots have attracted considerable interest due to their compositional and structural versatility and strong photoluminescence (PL) in the visible and near-infrared regions [1]. One of the most famous and effective, but complex method for their synthesis is the hydrothermal method. Hydrothermal synthesis is based on the ability of water to dissolve under the influence of high temperatures (from 100 °C to 500 °C) and pressures greater than 0.1 MPa (reaching almost 100 MPa) [2]. AgInS$_2$ nanoparticles obtained by hydrothermal synthesis have the average size of about 4.69 nm, demonstrate the intense luminescence with a maximum at 650 nm and a quantum yield of 21.6% [3]. In this work optical characterization of colloidal solutions of AgInS$_2$ nanoparticles, prepared at Yuriy Fedkovych Chernivtsi National University [4] was performed by absorption, luminescence and excitation luminescence spectroscopy. All analyses have been carried out using SDL-2 spectrometer. The instrument response functions of the corresponding devices were calculated for the correct analysis of the luminescence and excitation of luminescence spectra. The hydrodynamic sizes of the particles were determined by the technique of dynamic light scattering.

Results and discussion

In this work we present the spectral analysis of ternary semiconductor quantum dots of I–III–VI (I = Ag; III = In, and VI = S) with the various molar ratio of indium to silver. Corresponding characteristics of the studied samples are described in Table 1. Photo of the samples under the laser excitation at 406 nm is shown on Fig.1.

Spectral characterization includes exploration of absorption, luminescence and excitation of luminescence spectra. UV-vis absorption spectra of Ag-In-S colloidal solutions are presented on Fig.2,a. It was observed that an increase in the molar ratio of indium to silver leads to an integral decrease of absorption in visible spectral region with a pronounced decrease in the intensity of the shoulder around 450 nm. Luminescence spectra of Ag-In-S samples under excitation at 420 nm are presented on Fig.2b. Comparing the luminescence spectra, we have found distinct red shift of luminescence maximum with decreasing of In:Ag molar ratio. That is, the AgInS5 sample demonstrates intense luminescence with maximum at 670 nm, AgInS7 peak intensity at 630 nm and AgInS20 at 570 nm.

Table 1 Comparative characteristics of samples

	Sample №1 AgInS20	Sample №2 AgInS7	Sample №3 AgInS5
Molar ratio	20	7	5

Fig.1 Photo of Ag-In-S colloidal solutions with various molar ratio under laser excitation at 406 nm

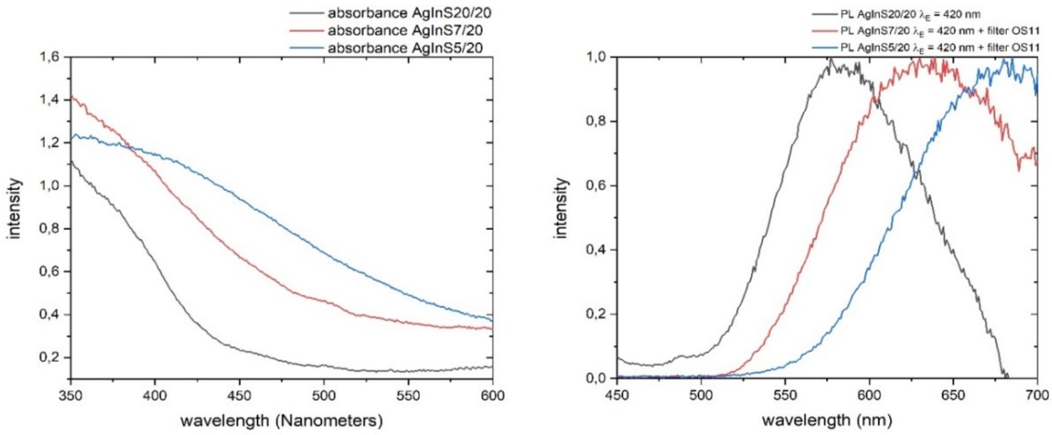

Fig.2 a) absorption spectra of Ag-In-S samples; b) luminescence spectra at 420 nm excitation

The size of the particles was determined by using the technique of dynamic light scattering (DLS). The DLS based on measurements on the time-dependent laser scattered intensity due to translational, or/and internal motions of molecules or particles. As a result, the electric field fluctuations are registered by photodetector. Exploring the autocorrelation function of this signal we calculate the hydrodynamic radius of investigated particles. Different lasers were used to check the correctness of the obtained results based on this technique. Fig. 3 presents the hydrodynamic size distribution of particles Ag-In-S obtained at different laser excitation. It worth to note that obtained hydrodynamic size isn't a real size of explored particles. It usually gives an estimate of the upper size limit.

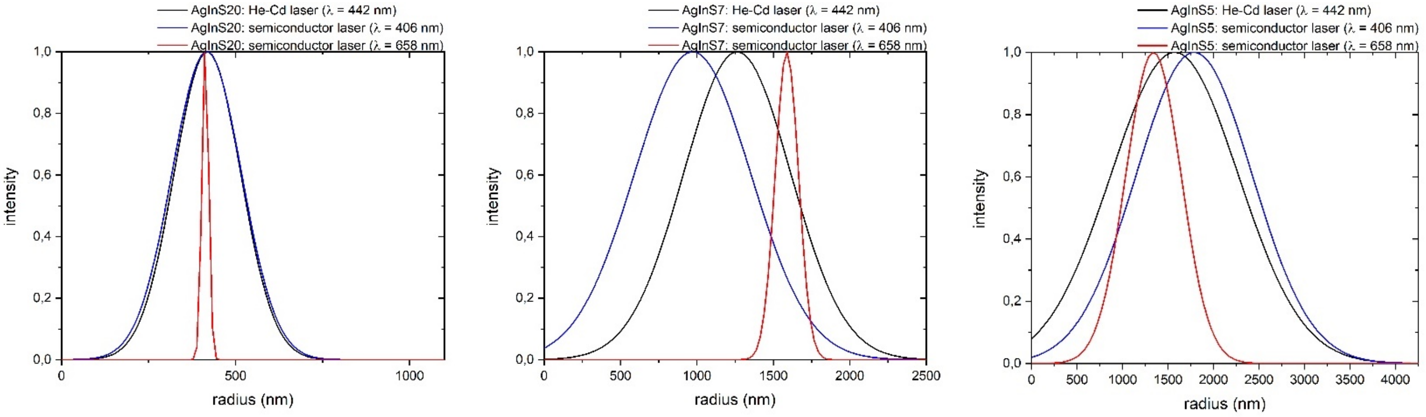

Fig.3 Hydrodynamic size distribution of particles of AgInS20, AgInS7, and AgInS5 colloidal solution

References

[1] Anne C. Berends, Mark J. J. Mangnus, Chenghui Xia, Freddy T. Rabouw, and Celso de Mello Donega. Optoelectronic Properties of Ternary I−III−VI2 Semiconductor Nanocrystals: Bright Prospects with Elusive Origins. J. Phys. Chem. Lett. 2019, 10, 1600−1616, https://doi.org/10.1021/acs.jpclett.8b03653

[2] M.G. Mizilevska V.O. Kotsyubynskyi, O.Kh. Tadeush, V.M. Sachko, O.Yu. Orenchuk Hydrothermal synthesis of nanodispersed titanium dioxide (review). *Physics and Chemistry of Solid State*, *17*(1), 98–107. https://doi.org/10.15330/pcss.17.1.98-107

[3] Hu, X., Chen, T., Xu, Y., Wang, M., Jiang, W., & Jiang, W. (2018). Hydrothermal synthesis of bright and stable AgInS2 quantum dots with tunable visible emission. Journal of Luminescence 2018, 200, 189-195, https://doi.org/10.1016/j.jlumin.2018.04.025

[4] N. Doskaliuk, Y. Babyuk, A. Hotynchan, G. Okrepka and Y. Khalavka. Tuning Optical Properties of AgInS$_2$ Quantum Dots by the Change of Ag-In Stoichiometry for their Light-emitting Applications. *2020 IEEE 10th International Conference Nanomaterials: Applications & Properties (NAP)*, Sumy, Ukraine, 2020, pp. 01NP05-1-01NP05-3, doi: 10.1109/NAP51477.2020.9309659.

SPECTRAL PROPERTIES OF TWO PYRROLOPYRIDINE DERIVATIVES

I. S. Klyuyev *, N. V. Bashmakova *, M. V. Bondar **, G. V. Klishevich **, A. M. Dmytruk, W. Kasprzyk ***, T. Świergosz****.**

**Taras Shevchenko National University of Kyiv, Volodymyrska Street, 60, Kyiv, 01601, Ukraine, email: klyuyev2011@mail.com*

***Institute of Physics National Academy of Sciences of Ukraine, Prospect Nauki, 46, Kyiv, 03028, Ukraine, email: mike_bondar@iop.kiev.ua*

**** Department of Biotechnology and Physical Chemistry, Faculty of Chemical Engineering and Technology, Cracow University of Technology, 24 Warszawska St., 32-048 Krakow, Poland*

*****Department of Analytical Chemistry, Faculty of Chemical Engineering and Technology, Cracow University of Technology, Warszawska 24, 31-155 Kraków, Poland.*

The spectral-luminescence properties of new pyrrolopyridine derivatives obtained under the syntheses of carbon nanodots were investigated in liquid solutions. Important photophysical properties such as extinction coefficient, Stokes shift and fluorescence quantum yield were determined from the absorption and fluorescence spectra. The obtained spectral characteristics of new pyrrolopyridine derivatives indicate the prospects of their application for design of multidisciplinary advanced functional materials.

Comprehensive research of new fluorescent heterocyclic structures with specific functional properties attracts wide interest for broad scientific and technological fields, such as organic optoelectronics [1], biochemical [2] and environmental sensing techniques [3], fluorescence microscopy [4], bioimaging [5], nonlinear optical materials [6], etc. The linear spectroscopic properties, photochemical stability, of new pyrrolopyridines were comprehensively investigated using the spectral methods.

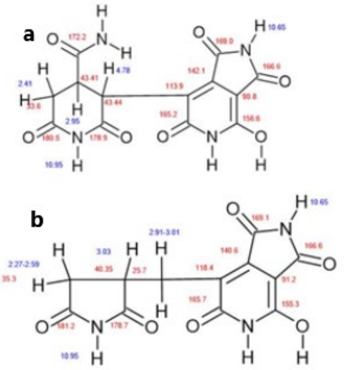

Fig. 1 Chemical formula of the 290_P(a) and 333_P(b).

The structure-property relationships of linear absorption, emission, and excitation anisotropy spectra, 3D fluorescence maps, and the quantum yields of photochemical stability of 290_P and 333_P were obtained for liquid solutions at room temperature. The absorption and fluorescence spectra of new pyrrolopyridines were obtained at room temperature in MeOH and distilled water. The absorption spectra were of structureless shape and exhibited no essential dependence on solvent polarity and relatively small maximum extinction coefficients in the main absorption bands. In spite of the relatively small values of the main absorption bands can be assigned to type electronic transitions from the S_0 state to the excited S_1 electronic state. Nearly constant values of the excitation anisotropy, in the main long wavelength absorption bands of 290_P and 333_P is evidence of the dominant role of the only one electronic transition $S_0 \rightarrow S_1$ in this range. The fluorescence spectra of new pyrrolopyridines exhibited only one structureless emission band, relatively large Stokes shifts.

Samples	$\lambda_{ab}^{\max}$ (nm)	$\lambda_{fl}^{\max}$ (nm)	Stokes shift (nm (cm^{-1}))	$\varepsilon^{max}\cdot10^{-3}$ (M$^{-1}\cdot$cm^{-1})	Φ_{fl}	$\Phi_{ph}\cdot10^{3}$

290_P in MeOH	414	520	106 (≈ 4920)	4.0 ± 0.5	0.53	-
290_P in water	415	540	125 (≈ 5580)	7.5 ± 1.0	0.25	1.2
333_P in MeOH	413	516	103 (≈ 4830)	3.3 ± 0.5	0.58	-
333_P in water	413	536	123 (≈ 5560)	3.6 ± 0.5	0.30	0.8

Photostability of pyrrolopyridines 290_P and 333_P was investigated in air-saturated distilled water at room temperature. Values of φ_{ph} in water were in the range of $\sim 10^{-3}$ and sufficiently close to each other. It should be mentioned that obtained level of photochemical stability is not so high as for typical laser dyes but acceptable for practical use.

Conclusions

Absorption, fluorescence and excitation spectra of pyrrolopyridines derivatives in water and methanol solutions were obtained. Important photophysical properties such as extinction coefficient, Stokes shift and fluorescence quantum yield were determined from the absorption and fluorescence spectra. Linear spectra of one-photon absorption are characterized by a relatively small extinction coefficient $\varepsilon \sim 10^{-3}$ $M^{-1}*cm^{-1}$. The fluorescence spectra are not depended on the excitation wavelength and no signs of violation of Kasha's rule were observed. The photodecomposition spectra of the samples were studied. The quantum yield of photodecomposition was determined for 290_P and 333_P in water. It is at the level of $\varphi_{ph} \sim 10^{-3}$, which is acceptable for practical use. The value of the fundamental excitation anisotropy of the samples was measured. It was found that in all samples a constant value of anisotropy r is observed in the contour of the main long-wave absorption, which indicates that within this contour only one electronic transition $S_0 \rightarrow S_1$ plays the main role.

References

1. J.-L. Wu, Y.-T. Lee, C.-T. Chen and C.-T. Chen, J. Chin. Chem. Soc., 2018, 65, 87-106.
2. M. Kumar, A. Rastogi, Raziullah;, A. Ahmad, M. K. Gangwar and D. Koley, Org. Lett., 2022, 24, 8729-8734.
3. W. Zhang, G. Li, L. Xu, Y. Zhuo, W. Wan, N. Yan and G. He, Chem. Sci., 2018, 9, 4444-4450.
4. Y. Cao, X. Liu, J. Zhang, Z. Liu, Y. Fu, D. Zhang, M. Zheng, H. Zhang and M.-H. Xu, ACS Chem. Neurosci., 2023, 14, 829-838.
5. G. S. M. Sundaram, K. Binz, V. Sharma, M. Yeung and V. Sharma, Med. Chem. Commun., 2018, 9, 946-950.
6. N. Arif, Z. Shafiq, S. Noureen, M. Khalid, A. Ashraf, M. Yaqub, S. Irshad, M. U. Khan, M. N. Arshad, A. A. C. Braga, A. H. Ragab and S. R. Al-Mhyawi, RSC Adv., 2023, 13, 464-477.

CREATION OF SOURCES OF COHERENT RADIATION ON THE BASIS OF CHANNELING OF ELECTRONS IN AN OPTICAL LATTICE

Vladyslav Desiak*, Mykhaylo Vysotskyy **
**Taras Shevchenko National University of Kyiv, Kyiv, e-mail: phvladkt@gmail.com*
***Taras Shevchenko National University of Kyiv, Kyiv, e-mail: mihas@knu.ua*

This study investigates the phenomenon of electron channeling through optical lattices generated in crossed laser fields and evaluates the possibility of creating sources of coherent stimulated emission based on such a system. The importance of the problem is primarily associated with the necessity of developing laser sources for the X-ray range. Traditional free-electron lasers operating in the X-ray range are complex and expensive systems, making the possibility of creating alternative methods for generating coherent high-frequency radiation an important task in modern physics.

Introduction

It is well known that when an electron enters a crystal at a small angle (Lindhard angle) with a selected orientation, it experiences a periodic force that shifts it towards the center of the channel. The electron undergoes scattering with a large value of the impact parameter, as a result, the path length in the crystal significantly increases. This phenomenon is known as electron channeling [1]. Electron channeling in crystals has been studied for a long time. However, in the work [2] the possibility of electron diffraction in the field of a standing wave (optical lattice, Fig. 1) was theoretically described. When a beam of relativistic electrons falls on an optical lattice, population inversion is possible, providing a potential opportunity to create a source of coherent high-frequency radiation (laser).

Stimulated emission from an optical lattice

The effective potential of the optical lattice for an electron can be obtained classically using the Kapitza formalism [3]. However, this method cannot be directly applied to a relativistic electron. Nonetheless, it is possible to transform to other coordinates using generating function $S = (z - \vartheta_0 t)P_z'$ [4]. Then, from the Hamiltonian equations, the equation of motion can be derived, from which the effective potential was obtained:

$$U_{eff}(x) = -\frac{{A_0}^2 e^2 k^2}{m\gamma_0\omega_0^2} f(\beta,\alpha)\cos\big(kx\cos(\alpha)\big), \text{ here } \beta = \frac{\vartheta_0}{c}, \gamma_0 = \frac{1}{\sqrt{1-\beta^2}}, k = \frac{\omega_0}{c},$$

$$f(\beta,\alpha) = \left(\frac{\beta - \sin(\alpha)}{1 - \beta\sin(\alpha)}\right)^2 - \frac{1}{2};$$

where ϑ_0, A_0, k are initial velocity of electron, vector potential, and wave vector of laser radiation.

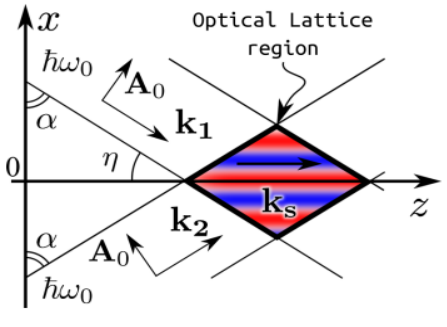

Fig. 4. Scheme of the formation of an optical lattice [4].

In the general case, when studying the motion of relativistic electrons in an optical lattice, it is necessary to solve the Dirac equation. However, it can be transformed into a second-order equation, which is similar to the Schrödinger equation [5]:

$$\left(-\frac{\hbar^2}{2m\gamma}\frac{\partial^2}{\partial x^2} + U_{eff}(x)\right)\psi = E_{\perp n}\psi.$$

In the semiclassical approximation we can obtain estimates of the maximum number of levels in the optical lattice, the distance between energy levels as a function of the level number, and the dispersion equation. For typical values of laser radiation that create an optical lattice $I \sim 10^{15}\frac{W}{cm^2}$, $\omega_0 \sim 10^{15} s^{-1}, \gamma_0 \sim 10^3$, the maximum number of levels can be estimated to be $n_{max} \sim 5 \cdot 10^4$.

The magnitude of level splitting for levels with small quantum numbers is the following:

$$\Delta\varepsilon \sim \left[-\frac{2}{\hbar}\int_{x_0}^{a/2} |p(x)|dx\right]\cos(ka)\text{, where } a \text{ is channel width, } x_0 \text{ is turning point.}$$

The results obtained above demonstrate that near the bottom of the channel, the effective potential can be approximated by a parabolic potential as followed: $U_{eff}(x) \approx \frac{m\gamma\Omega_0^2}{2}x^2$, where $\Omega_0 = \frac{eA_0kcos(\alpha)}{mc\gamma_0}\sqrt{8f(\alpha,\beta)}$ is transition central frequency; the number of levels in the system is large; the spreading of the levels near the bottom of the channel is small. Also, the quantum peculiarities of particle motion in the effective potential become much more pronounced at low energies (near the bottom of the channel). Therefore, for further calculations we have used the harmonic oscillator approximation.

The population inversion coefficients are determined as follows [6]:

$$C_n = \int_{-\frac{a}{2}}^{\frac{a}{2}} \psi_{\boldsymbol{k}'}^{out}(x, z = 0)\psi_n(x)dx.$$

It is appropriate to choose the wave function of the beam before entering the lattice in the form of a Gaussian beam:

$$\psi_{\boldsymbol{k}'}^{out}(x,z) = \int_{-\infty}^{\infty} f(k_x')e^{-ik_x'x - ik_z'z}dk_x', f(k_x') = f_0 \exp\left(-\frac{(k_x' - k_{x0}')^2}{\Delta k_x'^2}\right),$$

where k_x' is electron wave vector, $\Delta k_x'$ is electron wave vector dispersion.

Parameters for the beam were selected in such a way that a great population inversion is observed when electrons enter the channel (Fig. 2).

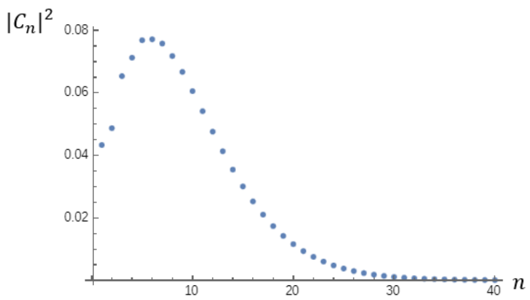

Fig. 5. Population inversion coefficients

The gain coefficient of stimulated emission is determined as follows:

$$\alpha_a = \frac{\pi^2c^2}{\Omega_0^2\tau}g(\Omega)(N_n - N_m),$$

where $g(\Omega)$ – emission line shape, τ – time of spontaneous decay, N_n – level n electron concentration.

The main mechanism for line broadening is the non-monochromaticity of the electron beam. Assuming that the energy distribution in the electron beam follows a Gaussian distribution, we can obtain:

$$g(\Omega) = \frac{g_0}{\sqrt{2\pi}\Delta\gamma}exp\left[-\frac{\left(\frac{g_0}{\Omega} - \gamma_0\right)^2}{2\Delta\gamma^2}\right]\frac{1}{\Omega^2},$$

where $g_0 = \frac{eA_0kcos(\alpha)}{mc}\sqrt{8f(\alpha,\beta)}$, $\Delta\gamma$ – energy dispersion.

Thus, for typical parameters $\delta = \frac{\gamma_{FWHM}}{\gamma_0} \sim 1\%, I \sim 10^{15}\frac{W}{cm^2}$, $\omega_0 \sim 10^{15}s^{-1}, \gamma_0 \sim 10^3$ [7,8], the line broadening at half maximum is $\Omega_{FWHM} \sim 10^9\ s^{-1}$; the transition central frequency in the electron system is $\Omega_0 \sim 10^{10}s^{-1}$.

Levels 2 and 3 were selected as working transitions. For typical values of the electron beam concentration $N_0 = 10^{10} \div 10^{18}\ cm^{-3}$ [7,8], the gain coefficient was calculated, which, considering the broadening, was in the range $\alpha_a \approx 10^{-5} \div 10^3 cm^{-1}$ At the same time, the maximum radiation frequency due to the Doppler effect in the laboratory system for such a system is $\Omega_1 \approx \Omega_0 2\gamma_0^2 \approx 3 \cdot 10^{17}\ s^{-1}$.

Conclusion

It has been demonstrated that the electron channeling effect in an optical lattice can be used to create sources of coherent high-frequency radiation. For typical parameters of laser radiation forming the optical lattice and optimal characteristics of the electron beam, the gain coefficient $\alpha_a \approx 10^{-5} \div 10^3 cm^{-1}$ indicates that such a system can be used to create promising laser sources in the X-ray range, which could compete with free-electron lasers in terms of performance. In our opinion, the optimal way to increase the gain coefficient lies in the usage of electron beams with higher electron concentrations.

References

[1] J.U. Andersen. Channeling and Blocking of Energetic Particles in Crystals. In: Particle Penetration and Radiation Effects Volume 2. Springer Series in Solid-State Sciences, vol 179. Springer (2014).

[2] P. L. Kapitza and P. A. M. Dirac, Math. Proc. Cambridge Philos. Soc. 29, 297 (1933).

[3] L.D. Landau and E.M. Lifshitz, The theoretical physics, Nauka 1, (1988)

[4] S. B. Dabagov A. V. Dik and E. N. Frolov. Channeling of electrons in a crossed laser field,Phys. Rev.ST Accel. Beams 18 (2015) 064002.

[5] V. G. Baryshevsky. Channeling, radiation and reaction in crystals at high energies, BGU Publ., (1982).

[6] Vysotskii, V., Vysotskyy, M. Peculiarities of influence of coherency processes at charged particles channeling on particle beams characteristics. EPAC 2006 - Contributions to the Proceedings, 2006, pp. 2041–2043.

[7] Lu, G., Li, Y., Hu, X., Chen, S., Xu, H., Zhu, M., Yan, W., & Chen, L. Divergence Angle Consideration in Energy Spread Measurement for High-Quality Relativistic Electron Beam in LWFA. Chinese Physical Society and IOP Publishing Ltd (2024).

[8] M. Iinuma. Experiments on beam deflection Experiments on beam deflection by crystal. Crystal Channeling for Large Colliders: Machine and Physics Applications. Mar 23, 2007.

STUDY OF PHOTOLUMINESCENCE IN RARE EARTH-DOPED CHALCOGENIDE SEMICONDUCTORS

O.V. Machulianskyi, V.V. Buteiets*****

** National Technical University of Ukraine "Igor Sikorsky Kyiv Polytechnic Institute"*
*Kyiv, Ukraine-, e-mail: ** machulansky@gmail.com, *** v.buteiets-me25@lll.kpi.ua*

In this work, the optical absorption spectra of single crystals were investigated $(Ga_{70}La_{30})_2S_{300}$, $(Ga_{69,75}La_{29,75}Er_{0,5})_2S_{300}$ *in the range of 600-1050 nm.*

The study of complex chalcogenide systems and crystalline compounds, particularly rare-earth-doped chalcogenide semiconductors, is an important component of modern materials science that investigates semiconductor compounds. These materials combine high transparency in the visible and near-infrared spectral range, low phonon energy, and relatively high solubility of rare-earth metals in both crystalline and amorphous environments.

Photoluminescence spectroscopy provides a powerful tool for elucidating the formation pathways of energy levels in rare-earth metal ions and analyzing transitions between excited states. These materials are promising for applications in photonic devices, lasers, optical amplifiers, light converters, as well as electro-optical switches and memory elements.

Investigating the optical properties of single crystals $(\mathrm{Ga}_{70}\mathrm{La}_{30})_2\mathrm{S}_{300}$, $(\mathrm{Ga}_{69,75}\mathrm{La}_{29,75}\mathrm{Er}_{0,5})_2\mathrm{S}_{300}$, is an important task that will enable the development of efficient materials for optoelectronics. Therefore, the aim of this work is to study the photoluminescence of single crystals $(\mathrm{Ga}_{70}\mathrm{La}_{30})_2\mathrm{S}_{300}$, $(\mathrm{Ga}_{69,75}\mathrm{La}_{29,75}\mathrm{Er}_{0,5})_2\mathrm{S}_{300}$ *in the range of 600-1050 nm.*

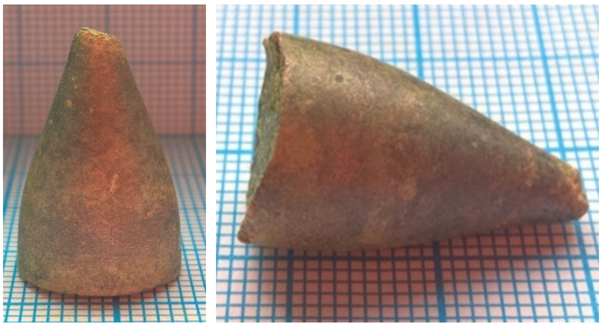

Single crystals $(\mathrm{Ga}_{70}\mathrm{La}_{30})_2\mathrm{S}_{300}$, $(\mathrm{Ga}_{69,75}\mathrm{La}_{29,75}\mathrm{Er}_{0,5})_2\mathrm{S}_{300}$ were grown by the flux-melt method from their primary crystallization region. The synthesis of the starting alloys at a maximum temperature of 1200 K and crystal growth were carried out in the same evacuated quartz container with a conical bottom. The growth process was carried out in a vertical two-zone furnace. The maximum temperature was 1200 K, and the temperature gradient at the crystallization front was 20 K/cm. After melting the charge, the ampoule was lowered at the maximum rate until the bottom of the ampoule reached the undercooling temperature. After crystallization of 10 mm of the melt along the length of the ampoule, growth was stopped, and then 6.0-8.0 mm of the crystallized melt was melted back and annealed for 100 hours. Then, the single crystal was grown at a lowering rate of 5 mm/day. After the completion of the process, both furnaces were cooled to 820 K at a rate of 50-70 K/day and the resulting single crystal was annealed for 100 hours.

The single crystals $(\mathrm{Ga}_{70}\mathrm{La}_{30})_2\mathrm{S}_{300}$, $(\mathrm{Ga}_{69,75}\mathrm{La}_{29,75}\mathrm{Er}_{0,5})_2\mathrm{S}_{300}$ have a grayish color, a diameter of 15 mm, and a length of 24 mm. The middle part of these single crystals was chosen for the study of optical properties. For the studies, they were given the form of plane-parallel plates with a thickness of d2=0.6±0.02 mm. The samples were ground and polished with abrasive powders and diamond pastes.

Photoluminescence studies were carried out using an MDR-206 monochromator and a silicon photodetector. Excitation was provided by a diode laser with a power of 400 mW and an emission maximum of 800 nm. Both excitation and detection were performed from the same surface of the sample.

Laser 1 emits electromagnetic radiation in the optical range, which falls on sample 4. The photo luminescent electromagnetic radiation in the optical range emitted by the sample is focused by mirror condenser 3 onto the

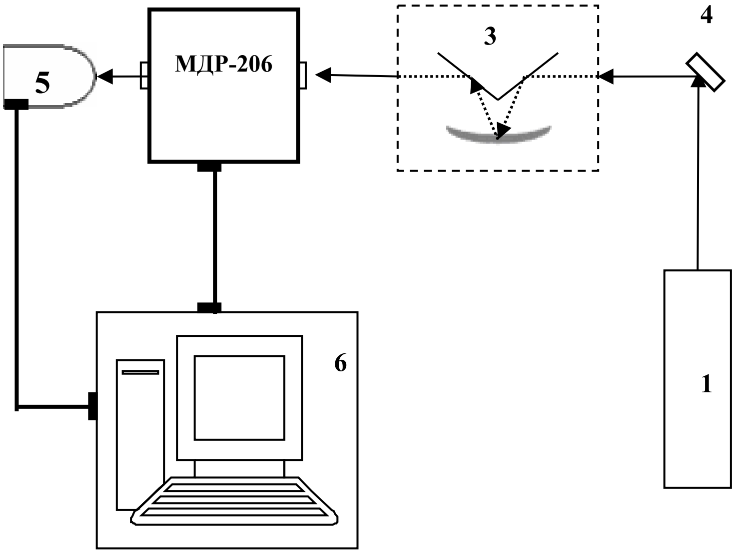

entrance slit of monochromator 2. From the exit slit of the monochromator, the beam reaches the photodetector, which registers the signal and converts the analog signal into a digital one and sends it to the computer monitor.

1 – Diode laser;
2 – MDR-206 monochromator;
3 – Mirror condenser;
4 – Sample;
5 – Silicon photodetector;
6 – Computer.

Under excitation by a laser with a power of 400 mW and a wavelength of 800 nm, anti-Stokes photoluminescence was observed in the spectral range of 510–560 nm. The emission spectrum consists of two peaks at 525 and 545 nm.

It has been determined that doping with a rare-earth metal (Erbium) shifts the absorption edge of electromagnetic radiation in the optical range towards the infrared spectral range. $(Ga_{69,75}La_{29,75}Er_{0,5})_2S_{300}$ can be recommended as an infrared signal converter to the visible range, but this requires further research.

References

1. 1. Fedotov V. V. Modern state of research on the optical properties of semiconductor materials [Text] / V. V. Fedotov // Technological audit and production reserves. - 2014. - No. 6/1. - P. 15-22;
2. Prokopiv V.V. Materials of electronic equipment [Text]: education. manual / VV Prokopiv. – Ivano-Frankivsk: Prykarpattia National University named after Vasyl Stefanyk, 2009. – 288p.
3. Frish S.E. Optical spectra of atoms [Text]: textbook / S.E. Frisch - St. Petersburg: "Lan" Publishing House, 2010. - 640 p.

POLARIMETRY: THEORY AND APPLICATIONS

POLARIZATIONAL PROPERTIES OF DEPOLARIATIVE MEDIUM WITH CIRCULAR AMPLITUDE ANISOTROPY

O.O. Bondiuchna*, I. S. Kolomiets, S. N. Savenkov, Ye. A. Oberemok
Faculty of Radiophysics, Electronics and Computer Systems, Taras Shevchenko National University of Kyiv,
64/13, Volodymyrska Str., Kyiv, Ukraine, 01601
** helen.bondiychna@gmail.com*

The class of depolarizing media with circular amplitude anisotropy was considered. Conditions for the parameters of anisotropy, and depolarization of the medium in which the differential Mueller matrix method can be applied, have been obtained. The integral Mueller matrix for this class of medium was calculated. The peculiarities of eigenwaves propagation in this class of medium were investigated.

Polarimetry is an effective technique for exploring the optical characteristics of various objects, including biological ones [1,2]. There is a significant interest in these materials due to their ability to depolarize light, particularly through anisotropic depolarization. This phenomenon refers to how the degree of depolarization varies based on the medium's change from the initial polarization state [3,4]. Anisotropic depolarization typically results from the anisotropic features within the medium. To analyze this, examining the solutions to spectral problems [4] proves invaluable, as these solutions reveal fundamental information about the eigenwaves. The primary objective of this study was to assess the polarization characteristics of a depolarizing medium characterized by circular amplitude anisotropy, utilizing the solutions to a spectral problem for this specific type of media.

The differential Mueller method is well-suited for characterizing the anisotropic and depolarizing properties of a medium. This method's utility stems from how its matrix elements correspond to various anisotropy types and their related depolarization effects. For example, a homogeneous medium exhibiting depolarization due to circular amplitude anisotropy can be effectively described using the following differential Mueller matrix [5]:

$$\mathbf{m}=\begin{bmatrix} \xi_0 & 0 & 0 & r_0+d_3 \\ 0 & \xi_0-d_7 & 0 & 0 \\ 0 & 0 & \xi_0-d_8 & 0 \\ r_0-d_3 & 0 & 0 & \xi_0-d_9 \end{bmatrix}, \qquad (1)$$

where the $r_0=\dfrac{2\pi}{\lambda}\left(k_l-k_r\right)$ - value of circular amplitude anisotropy, k_r, k_l absorption coefficient for wave with right and left polarizations respectively, $\xi_0=\dfrac{2\pi}{\lambda}k$ - isotropic absorption, d_3 - parameter of anisotropy depolarization, $d_{7,8,9}$ - parameters of isotopic depolarization.

According to the findings in [6], a 4x4 matrix must meet certain criteria to qualify as a Mueller matrix. Specifically, it is both necessary and sufficient that the eigenvalues of the corresponding 3x3 coherence matrix **C** are non-negative. These eigenvalues derive from functions of the elements within the differential Mueller matrix. By substituting the elements of Mueller matrix (1) into the coherence matrix, it has been determined that the non-negative of these eigenvalues is a critical condition **C** :.

$$\begin{cases} d_9 \le d_7+d_8 \\ 4d_7d_8 \ge \left(d_3+r_0\right)^2 \\ d_9>0 \\ \xi_0 \ge d_3+r_0 \end{cases} \qquad (2)$$

To calculate the integral Mueller matrix, a vector transport equation for the Stokes **S** vector $\dfrac{d\mathbf{S}(z)}{dz}=\mathbf{mS}(z)$ was used. Substituting the elements of the differential Mueller matrix (2) into the vector transport equation, and solving it with the initial conditions: $S_1(0)=S_{10}, S_2(0)=S_{20}, S_3(0)=S_{30}, S_4(0)=S_{40}$ on the method presented in [7], we obtained the following integral Mueller matrix:

$$M=\begin{bmatrix} e^{-\frac{d_9 z}{2}+z\xi_0}\left(\cosh\left(\frac{Az}{2}\right)+\frac{d_9\sinh\left(\frac{Az}{2}\right)}{A}\right) & 0 & 0 & \frac{2e^{-\frac{d_9 z}{2}+z\xi_0}(d_3+r_0)\sinh\left(\frac{Az}{2}\right)}{A} \\ 0 & e^{(\xi_0-d_7)z} & 0 & 0 \\ 0 & 0 & e^{(\xi_0-d_8)z} & 0 \\ -\frac{2e^{-\frac{d_9 z}{2}+z\xi_0}(d_3-r_0)\sinh\left(\frac{Az}{2}\right)}{A} & 0 & 0 & e^{-\frac{d_9 z}{2}+z\xi_0}\left(\cosh\left(\frac{Az}{2}\right)-\frac{d_9\sinh\left(\frac{Az}{2}\right)}{A}\right) \end{bmatrix}, \quad (3)$$

where $A=\sqrt{-4d_3^2+d_9^2+4r_0^2}$.

By solving the spectral problem for a given class of media [3], the following eigenvalues and the Stokes vectors of the eigenpolarization of the medium were obtained:

$$V_{1,2}=e^{\pm z\sqrt{r_0^2+d_9^2-4d_3^2}} \quad (4)$$

$$\mathbf{S}_{1,2}=\begin{bmatrix} 1 \\ 0 \\ 0 \\ \pm 1 \end{bmatrix} \quad (5)$$

Analyzing the obtained results, it can be noted that in this class of media with different phase velocities, different absorption and different degrees of depolarization, the left and right circularly polarized waves propagate.

Conclusions

The investigation into the polarization properties of a homogeneous depolarizing medium with circular amplitude anisotropy identified specific conditions for anisotropy and depolarization parameters that allow for description using the differential Mueller method. By solving the vector transport equation, an integral Mueller matrix was computed, detailing the polarization and depolarizing properties of the medium with a finite thickness. Furthermore, the solving of a spectral problem revealed that within this type of media, both right and left circularly polarized waves propagate, each characterized by distinct phase velocities, absorption rates, and degrees of depolarization.

References

[1] Shurcliff W.A. Polarized light-production and use / Shurcliff W.A. - Harvard: Harvard University Press, 1962 - 207 p.

[2] J.W. Hovenier, C.V.M. van der Mee, H. Domke, Transfer of polarized light in planetary atmospheres: basic, concepts and practical methods. Dordrecht: Springer, 2004.

[3] Azzam R.M. Ellipsometry and Polarized Light / R.M. Azzam, N.M. Bashara. - New York: North-Holland Publishing Company, 1977. – 584 p.

[4] Effective dichroism in forward scattering by inhomogeneous birefringent medium / S. N. Savenkov et al. // JQSRT. – 2009. – Vol.110, Iss.1-2. – P. 30-42.

[5] Ossikovski1 R., General criterion for the physical realizabi / R. Ossikovski1, V. Devlaminck // Opt. Lett. - 2014. - Vol. 39, No. 5. - P. 1216 - 1219.

[6] Azzam R.M.A. Propagation of partially polarized light through anisotropic media with or without depolarization. A differential 4 X 4 matrix calculus / R.M.A. Azzam // J. Opt. Soc. Am. - 1979. - Vol.68. - P. 1756 - 1767.

FEATURES OF PRIVILEGED POLARIZATIONS IN LONGITUDINALLY INHOMOGENEOUS MEDIA WITH LINEAR AMPLITUDE ANISOTROPY

D. V. Zabolotniy*, I. S. Kolomiets, S. N. Savenkov, Ye. A. Oberemok
Faculty of Radiophysics, Electronics and Computer Systems, Taras Shevchenko National University of Kyiv,
64/13, Volodymyrska Str., Kyiv, Ukraine, 01601
**nati.zajka@gmail.com*

The physical model of a longitudinally inhomogeneous anisotropic medium with linear amplitude anisotropy is considered. The differential Jones matrix which describes the anisotropy of an infinitely thin medium layer for the studied class of media is constructed. The equation for the evolution of the state of light polarization for this class of media was calculated. The polarization states of the privileged waves are calculated. The specifics of these polarization states are studied.

The history of investigation of inhomogeneous nondepolarizing media returns us to [1]. This problem was solved using the Jones matrix methods [2] where was considered type of longitudinal inhomogeneous medium with linear phase anisotropy. Particularly in [2] were considered examples of these medium. It was cholesteric liquid crystals and twisted nematics. Development of modern displays technology led to the fact that these types of liquid crystals very widely used [3]. However, as we know [4] for certain wavelengths in different types of cholesteric liquid crystals and twisted nematics besides linear phase anisotropy occurs as linear amplitude anisotropy. One of the main features of the anisotropy arising in longitudinally inhomogeneous twisted media are waves with privileged polarization states which propagate in such media as in the optically active media. To studding the features of such polarization in longitudinal inhomogeneous media with linear amplitude anisotropy the main goal of this work.

A non-depolarizing longitudinally inhomogeneous medium with linear amplitude anisotropy, by analogy with a medium with linear phase anisotropy [5], can be represented by a sequence of linear polarizers (thickness of this polarizers is considered to be much smaller than the size of the medium in the direction of light propagation), each rotated to the previous one by the same angle θ_0, as shown in Fig. 1

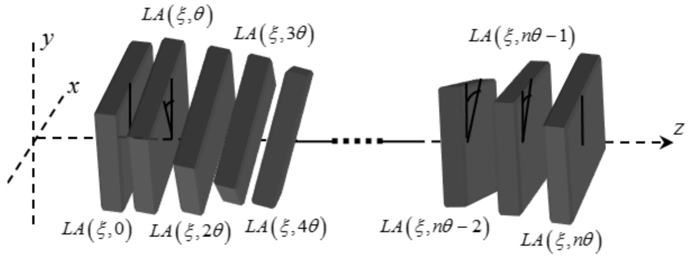

Fig. 1. Equivalent representation of a longitudinally inhomogeneous medium with linear amplitude anisotropy

On Fig. 1, all polarizers are identical and characterized by the same value of linear amplitude anisotropy $\xi = \frac{2\pi}{\lambda}\left(k_0 - k_e\right)z = \xi_0 z$, where k_0, k_e - absorption coefficients of ordinary and extraordinary waves, λ - wavelength of light and z - length of the medium in the direction of light propagation. The polarization properties of each polarizer can be described by the differential Jones matrix:

$$N = \frac{1}{2}\xi_0 \begin{bmatrix} 0 & e^{2i\theta_0 z} \\ e^{-2i\theta_0 z} & 0 \end{bmatrix}, \qquad (1)$$

To describe the evolution of the light polarization state in this class of media, instead of the transport vector equation, a scalar differential equation for a complex variable χ can be used [1]:

$$\frac{d\chi}{dz} = -N_{12}\chi^2 + \left(N_{22} - N_{11}\right)\chi + N_{21}. \qquad (2)$$

By substituting the elements of the differential matrix (1) in equations (2), the following equation was obtained:

$$d\chi / dz = -\frac{1}{2}\xi_0^{-2i\theta_0 z}\left(\xi_0^{4i\theta_0 z}\chi^2 - 1\right) \qquad (3)$$

One of the features of longitudinal inhomogeneous media is the remoteness of the eigenstates of wave polarization. However, this class of media is characterized by the privileged waves, the polarizations states of which (privileged polarizations) do not change the angle of ellipticity, but uniformly and continuously change their azimuth with each subsequent plane (polarizer) by the angle θ_0 of its return to the previous plane. To calculate the privileged polarizations, solutions of equation (3) are sought in the form $\chi_{1,2} = K_{1,2}e^{-2i\theta_0 z}$. As a result, the following dependences of the complex variables of the privileged polarizations on the anisotropy parameters of the medium were calculated:

$$K_{1,2} = \frac{2i\theta_0}{\xi_0} \pm \sqrt{\left(\frac{2i\theta_0}{\xi_0}\right)^2 + 1}, \qquad (4)$$

On Fig. 2 shows the dependence of the azimuth and ellipticity angle of the privileged polarizations (4) on the coordinate *z* in the direction of light propagation calculated on the basis of the formulas presented in [5]:

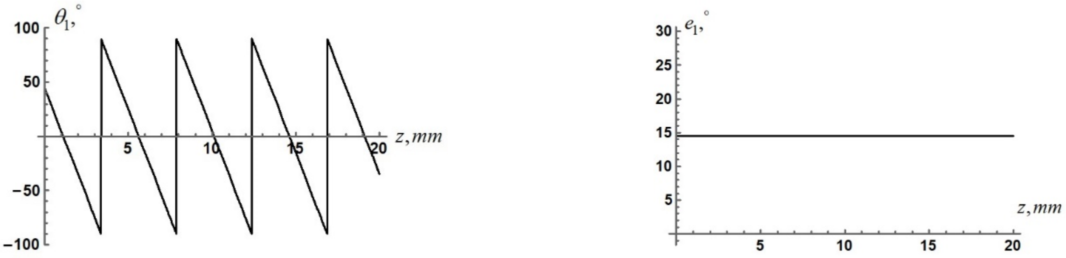

a ***b***

Fig. 2. Evolution of the azimuth a) and ellipticity angle b) of the privileged polarization with the coordinate z in a longitudinally inhomogeneous medium with linear amplitude anisotropy.

Analyzing equations (4) the following result was obtained:

1) At $4\theta_0^2 < \xi_0^2$, $K_{1,2}$ are two non-orthogonal linear privileged polarizations.

2) At $4\theta_0^2 = \xi_0^2$ we have $K_1 = K_2$ - the privileged polarizations coincide (degenerate case) and correspond to linear polarization with orientation 45 degree.

3) At $4\theta_0^2 > \xi_0^2$, $K_{1,2}$ are two nonorthogonal elliptical polarizations with the same orientation azimuth.

Conclusions

The class of longitudinally inhomogeneous media with linear amplitude anisotropy is characterized by the existence of prevailing polarizations. Such polarization states are generally non-orthogonal, and also, under the conditions established in this paper, they can be linear, elliptical, or even coincident.

References

[1] A.S. Marathay Matrix-Operator Description of the Propagation of Polarized Light through Cholesteric Liquid Crystals, *J. Opt. Soc. Am*, vol. 61, pp. 1363 – 1372, 1971.

[2] R.M.A Azzam., N.M. Bashara. Simplified Approach to the Propagation of Polarized Light in Anisotropic Media-Application to Liquid Crystals, *J. Opt. Soc. Am*., vol 62, pp. - 1252 – 1257, 1972.

[3]. P. García-Martínez, M. del Mar Sánchez-López et al. Accurate color predictability based on a spectral retardance model of a twisted-nematic liquid-crystal display, *Optics Communications*, vol 284, pp. 2441-2447, 2011.

[4]. S. Chandrasekhar, *Liquid crystals*. Cambridge University Press, 1980.

[5] R.M.A. Azzam, "Propagation of partially polarized light through anisotropic media with or without depolarization. A differential 4 X 4 matrix calculus," J. Opt. Soc. Am., vol. 68, pp. 1756-1767, 1979.

AUGMENTED REALITY IN LABORATORY WORK

O. Ivanyuta, A. Zheludkov
Taras Shevchenko National University of Kiyv, 64, Volodymyrska str., Kiyv, 01033, Ukraine
E-mail: oleksandr.ivanyuta@knu.ua

This study explores the application of augmented reality (AR) in the realm of education, specifically in conducting laboratory work. Created laboratory works with augmented reality on the topic "Measurement of dependence of metal and semiconductor resistance on temperature", "Research of gas discharge plasma" and "Hall effect"

Laboratory work is a fundamental component of the educational process, as it enables students to apply theoretical knowledge in a practical setting, thereby fostering critical thinking and problem-solving abilities. However, the increasing demand for educational flexibility and global accessibility necessitates the development of innovative approaches to laboratory instruction.

The utilisation of augmented reality (AR) in laboratories facilitates interactive sessions, thereby enabling students to explore scientific phenomena in a safe and controlled environment.

By selecting Unity as the primary tool, we crafted detailed scenarios utilising AR, simulations, and emulations, which are vital for promoting an interactive and active learning process.

The primary objective was to develop laboratories on topics such as "Measuring the temperature dependence of resistance in metals and semiconductors", "Investigating gas discharge plasma" and "The Hall effect."

For each laboratory activity, a scheme of the setup was depicted, enabling the experiment process to be controlled using augmented reality. Additionally, a graph and a table were available on the desktop, offering functionality for data analysis.

For example, for the work "Measuring the temperature dependence of resistance in metals and semiconductors", a model was developed that simulates the process of measuring the electrical resistance versus temperature for various materials, including metals and semiconductors.

Fig. 1 shows the instruments and measuring devices that display the calculated values during the simulation. The heating rate is set by the heater power supply. For a better effect of a real experiment, the ability to set the noise level has been added. Data analysis can be performed using the least squares method, and for semiconductor material, the graph can be linearised for LSM analysis.

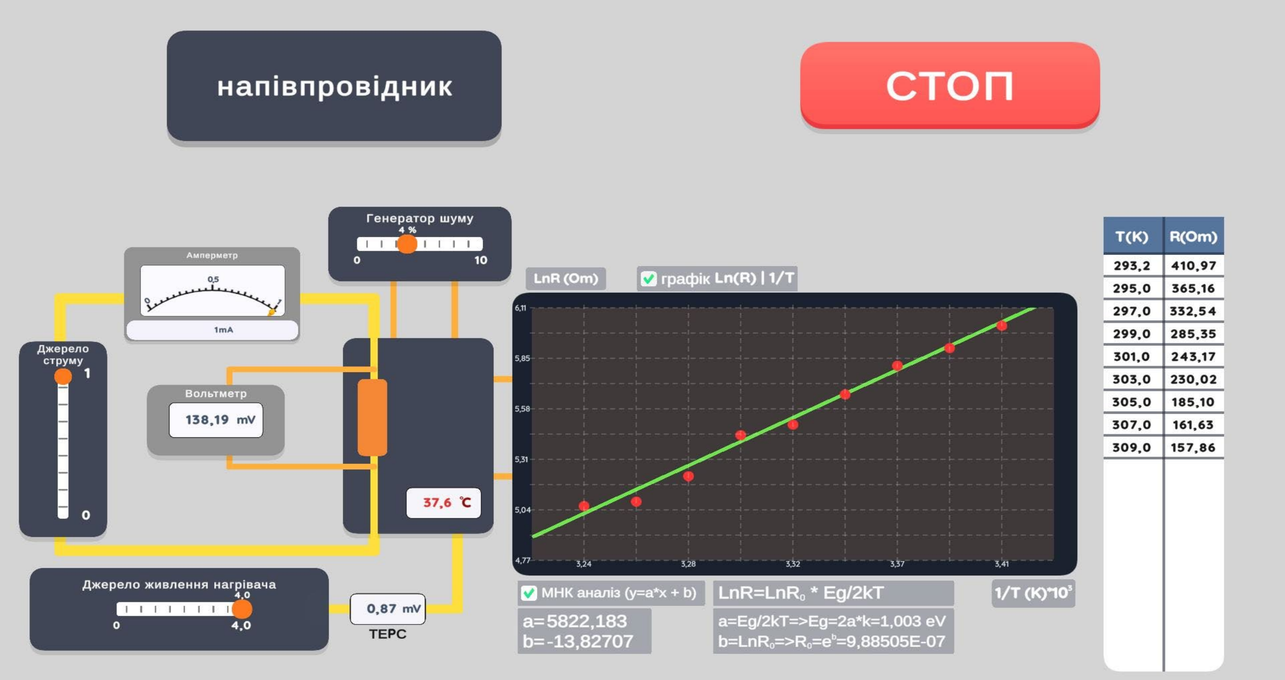

138,19 mV

37,6 ℃

0,87 mV

T(K)	R(Om)
293,2	410,97
295,0	365,16
297,0	332,54
299,0	285,35
301,0	243,17
303,0	230,02
305,0	185,10
307,0	161,63
309,0	157,86

a=5822,183
b=-13,82707

$LnR=LnR_0 * Eg/2kT$
$a=Eg/2kT=>Eg=2a*k=1{,}003$ eV
$b=LnR_0=>R_0=e^b=9{,}88505E-07$

Fig. 1. Image of the screen of the laboratory work "Measuring the temperature dependence of resistance in metals and semiconductors"

The work resulted in the identification of a significant aspect of the education sector, namely laboratory work and the utilisation of augmented reality as a means of implementing it. This approach to the utilisation of augmented reality in education allows for the incorporation of course materials, the maintenance of students' attention during training, and the assessment of their knowledge. Furthermore, it does not necessitate the utilisation of specialised equipment, thereby rendering it a valuable learning resource.

References

1. Virtual workshop on physics / V. M. Dubovyk // Problems of modern education - Kharkiv, 2020 - №44 - P. 109.
2. Virtual laboratory work in physics using interactive computer simulations / O.V. Slobodianyk // Collection of educational materials - Kyiv, 2022.
3. The use of augmented reality technology in a mobile-oriented learning environment of a university / E.O. Modlo - Problems of methods of physical, mathematical and technological education. - Kryvyi Rih, 2017. - p. 93.
4. Modelling and development of software for virtual laboratory work in the course of physics / E.P. Kulichenko - Qualification work - Kherson, 2022.
5. Virtual laboratories as an instrument of educational and scientific activity / O.V. Semenikhina, V.G. Shamonya // Pedagogical sciences - Sumy, 2011.

PHYSICS OF MAGNETISM

SYNTHESIS OF NICKEL-ZINC SPINEL FERRITES AND MAGNETIC CHARACTERIZATION

V. O. Zamorskyi[1], A. F. Kravets[1], D. L. Popadiuk[1], Yu. Yu. Shlapa[2], S. O. Solopan[2], A.G. Belous[2], A. I. Tovstolytkin[1]

[1]Institute of Magnetism of the NAS of Ukraine and MES of Ukraine,
36b Academician Vernadsky Blvd., UA-03142 Kyiv, Ukraine
[2] V.I. Vernadsky Institute of General and Inorganic Chemistry of the NAS of Ukraine, 32/34 Academician Palladin Ave., UA-03142 Kyiv, Ukraine
e-mail: 0vl0ad0@gmail.com

Ceramics made from nickel-zinc spinel ferrite [1] are intriguing for safe remote heating applications. The reason is that on the one hand, substituting nickel with zinc [2] allows tuning Curie temperature down to room temperatures; on the other hand, nickel-zinc ferrites have increased RF power dissipation per unit mass, due to magnetization increase in a significant region of substitutions over nickel ferrite [3]. It means that such ceramics in media under high frequency oscillating magnetic field (e.g. 100 kHz) heat up to its Curie temperature, but not higher. This way even using thermometer can be avoided.

Our current work is concerned with different synthesis methods of nickel-zinc ferrite nanoparticles. Such investigation is necessary since properties of nanoparticles may significantly depend on the method of synthesis, and that directly affects properties of ceramics. Our current investigation is a work-in-progress, but as an example of difference in magnetic properties due to synthesis method for a pair of samples $M_S(T)$ dependency is shown in figure 1. The difference between these samples is in chemical composition.

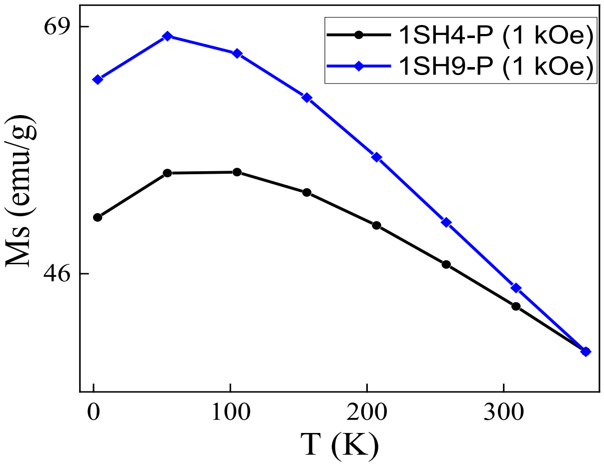

Fig. 1. Temperature dependencies of magnetization of samples S and P synthesized via solid-phase method and co-precipitation method respectively in a field of 1 kOe.

References

[1] S. Chikazumi, C. D. Graham / Physics of Ferromagnetism // Oxford University Press on Demand. – 2009. – 2e, – no. 94.

[2] Tovstolytkin A.I., Kulyk M.M., Kalita V.M., Ryabchenko S.M., Zamorskyi V.O., Fedorchuk O.P., Solopan S.O., Belous A.G. / Nickel-zinc spinel nanoferrites: Magnetic characterization and prospects of the use in self-controlled magnetic hyperthermia // J. Magn. Magn. Mater. – 2019. – V. – 473. – P. 422-427.

[3] Yelenich O.V., Solopan S.O., Kolodiazhnyi T.V., Dzyublyuk V.V., Tovstolytkin A.I., Belous A.G. Superparamagnetic behavior and AC-losses in NiFe2O4 nanoparticles // Solid State Sciences.-2013.-20.-P. 115-119.

NUMERICAL STUDY OF ABRIKOSOV VORTICES DEPINNING IN TYPE-II SUPERCONDUCTORS WITH COLUMNAR DEFECTS IN A TRANSVERSE MAGNETIC FIELD

Oleksii Hrechykha[1(*)], **Alexander Kasatkin**[2]

[1]*Kyiv Academic University, 36 Vernadsky blvd., Kyiv 03142, Ukraine*
[2]*G.V. Kurdyumov Institute for Metal Physics of NAS of Ukraine, 36 Vernadsky blvd., Kyiv 03142, Ukraine*
**E-mail: o.hrechykha@kau.edu.ua*

The bottleneck to achieving widespread superconductivity applications is that in high temperature superconductors, despite their generally high critical magnetic fields, the vortex array starts to move at much lower fields due to Lorentz force action, with subsequent energy dissipation and heat generation. To offset this problem, vortex pinning is introduced [1, 2] via dislocations, small particles or high energy heavy ion irradiation which creates non-superconducting amorphous columnar defects.

In this report we use Wolfram Mathematica to numerically consider a pinned vortex state in a type-II superconductor on a columnar defect in a magnetic field transverse to the defect axis. We minimize the energy functional of the vortex to find an equilibrium form of an elastic vortex thread, and the dependence of the displacement of the vortex ends on the surface of the sample on the Meissner current density. It is shown that at a certain critical value of the current density an abrupt change of vortex thread shape occurs, indicating a transition to the unpinned vortex state (Figures 1, 2).

The vortex end displacement and the vortex energy dependence on the current density are obtained, as well as the critical current density dependence on the thickness of the superconducting film. It is shown that the critical current density decreases as the thickness of the sample increases.

The time-dependent equation of vortex thread dynamics is solved. After considering different current frequencies, we conclude that there is a certain time it takes for the vortex to depin off a columnar defect in a transverse magnetic field. This result qualitatively agrees with known experimental results[3].

To clarify this finding, the non-stationary case of a symmetric magnetic field is studied. It is shown that after static current is switched on, the behaviour of the vortex thread depends on current density's relation to critical current density value: for $j<j_c$ the vortex is static, but for $j>j_c$ the vortice ends start moving immediately and eventually stretch far enough from the vortex center to cause depinning (Figures 3-5). We find that the larger the current density value, the less time it takes for this process to occur. Generally, raising thickness leads to an increase in depinning time, while decreasing vortex elasticity results in a change in critical current density's value.

One may assume that two separate critical current density values exist, with j_{c1} denoting vortice ends starting to move and j_{c2} denoting complete depinning. On the contrary, our results suggest that as long as $j>j_c$ condition is met, a vortex will depin eventually and no separation between the current density values is present for studied thickness and linear tension coefficient ranges.

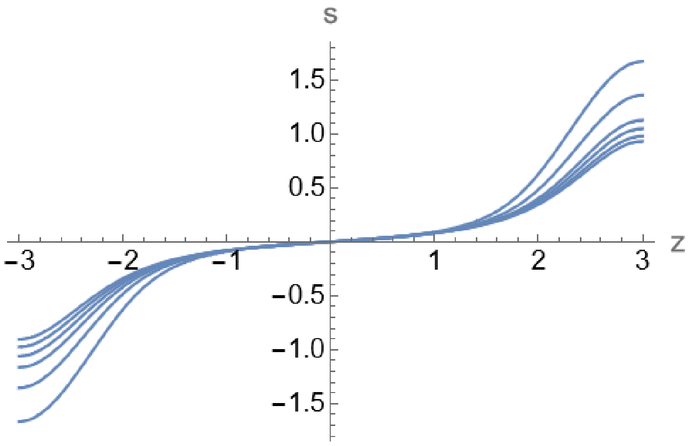

Figure 3. When j < jc the vortice remains static.

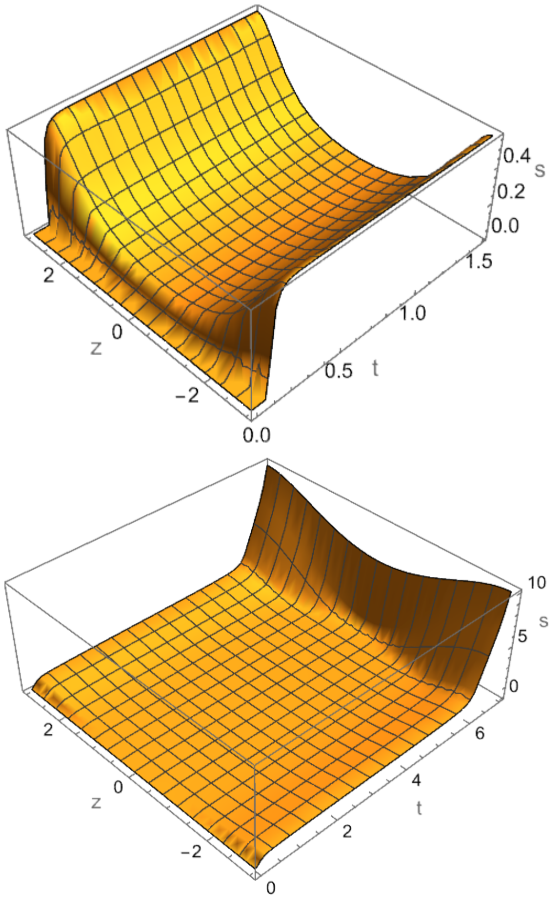

Figure 5. Vortex ends' movement at j > jc eventually leads to complete depinning of the vortex.

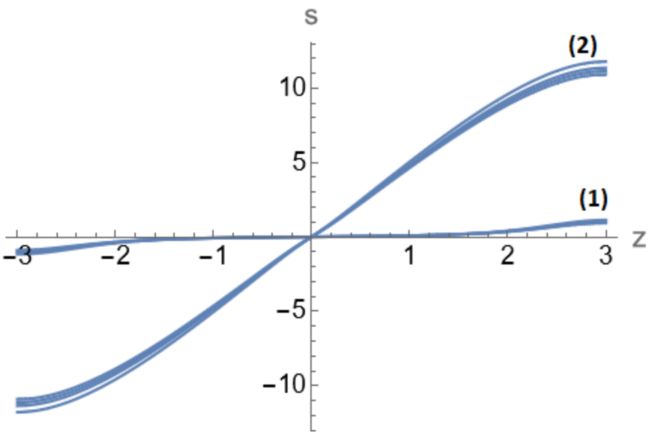

Figure 2. After reaching critical current density, we see grops of solutions (1) and (2) denoting pinned and depinned vortex states respectively.

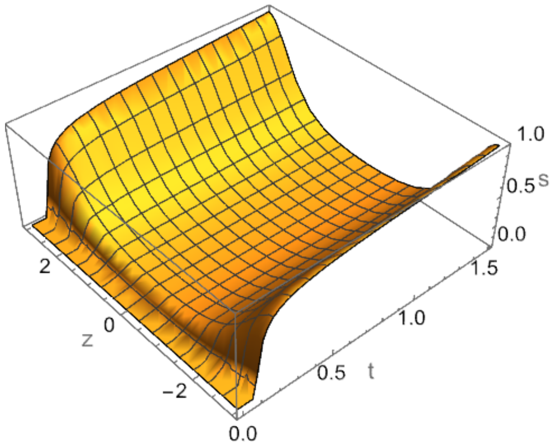

Figure 4. If $j > j_c$ vortex ends start moving immediately after the current is switched on.

References

1. Kwok W.-K., Welp U., Glatz A. [et. al.], Rep. Prog. Phys. 79, 116501 (2016).
2. Maiorov B., Baily S. A., Zhou H. [et. al.], Nat. Mater. 8, 398 (2009).
3. Smith A.W., Jaeger H. M., Rosenbaum T. F., Kwok W. K. [et. al.], Phys. Rev. B 63, 064514 (2001).

MATHEMATICAL PROBLEMS OF APPLIED PHYSICS

CHEMICAL REACTION IN AN ENDLESS TUBE

I.Sachok*, V.Obukhovsky**
Taras Shevchenko National University of Kyiv, Kyiv 01601, Ukraine
e-mail: *gyrik2002@gmail.com, **obukhovsky@knu.ua

The influence of nonlinearity of diffusion on the physico-chemical process of precipitation as a result of matter diffusion in a long tube was considered. Equations that describe the process were proposed. The influence of the neutral component was investigated and it was shown that the case of low concentrations of reactants (the neutral component prevails in the solution) corresponds to the case of linear diffusion.

Diffusion theory has been developing since the 19th century, when the diffusion equation, now known as Fick's law, was proposed [1]. A large number of experimental studies made it possible to come to the conclusion that, in general, the diffusion coefficient is not a constant and depends on the concentration of components. In recent decades, many expressions have been proposed to describe diffusion effects in various solutions [2-5].

In our work we consider the effect of precipitation that occurs during diffusion-reaction transformations using diffusion equations proposed in [5]. The following problem is solved: an infinitely long thin tube is divided into two halves - substance "1" (on the left), substance "2" (on the right); at the initial moment of time, the partition between these two halves is removed and mutual diffusion of both substances begins. As a result of the chemical reaction between the two liquids, a precipitate (substance "3") is formed. This sediment accumulates and after some time a "plug" of insoluble sediment will form in the tube. Then diffusion becomes impossible and the reaction will finished.

The system of differential equations that describes such a process has the next form[5]:

$$\frac{\partial M_1}{\partial t} + \left[M_1 \frac{\partial^2 M_2}{\partial x^2} - M_2 \frac{\partial^2 M_1}{\partial x^2}\right] = -\delta_0 M_1^n M_2^m \tag{1}$$

$$\frac{\partial M_2}{\partial t} + \left[M_2 \frac{\partial^2 M_1}{\partial x^2} - M_1 \frac{\partial^2 M_2}{\partial x^2}\right] = -(1-\delta_0) M_1^n M_2^m \tag{2}$$

$$\frac{\partial M_3}{\partial t} = M_1^n M_2^m \tag{3}$$

Here $M_i(x,t), (i = 1,2,3)$ – volume fractions of the corresponding components $\delta_0 = \gamma_1(\gamma_1+\gamma_2)^{-1}$ – dimensionless parameter of the interaction of substances 1 and 2 , $x \to x\sqrt{\gamma_1+\gamma_2}$ – normalized coordinate, $t \to t(\gamma_1+\gamma_2)$ – normalized time. As a result of such renormalization, the diffusion coefficient does not appear explicitly. For equations (1-3), the law of conservation take place:

$$M_1(x,t) + M_2(x,t) + M_3(x,t) = 1 \tag{4}$$

In addition to the study of dynamics of precipitation, the influence of neutral (non-reactive) components on sediment parameters was considered. The equation for a 4-component system can be written in the following form:

$$\frac{\partial M_1}{\partial t} + \left(M_1 \frac{\partial^2 M_2}{\partial x^2} - M_2 \frac{\partial^2 M_1}{\partial x^2}\right) + B_1\left(M_1 \frac{\partial^2 M_3}{\partial x^2} - M_3 \frac{\partial^2 M_1}{\partial x^2}\right) = -\delta_0 M_1^n M_2^m \tag{5}$$

$$\frac{\partial M_2}{\partial t} + \left(M_2 \frac{\partial^2 M_1}{\partial x^2} - M_1 \frac{\partial^2 M_2}{\partial x^2}\right) + B_2\left(M_2 \frac{\partial^2 M_3}{\partial x^2} - M_3 \frac{\partial^2 M_2}{\partial x^2}\right) = -(1-\delta_0) M_1^n M_2^m \tag{6}$$

$$\frac{\partial M_3}{\partial t} + B_1\left(M_3 \frac{\partial^2 M_1}{\partial x^2} - M_1 \frac{\partial^2 M_3}{\partial x^2}\right) + B_2\left(M_3 \frac{\partial^2 M_2}{\partial x^2} - M_2 \frac{\partial^2 M_3}{\partial x^2}\right) = 0 \tag{7}$$

$$\frac{\partial M_4}{\partial t} = M_1^n M_2^m \tag{8}$$

Here, a re-designation is introduced for the material coefficients comparing to that was used in [5]:

$$\gamma_1 \to \gamma_1 * d_{12}, \qquad \gamma_2 \to \gamma_2 * d_{12} \tag{9}$$

$$t \to t(\gamma_1+\gamma_2)d_{12}, \ \ x \to x\sqrt{\gamma_1+\gamma_2}, \ B_1 = \frac{d_{13}}{d_{12}}, \quad B_2 = \frac{d_{23}}{d_{12}}. \tag{10}$$

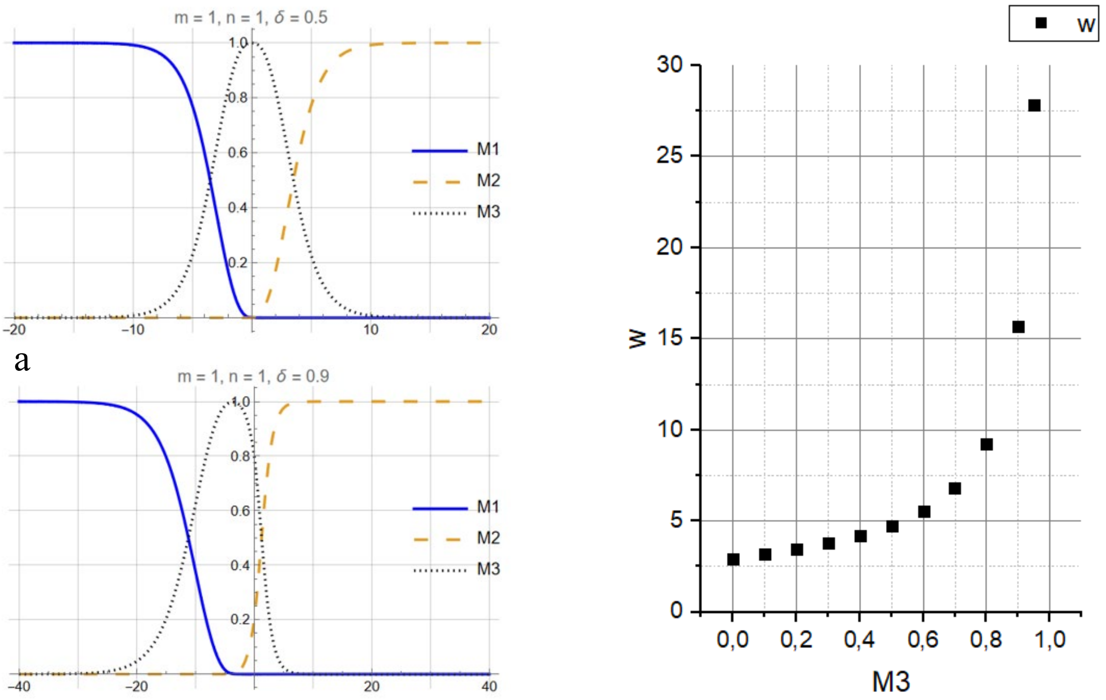

a
b
c

Fig. 1. Distribution of components along the length of the tube after the final of the reaction. Calculation parameters: a) δ = 0.5 and b) δ = 0.9; Fig. 1c – the dependence of the half-width of the sediment on the content of the neutral component using δ = 0.5.

Some calculation results are provided in Fig. 1. As can be seen, under the condition δ = 0.5, the precipitate is formed symmetric with respect to the coordinates of the initial location of the partition. After the formation of a "plug", the distribution of components does not change, since the "plug" stops the further diffusion of components. An important consequence of the nonlinearity of diffusion is that even in the presence of a substance concentration gradient, diffusion is stopped (because at the point of maximum sedimentation, the entire cross-section of the tube is occupied by an insoluble, non-diffusing component). The coefficient δ is determined indirectly by the size of the interacting molecules, which affects the position of the sediment maximum.

It can be seen from the figure 2c that the presence of a neutral component affects the value of the half-width of the sediment distribution. The last value was found using approximation by Gaussian functions. It can be seen that with an increase of the volume fraction of the neutral component, the width of the precipitation area increases. Moreover, when the relative concentration of the neutral component approaches unity (absolute maximum), this half-width goes to infinity. Such a case (small values of the concentration of reacting components) corresponds to the transition of nonlinear diffusion to the linear stage.

References

[1] A. Fick, Philos. Mag. Ser. 4 10, 30 (1855).
[2] L. S. Darken, Trans. AIME 175, 184 (1948).
[3] A. Vignes, Ind. Eng. Chem. Fundam. 5, 189 (1966).
[4] G. Moggridge, Chem. Eng. Sci. 71, 226 (2012)
[5] V. V. Obukhovsky, A. M. Kutsyk, V. V. Nikonova, and O. O. Ilchenko Phys. Rev. E 95, 022133 (2017)

ANALYTICAL APPROXIMATION OF THE “CLUB OF ROME” WORLD-3 MODEL

Shamin Denys Arseniyovych*- 2nd year Master's student, Faculty of Radiophysics, Electronics and Computer Systems, Taras Shevchenko National University of Kyiv, Kyiv;*
E-mail: denisshamin1@gmail.com ,
Obukhovskyi Viacheslav Volodymyrovych *- Doctor of Physical and Mathematical Sciences, Professor of the Institute of High Technologies, Taras Shevchenko National University of Kyiv.*
E-mail: obukhovsky@knu.ua.

The work is based on the World-3 model developed by researchers from the Club of Rome. The main goal of their research is to predict planetary development based on various parameters, such as population, economy, resource reserves, and environmental conditions. In our work, we propose differential equations for predicting the population, industrial production, food production, environmental conditions, natural resource reserves, and the number of robots (a formalized indicator of production productivity). The calculations are based on statistical data for the last 100 years.

The Club of Rome's forecasts are published as the results of numerical calculations. In our paper, we show that the analytical description of these results can be made on the basis of solving the following differential equations:

$$\frac{dN}{dt} = \left((b - m_1) + (f \cdot g) + (h \cdot g)\right) \cdot N \tag{1}$$

$$\frac{dm}{dt} = \left(\frac{(c \cdot g \cdot N)}{(r \cdot h)}\right) + m \cdot v \tag{2}$$

$$\frac{de}{dt} = w - s - c_1 - e2 - w1 + h1 \tag{3}$$

$$\frac{dP}{dt} = r_P \cdot P \cdot \left(1 - \frac{P}{k_1}\right) + tec + inv \cdot (v \cdot P) - e - \left((gl + 1) \cdot P\right) - (g \cdot P) \tag{4}$$

$$\frac{dR_{water}}{dt} = \frac{\left(r_{water} + R_{water} * \left(1 - \frac{R_{water}}{k_2}\right) - h_{water}\right)}{N} \tag{5}$$

$$\begin{gathered} \frac{dRbt_{ind}}{dt} = k_i \cdot Rbt_{ind} \cdot \left(1 - \frac{Rbt_{ind}}{M_i}\right) - \frac{Rbt_{ind}}{\tau_i} \\ \frac{dRbt_{ser}}{dt} = k_s \cdot Rbt_{ser} \cdot \left(1 - \frac{Rbt_{ser}}{M_s}\right) - \frac{Rbt_{ser}}{\tau_s} \\ \frac{dRbt_{ind}}{dt} + \frac{dRbt_{ser}}{dt} = Rbt \end{gathered} \tag{6}$$

The dynamics of the population *N* is described by the equation (1), which takes into account the natural growth, mortality from environmental problems, food and natural resources, and technological progress. The state of the environment *m* (2) takes into account the CO2 emissions, natural resources, population, pollution abatement rate, and technological progress. Food production *e* (3) includes global production, soil degradation, climate impact, food waste, water use, and advances in synthetic biology. Industrial production *P* (4) depends on growth rates, labor productivity, investment in innovation, total investment, global GDP, environmental losses, inflation, and availability of natural resources. The dynamics of renewable resources *R* (5), such as water and forests, takes into account the growth rates, carrying capacity of the environment, rate of depletion due to human activity, and the size of the population. The efficiency of modern production (labor productivity) is described on the basis of the concept of robots (6), whose number *Rbt* is projected based on the growth rates and production limits.

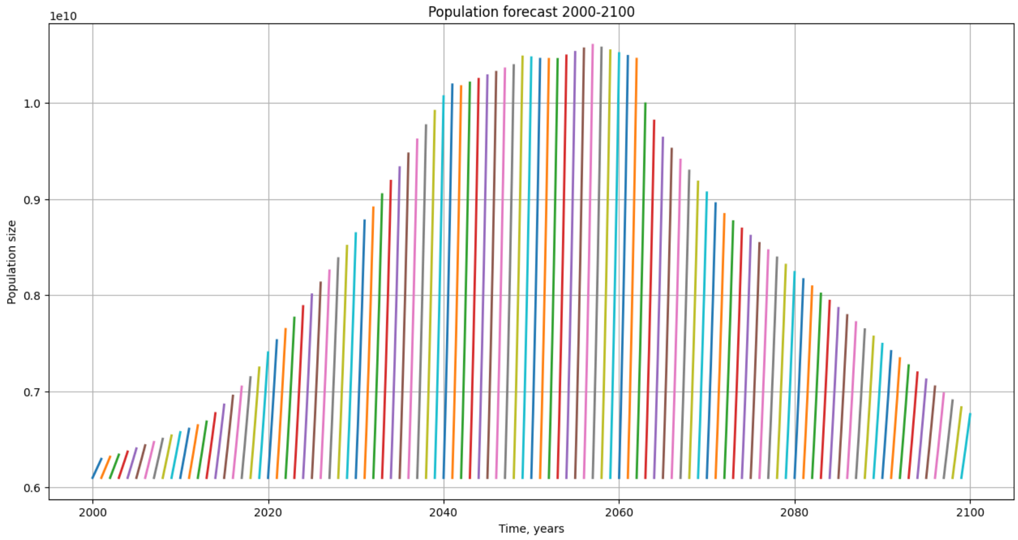

Figure 1. Modeling of global population dynamics. The maximum is estimated to occur in 2055, and the population will be more than 10 billion people at that time.

One of the results of the work is the methodology for taking into account the importance of technological progress and its impact on the development of society. Based on the calculations, it is confirmed that changes in the environment are essential for forecasting and making informed decisions towards achieving sustainable development.

References

[1] Meadows, D.H., D.L. Meadows, J. Randers, and W.W. Behrens III (1972), Limits to Growth: A Report for the Club of Rome's Project on the Predicament of Mankind, Universe Books, New York.

[2] Meadows, D.L., W.W. Behrens III, D.M., Meadows, R.F. Naill, J. Randers, and E.K.O. Zahn (1974), Dynamics of Growth in a Finite World, Wright-Allen Press.

[3] Meadows, D.H., D.L. Meadows, and J. Randers (1992), Beyond the Limits, Chelsea Green.

[4] Meadows, D.H., J. Randers, and D.L. Meadows (2004), Limits to Growth: The 30-Year Update, Chelsea Green.

COMPETITION BETWEEN TWO LANGUAGES TAKING INTO ACCOUNT THE INFLUENCE OF BILINGUALS

M.P. Volynets, V.V. Obukhovsky, M.V. Maksyuta
Faculty of Radiophysics, Electronics and Computer Systems Taras Shevchenko Kyiv National University of Kyiv, Glushkova ave., 4g, e-mail: volynetsmilena@gmail.com

The work examines the evolution of two languages competing with each other on the same territory. It is shown that as a result of the nonlinear interaction of two languages under equal initial conditions, different quasi-stationary values are possible after a certain time. Model was proposed by us includes bilinguals and differs in special cases when both languages continue to exist.

The problem of competition between different languages is very relevant for modern EU countries, so many studies are devoted to it. In particular, without pretending to a detailed description, we will focus on typical works [1 – 5] that have an impact on our research. Many computer studies of competition between different languages, which were initiated by Abrams and Strogatz [1], appeared mainly in physics journals using differential equations (mean-field approximation) or in the framework of agent-based simulations for two or more languages [2, 3].

The Abrams – Strogatz differential equation for the competition of language Y with a higher social status (1 – s) against another language X with a lower social status s has the following form:

$$dx/dt = (1-x)x^a s - x(1-x)^a (1-s), \qquad (1)$$

where x is the share of the population that uses language with a lower social status X, while the share (1 – x) speaks language Y, t is time, a is a parameter that determines the degree of nonlinear interaction between languages, s is the social status of a language with a lower social status. Unexpectedly, the exponent a was found to be roughly constant across cultures, with $a = 1.31\pm0.25$. (mean standard deviation; further details are available from the authors) [1,4].

Consider a system of two competing languages, X and Y, in which the attractiveness of a language increases both with the number of its speakers and with its status (a parameter that reflects the social or economic opportunities afforded to its speakers). When considering a symmetrical situation, when both languages at the initial moment of time have the same number of speakers $x(0) = 1/2$, we will have an exponential decline. In Fig. 1 shows the results of calculations for the values of a = 0.3; 0.6; 0.9; 1.2; 1.5.

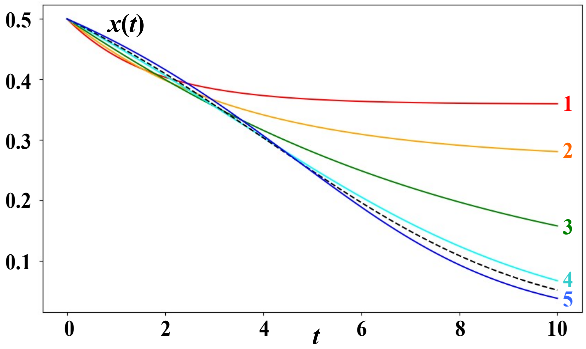

Fig. 1. Plots of the function $x(t)$ in the Abrams – Strogatz language competition model for values $a = 0.3; 0.6; 0.9; 1.2; 1.5$ (curves 1, 2, 3, 4, 5)

The next step in understanding language competition is to take bilinguals into account. There are works that have studied the topic of bilinguals [2,3,5]. Model was proposed by us includes bilinguals and differs in special cases when both languages continue to exist. Depending on the circumstances (the environment with which a person communicates), a bilingual may remain bilingual or gradually forget the language he practically does not use. In the future, the following designations are used: N_A – number of speakers of language A, N_B – number of speakers of language B, N_{AB} – number of speakers of both languages A and B (bilingual). The fate $C_n(t)$ of linguistic nasals at the moment of time t is as follows: $C_n(t) = N_n/(N_A + N_B + N_{AB})$, $0 \le C_n \le 1$.

Here $n = \{\mathrm{A}, \mathrm{B}, \mathrm{AB}\}$ the normalization condition $C_\mathrm{A} + C_\mathrm{B} + C_\mathrm{AB} = 1$ is fulfilled. Let us assume that speakers of language A communicate with other speakers of language A and bilinguals AB in language A (similarly for language B). In this case, interlanguage competition will be described by the following equations:

$$dC_{\mathrm{A,B}}/dt = C_{\mathrm{B,A}}\left(\alpha_{1,2}C_{\mathrm{AB}} - f_{\mathrm{B,A}}C_{\mathrm{A,B}}\right), \tag{2}$$

$$dC_{\mathrm{AB}}/dt = \left(f_\mathrm{A} + f_\mathrm{B}\right)C_\mathrm{A}C_\mathrm{B} - C_{\mathrm{AB}}\left(\alpha_1 C_\mathrm{B} + \alpha_2 C_\mathrm{A}\right), \tag{3}$$

where the coefficients α_1, α_2, f_A, f_B in equations (2), (3) are responsible for the mutual influence of different language media.

The results of the calculations are illustrated in Fig. 2a, b, which show the time dynamics of changes in different language media depending on various parameters under the initial condition of the absence of bilinguals (there is no mutual influence of languages).

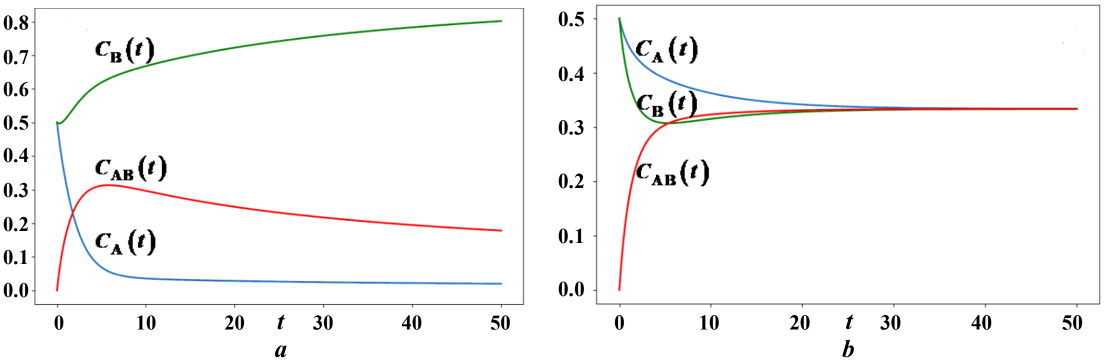

Fig. 2. Plots of functions $C_\mathrm{A}(t), C_\mathrm{B}(t)$, $C_\mathrm{AB}(t)$ under initial conditions $C_{\mathrm{A,B}}(0) = 0.5$ for *a*) $\alpha_1 = 0.1$, $\alpha_2 = 0.9$, $f_\mathrm{A} = 0.1$, $f_\mathrm{B} = 0.9$; *b*) $\alpha_1 = 0.3$, $\alpha_2 = 0.7$, $f_\mathrm{A} = 0.7$, $f_\mathrm{B} = 0.3$

As can be seen from Fig. 2a, b in contrast to the solutions of the Abrams – Strogatz equation [14], the language with a lower social status does not disappear, but decreases to a certain stationary value. Such a conclusion has great social significance and deserves further research.

References

[1] Daniel M. Abrams & Steven H. Strogatz: Modelling the dynamics of language death.
[2] J.J. Fort, J. Pérez-Losada, Hum. Biol. 84(6), 755 (2012).
[3] Armin Bunde, Jürgen Caro, Jörg Kärger, Gero Vogl (eds.): Diffusive Spreading In Nature, Technology And Society. URL: https://vdoc.pub/documents/diffusive-spreading-in-nature-technology-and-society-17tneg1480n0.
[4] Dietrich Stauffer, Xavier Castell´o, Victor M. Eguiluz, and Maxi San Miguel: Microscopic Abrams-Strogatz model of language competition.
[5] Jorge Mira, Luís F. Seoane, Juan J. Nieto: Importance of interlinguistic similarity and stable bilingualism when two languages compete.

RESEARCH OF THE AVERAGE INDEX OF UKRAINIAN BORSCH USING DIFFERENTIAL EQUATIONS OF FRACTIONAL ORDERS

O.O. Mazur, M.V. Maksyuta, V.V. Obukhovsky

Faculty of Radiophysics, Electronics and Computer Systems Taras Shevchenko Kyiv National University of Kyiv, Glushkova ave., 4g, mazur.oleksandr.oleksiyovych@gmail.com

The study examines the average index of the set of traditional ingredients for Ukrainian borscht – one of the most effective macroeconomic indicators of the standard of living of broad segments of the Ukrainian population in conditions of moderate and runaway inflation using differential equations of fractional orders. It is shown by solving these differential equations, continuous monitoring of price changes of the main ingredients and the total price of Ukrainian borscht can be carry out.

The average index of the ingredient set for Ukrainian borscht (“Ukrainian borscht index”) is the sum of the cost required to prepare this national dish according to the classic recipe. Here, instead of the more commonly used term “borscht set index”, we will use a more precise, in our opinion, term, which, as a function of time *t*, will be denoted as follows: $I_{\mathrm{U}}(t)$. We will calculate it by analogy with the international Big Mac index [1]:

$$I_{\mathrm{U}}(\tau)=\sum\nolimits_{k=1}^{N} C_k(\tau) \Big/ \sum\nolimits_{k=1}^{N} C_k(0), \tag{1}$$

where $C_k(0)$ is the initial price of the k-th ingredient, $C_k(\tau)$ is its price at the moment of relative time $\tau = t/T$ (the period *T* can be a week, decade, month, year, etc.), *N* is the number of ingredients of Ukrainian borscht. Usually, the following vegetable ingredients are considered: 1) potatoes – C_1, 2) table beets – C_2, 3) white cabbage – C_3, 4) onions – C_4, 5) red tomatoes – C_5, 6) carrots – C_6 (see, for example, [2]). Of course, pork (brisket) should be added to these products at least $-C_7$. So, we have seven main components of the ”borscht set” for Ukrainian borscht.

Based on the information available, for example, on the sites [3 – 6]), it is known that the prices of “borscht set” products may both rise and fall with different rates of inflation (deflation) against the backdrop of general inflation (deflation). Such price fluctuations are associated with many factors, the characteristics of which we will not delve into ~~on~~ (see, for example, [2]). So, in the general case, the price $C_k(\tau)$ can be expressed as follows:

$$\begin{aligned} C_k(\tau) = C_k(0)\{ & J_{k,1}(\tau)\theta(\sigma_{k,1}-\tau) + J_{k,1}(\sigma_{k,1}) J_{k,2}(\tau-\sigma_{k,1})\left[\theta(\sigma_{k,2}-\tau)-\theta(\sigma_{k,1}-\tau)\right] + \ldots + \\ & + J_{k,1}(\sigma_{k,1})\cdot\ldots\cdot J_{k,l_k-1}(\sigma_{k,l_k-2}-\sigma_{k,l_k-1}) J_{k,l_k}(\tau-\sigma_{k,l_k-1})\left[\theta(\sigma_{k,l_k}-\tau)-\theta(\sigma_{k,l_k-1}-\tau)\right]\}, \end{aligned} \tag{2}$$

where $0 < \sigma_{k,1} < \sigma_{k,2} < \ldots < \sigma_{k,l_k} < 1$, $\theta(\tau)$ is the Heaviside function, $J_{k,l_k}(\tau)$ is the index function (see, for example, [6]) of the price of the *k*-th ingredient at the l_k -th time interval. Substituting (2) into (1), we obtain

$$\begin{aligned} I_{\mathrm{U}}(\tau) = \sum\nolimits_{k=1}^{N} P_k(0) \sum\nolimits_{m=1}^{l_k} J_{k,m}(\tau-\sigma_{k,m-1})\left[\theta(\sigma_{k,m}-\tau)-\theta(\sigma_{k,m-1}-\tau)\right] \times \\ \times \prod\nolimits_{n=1}^{m-1} J_{k,n}(\sigma_{k,n-1}-\sigma_{k,n}), \end{aligned} \tag{3}$$

where $\sigma_{k,0}=0$, $\prod\nolimits_{n=1}^{0}(\ldots)=1$. $P_k(0) = C_k(0) \Big/ \sum\nolimits_{k=1}^{N} C_k(0)$ – the partial initial price of the *k*-th ingredient. We will assume that the function $J_{k,l_k}(\tau)$ can be found as a result of solving the following differential equation with the Caputo fractional derivative (see [7]):

$$D_0^{\alpha} J_{k,l_k}(\tau) - \lambda_{k,l} J_{k,l_k}(\tau) = 0, \ \left(\tau > 0; n-1 < \alpha < n; n \in \square; \lambda_{k,l_k} \in \square\right), \tag{4}$$

where λ_{k,l_k} is the dimensionless rate of change of the price of the *k*-th ingredient in the l_k -th time period (at $\lambda_{k,l_k} > 0$ the price index increases, and at decreases $\lambda_{k,l_k} < 0$). When (corresponding to the fractional exponents $0 < \alpha < 1$, $1 < \alpha < 2$) the solutions of equation (4) are written, respectively, in the following form [8]):

$$J_{k,l_k}(\tau)=E_{\alpha,1}\left(\lambda_{k,l_k}\tau^{\alpha}\right),\ J_{k,l_k}(\tau)=E_{\alpha,1}\left(\lambda_{k,l_k}\tau^{\alpha}\right)+\lambda_{k,l_k}\tau E_{\alpha,2}\left(\lambda_{k,l_k}\tau^{\alpha}\right). \tag{5}$$

Here $E_{\alpha,\beta}(x)=\sum_{k=0}^{\infty}\left[x^k/\Gamma(\alpha k+\beta)\right]$ is the Mittag-Leffler function [7, 8]. It should be noted that the first solution in (5) should be used in the case of moderate inflation, the second – in the case of runaway inflation. So, using (2), (3), (5), the values of $C_1(0)\approx 3$ ₴ (300 g), $C_2(0)\approx 2.4$ ₴ (200 g), $C_3(0)\approx 6.5$ ₴ (500 g), $C_4(0)\approx 4.8$ ₴ (150 g), $C_5(0)\approx 25.2$ ₴ (300 g), $C_6(0)\approx 5$ ₴ (200 g), $C_7(0)\approx 70$ ₴ (400 g), as well as statistical data of the “Ministry of Finance” for 2023 in Fig. 1*a*, *b* plots of the functions $C_k(\tau)$, $C(\tau)=\sum_{k=1}^{7}C_k(\tau)$, $P_k(\tau)=C_k(\tau)\Big/\sum_{k=1}^{7}C_k(\tau)$ and $I_{\text{U}}(t)$ are constructed.

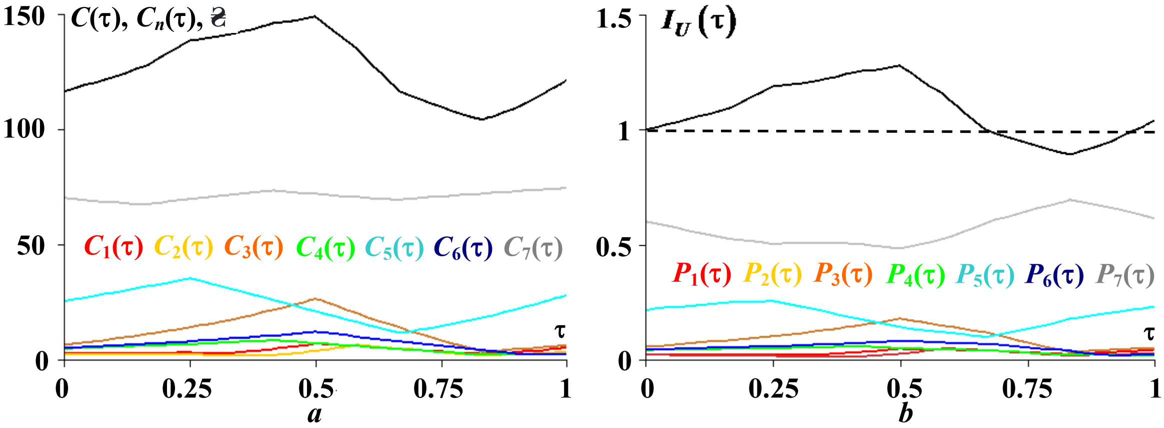

Fig. 1. Graphs of the functions $C_k(\tau)$ of ingredient prices and the full price $C(\tau)$ of Ukrainian borscht – (a), partial ingredient prices $P_k(\tau)$ and the “Ukrainian borscht index” $I_{\text{U}}(t)$ – (b)

References

[1] *Pam Woodall.* The Big Mac Index // The Economist. – September 1986.
[2] L.O. Boyko // Agrosvit, No. 7 – 8, 2021, pp. 46 – 52.
[3] https://index.minfin.com.ua/ua/markets/wares/foods/borzch.php.
[4] https://uapp.in.ua/vartist-borshhovogo-naboru-tendencii-listopada-2023/.
[5] https://tsn.ua/ukrayina/borschoviy-nabir-voseni-2023-roku-yak-zminilisya-cini-u-porivnyanni-z-litnimi-2423485.html.
[6] https://www.rbc.ua/ukr/styler/stoimost-borshchevogo-nabora-vzletela-nebes-1663084918.html.
[7] S.G. Samko, A.A. Kilbas, O.I. Marichev. Fractional Integrals and Derivatives Theory and Applications, Gordon and Breach Science: New York, 1993.
[8] A.A. Kilbas, H.M. Srivastava, J.J. Trujillo. Theory and Applications of Fractional Differential Equations. Elservier: Amsterdam, 2006.

RESEARCH ON THE KINETICS OF POPULATION OF QUANTUM LEVELS WHEN CHANNELING WEAKLY RELATIVISTIC POSITRONS IN HEXAGONAL CRYSTALS

D.M. Maksyuta, V.I. Vysotskii, S.V. Efimenko, M.V. Maksyuta
Faculty of Radiophysics, Electronics and Computer Systems Taras Shevchenko Kyiv National University of Kyiv, Glushkova ave., 4g, maksyuta.dima@outlook.com

In the study, the populations of quantum levels of transverse energy as a function of longitudinal coordinate are obtained through numerical solution of the system of kinetic equations for weakly relativistic positrons channeled in hexagonal crystals. Based on these data, the structure of radial profiles at various distances from the channel entrance is calculated, which are used to estimate the dechanneling lengths.

Let us consider the evolution of a beam of weakly relativistic positrons without angular dispersion, which impinges at zero angle with respect to the symmetry axes of hexagonal channels. The axes are perpendicular to the to the entrance surface of the hexagonal crystal with a thickness of L. Fig. 1*a* schematically illustrates the motion of a single positron along the z-axis of an isolated hexagonal channel. Further, we will investigate the motion of a positron with a Lorentz-factor $\gamma = 10$ in a Zn crystal, the interaction potential of which with c-axes was calculated in [1] using the Barrett approximation [2]. Fig. 1*b* shows in relative units $\xi = x/a$, $\eta = y/a$ (for the parameters a for hexagonal crystals see [3]) the 2D-plots in the planes xz and yz, respectively.

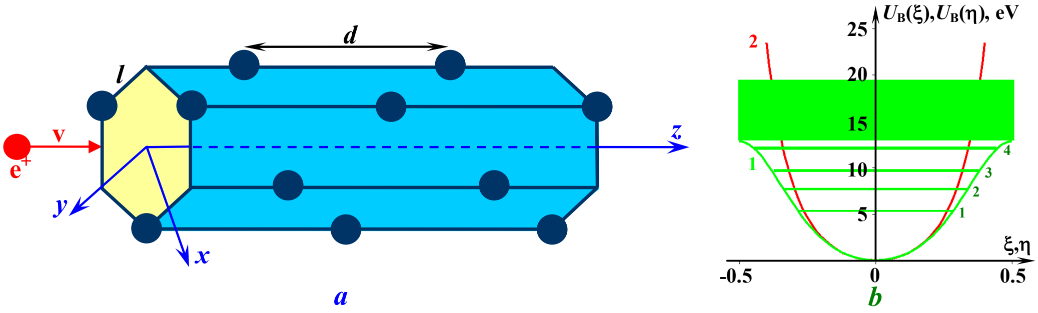

Fig. 1. (a) – a schematic representation of a positron motion in a hexagonal channel, (b) – 2D-plots of the interaction potentials of a positron with c-axes in a Zn crystal, respectively, in the xz plane (curve 1) and in the yz plane (curve 2); energy level system and representation of their widths arising during channeling of a positron with $\gamma = 10$

The analysis was conducted using the approximation function for potential energy $U_B(\rho,\varphi)$ obtained in [1]. As a result of the numerical solution of the Schrödinger equation, the quantum levels of the transverse energy ε_n are found (in Fig. 1b, four discrete levels are plotted with their widths that arise at $\gamma = 10$) along with the corresponding normalized wave functions $\psi_n(\rho,\varphi)$. Then, using the formula $P_n(0) = \frac{1}{S}\left|\int_0^{2\pi} d\varphi \int_0^{a/2} \rho\psi_n(\rho,\varphi)\, d\rho\right|^2$, where $S = a^2\sqrt{3}/2$ is the area of the entrance hexagonal channel with side $l = a/\sqrt{3}$, the populations of these quantum states at $z = 0$ are calculated. The initial radial profile (RP) of the probability of the positron's presence in this channel is calculated using the formula $\Pi(\rho,0) = \rho\sum_{n=1}^{4} P_n(0)\int_0^{2\pi} |\psi_n(\rho,\varphi)|^2\, d\varphi$. To calculate the RP $\Pi(\rho,z)$ at $z = vt$ an any distance from the entrance to the channel, the kinetics of populations of quantum levels of channeled motion are investigated.

For a small number N of such levels in the channel, when the dechanneling velocity is mainly determined by the particle transition rate into the continuous spectrum, and the back-capture into the channel can be neglected, such the investigation can be conducted using the following system of kinetic equations [4]:

$$dP_n(\zeta)/d\zeta = \sum_{m\neq n}^{N} \sigma_{mn} P_m(\zeta) - \sigma_n P_n(\zeta),$$

where $\zeta = z/L$ is the dimensionless longitudinal distance, $\sigma_n = \Gamma_n L/v$ is the dimensionless width of the n-th level. Here, $\Gamma_n = \sum_{m\neq n} w_{nm}$ is the width of the n-th level, which equals the total probability of the particle transition to other states, including the continuous spectrum, $\sigma_{nm} = w_{nm} L/v$ is the dimensionless probability of transition between the n-th and m-th quantum states per unit of dimensionless time. Taking into account only the inelastic scattering of positrons on the valence electrons of the crystal atoms, it is possible, as in [4] for electrons, to make sufficiently realistic estimates of the widths Γ_n of the quantum levels by the formula $\Gamma_n \approx \left(8\pi^2 e^4 Z\beta_v / Sd\hbar^2 c\right)\left\langle \rho^2 \right\rangle_n \ln\left(1/k_v^2 \left\langle \rho^2 \right\rangle_n\right)$, where $\left\langle \rho^2 \right\rangle_n = \int_S \rho^3 d\rho d\varphi \left|\psi_n(\rho,\varphi)\right|^2$, Z_v is the number of valence electrons in the atom of the hexagonal crystal, d is the distance between the crystal atoms c-axis, $k_v \sim 1/l$, $\beta_v \sim 0.1$. In this case, transition probabilities w_{nm} are chosen based on heuristic considerations when compared with experimental data provided in [4].

In Fig. 2a for $L \approx 10^2\,\mu m$ the graphs of functions $P_n(\zeta)$, $n = 1,2,3,4$, are plotted and in Fig. 2b the graphs of functions RP $\Pi(\rho,\zeta_k)$ are plotted at $\zeta_1 = 0$, $\zeta_2 = 0.2$, $\zeta_3 = 0.4$.

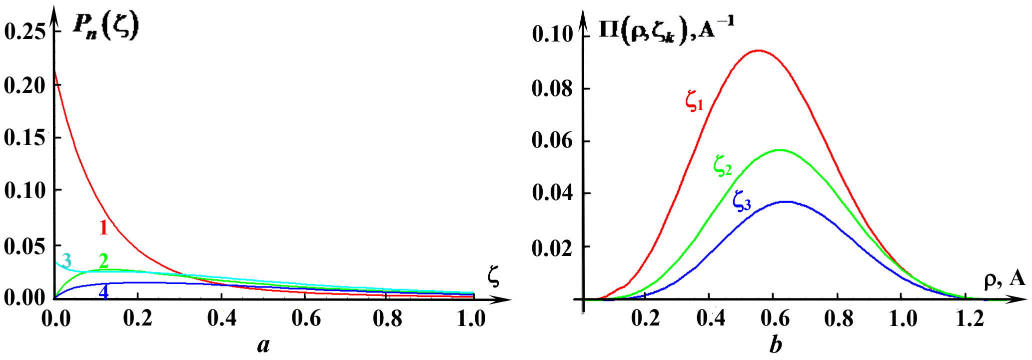

Fig. 2. Illustration for positrons channeled in a Zn crystal with $\gamma = 10$ *plots of the such functions:* $P_n(\zeta)$ *(corresponding to curves 1, 2, 3, 4) – (a);* $\Pi(\rho,\zeta_k)$ *at* $\zeta_1 = 0$, $\zeta_2 = 0.2$, $\zeta_3 = 0.4$ *– (b)*

Using such calculations, one can calculate the dechanneling lengths for all hexagonal crystals at different Lorentz-factors.

References

[1] N.V. Maksyuta, V.I. Vysotskii, D.N. Maksyuta, S.V. Efimenko, *Study of spontaneous radiation during axial channeling of relativistic positrons in hexagonal crystals*, Nuclear Inst. and Methods in Physics Research, A 1058 (2024) 168891.

[2] J.H. Barrett, Potential and stopping-power information from planar-channeling oscillations, Phys. Rev B 20(9) (1979) 3535.

[3] N. Ashcroft, N. Mermin. Solid State Physics. New York: Saunders College Publishing, 1976.

[4] V.A. Bazylev, N.K. Zhevago. Fast Particles Radiation in a Substance and in External Fields, Nauka, Moscow, 1987.

SURFACE PHYSICS, NANO- AND MICROELECTRONICS

PLASMON RESONANCE OF METAL-DIELECTRIC STRUCTURES BASED ON SILVER

I.K. Rudich*, O.V. Machulianskyi V.V. Hetmanchuk***,**
**National Technical University of Ukraine "Igor Sikorsky Kyiv Polytechnic Institute" Kyiv, Ukraine,*
*e-mail: *i.rudich-me25@lll.kpi.ua, **machulansky@gmail.com, ***v.hetmanchuk-me25@lll.kpi.ua*

The work investigates a multilayer structure of a sensor element based on the Kretschmann model with a functional thin silver film of 50 nm thickness. The influence of the wavelength on the optical properties of the system is demonstrated. The studied design contributed to the improvement of the operational characteristics of the sensor element..

The phenomenon of surface plasmon resonance (SPR) arises due to the coherent interaction between normal modes of collective oscillations of electron charge density and excitation photons at the metal-dielectric interface. Such coherent interaction can be achieved using the prism-based Kretschmann configuration employed in optical sensors widely used in modern biosensing elements. Most existing SPR sensors are based on the Kretschmann configuration. The choice of silver as the film material is due to its greater prevalence compared to other noble metals. Therefore, the aim of the work is to establish the influence of the incident wavelength on the functional characteristics of the sensor element.

Model and Modeling Results

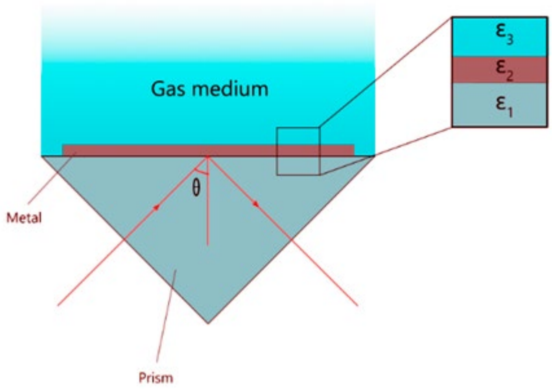

Fig. 1. Kretschmann configuration

The Kretschmann model was chosen for modeling, the scheme of which is depicted in Fig. 1. The sensor element used is a prism with a dielectric substrate coated with a nanoscale metal layer via immersion liquid..

During the investigation, the "Opal" software was utilized to determine the coefficients of electromagnetic wave reflection from the research object while varying the wavelength λ. This software allowed for the simulation of the specified optical element. The following optical parameters were employed for modeling: refractive index n, attenuation coefficient k, and variable wavelength. Additionally, structural parameters such as the thickness of the nanoscale layer d of the structure components were used. The respective values of these input data for individual components were chosen by default. The incident wavelength was varied within the range of 580 to 650 nm. The thickness of the nanoscale silver layer remained constant at 50 nm.

The modeling was performed for the scenario where the sensor element is influenced by external electromagnetic radiation with a variable wavelength λ from 580 to 650 nm. The primary aim of the modeling was to establish the influence of the change in optical wavelength on the reflection coefficient under constant structural parameters. Table 1 presents the investigated dependencies of the reflection coefficient variation at different wavelength values for fixed thickness values of the nanoscale silver film and silicon dioxide film.

Table 1

Wavelength	580	600	620	640	650
Reflection coefficient	0.00950848	0.015072	0.0326327	0.0574288	0.0319952

During the investigation, it was determined that as the wavelength of the electromagnetic radiation increases, the minimum value of the reflection coefficient decreases. This leads to a deterioration of the optical properties of the structure. The optimal wavelength in the visible spectrum of electromagnetic radiation is 580 nm. At this wavelength, the minimum value of the reflection coefficient is observed under the condition of surface plasmon resonance (SPR). At this wavelength of electromagnetic radiation, the efficiency of the sensor element remains maximal.

The study identified that the optical characteristics of the prism-based sensor element with specified parameters, based on a nanoscale silver film with a thickness of 50 nm, are best manifested at a wavelength of 580 nm for electromagnetic radiation. Macroscopic values of optical parameters were used for nanoscale components in the investigation. However, it is known that the actual values of optical parameters for nanoscale components differ significantly from bulk values, which requires additional research.

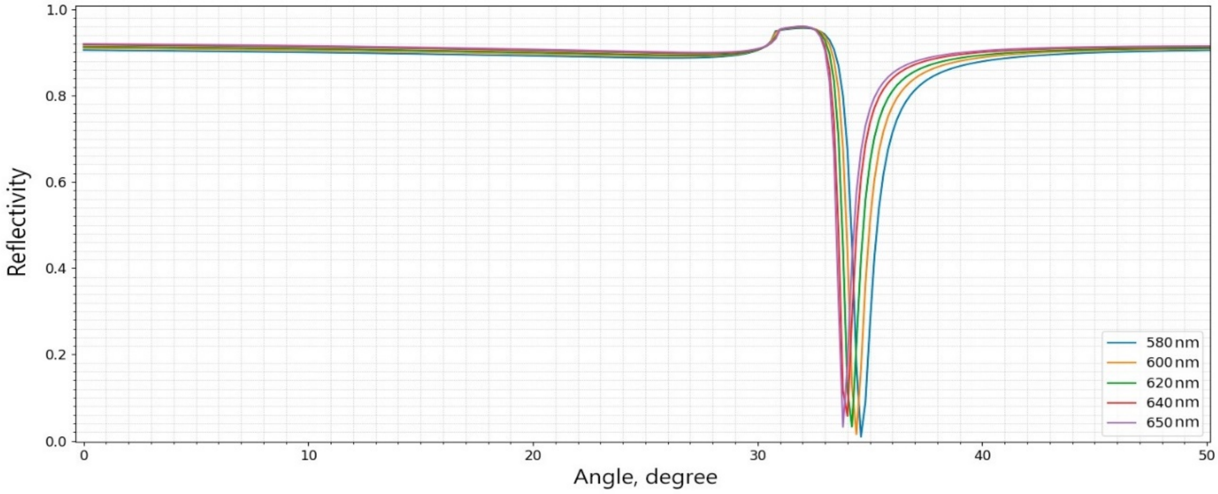

Fig. 2. The dependence of the reflection coefficient on the incident angle of the laser for the metal-dielectric sensor element structure at various wavelengths of incident light.

References

[1] B. Babych, Y. Yakymenko, O. Machulianskyi, M. Rodionov and V. Hetmanchuk, "Spectrally Selective Elements with Specified Optical Characteristics Based on the Nanostructured Composites," 2022 IEEE 41st International Conference on Electronics and Nanotechnology (ELNANO), Kyiv, Ukraine, 2022, pp. 64-69

[2] Hetmanchuk V., Machulianskyi O. "THE INFLUENCE OF THESTRUCTURAL PARAMETERS OF THE MATERIALS OF THE SENSITIVE ELEMENT OF THE OPTICAL SENSOR ON ITS SENSORY PROPERTIES", Ukraine, 2023

[3] J. B. Maury, S. Raikawar, Y. K. Prajapati та J. P. Saini, «A silicon-black phosphorous based surface,» Optik, т. 160, p. 428–433, 2018.

SILVER NANOPARTICLE-BASED SENSOR ELEMENT

V.V. Metelskyi*, O.V. Machulianskyi, V.V. Hetmanchuk*****
** National Technical University of Ukraine "Igor Sikorsky Kyiv Polytechnic Institute"*
*Kyiv, Ukraine-, e-mail: *v.metelskyi-me25@lll.kpi.ua, **machulansky@gmail.com, ***v.hetmanchuk-me25@lll.kpi.ua*

The study investigates the Surface plasmon resonance (SPR) sensor's element based on a silver film with a layer thickness of 50 nm. Sensitivity and quality factor are determined for the analyte with different materials and a refractive index change of 0,01. It is shown that depending on the material and refractive index, the quality factor values increase. For example, for the material SiO2, with a refractive index change of 0.01, the quality factor increases from 0,24 to 0,27.

Optical sensors are sensors whose operation is based on the detection and conversion of an optical signal into an electrical or other form suitable for analysis. Today, optical sensors are important components in electronic devices used in medicine, automation, biochemistry, consumer, and industrial sectors. There are many types of optical sensors, each with its own advantages depending on the field of application. One such type is sensors based on surface plasmon resonance (SPR). These sensors are actively researched, and new structures are created based on the SPR effect because they have many advantages, including high measurement sensitivity, simple design, short response time, etc. The main disadvantage of such sensors is low selectivity. Therefore, different structures need to be used for different substances under investigation. The current task is to calculate the parameters of sensors based on the SPR effect. Therefore, the purpose of this study is to investigate the sensitivity and quality factor of the SPR sensor's sensor element.

Model and Modeling Results

A surface plasmon polariton is a non-radiative electromagnetic surface wave that propagates parallel to the interface of a dielectric material with negative permittivity. Since the wave is located at the metal-dielectric interface, these oscillations are highly sensitive to any changes at this boundary, such as molecule adsorption on the surface of the sensor element. The excitation angle that induces SPR is related to the refractive index of the material and the wavelength of the electromagnetic radiation. This makes SPR a viable technique for detecting specific substances.

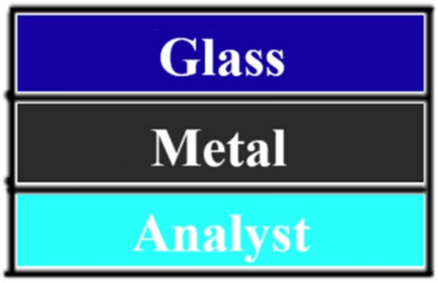

Figure 1 The structure of the optical sensor

So, in order to calculate the required parameters of sensitivity and Q-factor of the SPR sensor, simulations were carried out. The analyte is air with a refractive index of 1 and 1.01.

$$S = \left(\frac{\Delta\theta}{\Delta n}\right) \times \left(\frac{\lambda}{4\pi d}\right)$$

Where Δθ is the change in the angle of refraction when the refractive index changes, Δn is the change in this index, λ is the wavelength, and d is the thickness of the silver nanoscale film.

The formula of the Q factor of the sensor:

$$FOM = \frac{S}{FWHM}$$

Where S is the sensitivity of the sensor, FWHM is the full width at half height of the resonance graph.

We have the following simulation input data: the wavelength of the incident light λ = 540 nm; a silver nanoscale film with a thickness of 50 nm was used as a metal layer; this decision was made due to its optical characteristics; the refractive index of the analyte, n varied from 1 to 1.01 in steps of 0.01.

Parameters				
materials	SIO2		TIO	
n	1	1,01	1	1,01
Resonsnce angle	45,2	45,85	23,4	23,6
Rp min	0,0255145	0,0068918	0,62345	0,068825
Rp max	0,999859	0,999859	0,999693	0,999923
FOM	232,76	206,9	28,65	114,59
FWHM	0,24	0,27	0,6	0,15
S	55,86339		17,18873	

The result of the simulation is displayed in the form of a graph in Fig. 2. Based on these results, the sensitivity and Q-factor of the sensor for analytes from different substances were calculated when the refractive index changes. It was found that the sensitivity indicator for each material is different, and differs in value from the change in the refractive index

Figure 2. The graph of the dependence of the angle of incidence for two types of material on the change in the refractive index

References

[1] J. Y. Jing, Q. Wang, W. M. Zhao, B.T. Wang, "Long-range surface plasmon resonance and its sensing applications: A review". Optics and Lasers in Engineering, Volume 112, , pp. 103-118, 2019
[2] S. Gan, Y. Zhao, X. Dai, Y. Xiang, "Sensitivity enhancement of surface plasmon resonance sensors with 2D franckeite nanosheets". Results in Physics, Volume 13, 2019.
[3] Hetmanchuk V., Machulianskyi O. "THE INFLUENCE OF THESTRUCTURAL PARAMETERS OF THE MATERIALS OF THE SENSITIVE ELEMENT OF THE OPTICAL SENSOR ON ITS SENSORY PROPERTIES", Ukraine, 2023

THE ROLE OF CRYSTALLINE AND THIN-FILM PHOTOCELLS IN SOLAR PANELS: COMPARATIVE ANALYSIS OF TECHNOLOGIES AND PROSPECTS FOR USE

A.I. Shistka, T.M. Mazur

Ivano-Frankivsk National Technical University of Oil and Gas, St. Karpatska, 15, Ivano-Frankivsk, 76019, Ukraine, e-mail: andrijshistka@gmail.com, tetiana.mazur@nung.edu.ua

Solar panels are an integral part of solar power plants and solar power systems. They are the main devices that convert solar energy into electrical current. The main difference between solar panels and solar collectors is that solar panels directly convert light energy into electrical energy, while solar collectors are used to heat the coolant. Solar cells can be classified by the type of solar cells they are composed of, namely crystalline and thin film solar cells. Crystalline solar cells are divided into monocrystalline silicon solar cells and polycrystalline solar cells.

Monocrystalline silicon solar cells are a type of crystalline solar cell. Thanks to high-quality manufacturing, the energy conversion rate of monocrystalline silicon solar cells is 15-18%. They are square or square with rounded or cut corners, with a thickness of 0.2 to 0.3 mm. The color of solar cells can be from dark blue to black, and they can have an anti-reflective coating or gray without coating. The appearance of monocrystalline solar cells is uniform, which makes them aesthetically attractive and easy to use (*Fig. 1)* [1].

Polycrystalline solar cells are another type of crystalline solar cells. The energy conversion coefficient of polycrystalline solar cells ranges from 13 to 16%. They have a square shape and a thickness of 0.24 to 0.3 mm. The color can be blue with anti-reflective coating or silver, gray without coating. The appearance of these solar cells is a block of crystals of different directions, while some crystals can be clearly seen in the cut, which gives them a characteristic appearance *(Fig. 1)* [1].

Thin-film solar cells are divided into photocells based on indium and copper diselenide (CIS technology), photocells using cadmium telluride (CdTe technology), photocells using amorphous silicon (*Fig. 1)* [1].

Fig. 1. Types of Solar Panels

The main characteristics of photocells based on CIS technology include energy conversion coefficient of 9-11%, the shape of the element corresponds to the shape of the module, the thickness of the module in non-tempered glass is 2-4 mm, the color can vary from dark gray to black. The appearance of photocells is uniform, which makes them attractive from an aesthetic point of view and convenient to use.

Photovoltaic cells based on cadmium telluride (CdTe technology) and amorphous silicon represent another category of thin-film solar cells and have the following characteristics. For photocells based on cadmium telluride, the energy conversion rate is 8.5%, the shape of the element matches the shape of the module, the thickness of the module in non-tempered glass is 3 mm, the color can vary from mirror dark green to black, the appearance of photocells is uniform. For photocells based on amorphous silicon, the energy conversion coefficient is 5-7%, the shape corresponds to the shape of the module, the maximum size is 2x3 m, the thickness of the element in non-tempered glass is 1-3 mm, the color is from brown to blue or violet. The appearance is uniform [2].

These technologies make it possible to create solar cells with a greater level of flexibility and a wider range of applications.

Solar panels made from crystalline photocells are most often used in the construction of solar power plants. Typically, the service life of PV modules made from crystalline cells is 25 years. In 25 years, the solar cell capacity will be 80% of the current capacity. Typically, crystalline photo panels are made with an opaque PVB or Teflon backing, a glass or transparent EVA plastic or glass cover, and an aluminum frame [1].

CIS-based solar cells have the highest energy conversion ratio among thin-film modules. However, these modules are susceptible to corrosion from leakage currents generated during the manufacturing process due to the use of electrolysis. Therefore, when installing a station with CIS-based modules, it is necessary to ensure complete electrical isolation from the AC mains using a transformer inverter or a special isolation transformer. It is also recommended to install a differential circuit breaker on each of the lines connected to the inverter.

CdTe-based modules are not subject to corrosion. However, the cadmium they contain is a toxic element, which can cause acute and chronic poisoning. Therefore, used or damaged CdTe-based modules must be disposed of, which increases the cost of operating a solar power plant. CEs based on CdTe thin films have several advantages over traditional crystalline solar panels [2]. In particular, they have higher energy conversion efficiency: CdTe-based solar cells can have an efficiency of up to 22%, which is significantly higher than the efficiency of traditional crystalline solar panels [2,3]. They are also characterized by greater resistance to high temperatures: thin CdTe films can operate at high temperatures without a significant decrease in efficiency. And better performance under low illumination provides SCs based on thin CdTe films with the ability to generate electric current at low lighting levels, which makes them effective in cloudy weather or in shaded areas [3]. Solar cells based on CdTe thin films have some disadvantages, such as high production costs and lower resistance to ultraviolet radiation compared to crystalline solar panels [2,3].

Modules based on amorphous silicon have a low energy conversion rate, and their active elements may lose efficiency when exposed to solar radiation. Typically, there is a decrease in power within 6-12 months after installation, after which the modules reach a stable power level. The service life of such modules is about 10 years, which is much shorter than in the case of crystalline modules.

Thin film photomodules are often used in façade systems and design solutions. They are likely to replace crystalline modules in the future due to their greater production efficiency and lower energy costs.

To summarize, solar panels are a key technology in modern power generation. The choice of solar panel type should be made considering its characteristics, operating costs, and technical features to maximize the efficiency of the solar power plant.

References

[1] T. Markvart, & A. McEvoy, (Eds.). Practical handbook of photovoltaics: fundamentals and applications. Elsevier; 2003. https://www.elsevier.com/books/practical-handbook-of-photovoltaics/mcevoy/978-1-85617-390-2.

[2] T.M. Mazur,V.V. Prokopiv, M.P. Mazur, U.M. Pysklynets, “Solar cells based on CdTe thin films,” Physics and chemistry of solid state. Vol. 22, N 4, pp. 817-827, 2021. https://doi.org/10.15330/pcss.22.4.817-827.

[3] T.M. Mazur, M.P. Mazur, I.V. Vakaliuk, “Solar cells based on CdTe thin films (II Part),” Physics and chemistry of solid state. V. 24, N. 1, pp. 134-145, 2023. https://doi.org/10.15330/pcss.24.1.134-145.

THRESHOLD STOICHIOMETRIES FOR FORMATION OF DIFFERENT PHASE COMPOSITIONS OF Si OXYNITRIDE FILMS BY THERMODYNAMIC MODELING

Mariia Babiichuk*, Andrey Sarikov**

**Educational Scientific Institute of High Technologies, Taras Shevchenko National University of Kyiv, 4-g Hlushkova Avenue, 03022 Kyiv, Ukraine, e-mail: mariiababiichuk@knu.ua*

*** V. Lashkaryov Institute of Semiconductor Physics, National Academy of Sciences of Ukraine, 41 Nauky Avenue, 03028 Kyiv, Ukraine, e-mail: sarikov@isp.kiev.ua*

This work is devoted to a detailed thermodynamic study of the dependence of phase composition of Si oxynitride (SiO_xN_y, $0 \le x \le 2$, $0 \le y \le 4/3$) films on the film stoichiometry and fabrication temperature. The Gibbs free energy of a homogeneous SiO_xN_y and two-phase systems consisting of separated Si oxide and Si nitride phases was calculated for different x, y and temperature values. Based on the Gibbs free energy minima, transition from homogeneous SiO_xN_y phase to separated Si oxide and Si nitride at decreasing x or y values or increasing temperature is demonstrated. The dependences of the critical stoichiometry indices $y_{cr}(x_{cr})$ for the one-phase / two-phase transition are calculated.

Stoichiometric and nonstoichiometric Si oxynitride (SiO_xN_y, $0 \le x \le 2$, $0 \le y \le 4/3$) films have a wide range of electronics applications, which include CMOS devices, optical waveguides, and solar cells antireflection coatings and rear side passivation layers. Depending on the SiO_xN_y stoichiometry (values of x and y) as well as fabrication temperature, one- or two-phase system can be obtained [1, 2]. It is found experimentally that the latter consists of a mixture of generally nonstoichiometric Si oxide and Si nitride phases. Thermodynamic modeling [3] attributed formation of either system to its lower value of the Gibbs free energy at a given stoichiometry and temperature. The stoichiometries of the Si oxide and Si nitride phases in the two-phase systems are defined by the Gibbs free energy absolute minima. In this work, we carry out a detailed thermodynamic study of the phase composition of SiO_xN_y films as a function of the film stoichiometry and fabrication temperature and calculate the dependences of the critical stoichiometry indices $y_{cr}(x_{cr})$ for one-phase / two phase transition.

The Gibbs free energies of a homogeneous SiO_xN_y phase (G_{hom}) and a two-phase system (G_{sep}) are expressed as follows [3]:

$$G_{hom}(x,y,T) = G_{oxn}^{penalty}(x,y) - \Omega_{oxn}(x,y)\cdot T \tag{1}$$

$$G_{sep}(x,y,T,\alpha) = G_{oxide}^{penalty}(x,\alpha) - \Omega_{oxide}(x,\alpha)\cdot T + G_{nitride}^{penalty}(y,\alpha) - \Omega_{nitride}(y,\alpha)\cdot T \tag{2}$$

Here, $G_{oxn}^{penalty}(x,y)$, $G_{oxide}^{penalty}(x,\alpha)$ and $G_{nitride}^{penalty}(y,\alpha)$ are the total penalty energies of the $Si–O_aN_bSi_{4-a-b}$, $Si–O_aSi_{4-a}$ and $Si–N_bSi_{4-b}$ ($0 \le a, b \le 4$) structural units of the homogeneous SiO_xN_y, $SiO_{x'}$ and $SiN_{y'}$ phases, respectively, $\Omega_{oxn}(x,y)$, $\Omega_{oxide}(x,\alpha)$ and $\Omega_{nitride}(y,\alpha)$ are the configuration entropies related to all the possible arrangements of both O and N atoms in the SiO_xN_y phase, O atoms in the $SiO_{x'}$ phase and N atoms in the $SiN_{y'}$ phase, respectively, and T is the temperature. In the expression (2), the parameter α defines the portion of Si atoms in the Si oxide phase in a two-phase system (hence, the portion of Si atoms in the Si nitride phase is 1 – α). The stoichiometry indices of the Si oxide and Si nitride phases in a two-phase system depend on α as follows:

$$x' = \frac{x}{\alpha}, \qquad y' = \frac{y}{1-\alpha} \tag{3}$$

See [3, 4] for the details concerning deriving the expressions (1) – (3).

Minimum value of either of (1) and (2) as the function of x, y, T and α defines the homogeneous one- or separated two-phase state of the SiO_xN_y film. A comparison of $G_{hom}(x,y,T)$ and $G_{sep}(x,y,T,\alpha)$ at different values of x and y is shown in Fig. 1. As can be seen from Fig. 1a and b, formation of homogeneous

($G_{hom}(x,y,T) < G_{sep}(x,y,T,\alpha)$) and two-phase ($G_{hom}(x,y,T) > G_{sep}(x,y,T,\alpha)$ at certain values of α) systems is possible. Transition between the one- and two-phase system corresponds to the equality $G_{hom}(x_{cr},y_{cr},T) = G_{sep}(x_{cr},y_{cr},T,\alpha)$. The calculated dependences $y_{cr}(x_{cr})$ for several temperatures are shown in Fig. 2. The area above the dependence corresponds to homogeneous SiO_xN_y phase, while the bottom area corresponds to separated $SiO_{x'}$–$SiN_{y'}$ systems. Increase of the fabrication temperature of SiO_xN_y films leads to extension of the range of stoichiometries, at which homogeneous phases form.

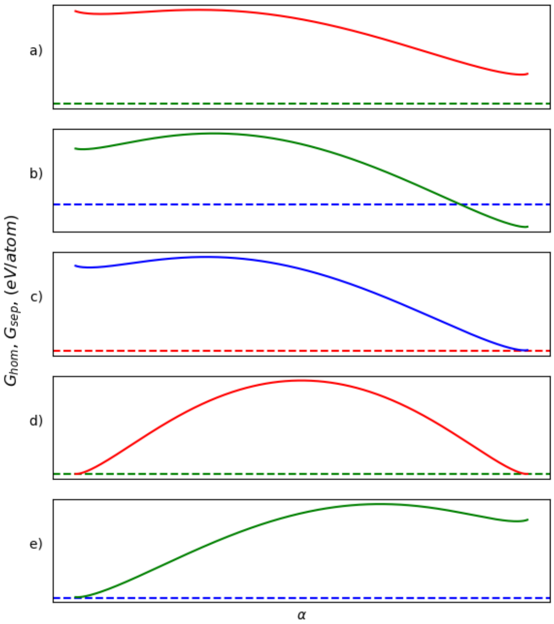

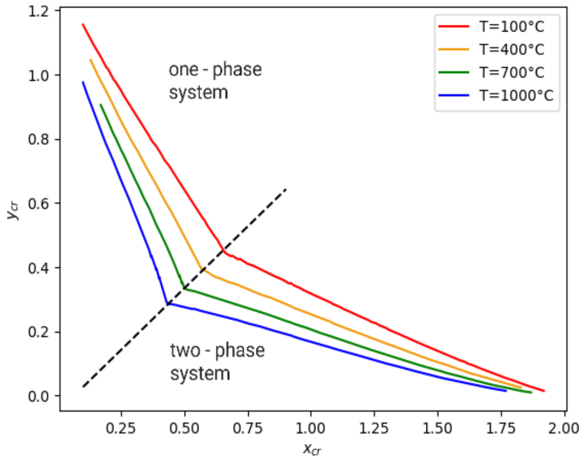

Fig. 1 (left). Gibbs free energies of homogeneous (G_{hom}) and separated into Si oxide and Si nitride phases (G_{sep}) Si oxynitrides versus α in the case of one-phase (a), two-phase (b) and threshold (c)-(e) systems

Fig. 2 (right). Dependences of the threshold SiO_xN_y stoichiometries $y_{cr}(x_{cr})$ at different temperatures

It can be also seen from Fig. 2 that the dependences $y_{cr}(x_{cr})$ consist of two segments, each of which can be approximated by a linear function. The left and the right segments correspond to the mutual arrangement of $G_{hom}(x,y,T)$ and $G_{sep}(x,y,T,\alpha)$ shown in Fig. 1c and e, respectively, while Fig. 1d represents the segment intersection point. As the minimum and the maximum values of α ($\alpha = \frac{x}{2}$ and $\alpha = 1 - \frac{3y}{4}$) correspond to formation of stoichiometric SiO_2 (with the rest Si forming nonstoichiometric $SiN_{y'}$) and Si_3N_4 (with the rest Si forming nonstoichiometric $SiO_{x'}$), proximity of the minima of $G_{sep}(x,y,T,\alpha)$ to these values means that the two-phase system should necessarily contain one quasi stoichiometric (SiO_2 or Si_3N_4) phase.

References

[1] .A. Gritsenko, R.W.M. Kwok, H. Wong, J.B. Xu, Short-range order in non-stoichiometric amorphous silicon oxynitride and silicon-rich nitride, J. Non Cryst. Solids 297 (2002) 96–101.

[2] D. Criado, I. Pereyra, M.I. Alayo, Study of nitrogen-rich silicon oxynitride films obtained by PECVD, Mater. Charact. 50 (2003) 167–171.

[3] I.P. Lisovskyy, M.V. Voitovych, A.V. Sarikov, S.O. Zlobin, A.N. Lukianov, O.S. Oberemok, O.V. Dubikovsky, Infrared study of the structure of silicon oxynitride films produced by plasma enhanced chemical vapor deposition, J. Non-Cryst. Solids 617 (2023) 122502.

[4] A. Sarikov, M. Zacharias, Gibbs free energy and equilibrium states in the Si/Si oxide systems, J. Phys.: Condens. Matter. 24 (2012) 385403.

THE IMPACT OF THE DIELECTRIC COATING ON THE REFLECTIVE PROPERTIES OF THE STRUCTURE “UNIAXIAL PLASMONIC METASURFACE-DIELECTRIC-METAL”

Mykola Beletskii, Ivan Popovych
Department of solid-state electronics A.Ya. Usikov Institute for Radiophysics and Electronics National Academy of Sciences of Ukraine, Kharkiv, Ukraine, email: bnnbeletski@gmail.com
Department of solid-state electronics A.Ya. Usikov Institute for Radiophysics and Electronics National Academy of Sciences of Ukraine, Kharkiv, Ukraine, email: ivdpopovich@protonmail.com

We study the reflective properties of the solid-state structure “uniaxial plasmonic metasurface-dielectric-metal” covered with a dielectric coating. Of particular interest are the conditions under which the incident on the structure p-polarized electromagnetic wave is has no reflection. As it has been shown, the dielectric coating significantly changes the parameters required to achieve reflectionless incidence. By adjusting its dielectric permittivity we can modify the incident p-polarized wave frequency required for the effect.

Introduction

In recent years metasurfaces have become rapidly growing research field because of the unique ability to control electromagnetic waves [1–2]. They have already found an application in wide variety of areas and were utilized to create ultrathin optic devices. Metasurfaces also allow modifying and enhancing properties of conventional structures and materials. In [3] it was shown how metasurface changes electromagnetic wave propagation through layered solid-state structure containing both dielectric and metal. In the present work, we study how dielectric coating influences the reflectionless incidence of the *p*-polarized electromagnetic wave through uniaxial plasmonic metasurface-dielectric-metal structure. We found that even with the coating it is still possible to observe reflectionless incidence assuming that the coating has required thickness. By increasing its permittivity value we can change the needed thickness as well as adjust required electromagnetic wave frequency.

Geometry of the problem

Geometry-wise the analyzed structure consists of the three separate layers and the metasurface injected between two of them. The first one $0 < z < d_1$ is a dielectric with permittivity ε_2 .

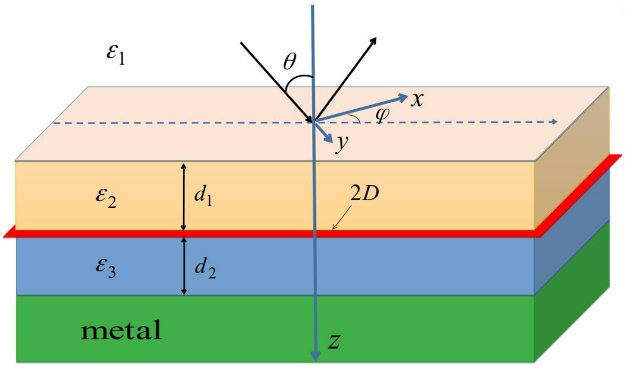

The second one between $d_1 < z < d_1 + d_2$ is also a dielectric which has permittivity ε_3 . And the last layer is perfectly conductive metal substrate that occupies the area $z > d_1 + d_2$. A uniaxial plasmonic metasurface is placed in between the first two layers $(z = d_1)$.

The angle φ is the angle between the major symmetry axis of the metasurface and the plane of the electric field of the incident p-polarized wave. Angle θ on the other hand is the angle of incidence of the wave on the solid-state structure. We considered the case when $\theta = 45°$ and $\varepsilon_3 = 2.0$. To work with the thickness of each dielectric layer we also defined $\delta_{1,2} = \frac{d_{1,2}\omega}{c}$.

Two-layered structure

It is known that for established configuration $\varphi \neq 0$ or $\varphi \neq 90°$ lead to arising reflected *s*-polarized waves [3]. Therefore, we were interested in the situation when the angle φ is either zero or right. For the first case, assuming there is no coating ($\delta_1 = 0$), with the fixed angle θ reflectionless incidence of the *p*-polarized electromagnetic waves occurs for two frequencies ω_1 and ω_2, which are symmetrically located relative to resonant frequency $\Omega_{\parallel} = 1.0$ for different thicknesses of the second dielectric layer: $\omega_1 \approx 0.976$, $\delta_2 \approx 0.377$ and $\omega_2 \approx 1.025$, $\delta_2 \approx 2.224$ [3]. For the second scenario $\varphi = 90°$ the required for the effect frequencies are located around the resonant frequency $\Omega_{\perp} = 1.2$. Corresponding pairs are $\omega_1 \approx 1.176$, $\delta_2 \approx 0.377$ and $\omega_2 \approx 1.225$, $\delta_2 \approx 2.224$.

The affect of the coating

Similarly to [3] by considering each component of electromagnetic wave separately, describing metasurface properties as an effective conductivity tensor, applying boundary conditions between layers and keeping in mind that we the incident wave should be fully absorbed and we were able to describe the condition for reflectionless incidence using permittivity and thickness for each dielectric layer and frequency values which allowed us to calculate the impact of the coating on corresponding parameters.

With fixed $\theta = 45°$ and $\varepsilon_3 = 2.0$ for $\varphi = 0°$ in case $\delta_2 \approx 0.377$ the required frequency ω_1 is shifting to the resonant frequency $\Omega_{\parallel}$. And by increasing ε_2 we observed two things: frequency shift becomes wider, but the coating thickness required for the effect of reflectionless incidence in contrary decreases.

For $\delta_2 \approx 2.224$ again value of the required frequency ω_2 is shifting back closer to the resonant frequency $\Omega_{\parallel}$, comparing to the structure with no coating. In addition, the needed thickness of the dielectric coating is inversely proportional to its permittivity.

For $\varphi = 90°$ with fixed θ and ε_3 the case is much alike. Introducing the coating make both frequencies ω_1 and ω_2 to be shifted closer to the resonant frequency $\Omega_{\perp}$ from the different sides. And the shift width is proportional to the dielectric permittivity of the coating.

Conclusion

It was shown that covering uniaxial-plasmonic metasurface-dielectric-metal structure with a dielectric coating significantly changes the behaviour of the incident p-polarized waves. Such coating can shift the required for the effect of reflectionless incidence frequency value closer to the resonant frequency. By increasing permittivity value of the dielectric coating we can observe that the frequency shift becomes wider and the required thickness value of the coating decreases.

Studied effects can be applied for improving the characteristics of the existing nanoelectronic and optical equipment as well as designing new types of devices.

References

[1] Born, M., Wolf, E., 2019. Principles of Optics. Cambridge University Press. ISBN-10:1108477437.

[2] Hui-Hsin Hsiao, Cheng Hung Chu, Din Ping Tsai, Fundamentals and Applications of Metasurfaces. Small Methods. 2017. Vol 1, no. 4. DOI: 10.1002/smtd.201600064 (date of access: 26.01.2024).

[3] M. M. Beletskii, I.D. Popovych. Non-reflective incidence of p-polarized electromagnetic waves on the solid-state structure “uniaxial plasmonic metasurface — dielectric layer — metal”. Radio physics and radio astronomy. 2023. Vol. 28, no. 2. P. 166-173. DOI: 10.15407/rpra28.02.166 (date of access: 09.10.2023).

THE THERMOCHROMIC MICROCOMPOSITE WITH A HIGH SENSITIVITY TO IONIZING RADIATION

Andrii Hrytsak*, Volodymyr Kapustianyk, Yurii Chornii*****
** Department of Physics, Ivan Franko National University of Lviv, Dragomanova str. 50, 79005 Lviv, Ukraine, e-mail: grytsak.andrew@gmail.com*
*** Department of Physics, Ivan Franko National University of Lviv, Dragomanova str. 50, 79005 Lviv, Ukraine, e-mail: kapustianyk@yahoo.co.uk*
**** Department of Physics, Ivan Franko National University of Lviv, Dragomanova str. 50, 79005 Lviv, Ukraine, e-mail: ychornii@gmail.com*

$[(C_2H_5)_2NH_2]CuCl_4$ (DEACC) single crystals were grown from an aqueous solution of $CuCl_2 \times 2H_2O$ and $[(C_2H_5)_2NH_2]Cl$ salts, taken in a stoichiometric ratio, by the method of slow evaporation at room temperature [1]. The nonpolarized absorption spectra of the microcomposites (MCs) were investigated at different temperatures in the spectral region from 400 nm up to 950 nm using a computerized ZMR-3 monochromator with a spectral resolution of 1 nm and a computerized AvaSpec -2048L spectrometer with a CCD linear detector. In order to compare the radiation effects in DEACC single crystals [2, 3] and microcomposites we used the similar source of ionizing radiation. The samples were irradiated by Co-60 (0.9 mR/h).

The temperature dependences of optical density of the microcomposites with polystyrene matrix obtained at the constant wavelength are compared with those for the samples irradiated with the different doses of radiation using Co-60 isotope (Fig.1, $\lambda = 633$ nm). The pristine sample is characterized by the $D(T)$ hysteresis loop of a nearly rectangular shape similar to those observed in a bulk crystal [4]. The sharp jumps of the absorption coefficient reveal the temperatures of the thermochromic PT at cooling ($T_t = 312$ K) and heating ($T_t = 327.6$ K) reflecting its first order. As it is clearly seen from Fig.1 and Fig.2, the thermochromic properties of the MCs based on DEACC were found to be very sensitive to the ionizing irradiation. Its impact consists in a considerable shift of the phase transition temperature derived from the $D(T)$ hysteresis loops toward lower values. Moreover, the comparatively low doses of irradiation cause the distortion of the loops reflecting a diffuse nature of the phase transition at heating. In spite to this, as it is clearly seen from the shape of the loops, at cooling the phase transition keeps a clear discontinuous nature.

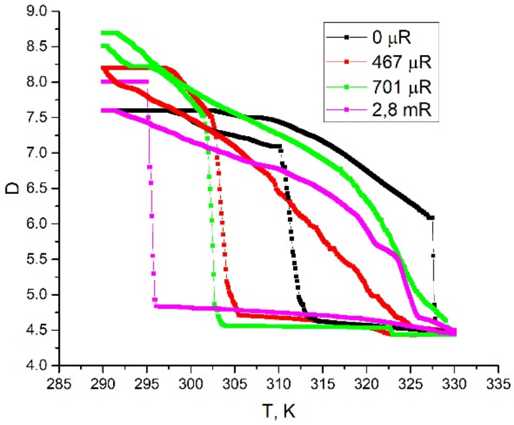

Fig. 1. The temperature dependences of the optical density of DEACC MCs at $\lambda = 633$ nm

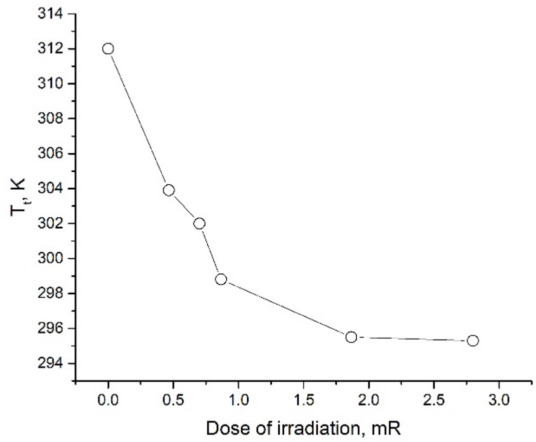

Fig.2. Dependence of the phase transition temperature on the exposure dose of radiation

For the pristine samples investigated in this work this temperature measured at heating (Fig.1) was found to be by 17 K higher than in the single crystal grown from the aqueous solution ($T_t = 311$ K). It is clear that the observed effect, first of all, is connected with the tensions arising within the interface between the matrix and the microcrystal. One can conclude that polystyrene chains during the process of polymerization create the chemical bonds, mostly, with the structural groups of diethylammonium cation – methyl, methylene groups and ammonium heads. These bonds cause a considerable lateral tension within the surface layers of the microcrystal [4, 5] that is followed by a widening of the low temperature phase stability range. The ionizing radiation leads to breaking of the mentioned bonds, due to which one can observe the thermochromic phase transition at lower temperatures.

References

[1] I. Oral, H. Guzel, G. Ahmetli, “Measuring the Young’s modulus of polystyrene-based composites by tensile test and pulse-echo method,” Polymer Bulletin, vol. 67, pp. 1893–1906, Jun. 2011.
[2] V. B. Kapustianik, *et al.* “Influence of γ-ray irradiation on the thermochromic phase transition in diethylammonium tetrachlorocuprate,” Journ. of IEEE, vol. 4, pp. 801 – 803, Aug. 1994.
[3] H. Křížová, *et al.* “Thermochromic and electrical properties of silica/DEA-CuCl4 sensory composite,” presented at the 62nd ICMD, Harrachov, Czech Republic, Sep 13-15 2022.
[4] V. Kapustianyk, Y. Chornii, S. Semak, “Thermochromic Properties of Nano- and Microcomposites Based on (NH2(C2H5)2)2CuCl4 Crystals,” J Phys Stud. vol. 24, no. 4, pp. 4707–4714, Dec. 2020.
[5] V. Kapustianyk., *et al.* “Spectroscopic Studies of the Size Effects in the Absorption Spectra of (NH2(C2H5)2)2CuCl4 Nanocrystals Incorporated into the PMMA Photopolymer Matrix,” Journal of Alloys and Compounds. vol. 493, no. 1, pp. 26-30, Mar. 2010.

PRACTICAL APPLICATIONS OF SCANNING PROBE MICROSCOPY IN THE ELECTROSTRUCTURAL CHARACTERIZATION OF SEMICONDUCTOR STRUCTURES

Petro Lytvyn
V. Lashkaryov Institute of Semiconductor Physics NAS Ukraine,
41, Nauky pr., Kyiv 03028, Ukraine, e-mail: plyt@isp.kiev.ua peter.lytvyn@ccu-semicond.net

Scanning probe microscopy (SPM) techniques are a well-established field with applications in a wide range of scientific and practical areas. These include materials science, condensed matter physics, semiconductor technologies, optical sciences, chemistry, medicine, biology and etc. In the semiconductor field, SPM stands out for its ability to probe local electronic properties with unprecedented spatial resolution and sensitivity to current and electric field. SPM's capability to simultaneously measure surface topography, currents, and forces has led to the development of specialized techniques. These include Kelvin-probe force microscopy (KPFM) for non-contact surface potential measurements, conductive atomic force microscopy (c-AFM) for local current measurements, scanning spreading resistance microscopy (SSRM), and scanning capacitance microscopy (SCM) for carrier profiling. However, the practical application of these SPM techniques often presents challenges due to the complexity of the image formation mechanisms and the contribution of multiple physical interactions at the nanoscale.

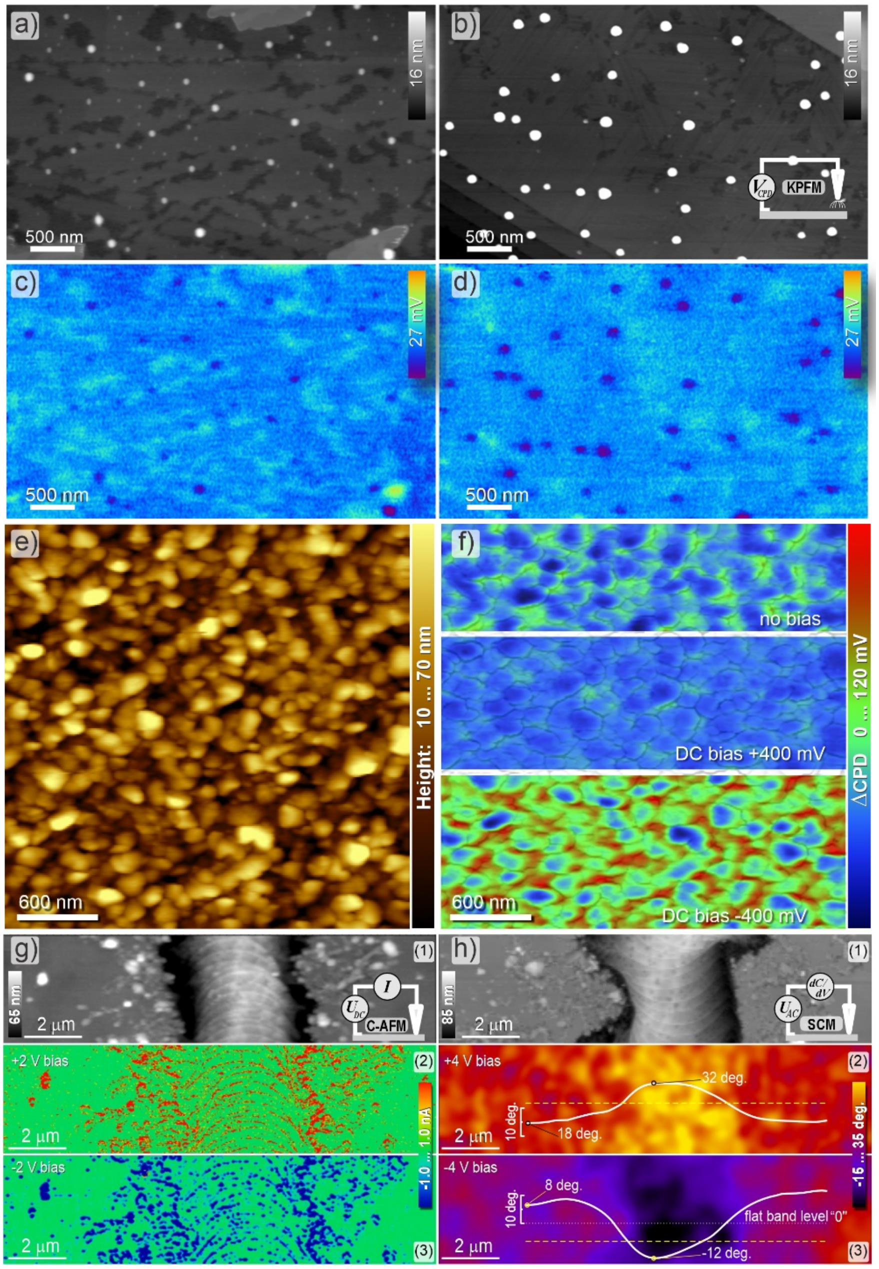

Fig. (a,b; c,d) AFM topography and corresponding KPFM maps of ZrO_2 nanoparticles on the highly-ordered pyrolytic graphite; (e,f) AFM and KPFM maps of the hydrogen-doped zinc oxide film; KPFM maps captured with and without external DC bias; (g) C-AFM maps (topography (1) and corresponding current flow (2,3)) in Ge:Sn structures captured at the +/–2 V bias applied to the sample; (h) SCM maps (topography (1) and corresponding dC/dV phase (2,3)) captured at the +/–4 V DC sample bias and 1.5 V AC voltage. Insets in h(2,3) show the dC/dV phase profiles across the dashed lines.

A review of recent original results in the SPM electrostructural characterization of nanoparticles, polycrystalline, and single crystal epitaxial films will be presented. Size-dependent effects of surface charge density in ZrO_2 nanoparticles (10 and 20 nm) were demonstrated using KPFM [1]. When these nanoparticles were compacted into layered barrier structures, a potential barrier was observed at the interlayer boundary during the water hydration process, resulting in a diode-like I–V characteristic. The dependence of the surface potential value on the particle size in micro- and meso-fractions of powdered ZnS:Mn was also illustrated [2]. Model representations showed that changes in surface potential with particle size – due to overlapping space charge regions from opposite surfaces – ranged approximately from $1 \leq R/L_{\text{eff}} \leq \sim 2.2$ (R is particle radius; L_{eff} is screening length), exhibiting high agreement with experimental data obtained via KPFM. It has been found that the change in the Fermi level position for ZnS:Mn particles, with sizes close to 30–40 nm, can reach about 300 meV compared to its position in bulk material. The impact of film thickness on the electrical properties, crystalline structure, and growth morphology of polycrystalline ZnO films, deposited by RF-magnetron sputtering and doped with methane, was investigated [3]. The grain and sub-grain boundaries were identified as the most conductive structural components of the doped ZnO films, attributed to enhanced diffusion of hydrogen dopants during the growth process. Conversely, the grain boundaries in magnetron-deposited vanadium oxide thin films demonstrated resistance several orders of magnitude higher than that of grains. It has been demonstrated that these differences can be controlled by the temperature and magnitude of the electric field applied to the sample, consistent with the well-known metal-insulator phase transition in this material [4]. The structure, composition, strain, morphology, and carrier distribution of Ge/GeSn nanostructures were studied at the nanoscale through a combination of HRXRD, SPM, TEM, EDXS, and SCM techniques. Large inhomogeneities in carrier distribution were found over the epitaxial layer surface covered with nanostructures, suggesting that complex interphase Ge-Sn interactions under Sn-rich conditions play a crucial role in the development of future GeSn-based devices. Confirming this, the switching of semiconducting behaviour from *p*-type to *n*-type under a tip-induced electric field was demonstrated for self-assembled Ge stripes [5, 6].

This review highlights recent, original results in the SPM electrostructural characterization of nanomaterials, emphasizing the versatility and impact of these techniques in the semiconductor field. From revealing size-dependent effects in nanoparticles to understanding the role of grain boundaries in charge transport and the conversion of conductivity type in micro-/nanowires, SPM has provided unprecedented insights into the local electronic properties of materials at the nanoscale. The sophisticated application of SPM techniques, combined with other characterization methods, has further expanded their capabilities, enabling a comprehensive understanding of complex nanostructures. As the techniques for sample preparation, measurement, and data analysis continue to be refined, the application of SPM in semiconductor nanotechnology is expected to grow, paving the way for the development of novel nanoscale devices and materials.

References

[1] Y.Y. Bacherikov, P.M. Lytvyn, S. V. Mamykin, et al., “Current transfer processes in a hydrated layer localized in a two-layer porous structure of nanosized ZrO_2”, J. Mater. Sci. Mater. Electron. 33 (2022) 2753–2764. https://doi.org/10.1007/s10854-021-07481-2.

[2] Y.Y. Bacherikov, P.M. Lytvyn, O.B. Okhrimenko, et al., “Surface potential of meso-dimensional ZnS:Mn particles obtained using SHS method”, J. Nanoparticle Res. 20 (2018) 316. https://doi.org/10.1007/s11051-018-4413-1.

[3] A. V Vasin, Y. V Gomeniuk, P.M. Lytvyn, et al., “Structural insight into nanoscale inhomogeneity of electrical properties in highly conductive polycrystalline ZnO thin films doped using methane”, J. Phys. D. Appl. Phys. 57 (2024) 155101. https://doi.org/10.1088/1361-6463/ad1791.

[4] P.M. Lytvyn, V.M. Dzhagan, M.Y. Valakh, et al., “Nanomechanical properties of polycrystalline vanadium oxide thin films of different phase composition”, Semicond. Physics, Quantum Electron. Optoelectron. 26 (2023) 388–397. https://doi.org/10.15407/spqeo26.04.388.

[5] A.V. Kuchuk, P.M. Lytvyn, Y.I. Mazur, et al., “Sn-guided self-grown Ge stripes banded by GeSn Nanowires: Formation mechanism and electric-field-induced switching from *p*- to *n*-type conduction”, Appl. Surf. Sci. 604 (2022) 154443. https://doi.org/10.1016/j.apsusc.2022.154443.

[6] S. Kondratenko, P. Lytvyn, A. Kuchuk, et al., “Conductivity-type conversion in self-assembled GeSn stripes on Ge/Si(100) under electric field”, ACS Appl. Electron. Mater. 3 (2021) 4388–4397. 10.1021/acsaelm.1c00561.

MODELING OF THE SCANNING TUNNELING MICROSCOPY IMAGES AND MATERIAL PROPERTIES USING THE DENSITY FUNCTIONAL THEORY

Dmytro Karakuts[1,*]
[1]*Taras Shevchenko National University of Kyiv, 01601 Kyiv, Ukraine*
**email: karakutzdw@gmail.com*

The density functional theory allows for the numerical evaluation of the local density of states in the given crystalline structure. The modern suites for numerical self-consistent plane wave calculations can be used to obtain the topological map of the local density of states, which allows for the computation of the scanning tunneling microscopy images in the Tersoff-Hamann approximation. Here, we illustrate this approach on the example of the hexagonal BN two-dimensional cell. Namely, we derive the material properties of this crystalline structure and calculate the scanning tunneling microscopy images for two bias voltages: negative -2 eV bias, and positive +2 eV bias. Although the calculations are conducted for the BN hexagonal cell, it can serve as an example of the approach which is applicable to a wide class of crystalline structures.

The advances in the electronic-structure theory and the development of tools for numerical analysis grant us the ability to analyse the properties and predict the scanning tunneling microscopy images of the given crystalline structure. This ability can complement current experimental studies significantly simplifying and hastening the material analysis.

In the current study, we numerically evaluate the local density of states of the BN hexagonal cell around the Fermi level. In the Tersoff-Hamann approximation [1], the scanning tunneling microscopy image corresponds to the topographic map of the local density of states, which are determined by the electron density contributions from all states that are between Fermi level and eV_S, where V_S is the applied sample bias, and e is the electron charge. In this approximation, the tunneling current is considered to be proportional to the local density of states, while other components that determine the interaction between the tip, such as the electron density of states of the tip and the tunneling matrix components are considered to be constant. Although it is applicable in the limit of very small tunneling voltages and the tip is considered as a spherical point source, this model provides the ability to interpret images and provides the internal property of the sample without the influence of the tip. For the more accurate calculation of the scanning tunneling microscopy image, the full Bardeen model should be used, as is shown in [2].

The computation of the local density of states is conducted by applying the density-functional theory as an approximation to solve the Schrödinger equation, where the Coulomb interaction between electrons is expressed by a functional of the electron density. To conduct the self-consistent plane-wave density-functional theory calculations, the QUANTUM ESPRESSO suite [3] is utilized.

The self-consistent plane-wave calculations for the BN crystalline cell, which is shown in Fig.1(a), result in the Fermi energy $E_F = -1.3598\, eV$. By conducting the subsequent non-self-consistent computation on a dense grid of k-points, we obtain the density of states and the band structure of BN hexagonal cell. Summation over all the single electron states that fall between the Fermi energy and eV_S at every point results in a desired local density of states as a topographic map, which in Tersoff-Hamann approximation is an expected scanning tunneling microscopy image.

The results of the computation are provided for two sample biases: negative bias with an energy $eV_S = -2\, eV$, and positive bias with an energy $eV_S = +2\, eV$. The images of the 2D local density of states are displayed using VESTA [4] and are shown in Fig.1(b,c). The switching of tunneling locations from boron to nitrogen in Fig.1(b,c) indicates the location of occupied and unoccupied energy states. Thus, considering positive sample bias probes the unoccupied states and negative bias probes occupied states, Fig.1(b,c) shows that in the hexagonal BN cell, the unoccupied states are concentrated near the boron, while the occupied states are located near the nitrogen.

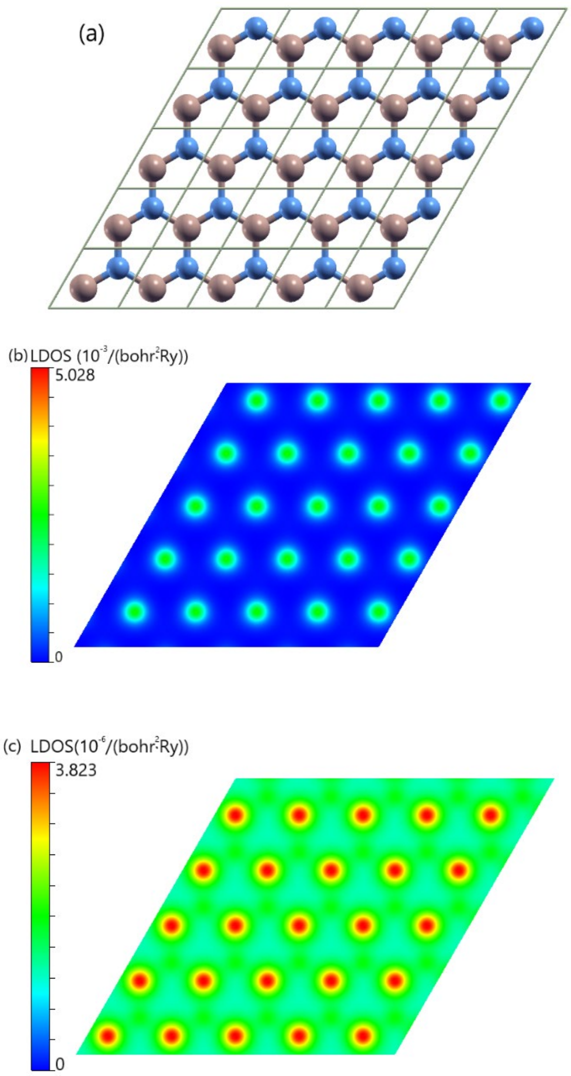

Fig. 1. (a) The visualization of the crystalline structure of the BN hexagonal cell using XCrySDen [5], the red atoms in the cell represent boron, the blue atoms – nitrogen.
(b) The local density of states of the BN hexagonal cell with applied negative sample bias $eV_S = -2\ eV$,
(c) The local density of states of the BN hexagonal cell with applied positive sample bias $eV_S = +2\ eV$.

References

[1] J. Tersoff and D. R. Hamann, Theory of the scanning tunneling microscope, Phys. Rev. B 31, 805-813 (1985)

[2] A. M. Goriachko, Spontaneous nanostructuring of metallic and semiconductor surfaces investigated be means of scanning tunneling microscopy, Kyiv (2018)

[3] P. Giannozzi, S. Baroni, N. Bonini, M. Calandra, R. Car, C. Cavazzoni, D. Ceresoli, G. L. Chiarotti, M. Cococcioni, I. Dabo, A. Dal Corso, S. Fabris, G. Fratesi, S. de Gironcoli, R. Gebauer, U. Gerstmann, C. Gougoussis, A. Kokalj, M. Lazzeri, L. Martin-Samos, N. Marzari, F. Mauri, R. Mazzarello, S. Paolini, A. Pasquarello, L. Paulatto, C. Sbraccia, S. Scandolo, G. Sclauzero, A. P. Seitsonen, A. Smogunov, P. Umari, R. M. Wentzcovitch, QUANTUM ESPRESSO: a modular and open-source software project for quantum simulations of materials, J.Phys.: Condens.Matter 21, 395502 (2009)

[4] K. Momma and F. Izumi, VESTA 3 for three-dimensional visualization of crystal, volumetric and morphology data, J. Appl. Crystallogr. 44, 1272-1276 (2011)A. Kokalj, XCrySDen—a new program for displaying crystalline structures and electron densities, J. Mol. Graphics Modelling 17, 176-179 (1999)

ON THE PHYSICAL NATURE OF FIELD EMISSION FROM ZNO NANOSHEETS

M.V.Strikha [1,2], **R.S.Khilinich**[1]

[1] *Taras Shevchenko National University of Kyiv, Faculty of Radiophysics, Electronics and Computer Systems, pr. Akademika Hlushkova 4g, 03022 Kyiv, Ukraine, e-mail: khilinich2@gmail.com*

[2] *V. Lashkaryov Institute of Semiconductor Physics, National Academy of Sciences of Ukraine, pr. Nauky 41, 03028 Kyiv, Ukraine, e-mail: maksym.strikha@gmail.com*

Low cost and the ability to form nanosheets make the semiconductor zinc oxide a promising material for sensors, modern photonics, and vacuum electronics. In [1], a high-performance cathode for field emission was created based on an inexpensive low-temperature chemical solution method on a glass substrate in the form of ZnO nanosheets and nanosheets decorated with silver Ag nanoparticles.

Since the Fowler-Nordheim formula derived for metals does not describe cold emission from a semiconductor, for theoretically modeling of the nanostructured ZnO-based cathode we have used the formula for the emission current density from an *n*-type semiconductor, where a sharp bending of the bands under the influence of an applied external field forms a near-surface 2D quantum well, in which electrons are concentrated:

$$J_{NS} = \frac{\hbar}{4em_e}\left(\frac{\varepsilon_o}{\varepsilon_s}\right)^2 M_{NS}\beta^2 F^2 \exp\left[-\frac{4\sqrt{2m_o}}{3\hbar e}\frac{\Phi_{NS}^{3/2}}{\beta F}\right].$$

Here, ε_o is the vacuum dielectric constant in SI units, ε_s is the relative permittivity of the semiconductor, m_o and m_e are the free electron mass and effective electron mass in the semiconductor, Φ_{NS} is the work function of the semiconductor, F is the electric field strength, β is the electric field enhancement coefficient near the edge of the nanosheet, and the M_{NS} factor is the fraction of the surface from which effective cold emission occurs.

It is shown that the possible range of effective values of the work function at the top of the nanosheet corresponds to the values of the field enhancement coefficient β of the order of magnitude of 20000. Such values of β and a nanosheet height of the order of μm correspond to subnanometer values of the radius of the nanosheet top, which is in good agreement with the experimentally known fact: that the field emission from the nanostructured surface almost all occurs from the top few atoms of the nanoprotrusion. Thus, the effective emission occurs only from a very small part of the total cathode surface, but the large value of the field enhancement coefficient β provides a noticeable current density of the order of $3 \cdot 10^{-4}$ A/m^2 for a turn on field of the order of $3 \cdot 10^6$ V/m.

The performed analysis allows us to determine the physical nature of the field emission process from ZnO nanosheets, which can be considered as promising and inexpensive emitters for new generation devices.

References

[1] Sheng-Joue Young, Yi-Hsing Liu, and Jen-Tse Chien. Improving Field Electron Emission Properties of ZnO Nanosheets with Ag Nanoparticles Adsorbed by Photochemical Method. *ACS Omega* **3**, 8135−8140 (2018).

PHYSICS OF SEMICONDUCTORS AND DIELECTRICS, SEMICONDUCTOR DEVICES

RENEWABLE ENERGY: IMPORTANCE, CHALLENGES, DEVELOPMENT

Y.O. Trinchuk, M.P. Mazur
Ivano-Frankivsk National Technical University of Oil and Gas, St. Karpatska, 15, Ivano-Frankivsk, 76019,
Ukraine, e-mail: yurii.trinchuk-et232@nung.edu.ua, myroslav.mazur@nung.edu.ua

Renewable energy is an energy industry specializing in the production and use of energy from renewable energy sources, which include: solar energy, geothermal energy, biofuels, wave energy, wind energy, biomass energy.

Renewable energy has many benefits that impact our society and the environment. Renewable energy sources do not emit harmful emissions, which reduces the negative impact on the climate and human health. Wind and solar power plants do not use water. This is important for areas with scarce water resources. Solar, wind, and geothermal energy are inexhaustible, limitless resources (Fig. 1) [1].

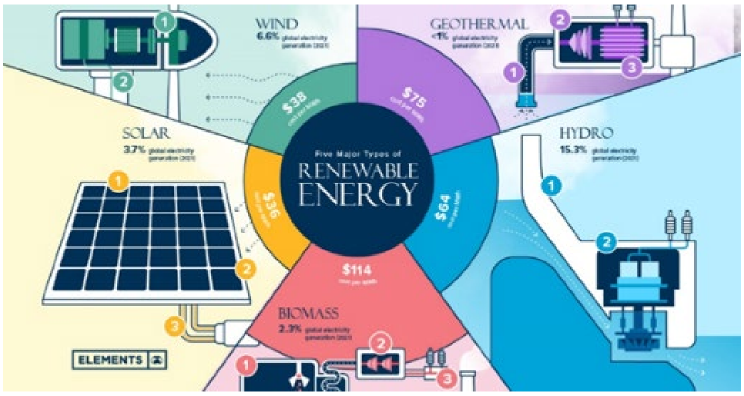

Fig. 1. Types of renewable energy

The importance of the transition to renewable energy is very important. Renewable energy sources (RES) do not emit harmful emissions, which reduces the negative impact on the climate and human health. RES does not depend on fuel imports, which makes the energy system less vulnerable to geopolitical and economic risks (Fig. 1).

There are many countries that are successful in renewable energy. Denmark is a leading country in the production and use of renewable energy. In 2022, renewable energy sources overall produced 81% of Denmark's electricity output and are expected to supply 100% of national electricity production from 2030. The country is also developing district heating and using cogeneration to produce electricity from waste heat [2].

Germany is actively developing renewable energy, in particular solar and wind. In 2019, 46% of Germany's electricity came from renewable sources. Declining coal use helped protect the climate, and prices for CO2 certificates rose, making gas-fired power plants more profitable. The German energy transformation is an ambitious but achievable goal and has become an example for many other countries [2].

Sweden uses hydroelectric power and biomass to power its energy system. It also provides financial support to energy efficiency projects in Ukraine. Sweden is an example of successful development of renewable energy and reduction of coal use.

Renewable energy faces several challenges and obstacles affecting its development in Ukraine. One of the key steps is the transition from an administrative to a market model for regulating energy markets, which is important but requires time and effort. Energy efficiency is another important step that requires active adoption of energy efficient technologies and practices. In addition, the military conflict led to the loss of energy transit routes. Such dependence can become critical in the event of geopolitical conflicts, therefore, reducing dependence and developing domestic renewable energy sources are priority areas for ensuring energy security [3].

The implementation of RES is important for Ukraine, especially in times of war, for reasons such as energy independence, economic stability, infrastructure sustainability, defense support. Ukraine lost a nuclear power plant, thermal power plants and several hydroelectric power plants. The losses of renewable energy sources as a result of war are limited access to the sea, temporarily inaccessible territories and destroyed infrastructure. According to official data, at the end of the last heating season, the Ukrainian energy system temporarily lost 90% of wind and more than 40% of solar generation as a result of hostilities on the part of Russia [4].

A clear strategy for promoting renewable energy needs to be developed as it is an important step in achieving sustainable development and energy independence. To increase the effectiveness of public policy in this area, special laws should be developed and adopted aimed at supporting the development of renewable energy. This may include the creation of special rules, simplification of procedures for obtaining licenses and permits, as well as the development of mechanisms for attracting investors. Such mechanisms may include tax incentives, subsidies, grants and other financial measures.

To ensure qualified personnel in the field of renewable energy, it is necessary to organize training programs for specialists, as well as create technical support centers where businesses and public organizations can receive advice on the implementation of RES. In addition, it is important to conduct information campaigns among citizens to show them the benefits of renewable energy and how to use it. This may include the inclusion of renewable energy issues in the curricula of schools and universities.

The next important step is to monitor the implementation of renewable energy projects and evaluate their effectiveness, which will allow us to analyze the results and make adjustments to public policy in this area. Ukraine is actively working on the development of RES to ensure energy security and stability, which are especially important in times of war. In particular, a National Action Plan for the development of renewable energy until 2030 has been developed.

The introduction of RES contributes to the sustainable development of the country and preservation of the environment.

References

[1] M.A. Green, E.D. Dunlop, J. Hohl-Ebinger, M. Yoshita, N. Kopidakis, &, H. Xiaojing, “Solar cell efficiency tables“ (Version 59), Progress in Photovoltaics: Research and Applications, 30, 1, 1062, 2021. https://doi.org/10.1002/pip.3506.

[2] See details here: https://uk.wikipedia.org/wiki/.

[3] T.M. Mazur,V.V. Prokopiv, M.P. Mazur, U.M. Pysklynets, “Solar cells based on CdTe thin films,” Physics and chemistry of solid state. Vol. 22, N 4, pp. 817-827, 2021. https://doi.org/10.15330/pcss.22.4.817-827.

[4] See details here: https://suspilne.media/353158.

APPLICATION OF LYSO WITH SIPM IN SPECTROSCOPY

Danylo Kovalenko*, Ruslan Yermolenko**
**TSNUK, Nuclear Physics Department, student, e-mail: danylo.kovalenko@knu.ua*
*** TSNUK, Nuclear Physics Department, professor, e-mail: Ruslan.Yermolenko@gmail.com*

This thesis represents the part of the research on spectrometers applied in restricted spaces. As the sensitive volume, we use scintillation crystals. According to this, we need to compact as much as possible the sizes of readout components which convert the visible light into electrical current pulses. One of the approaches to this is using the Silicon Photo Multiplier (SiPM) instead of Photo Multiplier Tubes (PMT). We are going to briefly describe in separate sections the Scintillation crystal property, readout electronics, and trial spectrum.

Introduction

Production of scintillator spectrometers may be highly case-sensitive. This gives a reason to make the read-out electronics based on SiPM more modular, to have the ability to adjust the sensitivity, rise time, noise filters, etc. to the used scintillator and experiment parameters. This necessitates comprehension of signal processing on different levels: light in the scintillator, current pulse in charge sensitive preamplifier, voltage pulse in shaping amplifier (SA), and processing in analog to digital converter (ADC) and analyzer. So the electronic parts of these levels should be both replaceable and adjustable.

Scintillation crystal

In this work, we will present the results of spectrum acquisition using a Lutetium-yttrium oxyorthosilicate (LYSO) scintillator. It's reasonable to use the Silicon compound scintillators in series with photodiodes because they are bridged by quantum efficiency due to close wavelength properties. In our case - the maximum emission wavelength of LYSO is around 450 nm which fits with the quantum efficiency of SiPM [1]. Our LYSO sizes are 26*4*4 cubic millimeters. To collect the scintillation light we used aluminum foil wrapping it around the edges. Due to the small size, LYSO will be inefficient for high-energy gamma quants spectrometry. GEANT4 simulation gave us a rough estimation for the photon energy range, in which the peak to total is significant, and it's up to 1 MeV (in an ideal condition, photons above 1.5 MeV will prominently stand out).

Readout electronics

Silicon photo-multipliers (or multi-pixel photon counter (MPPC)) are a matrix of single-photon avalanche diodes, which work in the Geiger regime under a voltage of 40-100V. The output current pulse amplitude is proportional to the number of photons that hit different pixels in a short time window - the decay time of the scintillator. The probability of detection of light photons ($N_{\gamma_{det}}$) (2) from all incoming fluency of photons ($N_{\gamma_{inc}}$) is dependent on the number of cells (N_{cells}) in the matrix and photon detection efficiency (1) (that also depends on geometry (ε_{geom}), quantum efficiency (QE), and applied bias voltage (P_{Geiger})). We use S14160 3010 MPPC by Hamamatsu Photonics [2].

$$PDE = (QE)\,(\varepsilon_{geom})P_{Geiger} \tag{1}$$

$$N_{\gamma\,det} = N_{cells}(1 - e^{\;N_{\gamma\,inc}*PDE/N_{cells}}) \tag{2}$$

Photons will produce the current pulse that is supposed to be integrated into the input capacitor and converted into voltage with amplification [3]. This scheme is named "charge sensitive preamplifier" (CSP). For our research, we use CSP CR-113 by Cremat Inc.

One of the approaches is to shape and filter the voltage pulse after CSP into a symmetric and compact Gaussian pulse [3]. That will leave information for pulse amplitude analysis only. We used the SA chip CR-200-1us-R2.1 by Cremat Inc.

Trial source

After we were sure that we could supervise pulse shapes at CSP and SA levels for ambient background (Fig. 1), we prepared the source. In this case, we used the Cs137. The resulting spectrum is presented in Figure 2. Precise calibration of the detector is not possible due to only one peak, we need a high activity source with known gamma lines in under 1MeV energy diapason for further investigation.

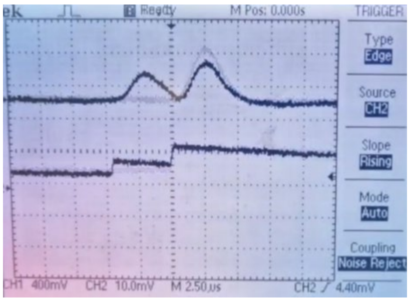

Fig. 1. Signals after CSP (below) and SA (above)

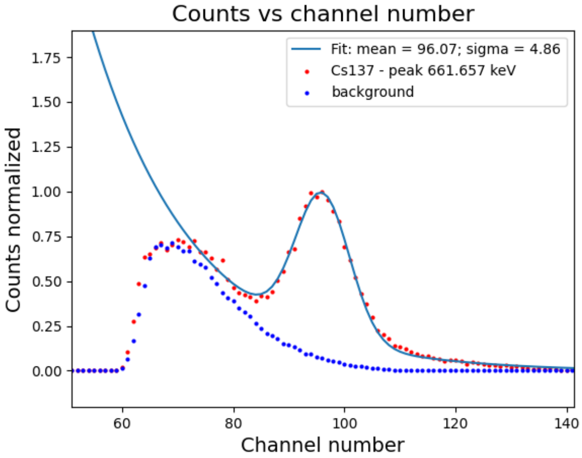

Fig. 2. Spectrum measurement using LYSO and SiPM

Summary

As for the development part, we are looking forward to making a calibration setup and organizing the quality assurance process of all signal acquisition levels. For further investigation, we are planning to enhance the sensitivity and resolution for detecting gamma-, beta-, and alpha radiation of different energies, by adjusting the pulse analyzer parameters.

References

[1] B.Grynyov, V.Ryzhikov, Jong Kyung Kim, Moosung Jae, “*Scintillator Crystals, Radiation Detectors&Instruments on Their Base*”, Ukraine – Kharkiv – 2004

[2] MPPC review by Hiromitsu Takahashi: https://indico.cern.ch/event/340417/contributions/1734373/attachments/1161577/1672607/hstd10_mppc.pdf.

[3] Lectures on pulse processing: https://ns.ph.liv.ac.uk/~ajb/ukgs_nis/pre-course-material/

MICROWAVE PROPERTIES OF COMPOSITES BASED ON POLYVINYLCHLORIDE AND $Ni_{0.5}Zn_{0.5}Fe_2O_4$ FERRITE

D.O. Zhytnyk*, I.V. Fesych*, I.P. Matushko*, Yu. V. Noskov, V.A. Moiseienko*****
and L.M. Grishchenko*
**Taras Shevchenko National University of Kyiv, Kyiv 01601, Ukraine, email: radiodima2000@gmail.com*
*** Kukhar institute of bioorganic chemistry and petrochemistry NAS of Ukraine; email: yuriy.noskov@gmail.com*
****Institute of Macromolecular Chemistry, NAS of Ukraine, Kyiv, Ukraine, email: vamrpd@gmail.com*

This study presents the synthesis of ferrite with the composition $Ni_{0.5}Zn_{0.5}Fe_2O_4$, the preparation of thin composite films using polyvinylchloride as the base material and ferrite as fillers, their study by the methods of SEM, TGA, XRD, PXRD, EDX and FTIR. The microwave absorbing properties of the resulting films in the Ka-band were investigated.

In recent years, considerable attention has been paid to the study of the properties of materials capable of reflecting or absorbing microwave radiation [1, 2]. Such research includes the development of materials to overcome electromagnetic interference, the creation of stealth technologies, the development of protective materials to protect against electromagnetic radiation and other similar purposes. The search for correlations between the composition of the composite material, the nature and concentration of fillers is important for understanding the mechanisms of its interaction with electromagnetic radiation when creating materials with adjustable properties.

The purpose of this work was to obtain composite materials (CM) based on polyvinyl chloride (PVC) and a magnetic filler and to study the nature of the interaction of the obtained CM with electromagnetic radiation in the ultra-high-frequency range.

The nanocrystalline $Ni_{0.5}Zn_{0.5}Fe_2O_4$ powder were synthesized using sol-gel method using glycine as fuel. the final calcination temperature was 650°C for 5 h in the muffle furnace at a heating rate of 5 °C min^{-1}. Production of PVC/ferrite films was carried out as follows: first, ferrite was ground in a mortar, then 0.2 g of PVC powder was mixed with the required amount of ferrite. The resulting mixture was ground in an agate mortar to a homogeneous state, placed in a mold on a polyamide substrate, and 70 mg of plasticizer (dibutyl phthalate) was added. Then it was pressed at 175 °C and a pressure of 10 MPa with a 1-minute holding time.

The following methods were used to study ferrite and composite films based on it: thermogravimetry and differential thermal (TG/DTA) analysis, powder X-Ray diffraction (PXRD), scanning electron microscopy (SEM). Microwave reflection loss and microwave transmission loss were measured with a network analyzer (NA) in the frequency band of Ka-band (26–38 GHz) to study-the microwave properties of the composited obtained.

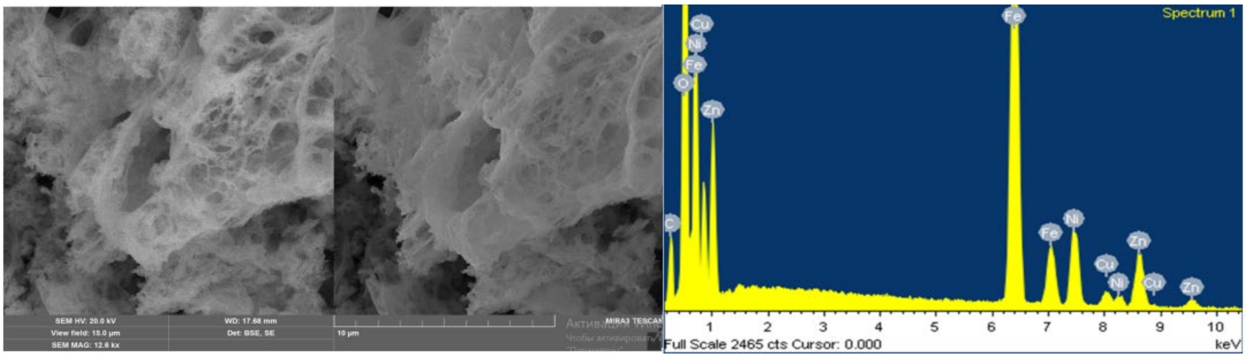

Fig. 1. SEM micrograph (a) and EDX analysis (b) of $Ni_{0.5}Zn_{0.5}Fe_2O_4$.

As shown in Fig. 1a, the nickel-zinc ferrite prepared at 650°C has a porous structure, which is probably due to the large gases released during nitrate-glycine mixture combustion. SEM photo of powder sample indicate the formation of agglomerates of very fine particles with almost spherical shape. Nanoparticles are agglomerated due to the presence of magnetic interactions among the particles. EDX photograph of the sample revealed only the emission peaks of their constituting elements such as Ni, Zn, Fe and O (Fig. 1b), with no other impurity.

When comparing the reflection loss value for samples with different ferrite concentrations, it was found that the concentration of the filler has a weak effect on the reflectance value in the Ka-band. The tendency towards an increase in reflection loss (Fig. 2a) with an increase in the proportion of ferrite in the composite is observed for samples with ferrite concentrations of 0.2% (-15.9dB), 1% (-15.4dB), 5% (-14.3dB), 30% (-14.2dB).

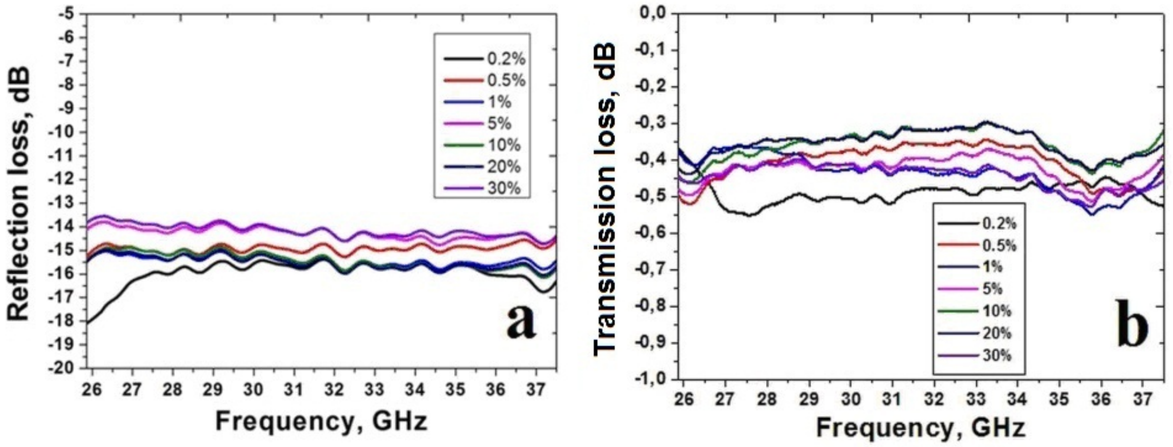

Fig. 2. Frequency dependences of microwave reflection loss (a) and transmission loss (b) for the composite PVC/$Ni_{0.5}Zn_{0.5}Fe_2O_4$ films.

In summary, $Ni_{0.5}Zn_{0.5}Fe_2O_4$ porous nanopowder have been successfully synthesized by a sol-gel method using glycine as the fuel, with an average crystallite size of 29.8±0.2 nm (modified Scherrer's method) and 31.3±0.1 nm (Williamson-Hall method). XRD measurements confirmed the formation of single cubic spinel phase. SEM analysis showed spherical-shaped particles forming agglomerates. Studies of the transmission and reflection of microwave power showed an insignificant effect of the concentration of the filler on the transmission of the wave, which gives grounds to call this material radio-transparent in this band, and a weak effect of the concentration of the filler on the reflection of the microwave power, which can be used to slightly change the amount of reflection in the Ka-band at the stage of creation of these composite materials.

Acknowledgment

This work was supported by the Ministry of Education and Science of Ukraine: Grant for the perspective development of the scientific direction: "Mathematical Sciences and Natural Sciences" at the Taras Shevchenko National University of Kyiv. Also, the work (I.V.F.) is supported by the European Union within the Project 101120397 — APPROACH.

References

[1] H. Lv, Z. Yang, H. Pan, R. Wu, "Electromagnetic absorption materials: Current progress and new frontiers," *Prog. Mater. Sci.,* 2022. vol. 127, June 2022, Art. no. 100946, doi:10.1016/j.pmatsci.2022.100946.

[2] X. Chen, "Enhanced microwave shielding effectiveness and suppressed reflection of chopped carbon fiber felt by electrostatic flocking of carbon fiber," *Compos. Pt. A-Appl. Sci. Manuf.,* vol. 139, Dec. 2020, Art. no. 106099, doi: 10.1016/j.compositesa.2020.106099.

MICROWAVE PROPERTIES OF COMPOSITES BASED ON POLYVINYLCHLORIDE AND CARBON BLACK

D. O. Zhytnyk*, I. P. Matushko*, Yu. V. Noskov, V. A. Moiseienko***,**
O. V. Mischanchuk ** and L. M. Grishchenko*****
**Taras Shevchenko National University of Kyiv, Kyiv 01601, Ukraine, email: radiodima2000@gmail.com*
***Kukhar institute of bioorganic chemistry and petrochemistry NAS of Ukraine; email: yuriy.noskov@gmail.com*
****Institute of Macromolecular Chemistry, NAS of Ukraine, Kyiv, Ukraine, email: vamrpd@gmail.com*
*****O.O. Chuiko Institute of Surface Chemistry, NAS of Ukraine, Kyiv, Ukraine, bigsnake@i.ua*

This study presents the preparation of thin composite films using polyvinylchloride as the base material and carbon black as fillers, their study by the methods of SEM, TPD MS, TGA, FTIR. The microwave absorbing properties of the resulting films in the Ka-band were investigated.

The electromagnetic spectrum in the frequency band from 0.3 GHz to 300 GHz, known as microwaves, is important for the smooth functioning of electronic devices and systems. Despite the convenience they bring to human life, radio frequency (RF) radiation poses a health hazard to the body. To mitigate its impact, it is extremely important to synthesize microwave-absorbing materials that can be used to shield electromagnetic interference [1, 2]. Moreover, at the moment, the demand for microwave absorbing materials due to their use in the military, commercial and household spheres is constantly increasing. The purpose of this work was to obtain composite materials (CM) based on polyvinyl chloride (PVC) and carbon material filler and to study the nature of the interaction of the obtained CM with electromagnetic radiation in the ultra-high-frequency band.

Carbon black (CB) of industrial production, consisting of 98.5% by mass of carbon, was used as a filler (Fig. 1). Obtaining of PVC/CB films was carried out as follows: first, CB was ground in a mortar, then 0.2 g of PVC powder was mixed with the required amount of the filler. The resulting mixture was ground in an agate mortar to a homogeneous state, placed in a mold on a polyamide substrate, and 70 mg of plasticizer (dibutyl phthalate) was added. Then it was pressed at 175 °C and a pressure of 10 MPa with a 1-minute holding time. The range of filler concentrations was 0.2-30 wt%. Optical photos of composite films are shown in Fig. 2.

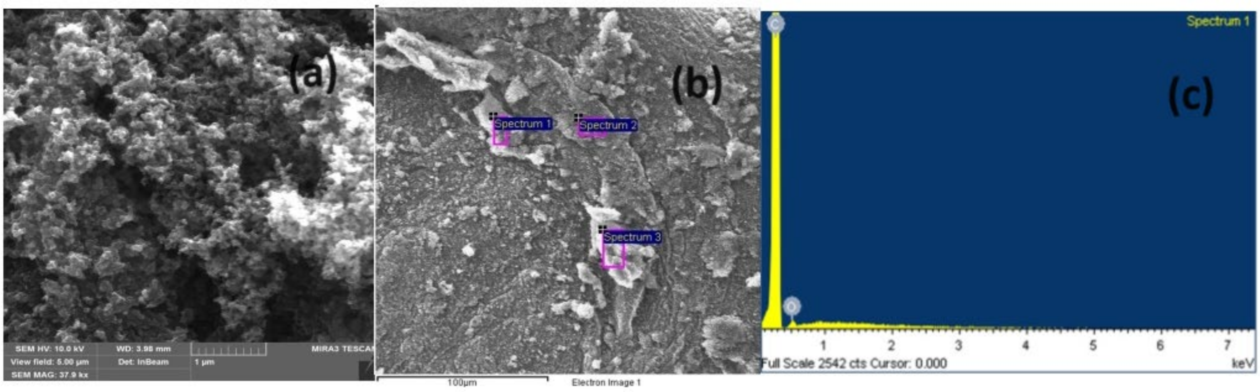

Fig. 1. SEM micrograph (a) and EDX analysis (b, c) of CB.

The following methods were used to study filler and composite films based on it: thermogravimetry and differential thermal (TG/DTA) analysis, thermally programmed desorption mass spectrometry (TPD MS) scanning electron microscopy (SEM), IR Fourier spectroscopy. Microwave reflection loss and microwave transmission loss were measured with a network analyzer (NA) in the frequency Ka-band (26–38 GHz) to study-the microwave properties of the obtained composites.

EDX photograph of the sample revealed only presence of carbon and oxygen, with no other impurity. According to the obtained data, the concentration of carbon is 98.5 wt%, and oxygen is 1.5 wt% respectively.

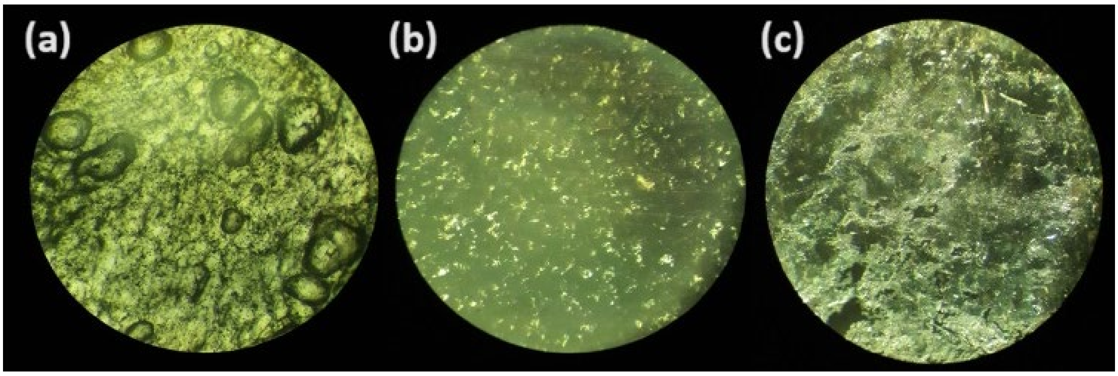

Fig. 2. Optical photographs of PVC/CB films with different concentration of the filler: 0.2%wt (a), 5%wt (b), 30%wt (c).

Table 1. Minimum, average, and maximum values of reflection loss and transmission loss for composite films PVC/CB

Sample	Reflection loss, dB			Transmission loss, dB		
	Min.	Mean.	Max.	Min.	Mean.	Max.
0.2%	-16.7	-15.8	-14.8	-0.8	-0.6	-0.4
1%	-15.8	-15.2	-14.5	-0.6	-0.5	-0.3
5%	-13.4	-12.8	-12.1	-1.0	-0.9	-0.7
10%	-9.8	-9.5	-9.1	-3.1	-2.9	-2.5
20%	-5.4	-5.1	-4.5	-5.4	-5.2	-5.0

Comparing the average values of reflectance in the Ka-band for PVC/CB samples, it can be concluded that an increase in the concentration of CB in the composite leads to a significant increase in the value of reflection. The tendency to increase the reflection value is observed at a concentration greater than 1 %, the reflection increases proportionally to the concentration of CB in the composite, and reaches its maximum at a concentration of 20%: -5.1 dB. Values of transmission values of microwave waves in the Ka-band for the studied samples are linear in the entire Ka-band, for large concentrations of CB in the composite, a slight decrease in transmission value is observed, the average value of which is the minimum for a sample with 20% filler content: -5.2 dB. Analyzing the tendency to decrease the transmittance with an increase in the concentration of the filler in the composite, it can be asserted that the amount of transmission of microwave power is insignificantly dependent on the concentration of the filler in the tested samples. The obtained composite material is transparent in the Ka-band for concentrations of CB up to 10%, and by changing the concentration of the filler, it is possible to adjust the amount of reflection of microwave power in the indicated band during the manufacturing process of the material.

Acknowledgment

This work was supported by the Ministry of Education and Science of Ukraine: Grant for the perspective development of the scientific direction: "Mathematical Sciences and Natural Sciences" at the Taras Shevchenko National University of Kyiv.

References

[1] V. Pratap, A. K. Soni, Himangshu B. Baskey, S. M. Abbas, A. M. Siddiqui, N. E. Prasad, “Electromagnetic and radar absorbing properties of γ $Fe_2O_3/Ba_4Co_2Fe_{36}O_{60}$-epoxy polymeric composites for stealth applications,” *Solid State Sci.*, vol. 113, March 2021, Art. no. 106553, doi:10.1016/j.solidstatesciences.2021.106553.

[2] T. H. Ting, “Synthesis, characterization of Fe_3O_4/polymer composites with stealth capabilities,” *Results Phys.*, vol. 16, March 2020, Art. no. 102975, doi:10.1016/j.rinp.2020.102975.

MEASUREMENT TECHNIQUE FOR DIELECTRIC RESPONSE OF NANOCOMPOSITES “PVDF-BATIO$_3$ NANOPARTICLES”

Oleksandr S. Pylypchuk[1], Serhii E. Ivanchenko[2], Denis Stetsenko[1], Oleksii Bereznykov[1], Oksana V. Leschenko[2], and Anna N. Morozovska[1]

[1] *Institute of Physics, National Academy of Sciences of Ukraine, 46, pr. Nauky, 03028 Kyiv, Ukraine*
e-mail: wh.denis.stetsenko@gmail.com, alexber36@gmail.com
[2] *Frantsevich Institute for Problems in Materials Science, National Academy of Sciences of Ukraine, 3, str. Omeliana Pritsaka, 03142 Kyiv, Ukraine*

In this work we present the technique for the dielectric response measurements of the flexible "PVDF - BaTiO$_3$ nanoparticles" nanocomposites. The addition of the nanoparticles to the PVDF matrix lead to the significant increase of the PVDF dielectric permittivity and enlarge the working temperature range. Obtained results can be useful for the development of flexible lead-free ferroelectric nanocomposites promising for the energy saving elements, modulators and electrocaloric coolers.

Introduction

High-k polymer dielectric materials, which are the main “working horse” for dielectric capacitors, have relatively low values of the relative dielectric permittivity (< 10) and a limited operating temperature range, and therefore cannot meet the growing requirements for high density of electrical energy storage (sometimes required in extreme conditions). Flexible nanocomposites, which contain ferroelectric nanoparticles with very high dielectric permittivity (>> 100) embedded in organic polymer matrix, are free from the above limitations and can be used in “super-capacitors”. The aim of this work, which continue our studies of the dielectric properties of the flexible dense electrocaloric nanocomposites, is to evolve the technique for the dielectric response measurements of "PVDF - BaTiO$_3$ nanoparticles" nanocomposites.

Description of the measurement technique

This paper presents the results of the study of PVDF nanocomposite films with BaTiO$_3$ nanoparticles with an average size of 30 nm (Fig. 1 (a,b)) in the temperature range (-200 – 200)°C and the frequency range (1 – 100) kHz. These samples were obtained by the film casting method. A suspension with BaTiO$_3$ nanoparticles is added to the PVDF liquid matrix. Due to the low viscosity of PVDF, several nanoparticles are compressed, forming a dense nanocomposite with a volume fraction of BaTiO$_3$ nanoparticles of about 30% upon drying. The dielectric permittivity of ceramics sintered at 1250°C from the same BaTiO$_3$ nanoparticle powder was investigated. The temperature dependence of the dielectric permittivity was established in two stages: heating and cooling.

The scheme of the experimental setup, which was used to heat the sample, is presented in Fig.1d. This device is a cylindrical furnace, inside which the sample and the thermocouple were placed, to establish the exact temperature of the sample. For low temperatures the setup, shown in Fig. 1e, was used, in which the temperature is determined using a germanium thermistor. In both cases, the sample was connected to an LCR-meter, which measured its capacitance at frequencies of 1, 10, and 100 kHz. Next, the dielectric permittivity was found using the flat capacitor formula.

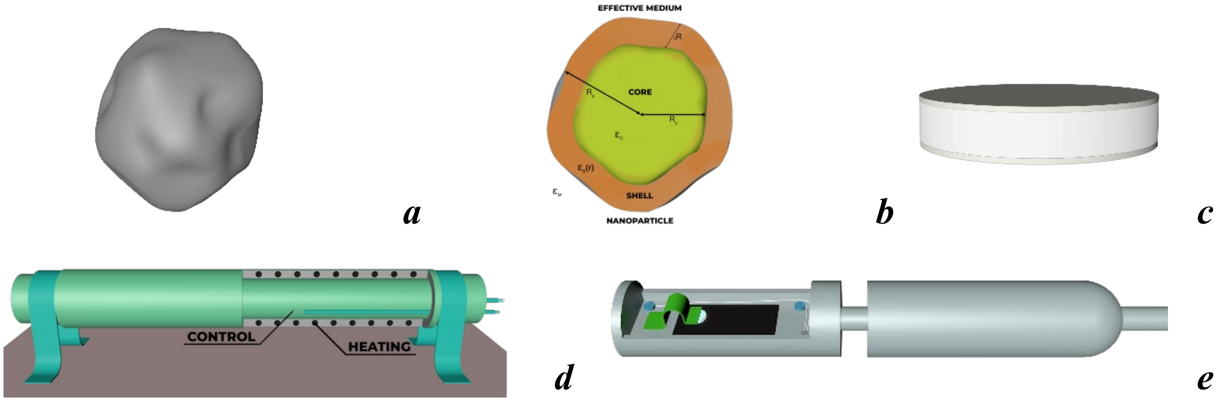

*Fig. 1. The core-shell model BaTiO$_3$ nanoparticle: the side view (**a**) and the cross-section (**b**); (**c**) the studied nanocomposite sample in the form of a pellet with silver contacts; (d) the scheme of the experimental setup for heating the sample from 15 to 180 ℃; (e) the scheme of the experimental setup for cooling the sample within the temperature range of (-200 – 15) ℃.*

Experimental Results

The results of the research are shown in Fig. 2. As can be seen from the graph, the dielectric permittivity of the pure polymer was measured up to 100°C, since at higher temperatures it started to melt. It can also be argued that the dielectric permittivity for this sample depends on the temperature only at low frequencies, and therefore, in subsequent measurements, the change in the dielectric permittivity occurred due to the addition of nanoparticles. A more interesting case is observed after adding nanoparticles to the PVDF matrix. This leads to a significant increase in dielectric constant, as well as an increase in operating temperatures, and enlarge the working temperature range. On the graphs of BT1+PVDF and BT2+PVDF, a jump in the dielectric permittivity is observed near -30°C. Measuring the dielectric permittivity of ceramics showed its increase in 30-50 times. It is also worth noting the presence of 3 peaks (-70, 30 and 125°C, respectively), which correspond to bulk phase transitions of BaTiO$_3$.

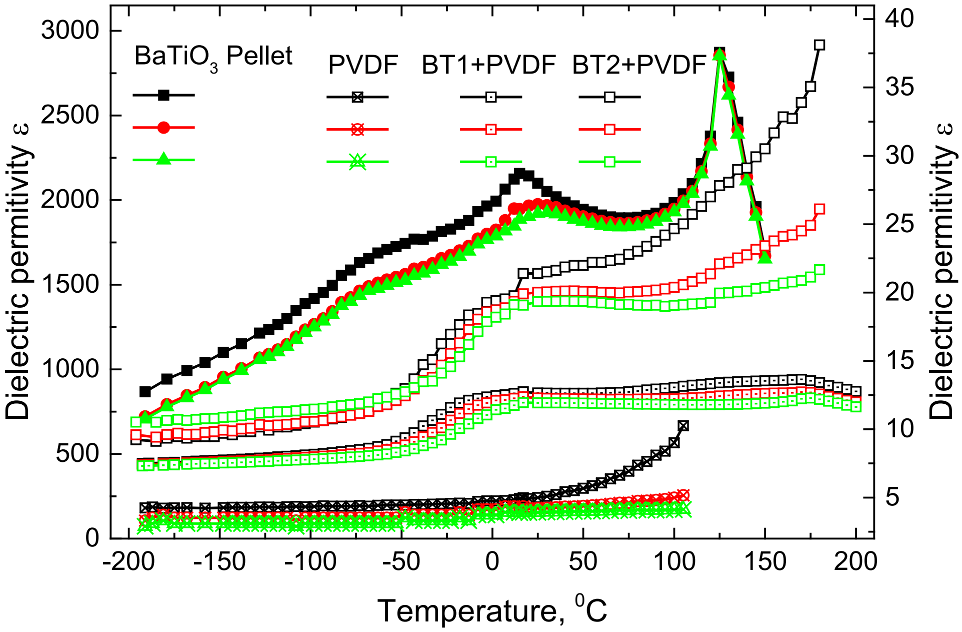

Fig. 2. Temperature dependence of dielectric permittivity of "PVDF - BaTiO$_3$ nanoparticles". The left scale corresponds to the dielectric permittivity of BaTiO$_3$ ceramics (marked "BaTiO3 Pellet"), the right - a 23-μm thick film of pure PVDF polymer (marked "PVDF"), BaTiO$_3$ + PVDF film of thickness 3 μm (marked "BT1+PVDF"). BaTiO$_3$ + PVDF film of thickness 203 μm (marked "BT2+PVDF"). The frequencies at which measurements were made are displayed in colors, as follows: black - 1 kHz, red - 10 kHz, green - 100 kHz.

Conclusions

We evolved the technique for the dielectric response measurements of "PVDF - BaTiO$_3$ nanoparticles" nanocomposites. Obtained results can be useful for the development of flexible lead-free ferroelectric nanocomposites promising for the energy saving elements, modulators and electrocaloric coolers.

References

[1] A. N. Morozovska, O. S. Pylypchuk, S. Ivanchenko, E. A. Eliseev, H. V. Shevliakova, L. M. Korolevich, L. P. Yurchenko, O. V. Shyrokov, N. V. Morozovsky, V. N. Poroshin, Z. Kutnjak, and V. V. Vainberg. Electrocaloric Response of the Dense Ferroelectric Nanocomposites. Ceramics International **50** (7b), 11743 (2024), https://doi.org/10.1016/j.ceramint.2024.01.079.

[2] O. Pylypchuk, S. Ivanchenko, Y. Zagorodniy, O. Leschenko, V. Poroshin, O. Bereznykov, M. Yelisieiev. Effective Dielectric Response of Dense Ferroelectric Nanocomposites (2024), https://doi.org/10.48550/arXiv.2401.07311.

MEDICAL PHYSICS

SPECTRA OF ULTRASOUND DOPPLER RESPONSE USING PLANE-WAVECOMPOUNDING TECHNIQUE

Evgen A. Barannik*, Mykhailo O. Hrytsenko**
**Department of Medical Physics and Biomedical Nanotechnologies, V.N. Karazin Kharkiv National University4 Svobody Sq., 61022, Kharkiv, Ukraine, e-mail:evgenij.a.barannik@karazin.ua*
***Department of Medical Physics and Biomedical Nanotechnologies, V.N. Karazin Kharkiv National University4 Svobody Sq., 61022, Kharkiv, Ukraine, e-mail:mykhailo.hrytsenko@student.karazin.ua*

Within the framework of a simple model of the sensitivity function, the Doppler spectra are considered for different ways of generating response signals using plane wave compounding. A Doppler spectrum is obtained for coherent compounding of signals received at different steering angles of waves during their period of changing. Compared to traditional diagnostic systems, the Doppler spectrum width is increased only by limiting the duration of the signals. There is no additional increase in the spectrum width if the compound signals are formed by adding with cyclic permutation, in which signals from each new wave angle are compounded. When a Doppler signal is formed directly from Doppler signals at different steering angles, the spectral width increases both in comparison with the traditional method of sensing with stationary focused ultrasound fields and with the case of coherent signal compounding. The obtained increase in the spectral width has an intrinsic physical meaning. The increase in width is connected with a dynamic change in the Doppler angle, which increases the interval of apparent projections of the velocities of motion of inhomogeneities along the direction of transmitting of a plane wave without inclination.

Results

The general idea behind synthetic aperture in ultrasound diagnostics is that the ultrasound response is recorded by all elements of the ultrasound transducer for a sequence of different emitted wave fields. The response for each point in space is then identified as a complex value for the different fields, which is coherently summed, resulting in a high-resolution image due to the focusing at each point in space [1].Using the synthetic aperture method, it is possible to implement imaging methods that use plane waves with different propagation directions or wave fronts with different spatial configurations [2,3].

The calculations have been implemented within the framework of the continuum model of the biological medium and the low-frequency Doppler signal under the pulsed mode of ultrasound wave emission depends on the motion of the density inhomogeneities and compressibility. It also depends on the complex sensitivity function over the emission-receiving field which may also depend on time. The time dependence is caused by small deviations of the wave vector from the wave vector of plane waves without inclination. To reduce the effect of the rectangular window on the calculated spectra Gaussian weighting window are used.

In the case of the synthetic aperture technology, it is possible to generate an ultrasonic Doppler response signal directly from discrete signal values from different sequential angles of revolution of the wave vector. For a given range of angles Φ, the ultrasonic Doppler response signals are registered for a limited period of time, after which the registration procedure is repeated periodically. Thenthe dispersion of the Doppler frequency spectrumequal to$\sigma^2 = 2\left(\frac{1}{T_W^2} + \frac{V^2}{a^2}\right)$.

There is another way to generate an ultrasonic Doppler signal. Discrete values are obtained by coherent compounding of complex signal values at different angles of rotation for the entire period of angle change T. Then the dispersion of this Doppler spectrum can be written as follows$\sigma^2 = 2\left(\frac{2}{T_W^2} + \frac{V^2}{a^2}\right)$and it is greaterthan the dispersion of the previous spectrum by $\Delta\sigma^2 = 2/T_W^2$.

The reason for the increase in the width of the Doppler spectrum when forming a signal from Doppler signalcounts obtained at different steering angles is the change in the projection of the motion velocity onto the direction of the current wave vector due to a change in the Doppler angle, as shown in Fig 1. This situation can be interpreted as a movement with acceleration.

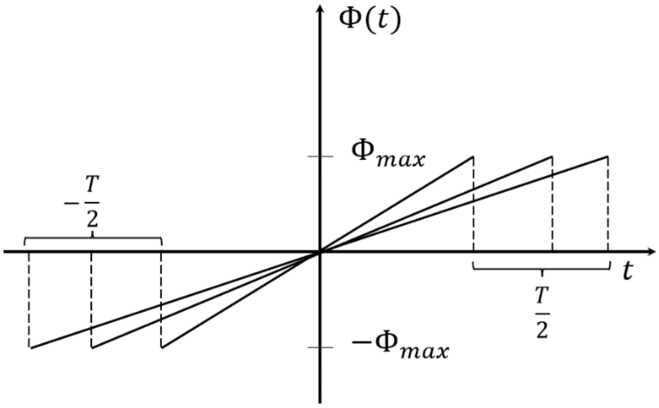

Figure 1. Model dependence of the wave vector deflection angle on time

Aceleration is inversely proportional to the time T_w. It is clear that both during acceleration and deceleration, the range of velocities during time T for a given range of angles is the same, so the width of the spectrum cannot depend on the sign of the acceleration. Because of this, in second dispersion, compared to first one, there is a quadratic acceleration term in the form of $2/T_W^2$.

Conclusions

The technology of plane wave compounding uses a periodic repetition of the sequence of waves with different inclinations. Therefore, a periodic extension of all time-dependent physical parameters naturally occurs, which leads to a limitation of the duration of ultrasonic Doppler response signals. The influence of limiting the duration of the response signals and its apodisation by weight windows on the spectral properties of the correlator of inhomogeneity motion and the spectrum of the sensitivity function of the ultrasonic system is determined. In contrast to the spectrum of the correlation function, the width of the sensitivity function spectrum depends on both the size of the measuring volume and the duration of the signals. Within the framework of a simple model of the sensitivity function, the Doppler spectra are considered for different ways of forming response signals using plane wave compounding. A Doppler spectrum is obtained by coherent compounding of signals received at different angles of inclination of waves during their repetition period. Compared to traditional diagnostic systems, the Doppler spectrum width is increased only by limiting the duration of the signals. There is no additional increase in the spectrum width if the compound signals are formed by accumulation with cyclic permutation, in which signals from each new wave angle are added. When forming a Doppler signal directly from Doppler signals at different inclination angles, the spectral width increases both in comparison with the traditional method of sensing with stationary focused ultrasonic fields and with the case of coherent signal accumulation. In terms of the internal physical meaning, the invented increase in the spectral width is connected with a dynamic change in the Doppler angle, which increases the interval of apparent projections of the velocities of motion of inhomogeneities along the direction of transmittingof a plane wave without inclination. The influence of nonlinear terms depending on the time of deviation of the wave vector from the wave vector without inclination requires additional study.

References

[1] I. Trots, A. Nowicki, M. Lewandowski, and Y. Tasinkevych, *Synthetic Aperture Method in Ultrasound Imaging,* (IntechOpen, London, UK, 2011). http://dx.doi.org/10.5772/15986

[2] G. Montaldo, M. Tanter, J. Bercoff, N. Benech, and M. Fink, IEEE Trans. Ultrason. Ferroelectr. Freq. Contr. **56**(3), 489 (2009). https://doi.org/10.1109/TUFFC.2009.1067

[3] I.V. Sheina, O.B. Kiselov, and E.A. Barannik, East Eur. J. Phys. (4), 5 (2020). https://doi.org/10.26565/2312-4334-2020-4-01

[4] Barannik, E. A., & Hrytsenko, M. O. (2024). Spectra of Ultrasound Doppler Response Using Plane-Wave Compounding Technique. *East European Journal of Physics*, (1), 476-484. https://doi.org/10.26565/2312-4334-2024-1-52

NONLINEAR REFRACTION COEFFICIENT INFLUENCE ON THE EFFICIENCY OF STIMULATED RAMAN SCATTERING

Oleksandr Mokhonko*, Anatoliy Ivanisik**
**Taras Shevchenko National University of Kyiv, e-mail: sashamohonko@gmail.com*
***Taras Shevchenko National University of Kyiv, e-mail: anatoliyivanisik@gmail.com*

Increasing the efficiency of stimulated Raman scattering is an urgent problem considering the scope of its application. In this work, we studied the nonlinear refraction coefficient on the efficiency of stimulated Raman scattering.

Stimulated Raman scattering

Stimulated Raman scattering is the light scattering in gases, liquids and crystals, which is accompanied by a noticeable change in its frequency. The origin of this effect is most conveniently explained within the framework of the quantum theory of radiation. According to it, frequency radiation is considered as a flow of photons with energy $h\nu$. In collisions with molecules, photons are scattered. In the case of elastic scattering, they will deviate from the direction of their movement without changing their energy (Rayleigh scattering). However, it may be that during the collision, energy exchange will occur between the photon and the molecule. At the same time, the molecule can both acquire and lose part of its energy in accordance with the rules of quantization: its energy can change by the amount ΔE, which corresponds to the difference in the energies of its two states. In other words, the value ΔE should be equal to the change in vibrational and (or) rotational energy of the molecule [1].

Efficiency of stimulated Raman scattering

However, the list of SRS-active media that have gained practical application is quite limited (hydrogen and methane under a pressure of tens of atmospheres, some crystals). Such optically stable and easy-to-use refractive as self-focusing liquids (toluene, benzene, xylene, etc.), in which SRS was historically observed for the first time [2].In connection with the relevance of this method and the above-mentioned problems, there is a need to improve the efficiency of stimulated Raman scattering. This will improve the sensitivity of analysis tools. What is especially important in analytical chemistry, biology, and medicine where Raman spectroscopy can be used to identify substances and study molecular properties with high accuracy [3].

Within the framework of this work, the influence of environmental parameters on increasing the efficiency of stimulated Raman scattering is checked. If the molecule acquires energy ΔE, then after scattering, the photon will have energy $h\nu-\Delta E$ and, accordingly, the radiation frequency $\nu-\Delta E/h$. And if the molecule loses energy ΔE, the radiation scattering frequency will be equal to $\nu+\Delta E/h$.

Radiation scattered with a lower frequency than that of incident light is called Stokes radiation, and radiation with a higher frequency is called anti-Stokes. When observing the Raman effect, the emphasis is often placed on the Stokes component, the main reason being that the Stokes component is usually observed better, this is due to the intensity and nature of the Raman effect itself.

In contrast to Rayleigh scattering of light, with Raman scattering, spectral lines are observed in the spectrum of scattered radiation, which are absent in the linear spectrum of primary light. The number and location of the lines that appear is determined by the molecular structure of the substance. By measuring the frequencies of these lines and knowing the frequency of primary radiation, it is possible to determine the frequencies of natural oscillations of the molecule, characteristic of each substance. This method for determining the structure can be especially effective in combination with IR spectroscopy.

The modified plane wave approximation was used to calculate the power of the Stokes (P_s) and laser (P_l) components under the self-focusing conditions described in previous works [4]. This approximation leads to the system of equations:

$$P_\ell + \frac{\lambda_s}{\lambda_\ell} P_s = P_{\ell 0},$$

$$\frac{dP_s}{dz} = GP_s \frac{P_\ell}{\pi a^2},$$

For the calculation, the parameters typical for the reconstruction of the multimode radiation of a ruby laser in toluene were used: $a_0=113\ mkm$; $a_f=5\ mkm$; $\lambda_\ell=649,3nm$; $\lambda_s=746,3nm$; $P_{cr}=25\ kW$; $n_0=1,48$; $L=35$cm; $G=1,17cm/MW$. The Wolfram Mathematica program was used to construct the energy dependence. Figure 1 shows a comparison of the efficiency SRS under the initial conditions n_0 and under changed conditions of nonlinear refraction coefficient $n_1=1.53$.

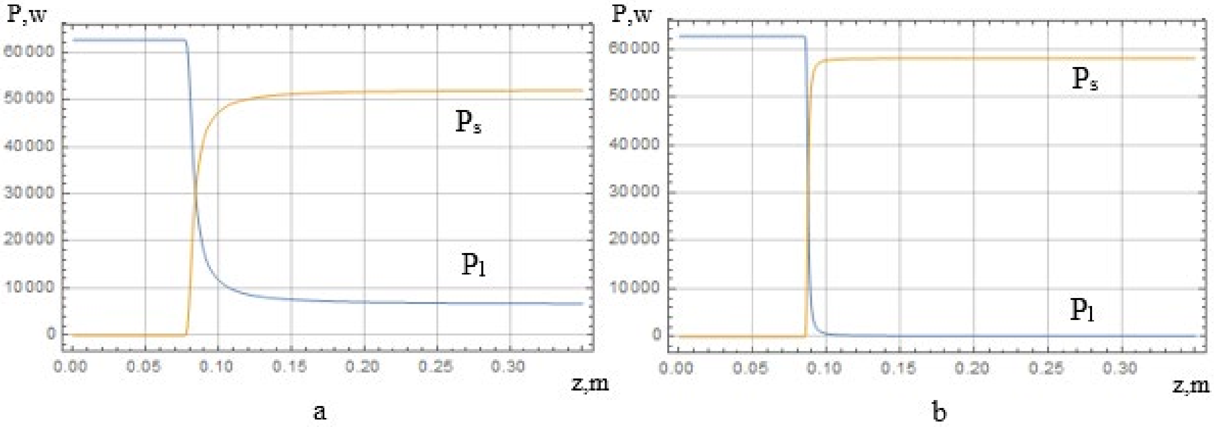

Fig. 1. Power dependence of the Stokes (P_s) and laser (P_l) components a - with a refraction coefficient of $n_0=1.48$, b - with a refraction coefficient of $n_1=1.53$

This paper proposes a method of increasing the efficiency of stimulated Raman scattering by increasing the nonlinear refraction coefficient. When the refraction coefficient increases, a more effective transformation of the laser component into the Stokes component is observed. It is also worth considering that if the n_1 is excessively increased, it may not be ensured. The goal of further research is to increase the n_1 while preserving other parameters. One of the methods can be the using of nanoparticles.

References

[1] Tipping, W.J.; Lee, M.; Serrels, A.; Brunton, V.G.; Hulme, A.N.. "Stimulated Raman scattering microscopy: an emerging tool for drug discovery" Chemical Society Reviews 2016

[2] G. Fibich A. L. Gaeta, "Self-focusing: Past and Present - Fundamentals and Prospects" Optics Express 2015

[3] J Prince, R.C.; Frontiera, R.R.; Potma, E.O.. "Stimulated Raman Scattering: From Bulk to Nano". Chem. 2017 Rev. 117 (7): 5070–5094. doi:10.1021/acs.chemrev.6b00545. PMC 5471143. PMID 27966347.

[4] Ivanisik A. I., Maly V. I., Ponezha G. V. "Stimulated Raman scattering in self-focusing media: new methods of experimental research" Bulletin of Kyiv University: Ser: f.-m. N. -1997. -B.4. -WITH. 239.

GRAY-SCALE GRADIENT DEEP LEARNING APPROACH FOR MEDICAL IMAGE QUALITY

Denys Sliusarenko*, Andrii Netreba**
**Faculty of RadioPhysics, Electronics and Computer Systems Taras Shevchenko National University of Kyiv, Kyiv 01601, Ukraine, email: d.fulhem@gmail.com*
***Faculty of RadioPhysics, Electronics and Computer Systems Taras Shevchenko National University of Kyiv, Kyiv 01601, Ukraine, email: avn@univ.kiev.ua*

A new approach for improving the quality of medical images using a deep learning model was proposed. Unlike traditional methods that process entire sets of images at once, the resulting model works with individual images, segmenting them into pixel intensity ranges based on grayscale. By dividing the image into these segments, our model effectively learns to denoise each segment individually, allowing for more targeted noise reduction. After denoising, the segmented images are reassembled to reconstruct the original image. The performance of this approach was evaluated using standard metrics such as PSNR and SSIM, considering Gaussian and Poisson types of noise. The results of the experiments demonstrate the high potential of this approach.

Introduction

We present a new approach to improve the quality of medical images using deep learning techniques. Our model works on individual images using segmentation based on gray gradients and a modified version of the U-Net architecture for effective noise reduction.

The segmentation process allows our model to focus on removing noise in each segment separately, while preserving the main characteristics of the image. Subsequently, the denoised segments are reconstructed to reconstruct the original image.

We evaluate the performance of our approach using standard metrics such as PSNR and SSIM, considering the types of noise commonly encountered in medical imaging. These metrics provide a qualitative assessment [1].

Proposed model and results

In this study, a non-standard approach to presenting images to the input of a neural network is proposed. The general idea is that instead of the entire data set in the form of 256*256 images, which are presented in full, which affects the statistical characteristic of the number of pixels, these images of the grayscale range are presented. division into these zones takes place based on the general statistics of the belongingness of zones of MR images of the brain to different tissues.

So far, we have focused on white and gray matter. the subtleties of the transitions between the fabrics are currently also poorly considered, which can be corrected in the future. T1 image was used. As a result, we obtained high values of PNSR (peak signal-to-noise ratio) and SSIM (structure similarity) indicators for weak and medium noise level, which consists of artificially added Gaussian and Poisson noises. U-net was used as the network to which this segmentation approach was additionally applied, since it has already managed to show good results and has an additional segmentation background[2-3].

In graphs 1-2, you can see that the signal-to-noise ratio decreases uniformly as the noise level increases, which means the high stability of the chosen approach.

In addition, the adaptability of the proposed approach allows for easy integration with other neural network architectures outside of U-net. This flexibility opens opportunities to explore different network architectures and adapt them to specific denoising tasks, potentially leading to further improvements in accuracy and reliability. Future work should focus on refining the segmentation boundaries between different tissues and investigating the applicability of the approach to other medical imaging techniques.

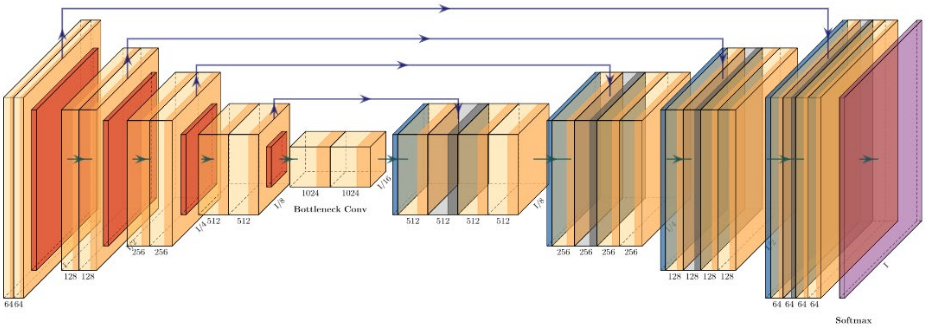

Figure 1. The used U-Net model

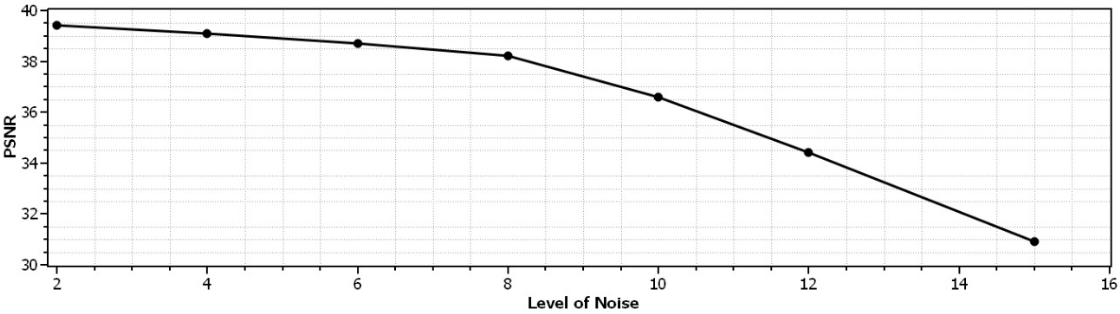

Figure 2. SSIM

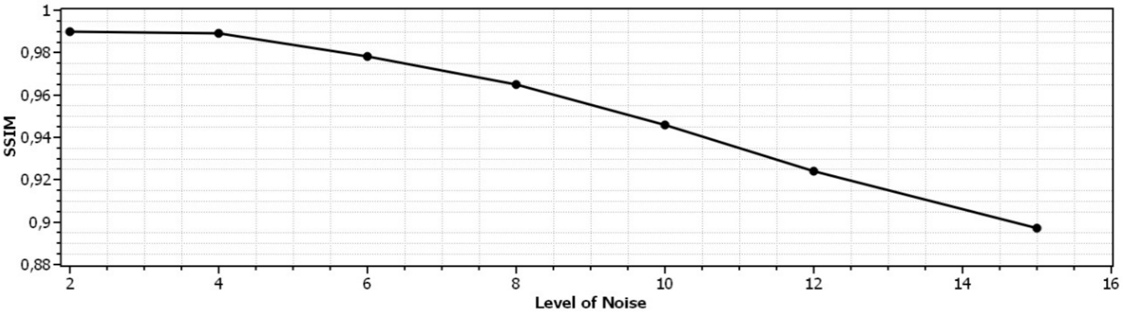

Figure 3. SSIM

Conclusions

Our contribution highlights the importance of customized deep learning solutions for denoising medical images and highlights the prospects of our approach in advancing the field of medical imaging. A neural network was developed that takes as input a segmented grayscale image and reconstructs denoised images. The obtained high values of psnr and ssim testify to the high quality of image recovery. Further work on finer segmentation can significantly increase fine detail.

References

[1] A. Hore and D. Ziou, 'Image Quality Metrics: PSNR vs. SSIM', in *2010 20th International Conference on Pattern Recognition*, Istanbul, Turkey: IEEE, Aug. 2010, pp. 2366–2369. doi: 10.1109/ICPR.2010.579.

[2] R. Komatsu and T. Gonsalves, 'Comparing U-Net Based Models for Denoising Color Images', *AI*, Oct. 2020, doi: 10.3390/ai1040029.

[3] D. Sliusarenko and A. Netreba, *MRI IMAGE DENOISING USING NEURAL NETWORK*. 2022. doi: 10.7937/K9/TCIA.2018.15quzvnb.

EXPERIMENTS AUTOMATION INTERFACE IN THE SPECTROMETRIC LABORATORY INFORMATION SYSTEM

Kushnir O. A., Radchenko S. P.
Taras Shevchenko National University of Kyiv, 63/13, Volodymyrska str., Kyiv 01601, Ukraine,
e-mail: xelambert@gmail.com, sprad@knu.ua

This work is devoted to the software and hardware means of communication of the spectrometer with the server on which the spectrometric laboratory information system works. The structure of the appropriate communication interface and the schematic solution for the communication of the spectrometer detection units with the server were developed, the requirements for the components of the circuit were determined, the PC interaction software with the microcontroller, which is part of the circuit technical solution, and the geometric placement of the CCD-detectors were developed, and to correct measurement the CCD-detector sensitive fields overlapping solution was proposed.

Introduction

Optical spectral analysis is one of the most common methods for identifying the quantitative and qualitative composition of substance. This area accounts for the majority (over 80%) of analyzes in metallurgy and machinery. This method is also widely used in laboratory practice for geological and environmental research, medical diagnostics, monitoring of bioluminescence of sea waters, diagnostics of plasma of rocket engines and other technology applications [1]. Old spectrum registration systems cannot be connected to computers and the software does not allow for the automation of measurements at the modern level. Solving this problem will provide opportunities for automating work with the spectrometer. In particular, this applies to the procedures of processing the optical emission spectra of radiation of various objects, in particular, plasma. Such a set of capabilities is currently not available in existing spectrometer work systems [2 – 5]. Therefore, as part of the work, it was also decided to integrate previously elaborated spectrometric laboratory information system with automating module of the diffraction optical spectrometer DFS-8 used in department laboratory (Fig. 1).

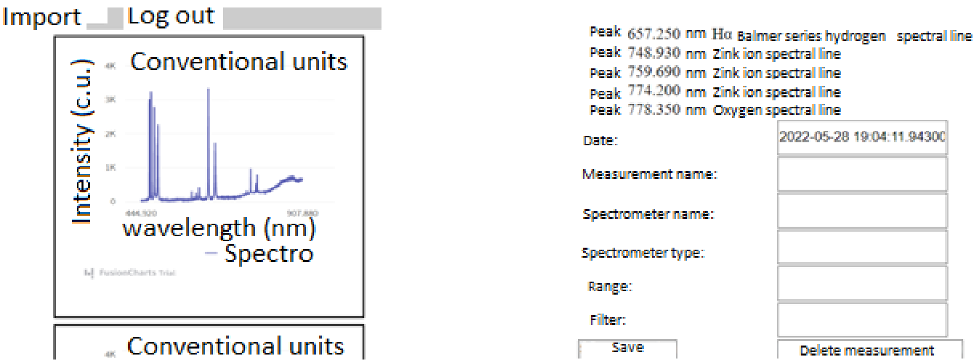

Peak 657.250 nm Hα Balmer series hydrogen spectral line
Peak 748.930 nm Zink ion spectral line
Peak 759.690 nm Zink ion spectral line
Peak 774.200 nm Zink ion spectral line
Peak 778.350 nm Oxygen spectral line

Date: 2022-05-28 19:04:11.9430
Measurement name:
Spectrometer name:
Spectrometer type:
Range:
Filter:

a ***b***

Fig. 1. – The web application interface of the spectrometric laboratory information system.
a – measured data library, b – data visualization structure (Data block).

Methods and results

A graphic representation of the system structure has been developed. The documentation of the main development boards available on the market with a microcontroller was analyzed, and the Arduino solution was chosen to solve this problem. The hardware and software requirements for the spectrometric laboratory information system and the communication functionality between the server and the microcontroller were analyzed, and the corresponding list of requirements for the server computer was determined. The documentation of linear CCD detectors available on the market and the financial component of each option were analyzed, and the ILX554 series was chosen to solve the problem. According to the detector documentation a functional scheme has been developed (Fig. 2).

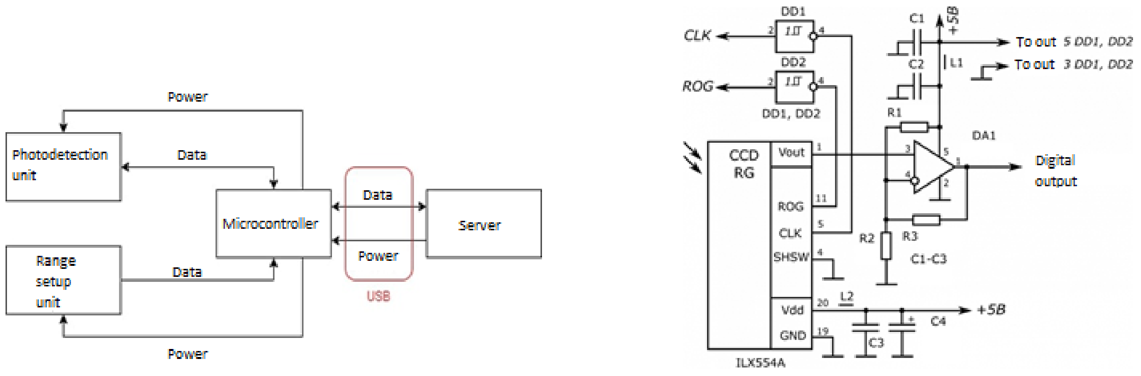

a ***b***

Fig. 2. – functional scheme, a – system block structure, b – electronic circuit.

For communication between the microcontroller and the PC, programs are written in C++ and C# for each device, respectively. The geometric placement of CCD detectors was developed. The correction procedure of pixels information obtained on the detectors edges was also proposed (Fig. 3).

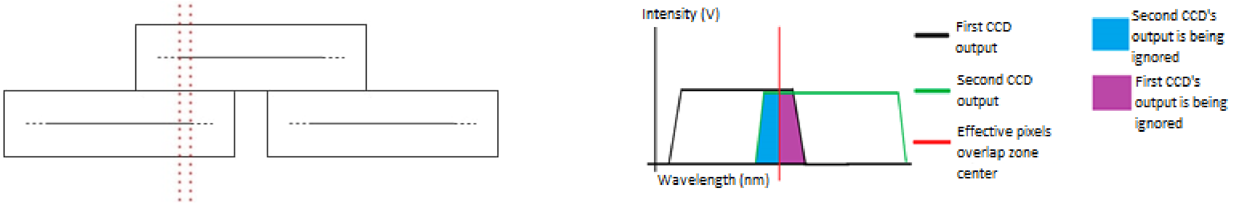

a ***b***

Fig. 3. – Correction procedure basis. a – CCD matrices position, b – sensors overlapping zone.

Conclusions

As a result of the work, a prototype of the spectrometric laboratory information system was created, into which an interface for automating spectrometric experiments was integrated. The developed system provides the researcher with the opportunity not only to receive and process information in digital form, but also to automatically recognize spectral lines. Thus, the time of routine work, costs of searching for information about the history and conditions of initiation of electric discharges, materials for their initiation and comparison of received spectral lines, etc., are reduced. The system provides the possibility of automated work with the spectrometer, analysis of spectrometric data, including automatic prediction of sample composition, instant receipt of relevant reference information, which is exported to the database of the application from the appropriate source of the National Institute of Standards and Technology NIST, which is new for the field of optical spectrometry. The developed tool allows you to automate work with the spectrometer and speed up the work process of spectroscopists, improve the productivity of their research.

References

[1] A charge-coupled device (CCD) spectrophotometer for measuring marine bioluminescence [Electronic resource] / A.C. Arneson, S. Benyamin, B. Jones, G.W. Schmidt. - 1988. – Resource access mode: https://www.int-res.com/articles/meps/43/m043p277.pdf

[2] HOLMARC UV-VIS-IR Spectrometers [Electronic resource] - Resource access mode: https://www.holmarc.com/pdf/8_Spectroscopy.pdf

[3] High-Resolution CCD Spectrometer [Electronic resource] - Resource access mode: https://www.spectralproducts.com/pdf/SM445.pdf

[4] USB4000 Fiber Optic Spectrometer. Installation and Operation Manual [Electronic resource] - Resource access mode: https://www.oceaninsight.com/globalassets/catalog-blocks-and-images/manuals--instruction-ocean-optics/spectrometer/usb4000operatinginstructions.pdf

[5] Design and construction of a digital CCD spectrometer [Electronic resource] - Resource access mode: https://www.fzu.cz/~dominecf/spek2/vu.pdf

ANALYZING GAZE DIRECTION AND SPEED THROUGH EEG DEVELOPING A METHODOLOGY FOR NON-INVASIVE NEUROPHYSIOLOGICAL MONITORING

I. B. Ryabko, O. O. Klymov, S. P. Radchenko
Medical Radiophysics Department, Faculty of Radiophysics, Electronics and Computer Systems,
Taras Shevchenko National University of Kyiv, Ukraine, Kyiv, Acad. Glushkova av., 4-g
e-mail: vanoryabko@gmail.com, alexander.ukzp@gmail.com, sprad@knu.ua

***Abstract**: This study develops a methodology for detecting the direction and speed of gaze using electroencephalography (EEG) with a 19-channel Neurokom EEG system and Neurokom Standard software [4]. By recording and analyzing EEG signals tagged with specific gaze directions via IBM SPSS Statistics software [5], we utilized factor analysis [2] and canonical correlation analysis to effectively determine gaze coordinates. This method adheres to the 10-20 system for electrode placement, ensuring standardized data collection [1].*

Introduction: This project highlights the importance of EEG in examining visual activity and cognitive process integration. The methodology encompasses experimental procedures where subjects adjust their gaze direction physically and mentally, with both eyes open and closed, in various orientations.

Theoretical Analysis:

1. **Preparation of the Covariance Matrix**: This matrix, or a correlation matrix, delineates inter-variable relationships.

2. **Extraction of Initial Orthogonal Vectors**: These vectors capture essential data, serving as the main components of the analysis.

3. **Rotation to Final Solution**: Techniques like Varimax rotation refine the factors for clearer results[3].

$$Varimax\ criterion = \frac{1}{p}\sum_{j=1}^{p}\left(\sum_{i=1}^{d}\left[\left(\sum_{k=1}^{p} v_{ik}^2\right)\cdot\left(r_{ij}^2 - \frac{1}{p}\sum_{k=1}^{p} v_{ik}^2\right)\right]\right)^2$$

4. **Principal component analysis**: (PCA is a statistical method used to reduce the dimensionality of data by transforming an original set of variables into a new set consisting of linearly independent components.

5. **Quantitative assessment**: The method of correlation analysis is used to identify the assessment of the strength of the connection between random values, signs or factors that characterize a certain real process or object.

Methodology: EEG data were captured using the standardized 10-20 system, which involves placing electrodes at consistent locations across the scalp to accurately represent brain activity and ensure reproducible results.

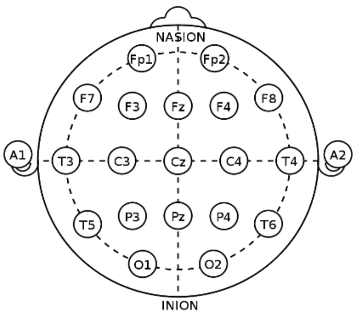

Fig. 1. Electrode locations of International 10-20 system for EEG (electroencephalography) recording

Research Results: Graphical analysis relative to lead Fp1 highlighted mental eye movements and the influence of significant coefficients. By the F9 factor from the set of patient №1, the direction of the gaze to the left can be determined. The downward gaze direction can be determined by factor F13 from the set of patient №2.The findings show that electrodes traditionally used for recording miotic movements can also detect eye movements, supporting the feasibility of non-invasive gaze tracking.

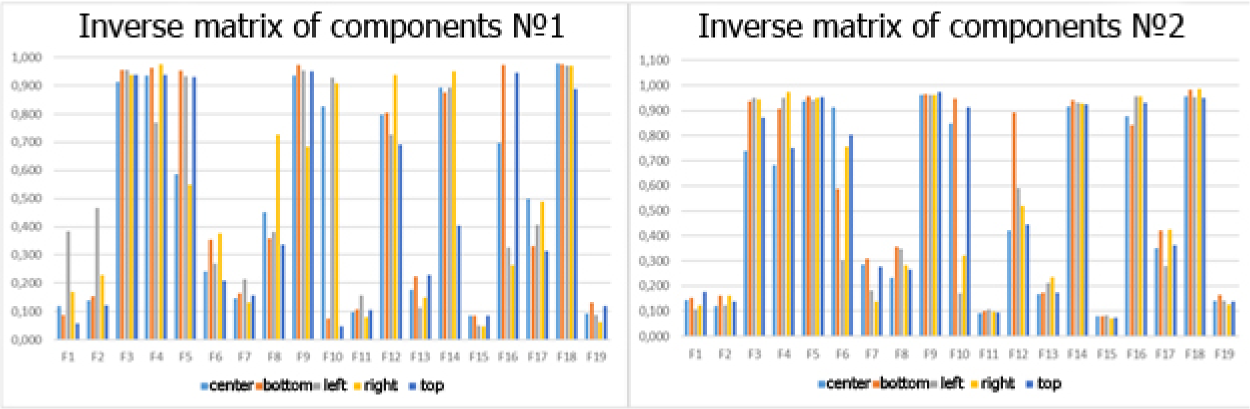

Fig. 2. Verification and analysis of correlations. Inverse component matrices.

As a result of work with an electroencephalograph, analyzes of EEG signals and studies of the results of these analyses, a method for determining the speed of the movement of a person's gaze was obtained and tested. It is proved that the correlations between the factors of the distribution of load coefficients among the same studies within the framework of one subject have positive results, which were used for testing the method.

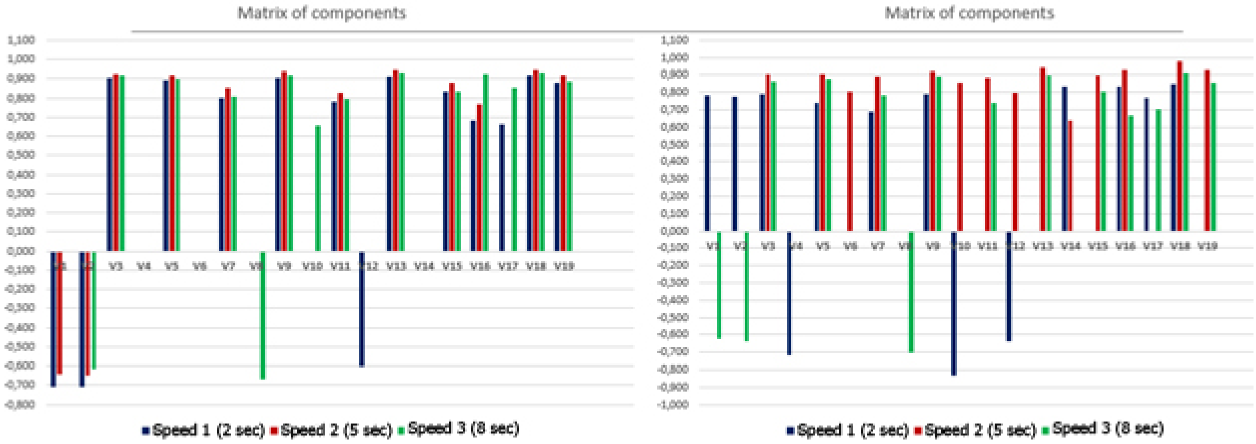

Fig. 3. Diagrams of factor loadings.

(Speed 1 (2 seconds of recording) is 17.5 centimeters per second. Speed 2 (5 seconds of recording) is 7 centimeters per second. Speed 3 (8 seconds of recording) is 4.375 centimeters per second.)

Conclusion: The research establishes a non-invasive method to predict gaze direction using EEG [6], applicable in neuromarketing, psychological research, and clinical practice. Future efforts will aim to enhance the accuracy of this methodology and extend its application to more dynamic settings.

References

1. Cherninsky A.O., Kryzhanovsky S.A., Zima I.G., "Electrophysiology of the Human Brain".
2. Factor Analysis: Cooley, V.W., and Lohnes, P.R. Multivariate Data Analysis. John Wiley & Sons, N.Y.
3. IBM Documentation v.29.0.0: Link
4. NeuroCom standard software: Link
5. IBM SPSS Statistics software v.22 (30-day trial version): Link
6. VISUAL ACTIVITY ELECTROENCEPHALOGRAMS PARAMETERS EXTRACTION O. O. Klymov, I. B. Ryabko, S. P. Radchenko.

PLASMA PHYSICS

SURFACE MODIFICATIONS IN RE-SOLIDIFIED LAYERS OF PERSPECTIVE MATERIALS UNDER POWER PULSED PLASMA LOADS

S. S. Herashchenko, V. A. Makhlai, I. E. Garkusha, Yu. V. Petrov, N. N. Aksenov, N. V. Kulik, P. B. Shevchuk, D. V. Yeliseyev, Y. E. Volkova, T. M. Merenkova

** National Science Center, 'Kharkov Institute of Physics and Technology', Institute of Plasma Physics, Kharkiv, Ukraine, e-mail: gerashchenko@kipt.kharkov.ua, stasgnk@gmail.com*

The surface modification of advanced materials was studied through a series of repetitive plasma pulses caused tungsten melting. Features of the affected surface layers in reference materials (IGP W, AM W/WTa, and EUROFER) for both fusion and fission applications were explored after exposure to plasma in the facilities (QSPA, MPC) with different durations of plasma pulses. A detailed surface analysis was carried out with Scanning Electron Microscopy. It was revealed that the plasma treatment led to the formation of a modified layer as a result of the rapid re-solidification of the exposed surface. The fine cellular structures appeared in the re-solidified layers of the irradiated materials, with typical cell sizes ranging from 150 to 500 nm. An increase in the roughness of the exposed surfaces was attributed to the presence of the cracks and re-solidified layer.

Introduction

Advanced high-performance materials used in nuclear power reactors, both for fission and fusion applications, must endure severe conditions such as high heat loads, particle bombardments, high-energy neutron irradiation, etc. [1, 2]. A comprehensive understanding of the mechanisms behind materials damage effects and dedicated efforts toward mitigation will yield substantial benefits that apply across various nuclear environments. Pulsed plasma facilities encompass a range of scenarios involving high heat and particle loads onto the surfaces. These facilities are used to make surface modifications [3, 4] for various technologies, study erosion mechanisms of different materials, and uncover the risks associated with plasma contamination by erosion products. This work is devoted to the characterization of surface modifications originated during a solidification process in materials under various plasma stream conditions, i.e., different pulse duration, plasma species, and applied heat loads.

Experimental device and diagnostics

The study of surface modifications under the high-power pulsed plasma streams was performed using two different facilities: QSPA Kh - 50 and MPC. The large-scale QSPA Kh - 50 device [3, 4] reproduced the fusion reactors transient conditions. The main parameters of the QSPA hydrogen plasma streams included an ion impact energy of about 0.4 keV, a maximum plasma pressure of 0.32 MPa, and a stream diameter of 18 cm. The plasma pulse shape was approximately triangular with a pulse duration of 0.25 ms. The plasma stream energy density was up to 3 MJ/m^2. The MPC facility [3] generated helium compressed plasma streams with a plasma density (n_e) around 10^{18} cm^{-3}, and a plasma energy density ranging from 0.05 to 0.5 MJ/m^2. The discharge half-period was equal to about 10 μs. The experiments were carried out using pure helium at an initial pressure of 266.64 Pa.

The heat loads onto the exposed surfaces were selected to operate above the melting threshold of the treated materials [3, 4]. The microstructure was examined using SEM (JSM 7001F) equipped with an energy-dispersive x-ray analysis system (EDXA, Inca Energy-350). Mass measurements were performed during the experiment to monitor the mass loss (ΔM) with an accuracy of ±15 μg.

Experimental results

Pulsed plasma exposures led to the surface modifications of samples made from various materials (Fig. 1). Samples of pure IGP tungsten with the transversal (T) grain orientation and in the recrystallized (R) state were used for the experiments. Two types of samples, which were produced using additive manufacturing (AM) based on the laser powder bed fusion (LPBF) method, were also tested. These materials took the form of nominal 1 cm cubes of lattice material in both pure W and W-6% Ta. Samples of EUROFER steel were also studied in the reported experiments.

Applied plasma loads caused the development of the re-solidified layers and cellular structures on the exposed surfaces. The formation of the re-solidified layers, accompanied by the presence of the cracks, progressive corrugations, pores, and spheres observed on the irradiated surfaces. The fine cellular structure with the typical cell size of 150…500 nm appeared in the re-solidified layer for materials including IGP W, AM W/Ta, and EUROFER samples. The sub-grain patterns probably were created by Bénard-Marangoni instability superimposed on the macro-grain solidification that is determined by the parameters of the temperature gradient and solidification rate [5].

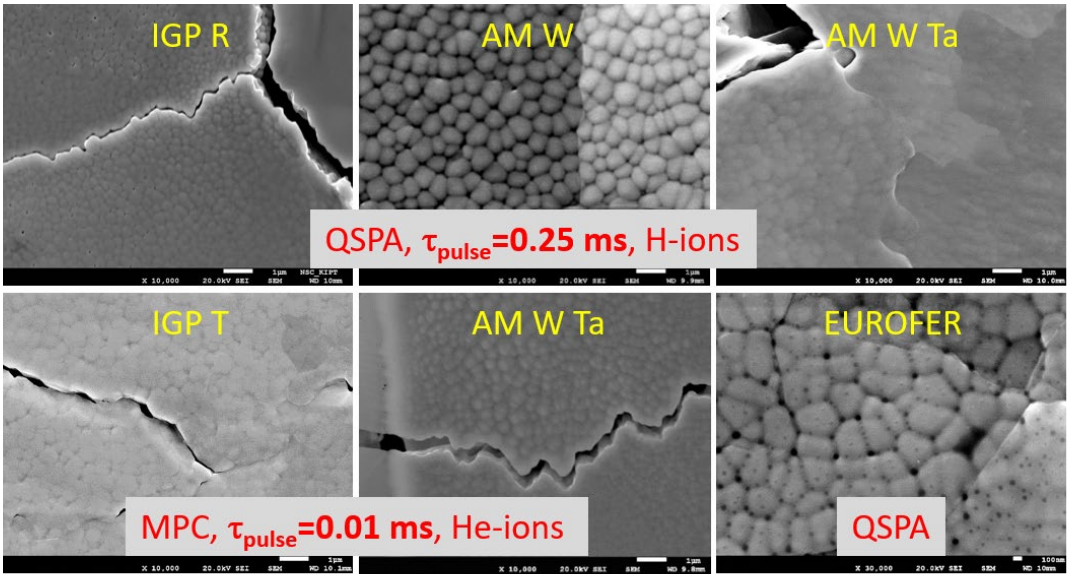

Fig. 1. SEM images of IGP R, IGP T, AM W/WTa, and Eurofer samples exposed to the hydrogen QSPA plasma, or to short - pulse helium plasma of MPC. Scale bars: 1 μm, and 100 nm.

Conclusions

The surface modifications due to the solidification process in various materials were characterized in the experiments performed at QSPA and MPC involving different plasma stream parameters, such as varying pulse duration, plasma species, and applied heat loads. A submicron-sized cellular sub-grain structure developed on the exposed surfaces. It can be attributed to the high-temperature gradient within the molten layer, influenced by the Bénard-Marangoni instability superimposed on the macro-grain solidification process.

References

[1] G. Pintsuk et al. Materials for in-vessel components // Fusion Engineering and Design. 2022, p. 112994
[2] L. Malerba et al. Multiscale modelling for fusion and fission materials: The M4F project // Nuclear Materials and Energy. 2021, v. 29, p. 101051.
[3] I. E. Garkusha et al, Materials surface damage and modification under high power plasma exposures // Journal of Physics: Conference Series. 2018, v. 959, p. 012004.
[4] V. I. Tereshin et.al. Pulsed plasma accelerators of different gas ions for surface modification // Review of Scientific Instruments. 2002, v. 73, p. 831.
[5] Lisong Zhang et al. Experimental and simulation studies on damage mechanisms of tungsten and molybdenum under compressed plasma flow irradiation // Nuclear Fusion. 2023, v. 63, p. 076010.

PROPERTIES OF SECONDARY DISCHARGE PLASMA IN CARBON DIOXIDE PLASMA

Shramenko Nataliia
Taras Shevchenko National University of Kyiv - KNU, e-mail: shramenkonatalia999@gmail.com

The paper presents the results of an experimental study of the plasma parameters of a secondary discharge of atmospheric pressure supported by a low-power rotating sliding discharge in a flow of carbon dioxide under the conditions of a significant excess of the volume of the current channel of the secondary discharge over the volume of the current channel of the independent discharge. Determination of plasma parameters was carried out by the methods of plasma emission spectroscopy using the SpecAir program. The estimation of the electric field strength in the plasma of the secondary discharge was made on the basis of the voltage drop on the secondary discharge when the length of the current channel of the discharge changes due to the change in the interelectrode distance.

Methods of plasma analysis

The parameters of the discharge plasma were determined based on the measured optical emission spectra - OES, in order to obtain the excitation temperature of the electronic levels of atoms.

Optical emission spectroscopy, as a powerful diagnostic tool for plasma, is often used to identify species and determine plasma parameters, such as temperature and density of electrons, temperature of excitation of electronic levels of atoms, vibrational and rotational temperatures of molecules, etc.

In appearance, optical spectra are divided into line spectra, which consist of individual spectral lines that correspond to discrete intensity values, band spectra, which consist of individual bands, each of which covers a certain interval of intensity values, and continuous ones, which cover a wide range of intensities.

Accurate measurement of absolute intensities is associated with significant experimental difficulties and requires knowledge of the sensitivity of the entire spectral system, i.e., a complex calibration procedure. In addition, very often only the relative values of transition probabilities are known. Based on this, Ornstein developed a spectroscopic method for determining temperature, which is based on measuring the relative intensities of spectral lines of the rotational structure of molecular bands or atomic emission lines. It is possible to determine the corresponding temperature of the population of energy levels by measuring the relative intensities of two lines I_1 and I_2 belonging to one atom or ion, with the energies of the upper levels E_1 and E_2, from the ratio:

$$R = \frac{I_1}{I_2} = \frac{\lambda_2 g_1 A_1}{\lambda_1 g_2 A_2} e^{-\frac{E_1 - E_2}{kT}} = const \cdot e^{-\frac{\Delta E}{kT}} \tag{1}$$

where A_1, A_2 are coefficients, g_1, g_2 are the statistical weight of the lower and upper levels, respectively, k is the Boltzmann constant, and T is the temperature.

Experimental setup

Experimental installation for activation of chemical transformations of gas-phase substances by the plasma of a secondary discharge supported by a rotating sliding discharge is presented in Fig. 1

Electrode 1 is fixed in the center of fluoroplastic and is powered by a direct current source. The outer cylindrical electrode 2 is grounded. Both electrodes are made of stainless steel. An arbitrary flow of air is introduced through two tangential inlets at the bottom, and the arc is first formed in the narrowest gap and then rotates stably in the ring between the electrodes.

The resulting rotating sliding discharge serves as an electrode for the secondary discharge maintained between it and the high-voltage electrode 3.

In the system with a sliding discharge, a larger volume of plasma is formed and the electrodes are destroyed less.

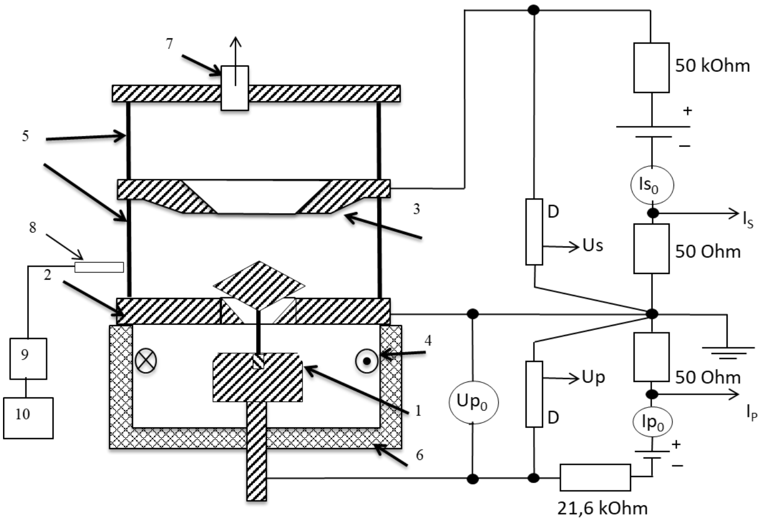

Fig. 1. An experimental installation for the activation of chemical transformations of gas-phase substances by the plasma of a secondary discharge supported by a rotating sliding discharge.

Determination of plasma parameters of discharges was carried out using UV and visible emission spectroscopy of plasma (200 - 1000 nm). Registration of radiation spectra was carried out using a Solar TII spectrometer.

References

[1] "Physico-chemical characteristics of plasma systems with rotary sliding discharge" V.Chernyak, et al., Resonance Phenomena in Atomic Systems, Uzhhorod, September 2023

[2] "Determination of vibrational and rotational temperatures in a gliding arc discharge by using overlapped molecular emission spectra" Tian-Liang Zhao et al 2013 J. Phys. D: Appl. Phys.

[3] A. Fridman. Plasma chemistry. Cambridge University Press. 978 (2008)

[4] https://www.nist.gov/pml/atomic-spectra-database

QUASI-PERIODIC PLASMA MOMENTUM DISTRIBUTION IN THE INTERACTION OF STRONG ELECTROMAGNETIC BEAM WITH THE DENSE PLASMA BARRIER

B.R. Mykhailenko, I.O. Anisimov
Taras Shevchenko National University of Kyiv, Faculty of Radiophysics, Electronics and Computer Systems
E-mail: mihaylenko.bogdan12@gmail.com

Early stages of supercritical plasma layer transillumination by strong electromagnetic beam simulation results are presented. The results demonstrate small-scale redistribution of plasma density. This redistribution is caused by electron fluxes that are stable in both directions and amplitude, occurring on the surface and deep within the barrier. These electron fluxes have no visible correlation among static electric fields. One can assume, they are masked by strong fluctuating fields caused by the relatively low number of particles per cell.

The study of wave propagation through typically opaque plasma regions has been studied for decades [1], with applications in space communications, plasma diagnostics, and laser thermonuclear fusion. Our previous works [2-3] investigated plasma barrier transillumination during high-power electromagnetic beam interaction, which forms a reduced-density channel. This paper presents preliminary findings on time-stable quasi-periodic electron momentum distribution which leads to plasma density redistribution over time.

The simulation was performed by the particles in cells method using the PIConGPU software package [4]. Our previous study explored measures, such as momentum projection, that effectively characterize plasma behavior and electron motion. Additionally, creating a profile of the standing wave, formed by the incident beam and its reflection, better visualizes beam-plasma interaction. Here we observe a temporally stable, quasi-periodic distribution of electron momentum along both horizontal and vertical axes, both on the surface and within the barrier. This distribution can potentially influence the early stages of channel formation within the plasma.

The following simulation parameters were used: hydrogen fully ionized plasma was treated, density – $9 \cdot 10^{12}$cm^{-3} (electron plasma frequency – 18 GHz); plasma temperature – 0.5 eV (isothermal plasma); the plasma layer thickness – 12.5 cm, radius – 21.5 cm; incident wave length – 3.33 cm (frequency – 9 GHz, i.e. plasma is opaque for this wave); pulse duration – 101 ns; pulse radius (at half maximum) – 5 cm; the maximum electric field amplitude is 0.964·MV/cm (4 times smaller than moderate wave in [2-3]).

The simulation results are shown in figs. 1-2, differing in time. Figures show the particle's density, impulse horizontal and vertical projection, electric field spatial distributions averaged in time over 2 ns period. Time averaging allows us to observe standing electromagnetic waves and remove flickering for impulse visualization.

During the process of channel formation (30-70 ns), strong electric fields and electron velocities arise, which determine the maximum of the visualization scale, in order to eliminate the phenomenon of "image overexposure". But at early stages (up to 20 ns), much more subtle effects occur, which are not noticeable on such an overestimated scale, but nevertheless have an impact on the barrier. We can observe a vertical quasi-periodic distribution of electron momentum which does not disappear after time-averaging and leads to the appearance of a series of grooves on the surface of the barrier (Fig. 1). At the same time, horizontal momentum distribution arises in the depth of the plasma, which leads to the appearance of a series of rarefactions, even though we cannot see any static fields penetrating deep into the plasma (Fig. 2).

Simulation results analysis leads to the following conclusion.

1. In the early stages of the transillumination process, a horizontal and vertical momentum distribution is observed on the surface and in the depth of the plasma barrier.
2. Since the momentum distribution is stable over time, it leads to a redistribution of the barrier density, creating grooves on the surface and rarefactions in the depth of it.
3. These two types of density redistribution proceed much faster than the ponderomotive force channel formation. Therefore, we can assume that it accelerates the process of channel formation for high electromagnetic beam intensities and makes transillumination possible for low intensities.

Acknowledgment

This work has been carried out within the framework of the EUROfusion Consortium, funded by the European Union via the Euratom Research and Training Programme (Grant Agreement № 101052200 -EUROfusion). Views and opinions expressed are however those of the author(s) only and do not necessarily reflect those of the European Union or the European Commission. Neither the European Union nor the European Commission can be held responsible for them.

[1] I.O.Anisimov, L.I.Romaniuk. // Ukr. Phys. Journ. Reviews. **6**, 101 (2010). In Ukrainian.
[2] B.R. Mykhailenko, I.O. Anisimov. // Probl. of Atomic Sci. and Techn. **№6 (130),** 64 (2020).
[3] B.R. Mykhailenko, I.O. Anisimov. // Probl. of Atomic Sci. and Techn. **4 (134),** 3 (2021).
[4] M Bussmann et al. // SC’13 Proc. Int. Conf. High Perform. Comp. Networking, Storage Anal. **60,** 1 (2013).
[5] G.M. Batanov, V.A. Silin. // Proc. Lebedev Phys. Inst. 73, 87 (1974). In Russian.

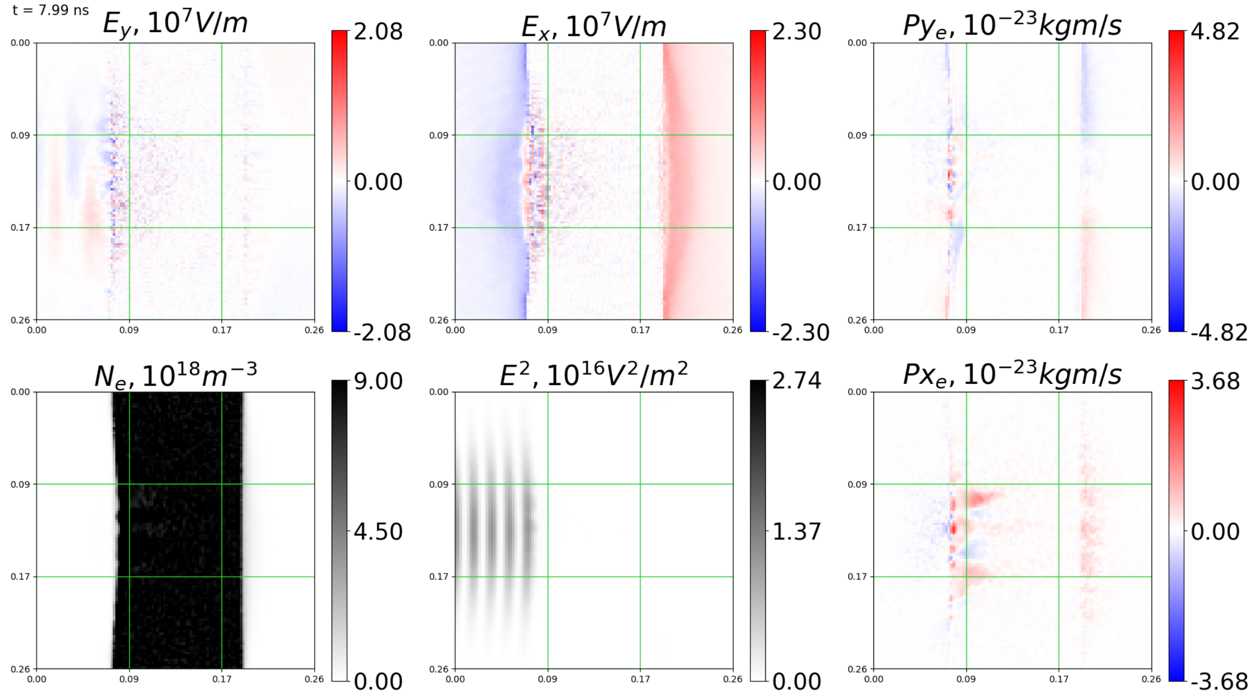

Fig.1. Electrons’ density, impulse and electric field time averaged distributions, when an electromagnetic beam is falling on plasma, at the time point 7.99 ns

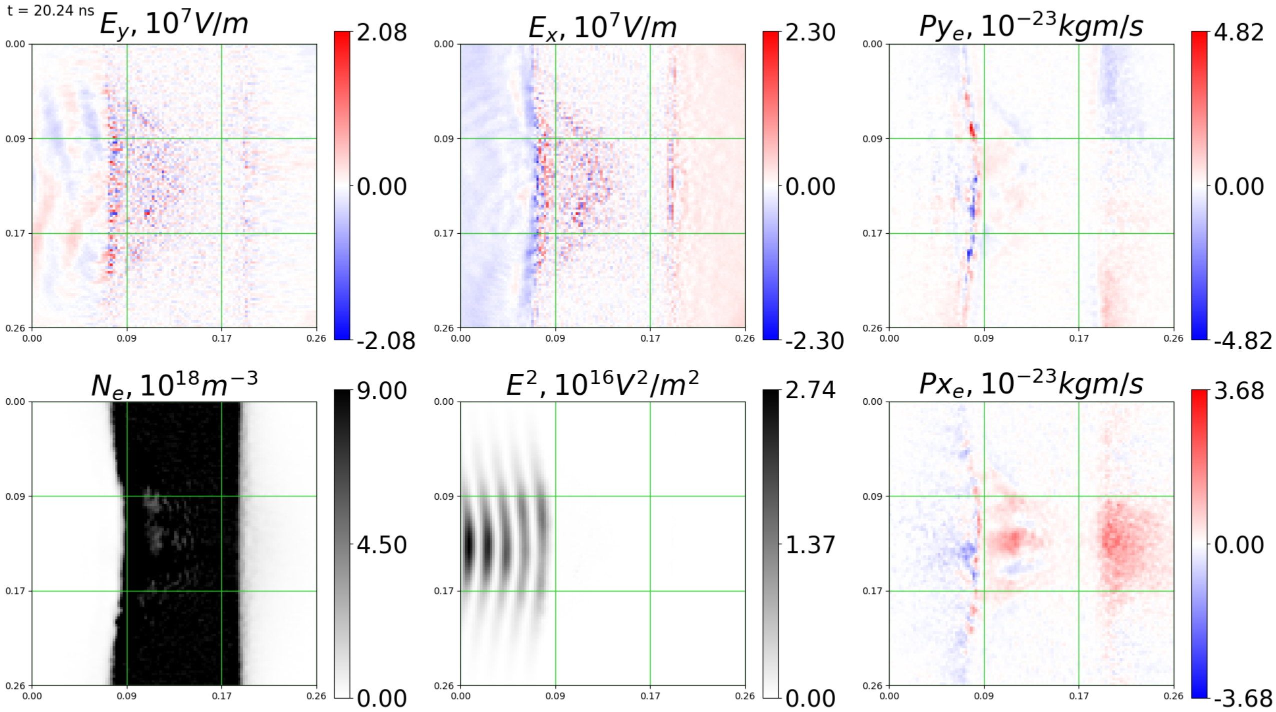

Fig.2. Electrons’ density, impulse and electric field time averaged distributions, when an electromagnetic beam is falling on plasma, at the time point 20.24 ns

GENERATION OF PLASMA PHENOMENA BY A TESLA TRANSFORMER

O. Ivanyuta, A. Ivanov
Taras Shevchenko National University of Kiyv, 64, Volodymyrska str., Kiyv, 01033, Ukraine
E-mail: oleksandr.ivanyuta@knu.ua

The paper considers natural plasma phenomena, describes their dynamic characteristics, their boundary conditions, and tests the possibility of their artificial generation by a Tesla transformer.

Plasma is a state of matter in which its atoms are ionised, i.e. electrons are detached from nuclei. Ionisation can occur, in particular, as a result of collisions of electrons accelerated in an electromagnetic field with gas atoms. In this work, a flat spiral Tesla coil was used for ionisation, the main advantage of which compared to the classical one is improved spark suppression, which can achieve higher voltages due to its geometry, which helps to suppress sparks.

To find the boundary conditions for plasma phenomena, various laws were used, one of which is Paschen's law, which states that the lowest ignition voltage of a gas discharge between two flat electrodes is constant at the same values of the product of gas pressure and electrode distance, a graphical representation of which can be seen in Pic. 1.

As a result of this work, natural plasma phenomena or visually similar to them, such as lightning, aurora borealis, and St. Elmo's lights, were artificially produced. Argon, neon, krypton and xenon gases were ionised to generate the aurora borealis-like phenomenon. An emulsion liquid was used to generate the St. Elmo lights,

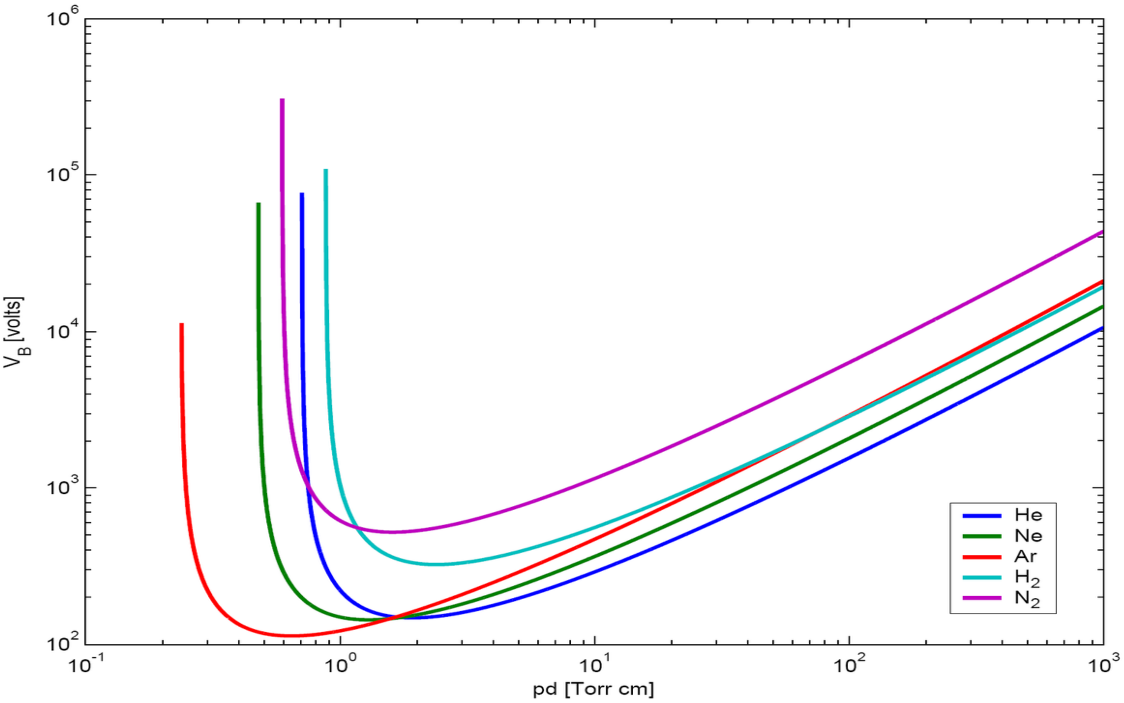

Fig. 1. Paschen curves

1. Plasma Physics / I.O. Anisimov ; - Kyiv : Taras Shevchenko National University of Kyiv, 2018. 229 p.
2. Fundamentals of radio electronics: a textbook / V.M. Kichak, Y.V. Krushevsky, D.V. Gavrilov - Vinnytsia: VNTU, 2010. 368 p.
3. Electricity and magnetism: a textbook / Didukh L.D. - Ternopil: Textbooks and manuals, 2020. 464 p.

OPTICAL EMISSION SPECTROSCOPY OF BREAKING ARC PLASMA BETWEEN COMPOSITE Cu-W ELECTRODES

V. Apanasenko, A. Murmantsev, A. Veklich, V. Boretskij
Taras Shevchenko National University of Kyiv, 63/13, Volodymyrska str., Kyiv 01601, Ukraine
vdapanasenko@knu.ua

This work is a part of wide investigation of surface interaction of Cu-W composite materials with thermal plasma of electric breaking arc. In this stage of study, the emission spectra of such a plasma were registered and treated to determine the temporal evolution of excitation temperatures in the plasma of breaking arc discharges between composite Cu-W electrodes at currents of 4, 50 and 104 A.

Introduction

Copper-tungsten (Cu-W) composites have attracted significant interest due to their excellent mechanical and thermal properties compared to traditional electrode materials. These composites combine high electrical conductivity, heat resistance, and superior erosion resistance. As such, Cu-W composites are increasingly viewed as ideal materials for applications that demand durable and reliable electrode or contact materials.

Recent studies have focused extensively on Cu-W composites. For example, the investigation by Cui et al. [1] identified two primary modes of surface erosion in W70Cu30 composites, with evaporation emerging as the predominant erosion mechanism. One another study [2] investigated the arc erosion behavior of Cu-W materials in a circuit breaker model, where the average temperature of the material surface was measured using a pyroscope. This study uncovered two distinct arc erosion processes, each significantly altering the structure of the contact surface and the electrode material after repeated arcs.

The objective of this research is to investigate the temporal behavior of metal vapor admixtures in the plasma of breaking arcs between Cu-W composite electrodes which were manufactured by shock sintering technology at 750°C with mass ratio of 30/70%. The goal of this study is to deepen understanding of the nature of plasma interaction with the surface of these composites, which may lead to improved methods for their fabrication.

Experimental Setup

Investigations were conducted in the High Current Laboratory at Brno University of Technology (BUT), Czech Republic, which primarily focuses on high power experimentation for the development and testing of various switching devices. The electrode setup included a stationary upper cathode holder and a moving anode holder, controlled by a pneumatic drive (Fig. 1).

Before each test, the electrodes were initially short-circuited. The pneumatic drive was activated approximately 60 ms after the experiment started, initiating the arc in the discharge gap [3].

Emission spectra of plasma were recorded using the Andor Shamrock 500i spectrograph. This device is equipped with a 150 1/mm diffraction grating and a blaze wavelength of 800 nm [4]. Each test captured 25 spectra, with an exposure time of 2.68 ms and a shift after exposure of 0.32 ms between recordings. The spectra collection spanned from 0 to 72 ms following the activation of the pneumatic drive. It is noteworthy that the visible emission of spectral lines started from about the 10th to the 15th millisecond, varying depending on the discharge.

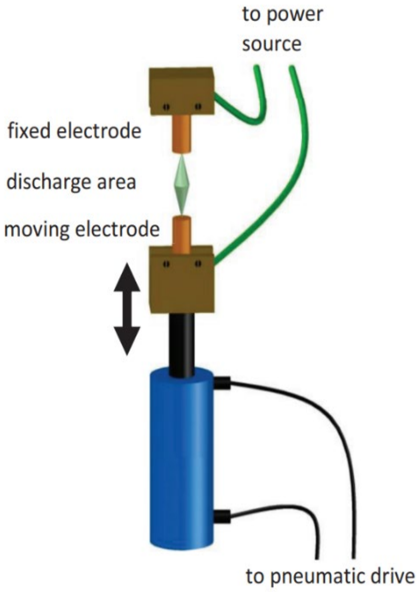

Fig. 1. Scheme of the electrode's assembly [3]

Each spectrum was rigorously analyzed to detect spectral lines corresponding to either copper or tungsten. For this analysis, the spectrometer was specifically calibrated to a central wavelength of 600 nm, covering a spectral range from 420 to 780 nm.

Temporal evolutions of excitation temperatures of the discharge plasma were determined by Boltzmann plot technique based on the emission intensity of both copper and tungsten spectral lines, namely Cu I 510.5, 515.3, 521.8 and 578.2 nm [5] and W I 484.4, 500.6, 505.3 and 551.5 nm [6] spectral lines.

Results and discussion

Thus, this makes it possible to carry out further investigation with calculation of equilibrium plasma composition and, consequently, the metal vapor content in discharge gap. The calculations carried allow us to determine the erosion resistance of various types of Cu-W composite electrodes under interaction with the thermal plasma of breaking arc discharges. The emission spectra of plasma are shown in Fig. 2.

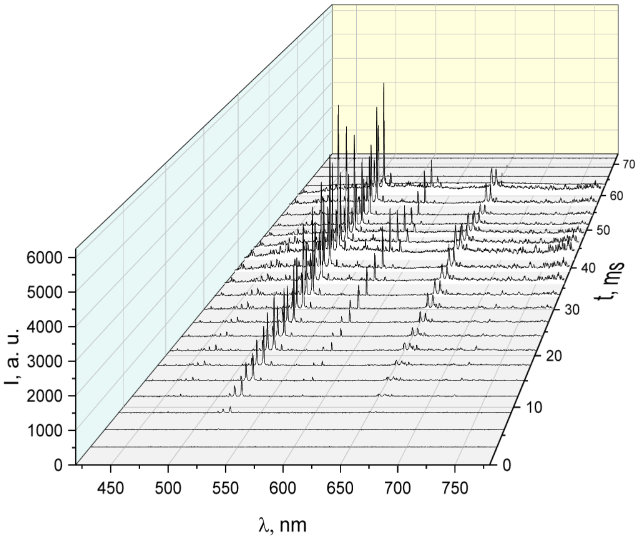

Fig. 2. Temporal evolution of emission spectra registered from arc discharge plasma at current of 104 A

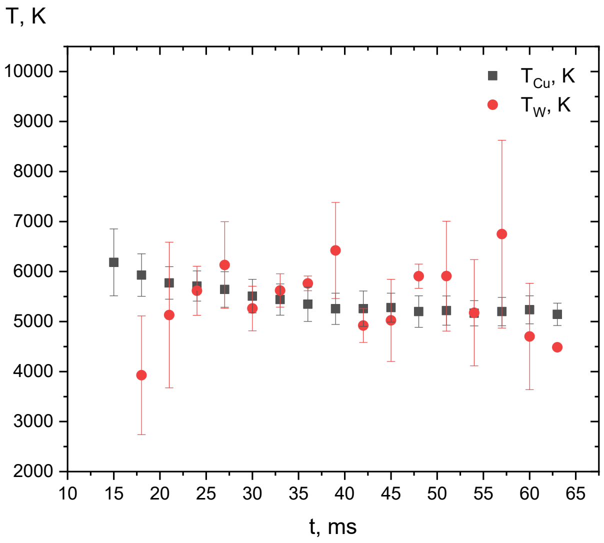

Fig. 3. Temporal evolution of distribution temperatures in the plasma of arc discharge between electrodes at current of 4 A

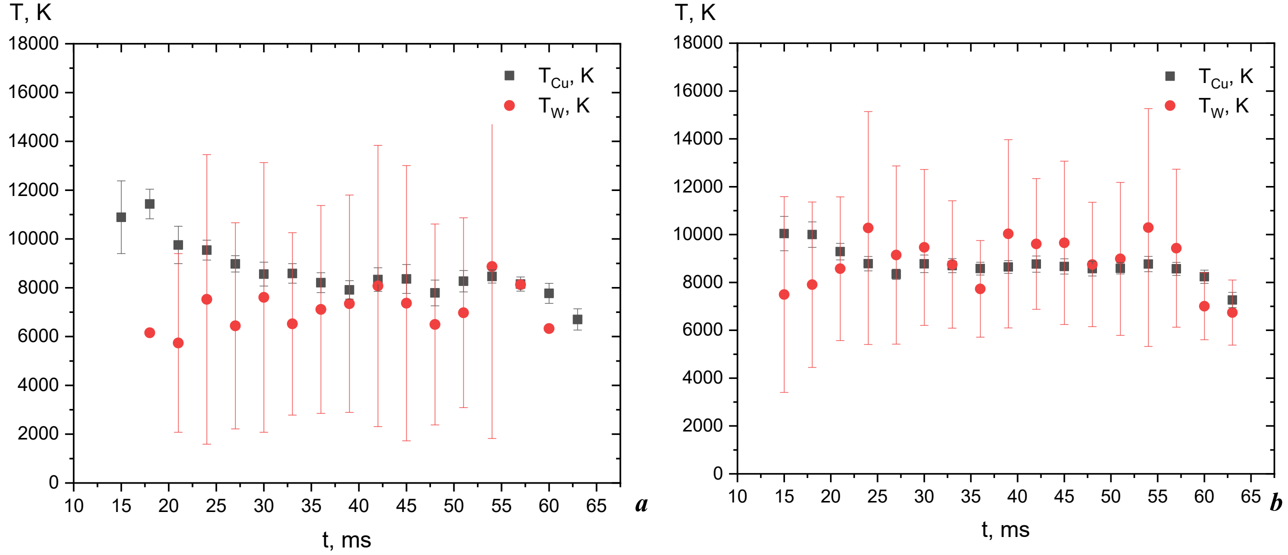

Fig. 4. Temporal evolution of distribution temperatures in the plasma of arc discharge between electrodes at current of 50 A (a) and 104 A (b)

The temporal evolution of the excitation temperatures obtained by Boltzmann plot technique based on Cu I and W I spectral lines in the plasma of electric arc discharge between Cu-W composite electrodes at current of 4, 50 and 104 A are shown in Fig. 3 and Fig. 4.

It is noteworthy that the temperature determined based on the emission intensity of tungsten spectral lines exhibits a significant error. This discrepancy is attributed to the resolution limitations of the spectrograph, which are insufficient to accurately distinguish the spectral lines of tungsten. One can see, the temperatures obtained based on both Cu I and W I coincide within the error of measurements. Therefore, it can be assumed that local thermodynamic equilibrium can be realized in such a breaking arc plasma.

Acknowledgements

This work has been carried out within the framework of the EUROfusion Consortium, funded by the European Union via the Euratom Research and Training Programme (Grant Agreement 101052200-EUROfusion). Views and opinions expressed are however those of the author(s) only and do not necessarily reject those of the European Union or the European Commission. Neither the European Union nor the European Commission can be held responsible for them. The authors consider it their pleasant duty to express gratitude to Dr. Bartlova, Dr. Šimek, Dr. Valenta, Dr. Kloć, for essential help in organizing and conducting experimental studies and useful advices during the preparation of this work for publication.

References

[1] Y. Cui, C. Niu, Y. Wu, M. Rong, L. Sun, H. Niu, and Q. Xiong, "Experimental study on the transformation of the W70Cu30 anode erosion mode in DC gaseous arcs-better insights into mechanisms of electrode erosion behavior using in-situ diagnosis." Journal of Physics D: Applied Physics, 52(47):474001, 2019. https://doi.org/10.1088/1361-6463/ab395f

[2] Y. Zhou, J. Humphries, J. Spencer, and J. Yan, "Surface average temperature measurement of Cu-W contact material burning in CO2": Preliminary study., Plasma Physics and Technology, 10(1):20–23, 2023. /https://doi.org/10.14311/ppt.2023.1.20

[3] A. Murmantsev, A. Veklich, V. Boretskij, M. Bartlová, L. Dostál, J. Píška, D. Šimek, A. Gajdos, and O. Tolochyn, "Thermal plasma of electric arc discharge between composite Cu-Cr electrodes: Optical emission and electrode surface interaction", Plasma Physics and Technology, 7(2):43–51, 2020. https://doi.org/10.14311/ppt.2020.2.43

[4] Oxford Instruments. Andor. Shamrock 500i High resolution, Extended Multi-track Czerny-Turner Spectrographs https://andor.oxinst.com/products/kymera-and-shamrock-spectrographs/shamrock-500i

[5] A. Murmantsev, A. Veklich, V. Boretskij, S. Fesenko, M. Kleshych, and O. Tolochin, "Investigation of thermal plasma of arc discharge between novel composite Cu-W materials", Problems of Atomic Science and Technology. 317 Series: Plasma Physics (29), 143(1):74–78, 2023. https://doi.org/10.46813/2023-143-074

[6] A.N. Veklich, A.V. Lebid, T.A. Tmenova, "Spectroscopic Data of W I, Mo I and Cr I Spectral Lines: Selection and Analysis", J. Astrophys. Astr. 2015, V. 604.

EFFECTS OF NON-EQUILIBRIUM PLASMA PROCESSING ON SOLUTIONS OF D-, L-ISOMERS

Valeriy Chernyak[1], Sergeiy Shulga[2], Volodymyr Trachevskiy[3], Vitalii Iukhymenko[1], Kostiantyn Iukhymenko[1], Daniil Tretiakov[1], Victor Diamant[4], Volodymyr Voskobijnyk[2] Olexander Tsymbaliuk[1], Sergeiy Nedovesov[1], Volodymyr Kyslyi[5], Oleksandr Kolomys[5], Yuliana Ponomarenko[1]
chernyak_v@ukr.net
1 - Taras Shevchenko National University of Kyiv, Faculty of Faculty of Radiophysics, Electronics and Computer Systems
2 - Institute of Hydromechanics NAS of Ukraine
3 - G. V. Kurdyumov Institute for Metal Physics of the N.A.S. of Ukraine
4 - V.I. Vernadsky Institute of General and Inorganic Chemistry NAS of Ukraine
5 - V. Lashraryov Institute of semiconductor physics of the N.A.S. of Ukraine

The study investigates fundamental aspects of plasma flow interaction with biomaterials in a plasma-liquid system. The motivation stems from the presence of equilibrium between concentrations of left and right isomers, as dictated by the equilibrium constant expression for a chemical reaction, $K=exp-\Delta G/RT$, derived from thermodynamic principles. Expression is valid for equilibrium and quasi-equilibrium systems. Therefore, deviation from the racemic ratio is possible only in a non-equilibrium system. In the investigated system, non-equilibrium is achieved by introducing significant directional (rotational) motion and a mechanism for rapid reduction of reactant energy (plasma is immersed in liquid). The influence on aqueous solutions of D-fructose, D-glucose, D-tartaric acid, and solutions in ethanol of D-fructose and L-proline was investigated. The results demonstrate a significant influence of the rotation direction on the polarization of the solution.

Mechanisms

As per the well-known chemical maxim in organic chemistry, “the synthesis of chiral compounds from achiral reactants invariably leads to racemic mixtures” [1]. This rule, is represented by the equilibrium constant expression, , where ΔG (the change in Gibbs free energy) = 0 for isomers. The prerequisite for employing this formula is equilibrium or quasi-equilibrium of the system. Thus, the sole means to attain an altered ratio with identical starting materials lies in creating a non-equilibrium system. So it is promising to introduce directed rotational motion, which has the potential to selectively influence various isomers based on their spatial configuration. A crucial aspect is the mechanism facilitating rapid energy reduction of formed compounds, facilitated by the plasma-liquid interface. This reduces the likelihood of reaction recurrence with loss of acquired polarization.

Experimental Setup and Results

Plasma activation of chemical transformations was executed in an open experimental system featuring a rotating sliding discharge immersed in liquid, depicted in Figure 1. The plasma reactor comprises an upper cathode flange, a central anode electrode, and a dielectric chamber with tangential gas supply inlets. CO2 served as the working gas, tangentially introduced into the dielectric chamber, inducing swirling gas flow along the system axis. The chamber design permits reversal of gas flow direction in the interelectrode gap of the electric discharge, which transitions from the dielectric chamber to the reaction quartz chamber. Gas outlet from the system was routed to a reverse condenser, then vented to the ventilation system.Physicochemical properties of solutions, including optical activity, UV and IR absorption spectra, Raman scattering spectra, proton and ^{13}C NMR spectroscopy, were inspected pre- and post-plasma activation. Optical activity was assessed via modulated laser polarimetry [2].

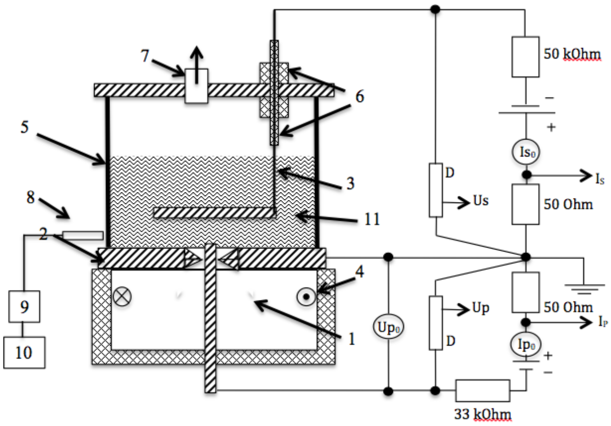

Fig. 1. Experimental setup with a rotating gliding discharge immersed in liquid.

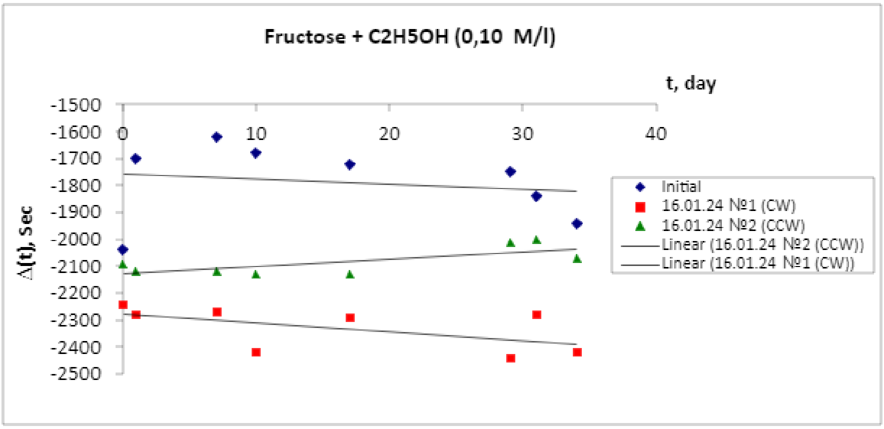

Fig. 2. Change in optical activity of D-fructose.

Results

Substance treatment in the reactor yielded significant impacts on the optical activity of certain processed samples. All substances exhibited temporal instability, with drift occurring in different directions depending on treatment. Some substances displayed not only quantitative differences but also changes in deviation signs (Fig.2), a novel finding that strongly supports hypotheses. Absorption spectra also demonstrated diverse compositional changes which are different for cw and ccw rotation directions. The results are reproducible.

References

[1] Morrison, R.T. and Boyd, R.N., 1987. Organic Chemistry, 5th ed. Allyn & Bacon Inc. p. 150.

[2] Plasmochemical synthesis of optically active substances // IEEE Transactions on Plasma Science. No. 3 (49), 1050-1054 (2021). DOI: 10.1109/TPS.2021.3064692].

CHARACTERISTICS OF THE PLASMA OF A SECONDARY DISCHARGE SUPPORTED BY A ROTATING GLIDING DISCHARGE IN CO_2

N. Shramenko[*], **V.Ya. Chernyak**[*], **V.V. Iukhymenko**[*], **S.S. Nedovesov**[*], **D.D. Tretiakov**[*], **O.M. Tsymbaliuk**[*], **K.V. Iukhymenko**[*]
[*] Faculty of Radiophysics, Electronics and Computer Systems Taras Shevchenko National University of Kyiv, Kyiv 01601, Ukraine, e-mail: chernyak_v@ukr.net

The paper presents the results of an experimental study of the parameters of the atmospheric pressure secondary discharge plasma supported by a low-power (~ 100 W) rotating gliding discharge in the air flow under the conditions of a significant excess of the length of the plasma channel of the secondary discharge from the length of the self-dependent sgiding discharge channel in the range of 1 ÷ 100.

Experimental set-up and methods

The experimental setup for the activation of chemical transformations of gaseous substances by a secondary discharge plasma sustained by a rotating gliding discharge is presented in Fig. 1.

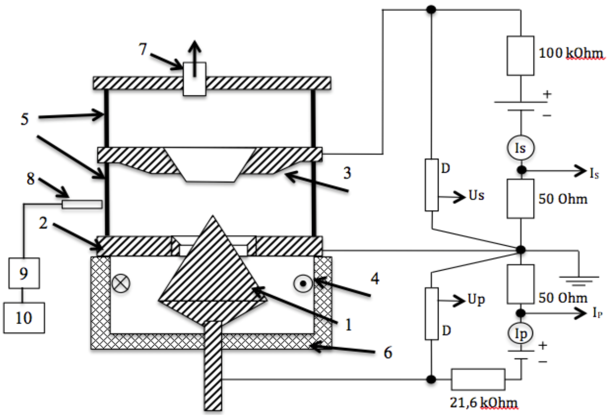

Fig. 1. Scheme of the system with a secondary discharge sustained by a rotating gliding discharge. 1 – cathode; 2 – anode; 3 –secondary discharge electrode; 4 – gas inlet; 5 – quartz cylinder; 6 – dielectric; 7 – gas outlet; 8 – optical fiber;9 – spectrometer; 10 – PC

The rotating gliding discharge ignites between the central electrode (cathode) (1), and the upper flange (anode) (2) in a vortex gas flow tangentially introduced into a cylindrical dielectric chamber (4). In the center of the anode, there is a conical-shaped hole with a diameter of 20 mm. A rotating gliding discharge is ignited between the cathode and the anode. The distance between the cathode and the anode is 1 mm. A quartz cylinder is mounted on the anode. On top of the quartz cylinder, there is a flange of the secondary discharge anode (3). CO_2 was used as the working gases, with a flow rate of 0 and 20 l/min. The gas was supplied tangentially to the axis of the system. The system's exhaust was connected to the ventilation system. BP 100 and BP 138 power sources were used for the discharges, with a voltage pulsation coefficient of 10% at a frequency of 100 Hz.

The plasma parameters of the discharges were determined using UV and visible emission spectroscopy of the plasma (200...1.000 nm). The emission spectra were recorded using a Solar TII spectrometer.

The radiation intensity of atomic lines was calculated using the formula:

$$I = N_0 \frac{g_e}{g_0} e^{-\frac{E_e}{kT}} A_{ei} h\nu_{ei} \qquad (1)$$

where N_0 - is the number of neutral atoms in 1 cm^3, g_e and g_0 are statistical weights of the excited and normal states; E_e - is the excitation energy of the upper state; T - is discharge temperature; k - is the Boltzmann constant.

The distributions of the intensities of the vibrational and rotational bands in the absence of reabsorption are recorded as follows:

(2)

where $\nu_{v`v``}$ - is the transition frequency; v` and v`` - are the vibrational quantum numbers of the upper and lower levels, respectively; $E_v(v`)$ - is the vibrational excitation energy for the excited electronic state; $q_{v`v``}$ - is the Franck-Condon factor; T_v^* - is the oscillating temperature; k - is the Boltzmann constant.

Accordingly, the intensity of the rotation line is written as:

(3)

where $\nu_{J`J``}$ - is the transition frequency; J` and J`` - are the rotational quantum numbers of the upper and lower levels, respectively; $E_r(J`)$ - is the value of the rotational term for the excited electronic state; $S_{J`J``}$ - is the intensity factor, which determines the relative transition probability (Henl-London factor); T_r^* - is the rotational temperature; k - is the Boltzmann constant.

Results

The emission spectrum of the secondary discharge plasma is presented in Fig. 2. The spectrum was measured with the following discharge parameters. Current of the independent discharge (primary discharge) = 200 mA, current of the secondary discharge = 68 mA. CO_2 flow was 0 L/min.

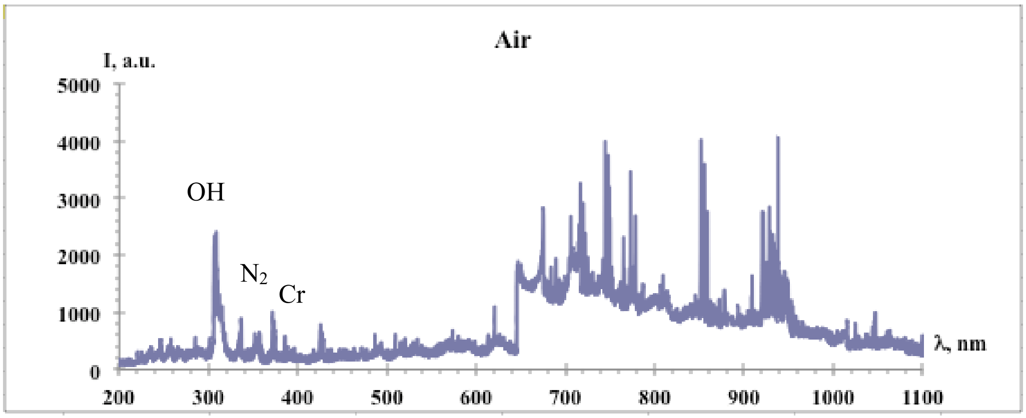

Fig. 2. Emission spectrum of the secondary discharge plasma

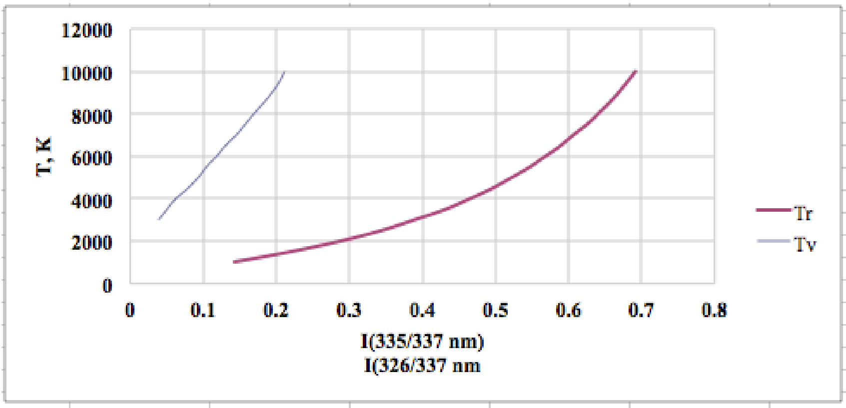

Fig. 3. Calibration curves

Population temperatures of electronic levels of atoms (Cr), vibrational and rotational levels of molecules (N_2) were determined using calibration curves (Fig. 3).

Population temperatures of vibrational levels for a nitrogen molecule = 5500 K. Rotational levels for a nitrogen molecule = 3500 K. The electron levels population temperature amount to ≈ 3.600 K. This indicates that the plasma of the secondary discharge supported by a rotating gliding discharge is non-isothermal.

CHARACTERISTICS OF THE PLASMA OF A SECONDARY DISCHARGE SUPPORTED BY A ROTATING GLIDING DISCHARGE IN AIR

O.O. Zavajenko*, **V.Ya. Chernyak***, **V.V. Iukhymenko***, **S.S. Nedovesov***, **D.D. Tretiakov***, **O.M. Tsymbaliuk***, **K.V. Iukhymenko***

** Faculty of Radiophysics, Electronics and Computer Systems Taras Shevchenko National University of Kyiv, Kyiv 01601, Ukraine, e-mail: chernyak_v@ukr.net*

The paper presents the results of an experimental study of the parameters of the atmospheric pressure secondary discharge plasma supported by a low-power (~ 100 W) rotating gliding discharge in the air flow under the conditions of a significant excess of the length of the plasma channel of the secondary discharge from the length of the self-dependent sgiding discharge channel in the range of 1 ÷ 100.

Experimental set-up and methods

The experimental setup for the activation of chemical transformations of gaseous substances by a secondary discharge plasma sustained by a rotating gliding discharge is presented in Fig. 1.

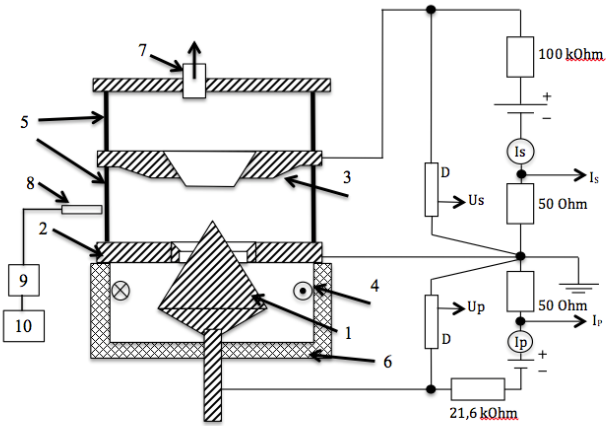

Fig. 1. Scheme of the system with a secondary discharge sustained by a rotating gliding discharge. 1 – cathode; 2 – anode; 3 –secondary discharge electrode; 4 – gas inlet; 5 – quartz cylinder; 6 – dielectric; 7 – gas outlet; 8 – optical fiber;9 – spectrometer; 10 – PC

The rotating gliding discharge ignites between the central electrode (cathode) (1), and the upper flange (anode) (2) in a vortex gas flow tangentially introduced into a cylindrical dielectric chamber (4). In the center of the anode, there is a conical-shaped hole with a diameter of 20 mm. A rotating gliding discharge is ignited between the cathode and the anode. The distance between the cathode and the anode is 1 mm. A quartz cylinder is mounted on the anode. On top of the quartz cylinder, there is a flange of the secondary discharge anode (3). Air, N_2, or CO_2 were used as the working gases, with a flow rate of 0 and 20 l/min. The gas was supplied tangentially to the axis of the system. The system's exhaust was connected to the ventilation system. BP 100 and BP 138 power sources were used for the discharges, with a voltage pulsation coefficient of 10% at a frequency of 100 Hz.

The plasma parameters of the discharges were determined using UV and visible emission spectroscopy of the plasma (200...1.000 nm). The emission spectra were recorded using a Solar TII spectrometer.

The radiation intensity of atomic lines was calculated using the formula:

$$I = N_0 \frac{g_e}{g_0} e^{-\frac{E_e}{kT}} A_{ei} h\nu_{ei} \qquad (1)$$

where N_0 - is the number of neutral atoms in 1 cm^3, g_e and g_0 are statistical weights of the excited and normal states; E_e - is the excitation energy of the upper state; T - is discharge temperature; k - is the Boltzmann constant.

The distributions of the intensities of the vibrational and rotational bands in the absence of reabsorption are recorded as follows:

(2)

where $\nu_{v'v''}$ - is the transition frequency; v\` and v\`\` - are the vibrational quantum numbers of the upper and lower levels, respectively; $E_v(v')$ - is the vibrational excitation energy for the excited electronic state; $q_{v'v''}$ - is the Franck-Condon factor; T_v^* - is the oscillating temperature; k - is the Boltzmann constant.

Accordingly, the intensity of the rotation line is written as:

(3)

where $\nu_{J`J``}$ - is the transition frequency; J` and J`` - are the rotational quantum numbers of the upper and lower levels, respectively; $E_r(J`)$ - is the value of the rotational term for the excited electronic state; $S_{J`J``}$ - is the intensity factor, which determines the relative transition probability (Henl-London factor); T_r^* - is the rotational temperature; k - is the Boltzmann constant.

Results

The emission spectrum of the secondary discharge plasma is presented in Fig. 2. The spectrum was measured with the following discharge parameters. Current of the independent discharge (primary discharge) = 180 mA, current of the secondary discharge = 48 mA. Air flow was 15 L/min.

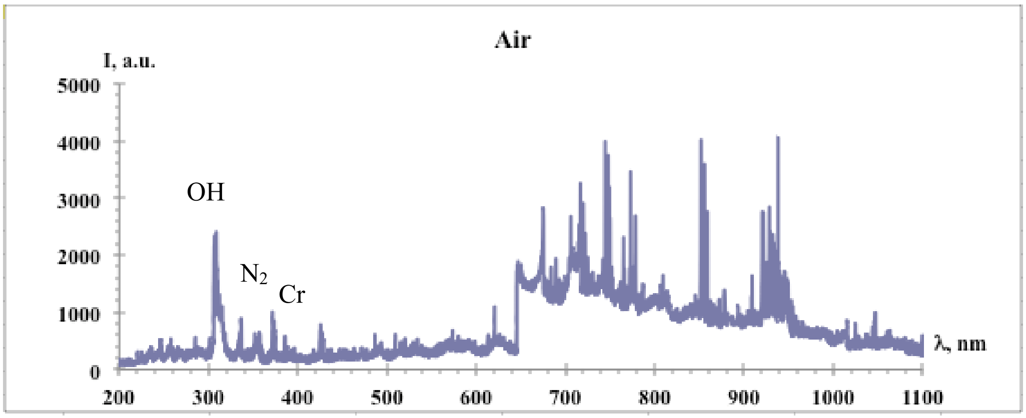

Fig. 2. Emission spectrum of the secondary discharge plasma

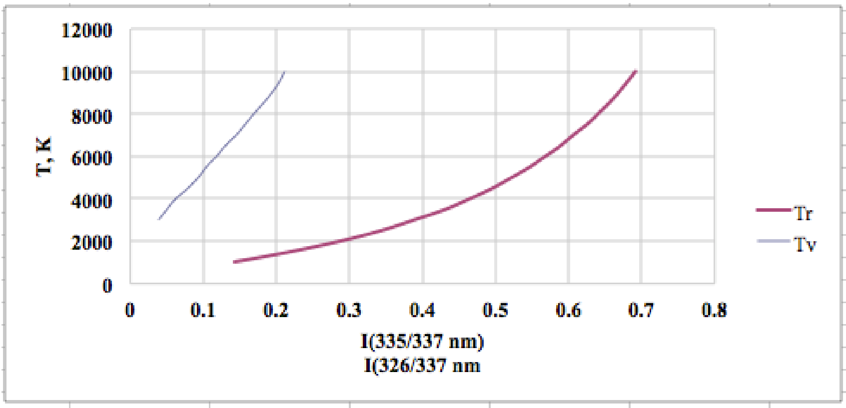

Fig. 3. Calibration curves

Population temperatures of electronic levels of atoms (Cr), vibrational and rotational levels of molecules (N_2) were determined using calibration curves (Fig. 3).

Population temperatures of vibrational levels for a nitrogen molecule = 5500 K. Rotational levels for a nitrogen molecule = 3500 K. The electron levels population temperature amount to ≈ 3.600 K. This indicates that the plasma of the secondary discharge supported by a rotating gliding discharge is non-isothermal.

PLASMA PARAMETERS OF A GLIDING DISCHARGE IMMERSED IN SOLUTIONS OF OPTICALLY ACTIVE ISOMERS

U. Ponomarenko[*], V.Ya. Chernyak[*], Sergeiy Shulga[**], V.V. Iukhymenko[*], S.S. Nedovesov[*], D.D. Tretiakov[*], O.M. Tsymbaliuk[*], K.V. Iukhymenko[*]

** Faculty of Radiophysics, Electronics and Computer Systems Taras Shevchenko National University of Kyiv, Kyiv 01601, Ukraine, e-mail: chernyak_v@ukr.net*

*** Institute of Hydromechanics NAS of Ukraine*

The paper presents the results of an experimental study of the parameters of the atmospheric pressure discharge plasma supported by a low-power (~ 100 W) rotating gliding discharge in the air flow under the conditions of a significant excess of the length of the plasma channel of the discharge from the length of the self-dependent sgiding discharge channel in the range of 1 ÷ 100.

Experimental set-up and methods

An experimental setup with a rotating gliding discharge immersed in a liquid is presented in Fig. 1. The plasma generator consists of a central electrode (cathode), an upper flange (anode) and a dielectric chamber with holes for tangential supply of the working gas. The central part of the anode has a conical shape with a hole in the center. The diameter of the hole is 3 mm. A rotating gliding discharge is ignited between the cathode and the anode. The distance between the cathode and the anode is 1 mm. A quartz tube is placed on the anode, into which the test liquid is poured. A flange is placed on top of the quartz tube, into which an annular secondary discharge electrode is mounted, which was immersed in liquid. As the working gas was used CO_2, the flow amounted to 10 and 15 l/min. The gas was fed tangentially to the system axis. The system outlet was connected to the ventilation system.

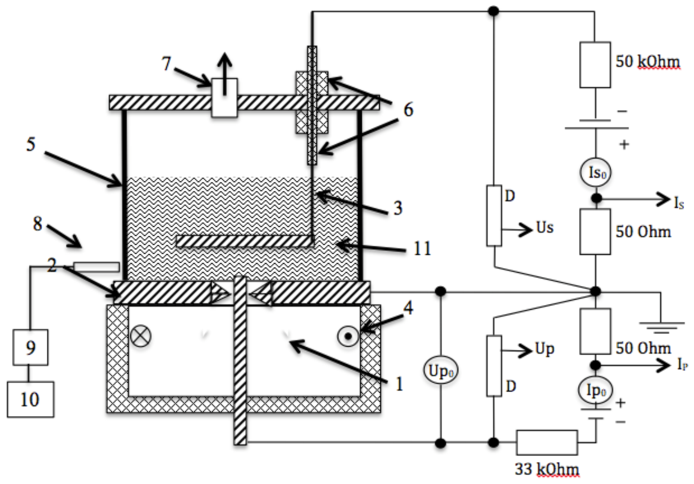

Fig. 1. Scheme of the system with a secondary discharge immersed in a liquid supported by a rotating gliding discharge: 1 – high-voltage electrode of the primary discharge; 2 – grounded electrode; 3 – high-voltage secondary discharge electrode; 4 – dielectric chamber; 5 – quartz cylinder; 6 – dielectric; 7 – gas

BP 100 source with a voltage ripple factor of 10% at a frequency of 100 Hz were used as power sources for discharges.

The plasma parameters of the discharges were determined using UV and visible emission spectroscopy of the plasma (200...1.000 nm). The emission spectra were recorded using a Solar TII spectrometer.

The radiation intensity of atomic lines was calculated using the formula:

$$I = N_0 \frac{g_e}{g_0} e^{-\frac{E_e}{kT}} A_{ei} h\nu_{ei} \qquad (1)$$

where N_0 - is the number of neutral atoms in 1 cm^3, g_e and g_0 are statistical weights of the excited and normal states; E_e - is the excitation energy of the upper state; T - is discharge temperature; k - is the Boltzmann constant.

The distributions of the intensities of the vibrational and rotational bands in the absence of reabsorption are recorded as follows:

(2)

where $\nu_{v`v``}$ - is the transition frequency; v` and v`` - are the vibrational quantum numbers of the upper and lower levels, respectively; $E_v(v`)$ - is the vibrational excitation energy for the excited electronic state; $q_{v`v``}$ - is the Franck-Condon factor; T_v^* - is the oscillating temperature; k - is the Boltzmann constant.

Accordingly, the intensity of the rotation line is written as:

(3)

where $\nu_{J`J``}$ - is the transition frequency; J` and J`` - are the rotational quantum numbers of the upper and lower levels, respectively; $E_r(J`)$ - is the value of the rotational term for the excited electronic state; $S_{J`J``}$ - is the intensity factor, which determines the relative transition probability (Henl-London factor); T_r^* - is the rotational temperature; k - is the Boltzmann constant.

Results

The emission spectrum of the discharge plasma in a liquid is presented in Fig. 2. The spectrum was measured with the following discharge parameters. Current of the independent discharge (primary discharge) = 100 mA. CO_2 flow was 10 L/min.

Population temperatures of electronic levels of atoms (O) and rotational levels of molecules (OH) were determined using calibration curves (Fig. 3).

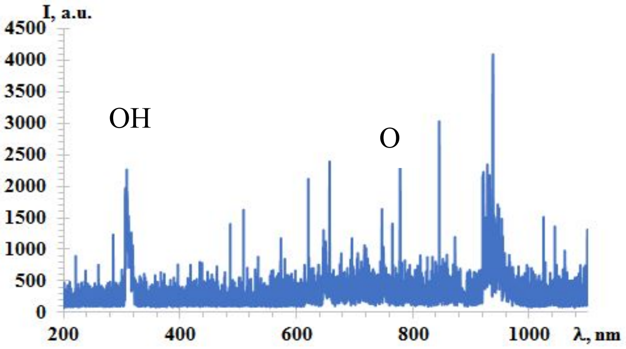

Fig. 2. Emission spectrum of discharge plasma

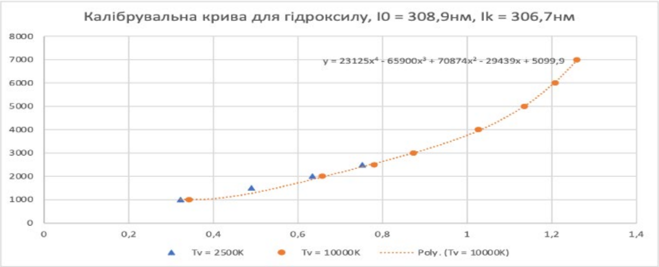

Fig. 3. Calibration curve for OH

Population temperatures of rotational levels for a OH molecule = 2900 K. The electron levels population temperatures determined on atoms O = 6800 K. This indicates that the plasma of the secondary discharge supported by a rotating gliding discharge is non-isothermal. The addition of sugars to the plasma leads to a decrease in the temperature of the metals.

COMPUTER TECHNOLOGIES

DECENTRALIZATION OF INFORMATION PROCESSING IN IOT INFRASTRUCTURE

Valerii Sribnyi*, Leonid Chepel, Yuriy Boyko*****
** Taras Shevchenko National University of Kyiv, Ukraine, Kyiv, e-mail: v.sribnyi.ua@gmail.com*
*** Taras Shevchenko National University of Kyiv, Ukraine, Kyiv, e-mail: leonid.chepel@knu.ua*
**** Taras Shevchenko National University of Kyiv, Ukraine, Kyiv, e-mail: yuriyboyko@knu.ua*

The current state of development of information technology demonstrates a tendency in the introduction of automated processes of information processing with an additional stage of their distribution across several parts of the system, in order to increase availability, speed and fault tolerance of the system. The largest direction of this trend is IOT technologies, which mainly exist within centralized infrastructures that need decentralization.

IOT infrastructure as an example of the problem of centralization

In its structure, IOT infrastructure is a network of IOT devices that are connected through intermediate devices to centralized data processing nodes. This approach is characterized by the need to preserve and process the constantly increased volume of information that some IOT devices cannot do on their own, due to the limitation of their functionality. This is not only a matter of information processing, but also in its safe transmission [1]. This is due to the use of intermediate devices that act as a bridge between IOT devices and a centralized node.

The problem of this approach follows from complete dependence on the centralized node, which, in case of failure of its work, paralyzes the work of the entire infrastructure. Modern information processing processes solve this problem by introducing additional systems that serve as additional nodes of information processing at the centralized node level, or the use of cloud solutions, the reliability and availability of which relies on service providers, which is demonstrated in fig. 1. The first option demonstrates partial decentralization of infrastructure, but entails the need to add new centralized nodes to the system, which in turn increases the cost of the infrastructure itself and requires complete duplication of functionality on them. The second option is only a partial solution to the problem, since we relay it to third parties and transfer access to all data, which in some cases is unacceptable. Additionally, the described approaches do not address the problem of secure data transfer, which is necessary in IOT [4].

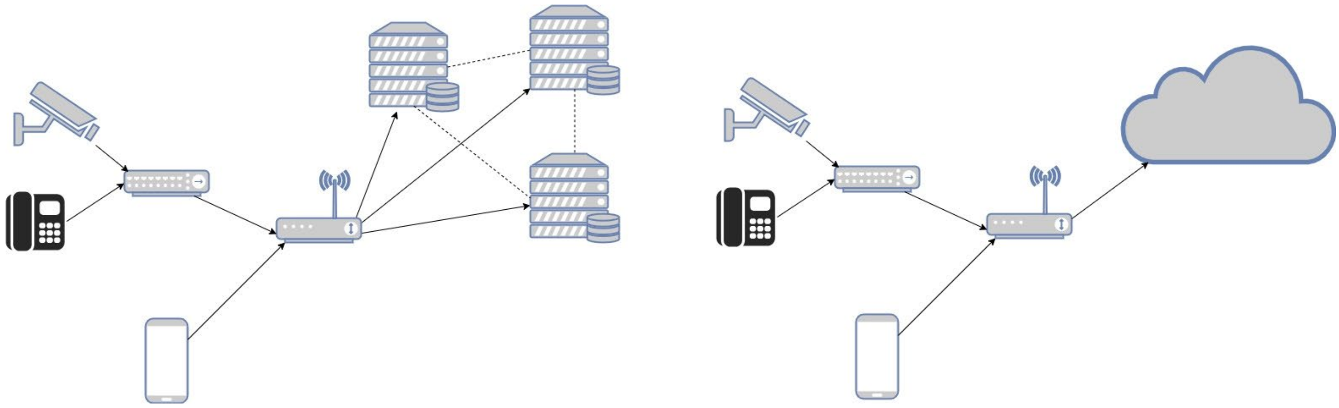

Fig. 1. IOT infrastructure with multiple centralized nodes and with cloud processing

Decentralization of IOT infrastructure at the expense of blockchain

The previously mentioned methods for solving the problem of centralization are partial and in some cases economically unjustified. To fully solve the problem of centralization of infrastructure, it is necessary to apply approaches that are based in their functionality on the distribution of processing tasks throughout the network with built-in information protection. One of such tools is blockchain - a distributed structure of secure data processing and storage, the deployment of which can take place within an existing infrastructure [2, 3].

The principle of the blockchain is to distribute all network information in encrypted form for all its participants, fig. 2, in full or partial form, which may be necessary for IOT devices. The information itself has the appearance of a sequence of records (blocks), each of which is associated with the previous block and points to it. When you enter information in the blockchain, it cannot be removed. Modern implementations of the blockchain additionally allow for parallel processing of information by usage of custom consensus protocols or smart-contracts [5, 6].

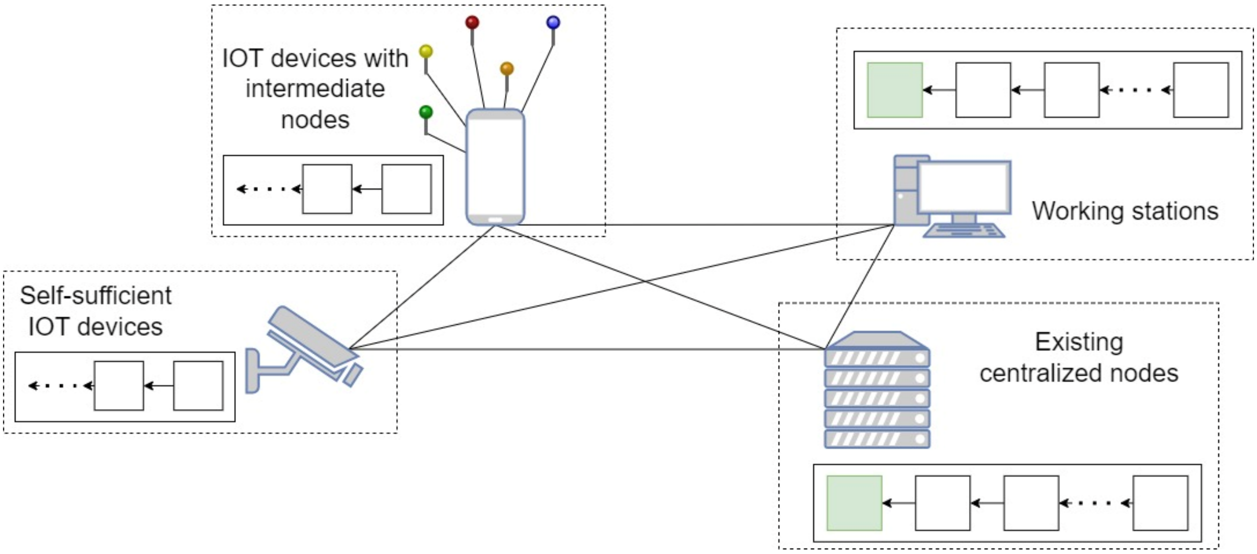

Fig. 2. IOT infrastructure with blockchain integration

Therefore, the problem of centralization of information processing in the IOT infrastructure is a significant drawback of the generally accepted method of infrastructure implementation, the solution of which is currently partial. The introduction of blockchain, which was created for the purpose of distributed processing and storage of information, allows to achieve complete decentralization of information processing within the existing infrastructure.

References

[1] Abdulhamid, Alhassan & Kabir, Sohag & Ghafir, Ibrahim & Lei, Ci. (2023). Safety and Security Issues in the IoT Domain. URL: https://www.researchgate.net/publication/372748061_Safety_and_Security_Issues_in_the_IoT_Domain

[2] Alajlan, Razan & Alhumam, Norah & Frikha, Mounir. (2023). Cybersecurity for Blockchain-Based IoT Systems: A Review. Applied Sciences. 13. 7432. 10.3390/app13137432. URL: http://dx.doi.org/10.3390/app13137432

[3] Verma, Rajat & Dhanda, Namrata & Nagar, Vishal. (2022). Security Concerns in IoT Systems and Its Blockchain Solutions. 10.1007/978-981-16-4284-5_42. URL: http://dx.doi.org/10.1007/978-981-16-4284-5_42

[4] Khalil, Usman, Owais Ahmed Malik, Mueen Uddin, and Chin-Ling Chen. 2022. "A Comparative Analysis on Blockchain versus Centralized Authentication Architectures for IoT-Enabled Smart Devices in Smart Cities: A Comprehensive Review, Recent Advances, and Future Research Directions" *Sensors* 22, no. 14: 5168. URL: https://doi.org/10.3390/s22145168

[5] Mays Alshaikhli, Tarek Elfouly, Omar Elharrouss, Amr Mohamed, Najmath Ottakath, Evolution of Internet of Things from Blockchain to IOTA: A Survey. IEEE Access, vol. 10, 844. URL: http://dx.doi.org/10.1109/ACCESS.2021.3138353. doi:10.1109/ACCESS.2021.3138353.

[6] Dedeoglu, Volkan & Jurdak, Raja & Dorri, Ali & Lunardi, Roben & Michelin, Regio & Zorzo, Avelino & Kanhere, Salil. (2019). Blockchain Technologies for IoT. URL: http://dx.doi.org/10.1007/978-981-13-8775-3_3. doi: 10.1007/978-981-13-8775-3_3.

COREFERENCE RESOLUTION IN UKRAINIAN-LANGUAGE TEXTS USING CONVOLUTIONAL LONG SHORT-TERM MEMORY NEURAL NETWORS

Biletskiy P. V., Tkach Y. V.
Faculty of Radiophysics, Electronics and Computer Systems, Taras Shevchenko National University of Kyiv,
64/13, Volodymyrska Str., Kyiv, Ukraine, 01601, e-mail: juliatkach2003@gmail.com

The created program processes input data and prepares it for training the neural network. It also enables training and utilizing a convolutional LSTM neural network for coreference resolution in texts.

Introduction

The task of coreference resolution is a key aspect in natural language processing (NLP). NLP has a wide range of uses in different fields such as machine translation, real-time voice assistants, information retrieval systems, and more. Coreferential objects are syntactic units of text that refer to the same entity in the given context: "*Za viknom rozpustyla kosy vysoka topolia. Yii hillia maizhe torkalos zemli.*"

The coreference resolution in Ukrainian-language texts, similarly to other texts in Slavic languages (such as Czech, Polish, etc.), has certain characteristics related to word order in sentences. Therefore, methods for coreference resolution should take this quality into account to increase the accuracy of detecting coreferential objects. In contrast, for example, the English language does not have these features.

Application

There are already existing solutions for coreference resolution in Ukrainian language, which include decision trees, convolutional neural networks, bidirectional long short-term memory networks, and others [1]. In this work, convolutional long short-term memory network (ConvLSTM) [3][4] was proposed and examined for the coreference resolution.

The entity-mention approach was chosen for coreference resolution. Contrary to individual word pair analysis, entity-mention approach processes entire sentences or texts to form coreference clusters. The created program includes functionality for processing natural language by a computer system using vector representations of words (1024 values represent the result of word to vector transformation by the ELMo library [2], 6 values are additional features and 1 value is used to denote the coreferential pair of words under consideration). For training the neural network and verifying the correctness of its operation, a corpus of Ukrainian texts containing over 360,000 words was used.

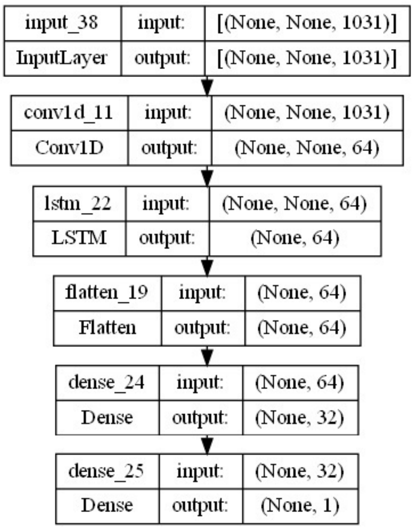

Fig. 1. Architecture created ConvLSTM

The *Fig. 1* illustrates the architecture of the neural network used in this work. **InputLayer** accepts input text with an indefinite number of vectorized words (1031 features). **Conv1D** [3] reduces the number of significant features to 64, which speeds up training the model. This allows the model to adapt to local dependencies within individual words. **LSTM** [4] helps the model adapt to long-term dependencies in data sequences, improving model accuracy. **Flatten** layer convert inputs to a one-dimensional tensor. **Dense** layer contains 32 units, To summarize results from previous layers. **OutputLayer** is output dense layer with 1 output neuron for binary classification of pair of chosen objects

Results

The *Fig. 2* illustrates the accuracy of the ConvLSTM network. For training and validation, a balanced sample was used - the number of coreference and non-reference objects has a ratio of 1:1. For the training sample, the accuracy is about 97%, for the validation sample, the value is about 80%.

The *Fig. 3* illustrates that overfitting occurs at epoch 13-14. Therefore, in order to avoid overfitting, early stopping was used to stop the training and recover the best weights.

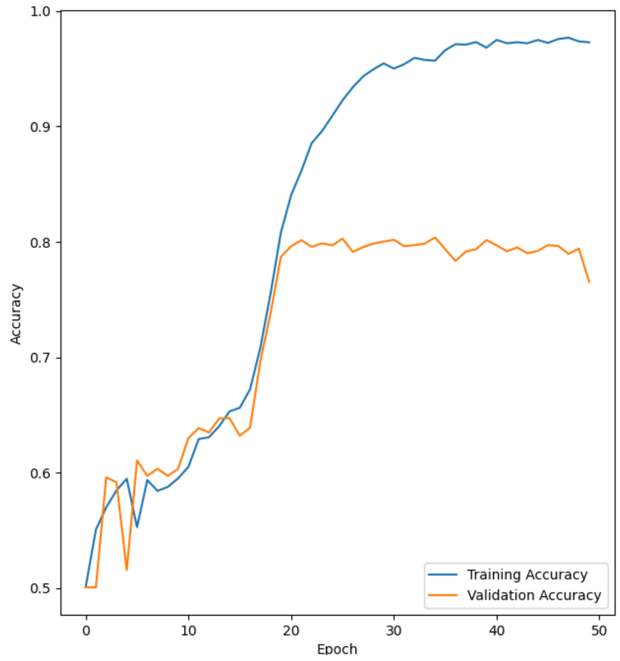

Fig. 2. Training and Validation Accuracy

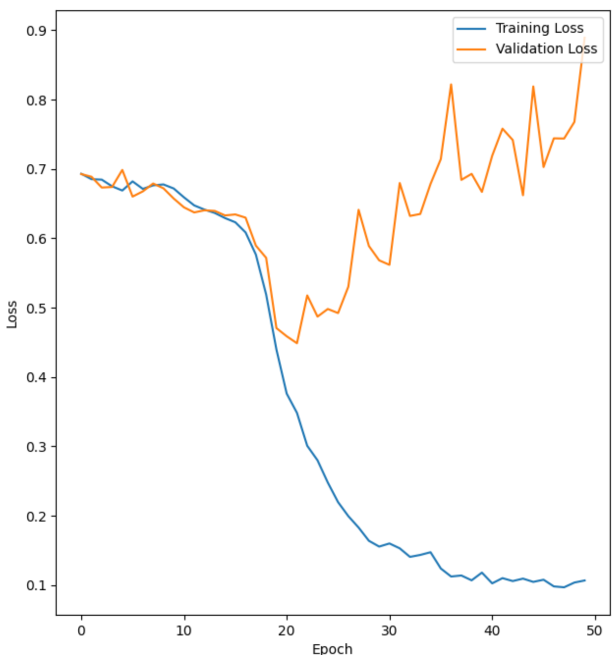

Fig. 3. Training and Validation Loss

Conclusions

The paper considers the Coreference resolution task. A Python application for coreference object detection in Ukrainian-language texts was created. The classification accuracy of 80% and 98% was achieved on validation and training samples respectively. This ConvLSTM model allows working with texts of variable length and to consider both local and contextual features, thus contributing to the improved accuracy of the neural network.

References

[1] S. D. Pogorilyy, P. V. Biletskyi. Coreference Resolution Algorithm for Ukrainian-Language Texts Using Decision Trees. Problems in programming 2022; 3-4: p.p. 85-91. DOI: https://doi.org/10.15407/pp2022.03-04.085
[2] See details here: https://github.com/HIT-SCIR/ELMoForManyLangs
[3] See details here: https://www.tensorflow.org/api_docs/python/tf/keras/layers/Conv1D
[4] See details here: https://www.tensorflow.org/api_docs/python/tf/keras/layers/LSTM

CREATION OF AN ELECTRONIC LEARNING SYSTEM BASED ON DISTRIBUTED MOODLE INSTALLATIONS

Lukashov Oleksandr
Taras Shevchenko National University of Kyiv, , e-mail: bloodelf@knu.ua

The new paradigm of education requires updating professional education and applying modern forms, methods and technologies of learning (e-learning).

E-Learning

The new paradigm of education requires the renewal of professional education and the use of modern forms, methods and technologies of learning, including e-learning. The advantages of e-learning are becoming increasingly important in this context:

Flexibility - E-learning allows learners to study at their own pace and at a time that is convenient for them.

Accessibility - With e-learning, educational resources can be accessed from anywhere with an internet connection.

Interactivity - Modern e-learning platforms often include interactive exercises, quizzes, games and other methods that encourage active learning.

Individualisation - E-learning allows you to customise the learning process to the needs of each individual learner.

Cost-effectiveness - The use of e-learning can reduce the cost of training, including the printing of textbooks and other materials.

Thus, the modernisation of vocational education includes the integration of e-learning to provide more efficient, affordable and flexible learning for modern learners.

Such an educational process can be organised using the Moodle learning environment.

Moodle

Moodle is the most advanced and widespread system of its kind in Ukraine and globally. Currently, Moodle has about 400 million users worldwide and continues to grow at a much faster pace than its competitors. A landmark event took place in 2018. According to statistics, the use of the Moodle platform in the world exceeded the use of all other platforms combined. Fig. 1.1.

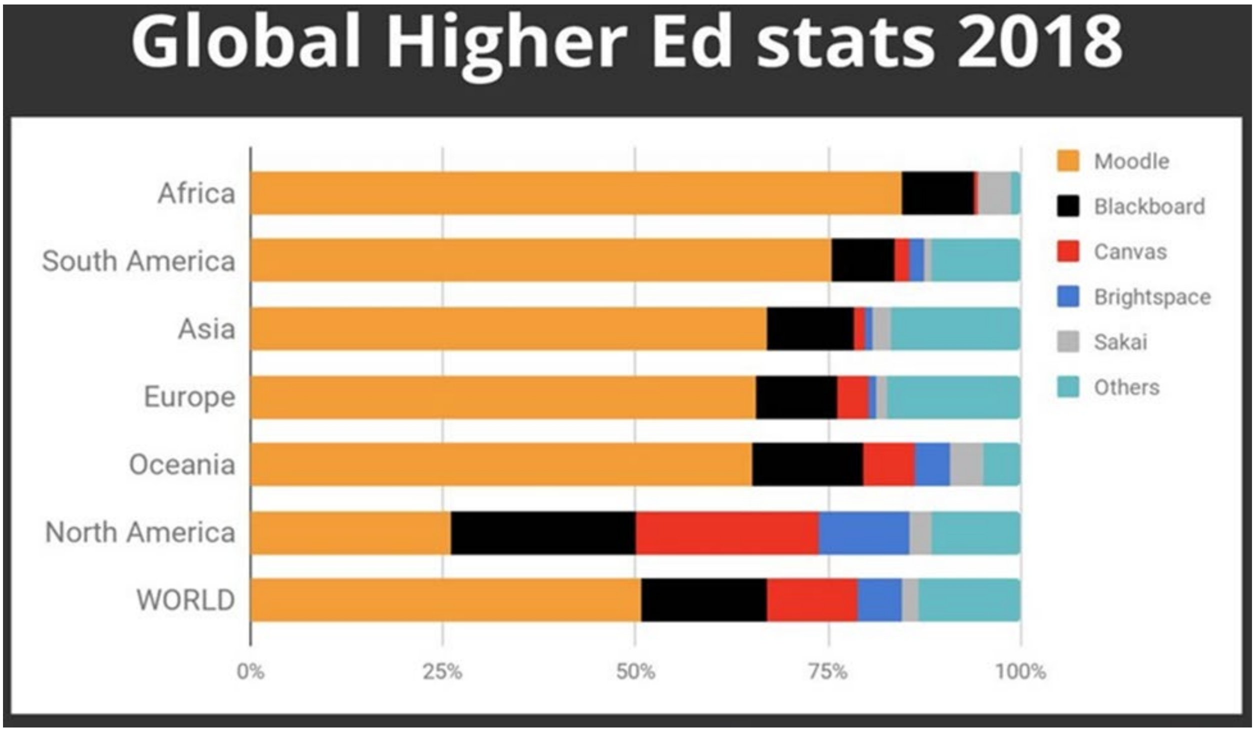

Fig. 1.1 Statistics on the use of the Moodle service in the world. [1]

The main advantages of Moodle include its free and open source nature, which allows users to adapt and extend its functionality to suit their needs. Another important feature is its modularity, which allows for the addition of various features and extensions depending on the user's needs.

In the case of distributed Moodle installations, it is open source and modularity that make it possible to create a single learning system.

A unified authorisation and authentication mechanism in distributed Moodle systems can be solved by using a workspace service, such as Google Workplace or NextCloud, because these services will allow you to create a unified authorisation and authentication system that allows you not to create accounts for each user, but to access courses, use a single method of authorisation and authentication using the OAuth2 protocol.

References

[1] Що таке Moodle [Електронний ресурс] – Режим доступу до ресурсу: https://moodle.org/mod/page/view.php?id=8174

[2] Організація дистанційного навчання в Moodle [Електронний ресурс] – Режим доступу до ресурсу: https://osvita.ua/vnz/high_school/72285/#google_vignette

INSTALLING, CONFIGURING, AND BOOTSTRAPPING SINGLE NODE OPENSTACK CLUSTER AND COLLECTING STATISTICS OF WORKING INSTANCE

Kucher Denys*, Ievgen Sliusar**
**Taras Shevchenko National University of Kyiv, 1st-year master's student, e-mail: denmaen2@gmail.com*
*** Taras Shevchenko National University of Kyiv, Address, Ph.D., associate professor: slu@knu.ua*

OpenStack[1][4] is an open-source platform for building and managing cloud infrastructures. The speed of deploying and utilizing OpenStack can depend on several factors such as the scale of resources, the availability of technical skills within the team, hardware capabilities, and more.

It's essential to properly configure and optimize the OpenStack[2] setup to achieve optimal performance. Additionally, considering best practices for scalability, security, and management is crucial.

The research machine

A computer with an 8th generation Intel Core I5 processor and 32 GB of RAM was taken as the research machine. Juju[3] is an open-source application modeling tool developed by Canonical, the company behind Ubuntu. Ubuntu 22.04.3 live-server was put as OS because of the easier installation process and all documentation on OpenStack[1][4] configuring. OpenStack also may be configured and installed on Red-Hat/CentOS-based systems and Suse Linux, but this process may be more complicated as there is not so much automation as Canonical has

The installation process

Openstack[4] contains many components, each of which performs a certain function and is interrelated with others. The Nova[2] component in OpenStack[1] is responsible for managing and provisioning compute resources, including virtual machines and other instances, Cinder[2] is a crucial component in OpenStack[2] responsible for providing block storage services to instances, Neutron[2] is the networking component in OpenStack[2] responsible for providing network connectivity to instances, Keystone[2] is the Identity service component in OpenStack[2], responsible for authentication and authorization.

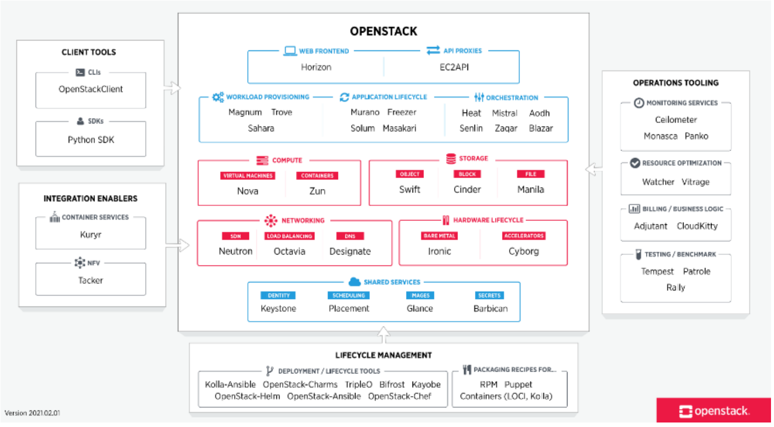

Fig. 1. This illustration shows the infrastructure of the OpenStack

Installation[1][5] of all components, configuring and bootstrapping the cluster model with options that allow us to create virtual machines, administrate, and fully use them.

The testing and Statistics

Results of testing provided below give information about how productive may instances and the server be working simultaneously on MPI C programs calling processor information and the AI python getting the result of machine learning of MNIST with tensorflow, both in the right part of the Fig.3

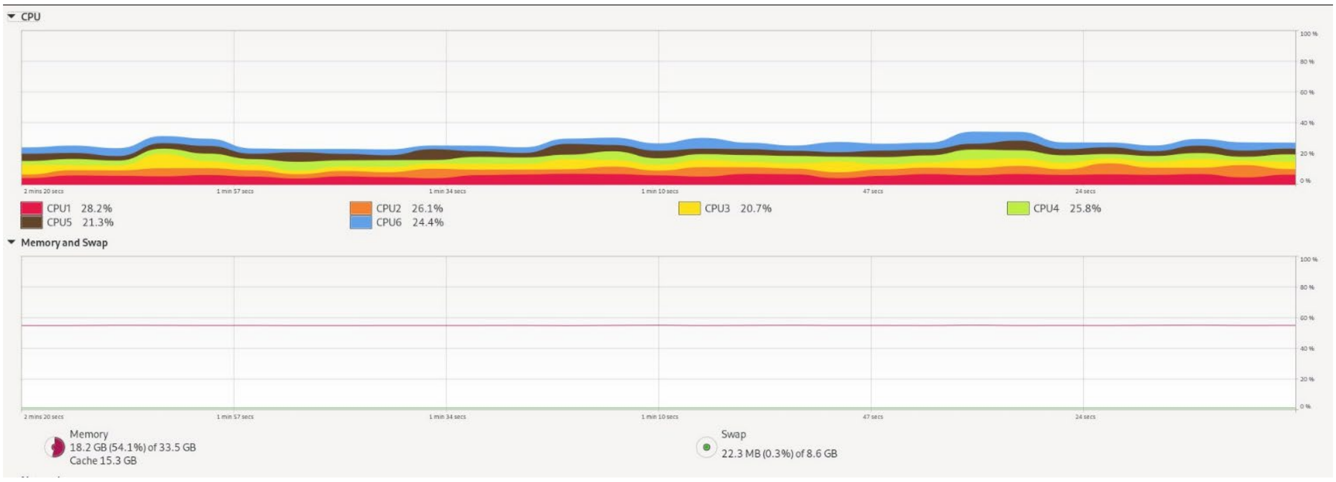

Fig. 2. The statistics of the regular work of the cluster

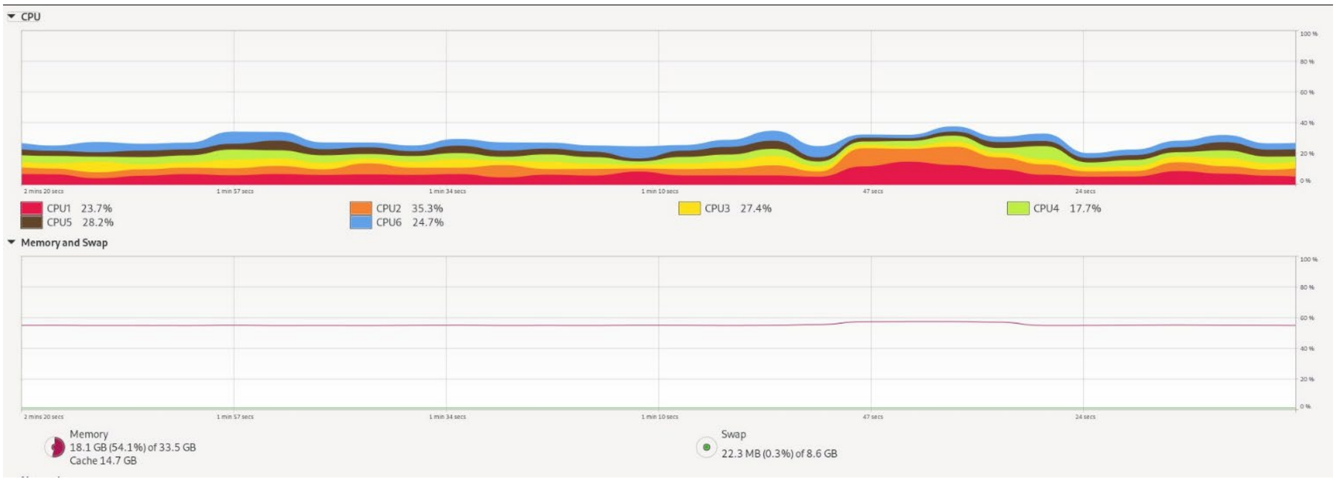

Fig. 3. The statistics of the cluster operation under load

References

[1] https://ubuntu.com/openstack/tutorials - Tutorials on how to install, configure, and bootstrap OpenStack
[2] https://www.openstack.org/ - Official site
[3] https://juju.is/ - open-source application modeling tool for configuring OpenStack
[4] https://dl.acm.org/doi/abs/10.1145/2628194.2628195 - Tiago Rosado, Jorge Bernardino - 18th International Database Engineering - An overview of OpenStack architecture
[5] K Pepple - 2011 - book about deploying OpenStack

APPLICATION OF THE MARKOV PROCESS-BASED MODEL FOR MACROECONOMIC FORECASTING

A.D. Volkov*[1] **, V.V. Obukhovsky***[2]
**Taras Shevchenko Kyiv National University, 01601, Kyiv, str. Volodymyrska, 64/13, Kyiv, Ukraine*
1. vvolkoffanton@gmail.com, +380669021190;
2. obukhovsky@knu.ua

Abstract. *The work is dedicated to macroeconomic modelling using the Markov process and the evaluation of the predictive efficiency and quality of analysis of these models. The RStudio software environment was used for the calculations, and the data was taken from open sources*

Introduction

There are models for short-term forecasting of business cycles that, by adapting the structure to changing observational characteristics, can predict the probability of shocks and downturns.. A hidden variable that changes its states according to a matrix of transition probabilities controls the switching mechanisms. In other words, one structure switches to another when the regime changes, which allows for more complex economic patterns [1]. Based on the assumption that macroeconomic indicators have the property of Markovian switching of "modes" in which the economy operates, a large set of models with Markov switching is used not only in theoretical studies, but also for real-world applications in economic activity.

The aim of this work is to build and evaluate the efficiency of Markov switching model (MSM) in macroeconomic analysis

Logistic regression MSM for forecasting the probability of recession

The US Federal Reserve has a chart for estimating the smoothed probability of recession, but it only retrospectively shows the presence or absence of recession based on analysis of a set of variables. Smoothed recession probabilities for the United States are obtained from a dynamic-factor MSM applied to four monthly coincident variables: non-farm payroll employment, the index of industrial production, real personal income excluding transfer payments, and real manufacturing and trade sales. This model was originally developed in [2]

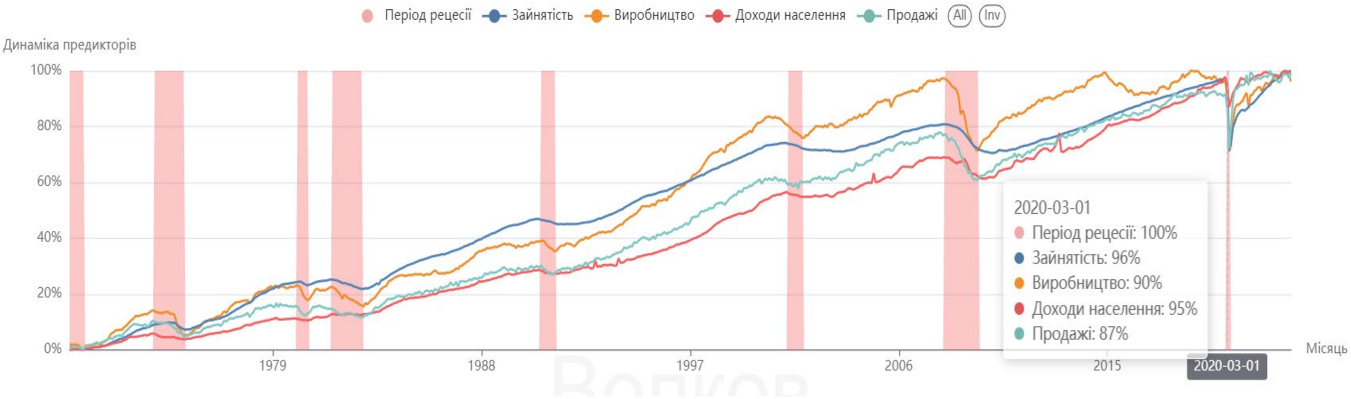

Fig. 1. Dynamics of inflation predictors corresponding to recession periods

The goal was to create a forecast for the first 6 months of 2022 based on monthly data from January 1970 to December 2021 using the same variables as described in [2]. The model is implemented with the MSwM package using expectation-maximization algorithm (1000 iterations). The basic model used is a logistic regression with two Markov switching modes. [3]

Research results

According to the model, there was no recession in the United States in 2022. Prediction for no recession was correct, as far as we know from current data.

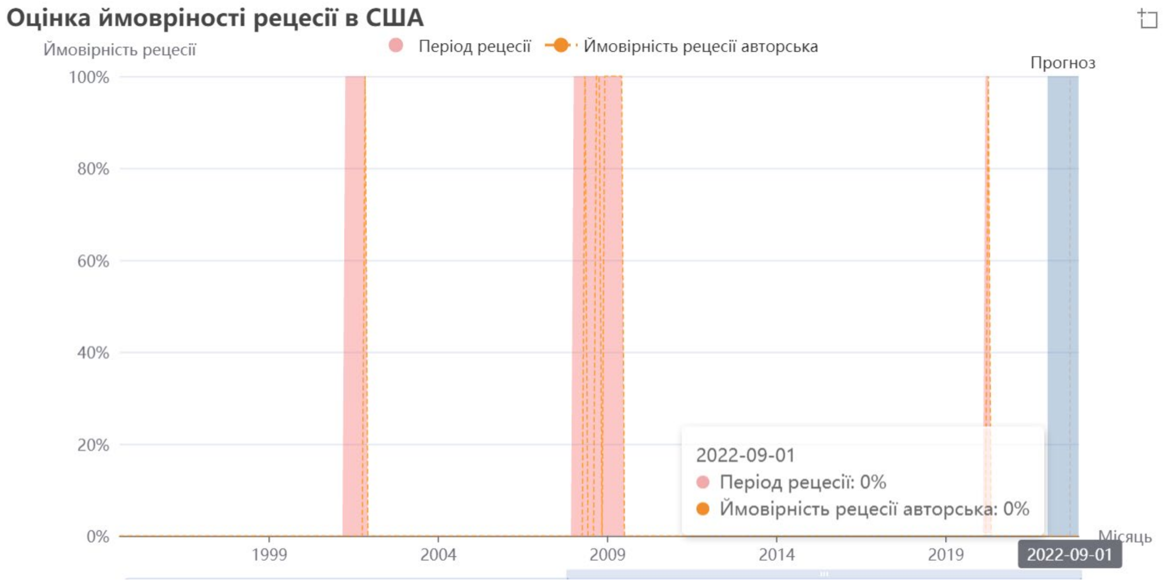

Fig. 2. *Recession probability forecast for 2022*

Out of 546 periods when there was no recession, the model incorrectly identified a recession 0 times. However, 53 recession periods were missed and 31 were correctly identified, i.e., the model's recall for the “recession” mode is only 0.37

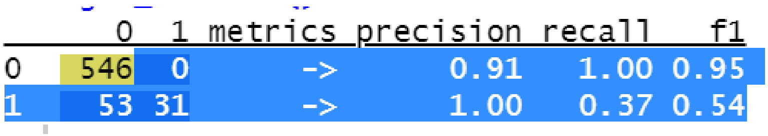

```
     0   1 metrics precision recall   f1
0  546   0      ->      0.91   1.00 0.95
1   53  31      ->      1.00   0.37 0.54
```

Fig. 3. *Metrics of the model*

Calculation of the model's predictive performance (F-score) is 0,745 for combined “recession” and “no-recession” modes. This makes it possible to conclude that the model we have implemented is good at estimating the presence of a recession and forecasting its absence, at the same time being poor at predicting its presence

Macroeconomic indicators are indeed characterized by Markov switching when it comes to modeling and forecasting these indicators, because taking into account the presence of switching in the model improves its forecasting efficiency

The results of the study can be used to create predictive economic models that can also be used in machine learning [4]

References

[1] Hamilton, James D. “Macroeconomic Regimes and Regime Shifts” in *Handbook of Macroeconomics*, edited by Harald Uhlig and John Taylor. Cambridge, MA,USA: NBER Working Paper No. 21863, 2016. [Online]. Available: https://www.nber.org/system/files/working_papers/w21863/w21863.pdf

[2] Marcelle Chauvet, “An Econometric Characterization of Business Cycle Dynamics with Factor Structure and Regime Switching” University Avenue Riverside, CA, USA: Department of Economics UCR, 1998. [Online]. Available: https://faculty.ucr.edu/~chauvet/ier.pdf

[3] Sachin D., “The Markov Switching Dynamic Regression Model”, timeseriesreasoning.com, https://timeseriesreasoning.com/contents/markov-switching-dynamic-regression-model/ (accessed Feb. 1, 2024)

[4] Melike Bildirici, Özgür Ersin, “Markov Switching Artificial Neural Networks for Modelling and Forecasting Volatility: An Application to Gold Market”, Procedia Economics and Finance, volume 38, pp 106-121, 2016. [Online]. Available: https://www.sciencedirect.com/science/article/pii/S2212567116301836

MODELING A VIDEO SURVEILLANCE SYSTEM USING COMPUTER VISION

V. Shapovalenko *, O. Bauzha **
Taras Shevchenko National University of Kyiv, 63/13, Volodymyrska str., Kyiv 01601, Ukraine
** e- mail: shapovalenko.vladyslav@gmail.com*
*** e-mail: asbauzha@knu.ua*

This work is devoted to developing a video tracking system using an Arduino board as the main element of the positioning system, as well as the Python programming language and the OpenCV computer vision library for determining and transmitting object coordinates in the video stream. During development, it is possible to introduce already trained classifiers to determine face coordinates. In this work the possibility of face detection in different lighting conditions, and the methods of transferring the processed information to the microcontroller were investigated.

Introduction

Video surveillance is a technology used to record and playback video to monitor people or objects. It is used in various fields [1]. Video surveillance systems using computer imaging are now becoming more common. For instance, international airports have important infrastructure. Therefore, its security system consists of many important security elements aimed at ensuring the safety of passengers and employees of the airport, so the task of supporting airport video surveillance operators with the help of modern artificial intelligence (AI) solutions[2] is very relevant. There are many other applications of this technology. They could be used in healthcare, traffic-controlling, high-precision engineering etc.

The model of the video surveillance system

Computer vision technology is incorporated into a complex consisting of a camera positioning system and software. The Arduino Mega 2560 board controls the camera positioning system. The software is written in the Python programming language using the OpenCV library.. In general, the system works in two modes, between which you can switch.

- Manual mode involves controlling the camera's position using the joystick to search for a face if it is out of frame. After the face is found, the red LED will light up, so you can switch to automatic mode.
- In automatic mode, the positioning system will automatically guide the camera so that the face remains in the center of the frame.

Development of the hardware part of the layout

The hardware part of the layout includes several main modules in addition to the Arduino board. Among them is a web camera positioning system, consisting of a holder in which two servo motors are mounted, which allow you to control the position of the video camera in two axes, a joystick that allows you to control the camera in manual mode, as well as a light indication system that shows in which mode the circuit is currently in, and whether a face was found in the video stream.

Figure 1 shows the schematic diagram of the layout (a) and the assembled layout (b).

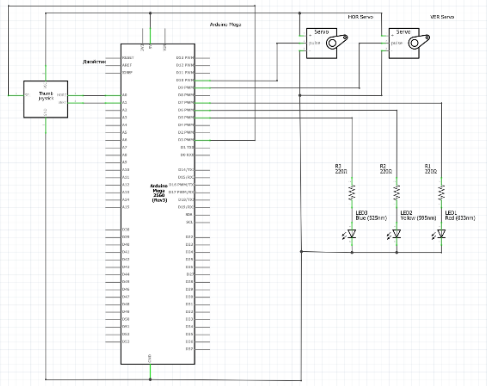

Fig. 1a. The schematic diaram of the layout

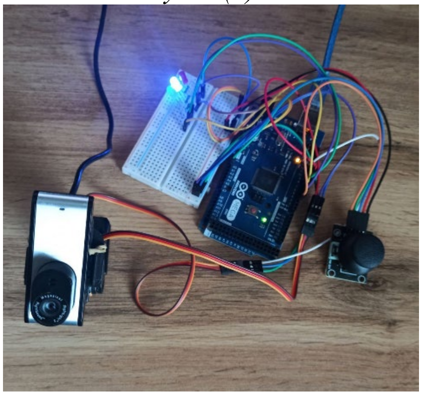

Fig. 1b. The assembled layout

Development of the software part of the layout

The program code for determining the coordinates of the face in the frame and sending these coordinates to the Arduino board for their further processing was written in the Python language using the OpenCV library. Sending this data is provided by the methods of the PySerial library. An example of face detection in a video is shown in Figure 2.

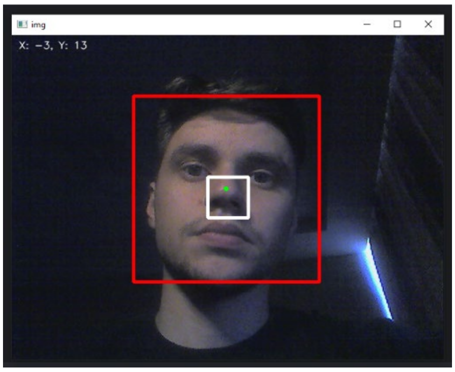

X: -3, Y: 13

Fig. 2. Determining the position of a face in a video stream

For face identification, the program uses the Haar cascade [3] - a machine-learning method used to detect objects in images and videos. It is based on the use of Haar primitives, which are simple rectangular regions with different brightness values. Examples of such cascades can be found on the official OpenCV page on GitHub.

Conclusions

While developing the layout, several techniques were used, which should be paid attention to when working on similar projects. Among the special methods used in the development were the following:

- Using the various available classifiers provided by OpenCV to test the performance of the scheme. For instance, when the space for testing is limited, a classifier that identifies hands was used to test the installation. This way, you can do tests without leaving it for a long distance and making adjustments directly during testing.
- It was experimentally determined that haarcascade_frontalface_alt.xml is best suited for face detection in poor lighting conditions, as it performed best in uneven lighting conditions. However, for other cameras, other ready-made options, or a classifier developed by yourself, may be suitable.
- An additional “zone of interest” was added to the frame to test the layout. Accordingly, the scheme had to work when the central point of the specified face went beyond this zone. Accordingly, by changing the dimensions of the zone, as well as the operation parameters of the circuit, you can determine the most optimal values for the operation of the layout.
- The coordinates of the center of the face were transmitted to the microcontroller through the serial port in a specified format. Namely “X<value of X>Y<value of Y>. In the code for the microcontroller, a restriction was imposed on the coordinate values - this is the extension of the web camera (640x480). Accordingly, other values may be used for informational messages. It should be noted that for the scheme to work correctly, a single format should be used.
- For smoother operation of servos in layouts using computer vision, it is better to use linear interpolation, and not just scaling the values obtained from the joystick and then writing them using the write function, since the latter method works very sharply, which leads to loss of stabilization and distortion images.

References

[1] Video Surveillance History. – 2023. – Retrieved from: https://ipvm.com/reports/history-video-surveillance

[2] Artificial Intelligence Systems for Supporting Video Surveillance Operators at International Airport / [M. Sujkowski, J. Kozuba, P. Uchroński and others.]. // Transportation Research Procedia. – 2023. – №74. – P. 1284–1291

[3] Haar Cascade Face Detector Quality Dependence on Training Dataset Variability / [S. Nikolaiev, Y. Tymoshenko, K. Matviiv]. // Research Bulletin of the National Technical University of Ukraine Kyiv Politechnic Institute. – 2017. – №6. – P. 38–46

ANOMALY DETECTION IN MONITORING SYSTEM METRICS OF UKLON COMPANY

Anton Matsyshyn*, Andriy Konovalov**
Taras Shevchenko National University of Kyiv,
Faculty of Radiophysics, Electronics and Computer Systems
*e-mail: * anton.matsyshyn@outlook.com, ** konam@knu.ua*

The work presents models for anomaly detection in the monitoring system metrics of the company Uklon [1] based on the LOF and HDBSCAN algorithms. The model based on HDBSCAN demonstrates higher accuracy in anomaly detection. It is shown that adjusting the sensitivity threshold for anomaly detection allows to control the rate of anomaly detections without the need for model retraining.

Introduction

Robust detection of anomalies in the performance metrics of computer systems allows engineers to react to system failures in time and fix them promptly. Existing monitoring systems (e.g., Grafana) provide the ability to analyze individual system metrics but lack the tools for comprehensive analysis of multivariate time series. At the same time, machine learning methods demonstrate high accuracy in solving such tasks [2]. This work presents models for anomaly detection in the monitoring system metrics of the Uklon company [1] based on the LOF [3] and HDBSCAN [4] algorithms with the ability to control the sensitivity threshold for anomaly detection.

Dataset

The dataset consists of 22 technical metrics from the monitoring system of the Uklon company with timestamps [5]. The data were collected from March 15, 2023, to April 14, 2023, with a 5-minute interval, corresponding to 8615 data points at consecutive time moments. Thus, the data are represented as a multivariate time series. The anomaly label in the dataset is absent. Some data points in the time series can be identified as anomalous due to incorrect values based on the context of the corresponding feature. For example, the Apdex feature represents the relative proportion of successfully processed requests and has values in the range [0, 1]. A value of 0 usually indicates the absence of any requests due to system failure. A similar analysis was performed for all features in the dataset. Points with incorrect values in at least one metric were identified as anomalies and removed from the dataset. After this cleansing, the dataset size was reduced to 8187 instances. The division into training, validation, and test sets was done chronologically: the training set spans time range from March 15 to April 4 (approximately 60%), the validation set spans from April 4 to April 9 (approximately 20%), and the test set spans from April 9 to April 14 (approximately 20%).

Model building and quality evaluation

Python was used for building program models, utilizing implementations of the LOF and HDBSCAN algorithms in the scikit-learn and hdbscan libraries. Data preprocessing involved taking the base-10 logarithmization of the ConsumerLag feature and standardization of all features with parameters determined from the training set. The models were trained on the training set. To evaluate the anomaly detection accuracy by the models, the approach [6] was employed, which involves artificially generating random values within the range of each feature from its minimum to maximum values at random time points for a given set. In this case, it can be approximated that all generated random feature values are anomalies, while all original dataset values are normal. This approach allows a simplified evaluation of model quality using classic binary classification metrics such as precision, recall, and F1 score. Fitting parameters were performed by maximizing the F1 score on the validation set.

Results

Figure 1 illustrates the comparison of quality metrics for models based on the LOF and HDBSCAN algorithms, evaluated on the test set. As seen, all metrics values for the LOF model are lower than the corresponding values for the HDBSCAN model. Figure 2, as an example, demonstrates the original time series of three features, Apdex, Gen1Collections and MemoryTotal, on the test set without artificially generated anomalies. Vertical lines denote anomalous points detected by the HDBSCAN model for two values of sensitivity threshold *b*, which determines the minimum probability at which a point is considered an anomaly. It is seen that overall, the model adequately detects anomalous points, and adjusting the sensitivity threshold *b* allows to control the rate of detected anomalies without the need for model retraining.

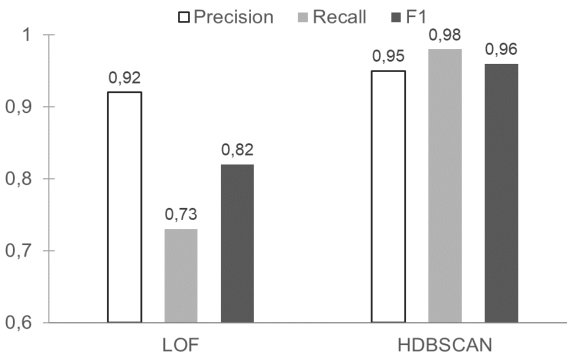

Fig. 1. Values of quality metrics of LOF and HDBSCAN models.

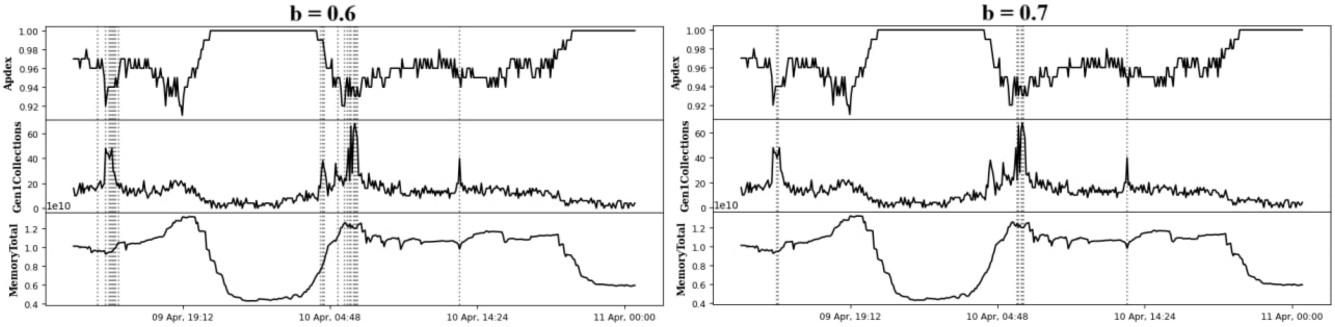

Fig. 2. Examples of anomaly detection by the HDBSCAN model for different values of the sensitivity threshold b.

Conclusion

The paper introduces anomaly detection models for Uklon company's monitoring system metrics, utilizing the LOF and HDBSCAN algorithms. It is found that the HDBSCAN-based model exhibits superior accuracy in anomaly detection. Moreover, it is demonstrated that by adjusting the anomaly detection threshold, engineers can regulate the rate of anomaly detections across various scenarios without necessitating model retraining.

References

[1] "Uklon - More than a taxi. Online ride-hailing service," Uklon UA. Accessed: Apr. 27, 2024. [Online]. Available: https://uklon.com.ua/en/.

[2] Y. Su, Y. Zhao, C. Niu, R. Liu, W. Sun, and D. Pei, "Robust Anomaly Detection for Multivariate Time Series through Stochastic Recurrent Neural Network," in Proceedings of the 25th ACM SIGKDD International Conference on Knowledge Discovery & Data Mining, Anchorage AK USA: ACM, Jul. 2019, pp. 2828–2837. doi: 10.1145/3292500.3330672.

[3] M. M. Breunig, H.-P. Kriegel, R. T. Ng, and J. Sander, "LOF: identifying density-based local outliers," SIGMOD Rec., vol. 29, no. 2, pp. 93–104, Jun. 2000, doi: 10.1145/335191.335388.

[4] R. J. G. B. Campello, D. Moulavi, and J. Sander, "Density-Based Clustering Based on Hierarchical Density Estimates," in Advances in Knowledge Discovery and Data Mining, vol. 7819, J. Pei, V. S. Tseng, L. Cao, H. Motoda, and G. Xu, Eds., Berlin, Heidelberg: Springer Berlin Heidelberg, 2013, pp. 160–172. doi: 10.1007/978-3-642-37456-2_14.

[5] "Uklon monitoring system metrics dataset." GitHub, Inc. Accessed: Apr 29, 2024. [Online]. Available: https://github.com/anton-matsyshyn/dataset.

[6] «2.7. Novelty and Outlier Detection», scikit-learn. Accessed: Apr 29, 2024. [Online]. Available: https://scikit-learn.org/stable/modules/outlier_detection.html.

RADIO ENGINEERING AND COMMUNICATIONS

THE SYSTEM OF FUTURE SPECIALISTS TRAINING IN THE FIELD OF APPLIED PHYSICS AT THE UNIVERSITIES OF GREAT BRITAIN

Olena Tytova
Educational and Scientific Institute of Philology, *Taras Shevchenko National University of Kyiv, 64/13, Volodymyrska Str., City of Kyiv, Ukraine, 01601, olenatytova2020@gmail.com*

The article analyzes the activities of British Universities and it describes the programmes that make up a system of professional training in the field of applied physics. It examines modern trends in the research carried out by the experts in this field at top universities in Great Britain.

The development of innovative educational technologies in developed countries requires appropriate content such as modernization of higher education in Ukraine, and the training of future specialists in the field of applied physics in particular. Great Britain is one of the world developed countries that has gained positive experience in this area. The experience of Great Britain is extremely important in applied physics training.

You may major in applied physics at the following universities:University Of Oxford, University Of St Andrews, Imperial College London,Durham University, Loughborough University, University Of Bath,University College London, University Of London. The UK offers: world-leading education and research,vibrant and inclusive student life, pathways to build your future immersion in English.

The UK is home to some of the world's most prestigious universities. Below is a table detailing the top 14 institutions in the country, ranked according to their overall scores and their placement in the QS World University Rankings for 2024.

Top universities to study in the UK:

#	University	Overall Score	QS Rank 2024
1	University of Cambridge	99.2	2
2	University of Oxford	98.9	3
3	Imperial College London	97.8	6
4	UCL	92.4	9
5	The University of Edinburgh	86.1	22
6	The University of Manchester	82.2	32
7	King's College London	79.3	40
8	The London School of Economics and Political Science (LSE)	76.9	45
9	The University of Warwick	68.6	67
10	University of Leeds	65.5	75
11	University of Glasgow	65.2	76
12	Durham University	65.1	78
13	University of Southampton	63.5	81
14	University of Birmingham	63.0	84

It is possible to study in the UK without taking IELTS or an equivalent English language proficiency test. Several universities offer courses where this isn't a requirement, but these are in the minority so you should generally assume it will be needed for most courses, particularly at more competitive universities.

When you decide to study in United Kingdom, you can access universities that rank highly in Applied Physics, improving your job prospects. You also get the opportunity to stay back in United Kingdom once you've graduated with a post-study work visa. There are plenty of universities on offer. Choose from 6 institutions and 10 courses. Top 6 Applied Physics universities in United Kingdom are: Swansea University,

University of Essex, Nottingham Trent University, University of Birmingham, University of Strathclyde, Queen's University Belfast. 10 courses are available:

You don’t have to stop at Applied Physics courses in United Kingdom, you can narrow down the focus of this subject even further into particular specializations:

- MSc by Research Applied Physics and Materials
- MSci (Hons) Theoretical Physics and Applied Mathematics
- BSc (Hons) Applied Physics
- MSc (by Dissertation) Applied Physics
- MPhil Applied Physics
- PhD Applied Physics
- PgDip Applied Physics
- Postgraduate Diploma Applied Physics
- MSc Applied Physics
- BSc (Hons) Applied Mathematics and Physics

The Natural Sciences degree allows you to pick two areas of specialization, giving a broader and more complete scientific education. The Natural Sciences programmes are flexible degrees drawing together elements of physics/astrophysics, mathematics, chemistry, earth sciences, life sciences, maths/statistics and science and technology studies.

Profound analysis of the UK experience will allow to identify modern trends of higher education in general and future specialists training in applied physics in higher educational institutions of the country, in particular, and will promote positive ideas in higher education of Ukraine.

References:

1. Бобрицька В. І. Педагогічні умови застосування технології «case-study» у вищих навчальних закладах Великої Британії / В. І. Бобрицька // Вісник Черкаського національного університету. Серія : Педагогічні науки. – 2012. – № 15 (228). – С. 12–17.
2. Лещинський О.П. Сучасні тенденції вдосконалення змісту навчання фізики у Великобританії// Педагогіка і психологія.-2002.-№4.- С.127-133.
3. Department of Physics and Astronomy Faculty of Mathematical and Physical Sciences [Електронний ресурс]. – Режим доступу: http://www.phys.ucl.ac.uk
4. London’s Global University [Електронний ресурс]. – Режим доступу: http://www.ucl.ac.uk/
5. Multidisciplinary University Research Initiatives (MURI) Program [Електронний ресурс]. – Режим доступу:http://www.onr.navy.mil/Science-Technology/Directorates/office-research-discovery-invention/Sponsored-Research/University-Research-Initiatives/MURI.aspx
6. Physics degree courses in UK [Електронний ресурс]. – Режим доступу: https://www.educations.com/applied-physics/europe
7. Top Applied Physics Courses in the United Kingdom [Електронний ресурс]. – Режим доступу: https://www.educations.com/applied-physics/europe
8. Applied Physics Courses in UK [Електронний ресурс]. – Режим доступу: https://edvoy.com/countries/applied-physics-courses-uk/ND

SYNCHRONIZATION OF CAMERAS FOR MEASUREMENT OF ARC DISCHARGE PARAMETERS

V. Kashchenko, **S. Fesenko**, **A.Veklich.**
Taras Shevchenko National University of Kiev, 63/13, Volodymyrska str., Kyiv 01601, Ukraine
e-mail: vitykashcenko@gmail.com

This work is devoted to the development of the synchronization unit for two Nikon D7100 cameras for studying the plasma of non-stationary free-burning arc discharges between copper-based fusible electrodes. The synchronous registration is controlled by a specially designed device based on the ATmega48 microcontroller. The signal for synchronous recording is supplied via a coaxial cable. Data exchange with the ports of various devices and power is carried out through the RS-485 bus. The UART protocol is used to implement the interface between the personal computer and the synchronization unit.

Introduction

Devices for recording the intensity of laser radiation are, perhaps, the most important elements of two-channel laser absorption spectroscopy [1] (LAS) in plasma diagnostics, since the accuracy of the measured plasma parameters directly depends on the quality of the fast and synchronous operation of the recording devices. Therefore, a detailed study of the advantages of the necessary recording devices in the experimental setup plays an important role in the study of arc discharge plasma by the LAS method. For the planned experiment, a scheme of dividing the probing laser beam into two beams with the same/defined ratio of intensities between the divided beams was implemented (Fig.1). The goal of splitting the output laser beam is the simultaneous registration of the two obtained intensities. One of the split beams immediately enters the recording device, and the other will pass through the plasma object and only then be registered.

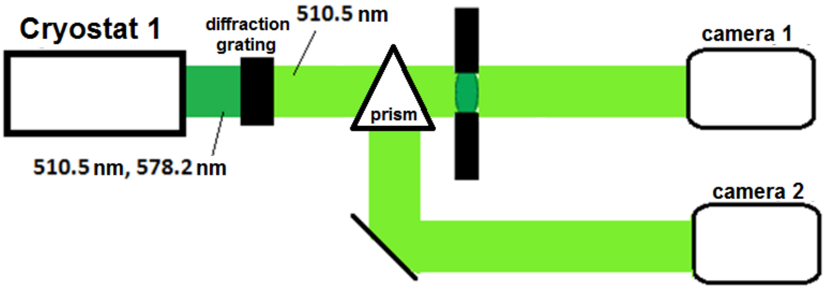

Fig.1. Optical scheme for laser absorption spectroscopy with parallel registration of radiation on two recording devices.

The development of the syncronious control unit

Nikon D7100 cameras were chosen as recording devices. The ML-L3 universal remote control was used for registration by both Nikon cameras. The remote control allows to use only frame-by-frame photo mode without the ability to shoot video, so registration synchronization plays an important role. The first synchronicity study showed a random discrepancy in time registration, so the goal was to tightly synchronize the registration on a pair of cameras.

The protocol of the ML-L3 remote control was specially recorded to manage registration from the computer and each camera independently (Fig.2). Then, the board based on the MC ATmega48 [2] with four parallel output channels was designed for transmitting information to the cameras according to the recorded protocol, where two channels are reserved for the future (Fig.3). When an external signal is received, the synchronization command of the cameras will be transmitted simultaneously on all channels.

The developed device (see Fig.4) made it possible to strictly synchronize the operation of a pair of cameras in the mirror pre-raising mode with an accuracy of about microseconds.

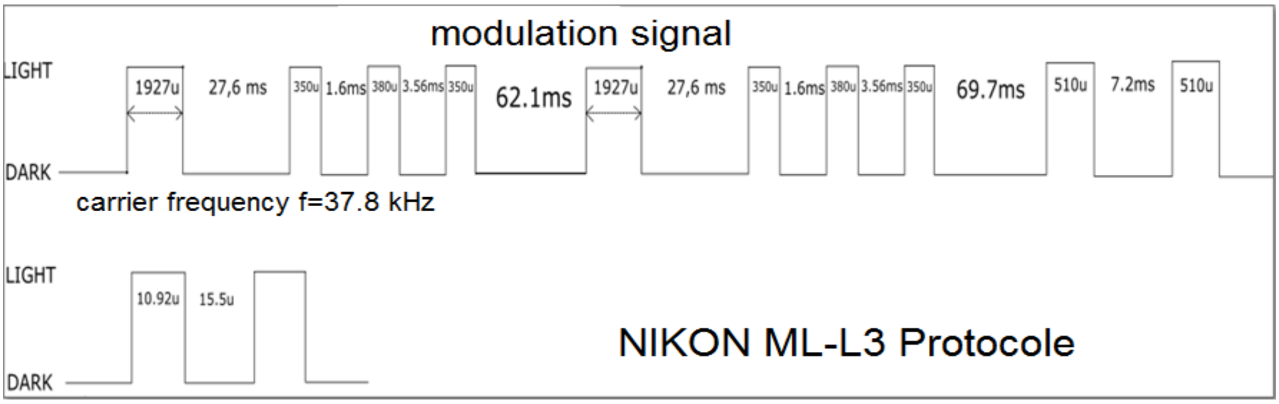

Fig.2. The protocol of the ML-L3 remote control.

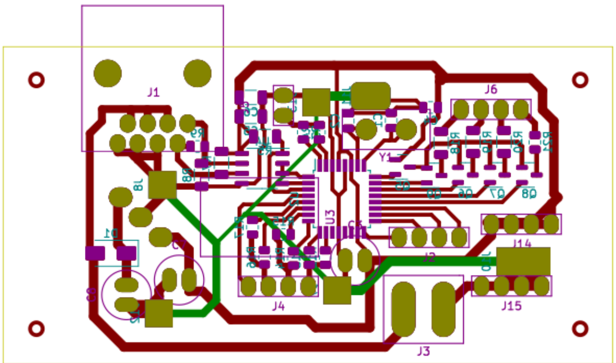

Fig.3. Diluted printed circuit board.

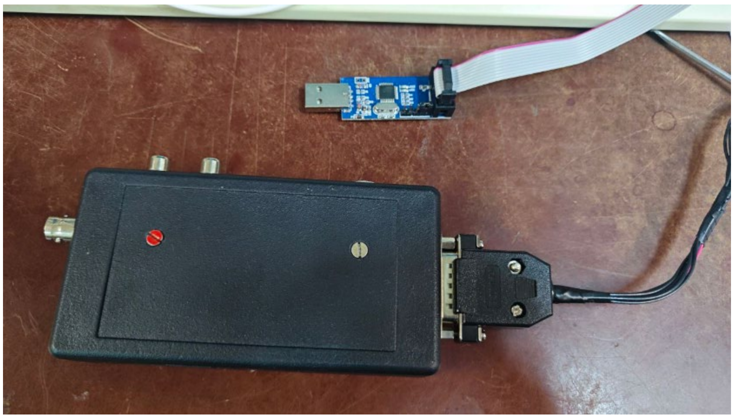

Fig.4. Completed device for two channels.

References

[1] D. Kalanov, R. Kozakov et al., “Spatially resolved LAAS diagnostics of a free-burning Ar arc: Analysis of line broadening”, Journal of Quantitative Spectroscopy and Radiative Transfer 265(11).

[2] ATmega48 Datasheet [Electronic Resource] – Mode of access: https://www.alldatasheet.com/datasheet-pdf/pdf/83740/ATMEL/ATMEGA48.html

DETERMINATION OF THE AMPLITUDE CHARACTERISTIC AND CALIBRATION OF THE 8MM RANGE SCANNING RADIOMETER

Maltsev V. P., Mogyla A. A.
Institute of Radiophysics and Electronics of the National Academy of Sciences of Ukraine, Kharkov,
e-mail: valentynmaltsev@gmail.com

Formation of radio images of the substrate surface with objects located on it can be done using active and passive radio channels. The active channel works better when scanning with floor corners, when the signal from various objects is reflected back, and from the floor surface further into the environment. Therefore, a significant contrast is observed, even if the object and the underlying surface have the same reflectance. But when the scanning angles are increased at the input of the receiver, there is an increase in the level of the signal reflected by the substrate surface, due to which the contrast is greatly reduced. Therefore, to construct such radio images, you can use a passive radiometric channel that measures the radio brightness temperature, which depends on the temperature and reflectivity of the body in the operating frequency range. This makes it possible to build radiometric images of the environment for the inventory of agricultural land, monitoring the ripening of crops, searching for hidden fires (for example, on peatlands) and others.

For this, a prototype of a scanning radiometer with an 8 mm range [1] was developed and manufactured, which allows building radiometric images in the 8 mm range (Fig. 1). The device has a two-coordinate scanning antenna system capable of rotating 360° continuously in azimuth and in the range from -5° to 90° in elevation. The antenna is built according to the Cassegrain scheme, has a diameter of 406 mm and a directional pattern width of 1.4°. The radiometric receiver is located directly on the rear part of the antenna, and transmits the measured values with a given discreteness and accumulation time to a PC for processing and construction of radiothermal images. The radiometric receiver is built according to a superheterodyne scheme with dual-band reception. The main amplification and selection takes place at the intermediate frequency. Fluctuation sensitivity of the receiver is 0.3°K.

Fig. 1. General view of radiometer system

To determine the absolute radio brightness temperature, it is necessary to construct an amplitude characteristic [2]. For this purpose, an attenuator was added between the antenna and the input of the radiometer and measurements of the dependence of the temperature at the input of the radiometer on the attenuation in the radiometer for known cold and hot sources of radiation were carried out (Fig. 2a). The clear sky at the zenith with a temperature of 26.6°K was used as a cold source, and a calibrated noise generator with a radio brightness temperature of 4786.5°K was used as a hot source. The amplitude characteristic was calculated according to the ratios $\mathrm{T}_{\mathrm{inrm}}^{\mathrm{c}} = \mathrm{T}_r - \frac{1}{\mathrm{L}}\left(\mathrm{T}_\mathrm{r} - \mathrm{T}_\mathrm{sky}\right)$ та $\mathrm{T}_{\mathrm{inrm}}^{\mathrm{h}} = \mathrm{T}_\mathrm{r} - \frac{1}{\mathrm{L}}(\mathrm{T}_\mathrm{r} - \mathrm{T}_\mathrm{NG})$, where $\mathrm{T}_{\mathrm{inrm}}^{\mathrm{c}}$ and $\mathrm{T}_{\mathrm{inrm}}^{\mathrm{h}}$ – temperature values for cold and hot radiation taking into account attenuator losses, T_r – physical radiometer temperature, L - attenuator losses, T_sky – clear sky temperature, T_NG – noise generator temperature. As a result of the experiment, the amplitude characteristic (Fig. 2b) was obtained, which is shown by a solid curve, which almost coincides with the linear - dotted line.

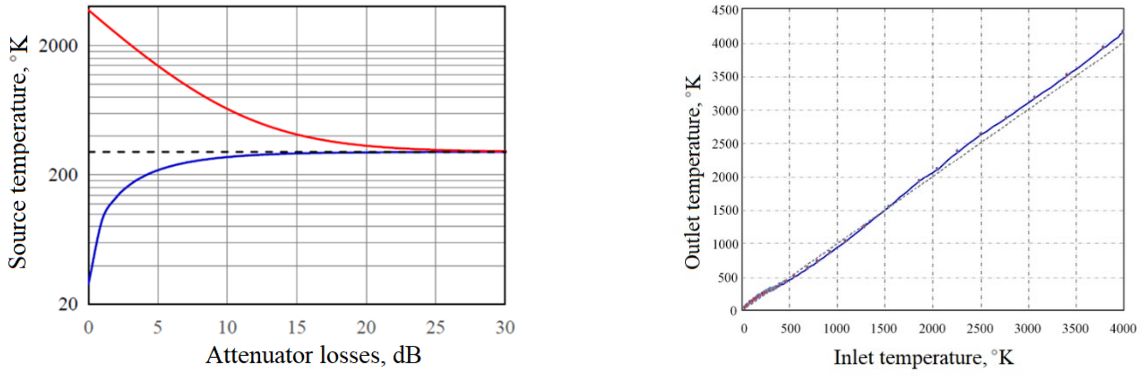

a) b)

Fig. 2. Dependence of the measured temperature of hot and cold noise sources on attenuation in the attenuator (a), amplitude characteristic of the radiometer (b).

Radiometer calibration is also necessary for field measurements. For this, the radio brightness temperature was measured for two points: for a radiometer located in an isothermally closed metal surface (Fig. 3a) and for a clear sky at the zenith (Fig. 3b). In the first case, thanks to the re-reflection of radiation in the medium of the closed surface, the radio brightness temperature coincides with the physical one, in the second case, one can be guided by the measured clear sky temperature of 28.6K. Further determination of the temperature during field measurements was carried out taking into account the amplitude characteristics and the measured calibration coefficients.

a) b)

Fig. 3. Radiometer calibration process.

References

[1] Войтович О. А., Лінкова А. М., Могила А. А., Мальцев В. П., Руднєв, Г. А., Хлопов Г. І., Грибский О. П., Маковенко С. В., Мальцев С. Б., Миронюк С. В., Павленко В. Д., “Багатофункціональний сканувальний радіометр Ка діапазону з адитивно-шумовим пілот-сигналом”, Радіотехніка, 2019, Вип.197.

[2] Fawwaz T. Ulaby, Richard K. Moore, Adrian K. Fung, “Microwave remote sensing: fundamentals and radiometry”, Addison-wesley publishing company, 1981.

STAND FOR TESTING BLDC MOTOR CONTROL ALGORITHMS SUITABLE FOR ONE-AXIS GYROSTABILIZATION

R. Andriichuk, V. Boretskij
Taras Shevchenko National University of Kyiv, 64/13, Volodymyrska Street, Kyiv, Ukraine,
e-mail: r.andriichuck@gmail.com

This research introduces a new testing platform – a one-axis gyrostabilization stand – specifically designed to evaluate BLDC motor control algorithms. This stand employs a dedicated motor to create controlled angular disturbances based on predefined scenarios. The motor being tested, equipped with gyroscopes on its rotor, receives real-time feedback from these sensors. To ensure optimal performance, the frequency responses of both the disturbance-generating motor and the gyrostabilizing motor were analyzed.

Introduction

Brushless direct current (BLDC) multivinding motors are finding increasing applications in various industries due to their high efficiency, reliability, and precise controllability. Achieving accurate control of BLDC motor position, speed, and torque is crucial for optimal performance in these applications [1-2]. Traditional testing methods often employ fixed setups or external disturbance sources, such as turntables, which may not adequately reflect real-world operating conditions. Additionally, the use of such external equipment instead of the final product's chassis can introduce delays in the development process [3].

This paper describes the design, and methodology of using a one-axis stand for testing BLDC motor control algorithms, particularly focusing on position, speed, and torque control for gyrostabilization purposes.

This approach offers several advantages over traditional testing methods, including:

- Simulating Real-World Disturbances: The gyrostabilization stand can generate dynamic and controllable disturbances, mimicking real-world operating conditions more effectively than fixed setups.
- Evaluating Control Algorithm Performance: By actively compensating for disturbances, the control algorithms can be evaluated for their robustness and ability to achieve precise motor control.
- Improved Testing Efficiency: The gyrostabilization stand allows for comprehensive testing of various control algorithms such as position control, speed control, and torque control in a single, versatile platform [4].

Experimental setup

The primary goal of the experimental setup was to develop a system capable of replicating real-world angular disturbances and utilizing actuators and sensors to evaluate the applicability of classical control strategies for brushless motors, including position control (servo control), speed control, and torque control. Following this concept, both hardware and software components were selected and developed to simulate platform oscillation scenarios, collect gyroscope data, and perform control algorithms.

Hardware Components:

- ODrive v3.6 Brushless Motor Control Board.
- TLE5012 Absolute Magnetic Encoders.
- Array of gyroscopes is constructed using an array of 16 LSM6DS3 sensors with 16-bit resolution and configured at ±250 DPS [5]. The array consists of two PCBs, each equipped with eight sensors, positioned along the rotational axis X with an equal offset of 12 mm. Data from each sensor is acquired at a frequency of 800 Hz. The array was attached to the rotational axis separately for each of the motors under examination to have better feedback on sensors.
- STM32F407VET6 is the core of the data acquisition system and driver control system of the motor position.

The Fig. 1. illustrates the arrangement of actuators and the array of gyroscopes:

1. MP100 120T Motor: This motor generates angular disturbances.
2. DYS GBM5208-75 Motor: This motor is used for gyrostabilization.
3. Virtual Gyroscope: This represents the virtual gyroscope assembly.

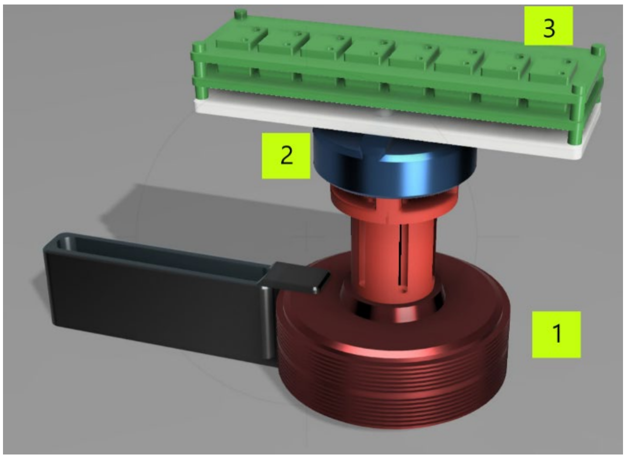

Fig. 1. The topology of actuators and feedback sensor on the testing platform.

Results and Discussions

A series of repeatable experiments were conducted to evaluate the suitability of the proposed configuration for assessing various brushless motor control strategies. Both motors were tested in servo mode following a specified trajectory. This trajectory was set by a sinusoidal law, with linear frequency modulation from 0 to 20 Hz and the position changing within a fixed range of ±0.1 revolution. Before each experiment, each gyroscope was calibrated. Data from all sensors were averaged, and static calibration was performed using the averaged data.

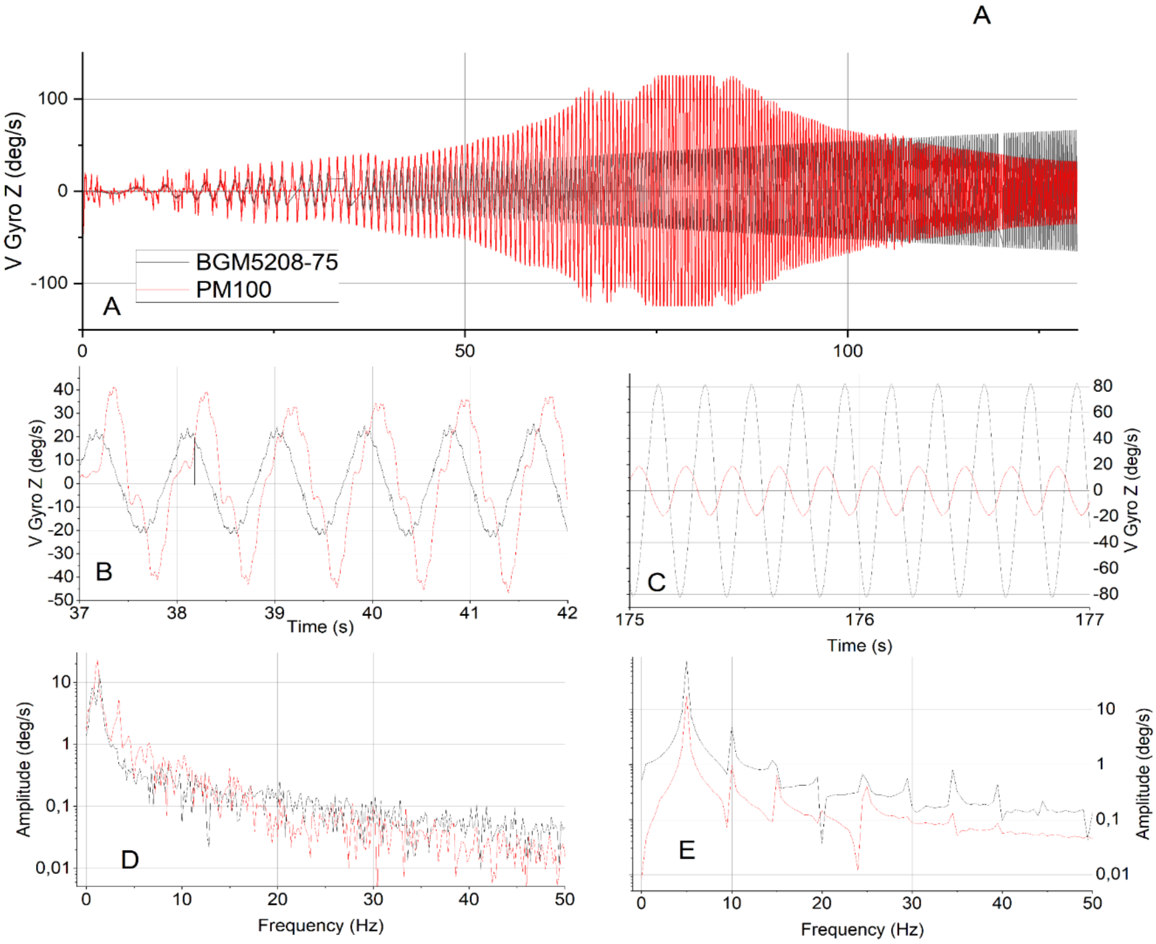

Fig. 2. Motor Response to Control Signal (A - Overall experiment, B and D - Motor rotational speed and oscillations frequency during 37-42th seconds of the experiment, C and E - Motor rotational speed and oscillations frequency during 175-177th seconds of the experiment)

The angular speed for both motors is shown in Fig. 2B at 1 Hz range oscillations. The oscillations are nearly sinusoidal, but there are spikes around the extrema with a frequency of around 5-10 Hz (Fig. 2D). The observed waveform distortions and motor response oscillations may stem from a nonoptimal control signal (PID regulator settings) [5], mechanical design flaws, or the discrete winding structure of motors. Although both motors have identical control signals, the amplitude for PM100 is almost twice that for GBM5208.

The data on the angular speed at 5 Hz are shown in Fig. 2C, as well as, their FFT spectra in Fig. 2E.
It can be observed that GBM5208 successfully replicates the shape of the control signal and oscillates without any visible deviations or distortions. PM100 does not demonstrate such faithful signal reproduction but maintains a sinusoidal waveform without significant distortions. This behavior could be attributed to several factors:

- Insufficient supply voltage: Motor PM100 may be operating with insufficient supply voltage, limiting its ability to accurately follow the control signal.
- Higher pole-pair count: Motor PM100 has a higher pole-pair count (23) compared to motor GBM5208 (7 pole-pairs), which introduces additional complexity in control due to increased electromagnetic interactions.
- Heavier mass: Motor PM100 has a mass three times greater than motor GBM5208, making it more challenging to control and respond dynamically to the control signal.

An experimental investigation was carried out to assess the performance of two brushless motors earmarked for future implementation in a gyrostabilization system. The speed response of each motor to a control signal using an array of homogeneous gyroscopes was evaluated in this study. The motors showed the capability to track the control signal waveform. However, signal distortions were observed at 1 Hz region. Thus, further refinement of the experimental setup and additional experimental tests are necessary to determine the main factors of such behavior.

References

1. Bhim Singh, Sanjeev Singh, (2009) “State of the Art on Permanent Magnet Brushless DC Motor Drives”, Journal of Power Electronics, Vol. 9, No. 1, January 2009, DOI: 10.1.1.453.6253.
2. Barrero F., Duran M. J., (2016), "Recent advances in the design, modelling, and control of multiphase machines: Part I.," IEEE Transactions on Industrial Electronics, vol. 63, no. 1, pp. 449-458.
3. Botero-Valencia, J., Marquez-Viloria, D., Castano-Londono, L., & Morantes-Guzmán, L. (2017). A low-cost platform based on a robotic arm for parameters estimation of Inertial Measurement Units. *Measurement*, *110*, 257-262. https://doi.org/10.1016/j.measurement.2017.07.002
4. Wach, P. (2011). Brushless DC Motor Drives (BLDC). In: Dynamics and Control of Electrical Drives. Springer, Berlin, Heidelberg. https://doi.org/10.1007/978-3-642-20222-3_4
5. J. Wang and E. Olson, “High-Performance Inertial Measurements Using a Redundant Array of Inexpensive Gyroscopes (RAIG),” in 2015 IEEE International Conference on Multisensor Fusion and Integration for Intelligent Systems (MFI), San Diego, CA, USA, 2015, pp.71-76.
6. Aström K. J., Hägglund T., (1995), "PID Controllers: Theory, Design, and Tuning," 2nd edition, Research Triangle Park, NC: Instrument Society of America.

2D RAMAN GAIN DYNAMICS BY SPECTRAL AND DISTANCE DISTRIBUTION IN TELECOMMUNICATION SILICA FIBERS

Kononenko A.A. [*], **Felinskyi G.S.** [**], **Felinskyi S.G.** [**].
Taras Shevchenko National University of Kyiv, Kyiv, Ukraine,
[*] *Faculty of Radiophysics, Electronics and Computer Systems e-mail:* kononenko@knu.ua
[**] *Educational and Scientific Institute of High Technologies e-mail:* felinskyi.gs@gmail.com, felinskyi.sg@gmail.com

The modeling results of the two-dimensional spectral-spatial distribution of Raman gain of optical signals and its dynamics as function of the pumping power in TrueWave RS^{TM} active fiber in comparison to G.652 standard silica fiber are presented in this paper.

The modern progress in the development of terabit telecommunications is achieved duo to the exploration of the full transparency window of silica fiber owes much to using of non-linear optical light amplification based on stimulated Raman effect. Among the recent achievements in the fiber light amplification modeling, it is worth noting the development of the analytically approximating technique for complex continuous-type Raman gain profiles [1]. This opens up the possibility to resolve the number of current problems of the dynamics of distributed Raman amplification, which remain insufficiently studied even in standard telecommunications fibers [2].

Theory basics

The 2D fiber Raman amplification (FRA) coefficient $G_{on/off}(\lambda, L)$ in dB as function of both the optical signal wavelength λ band and fiber length L can be expressed in the following form [2]:

$$G_{on/off}(\lambda, L) = 4.343 \cdot \left\{ g_R \left(\frac{1}{\lambda_p} - \frac{1}{\lambda} \right) P_0 \frac{[1-\exp(-\alpha_p L)]}{\alpha_p} - \alpha_s L \right\}, \qquad (1)$$

where P_0 is the pumping power, α_s and α_p denote the attenuation constants corresponding to the Stokes frequency and the pumping wavelength λ_p, and the numerical coefficient is $10\, lg\, e = 4.343$. The Raman gain profile $g_R(\lambda)$ is expressed directly by the difference between the corresponding wave numbers (inversed wavelengths).

Recently [2] we have introduced the term of the critical signal power as $P_s^{cr} = (\omega_s/\omega_p)(\alpha_p/g_{R_{max}})$. So the applicability criterion of undepleted pumping approximation takes the form of following inequality: $P_s \ll P_s^{cr}$.

Modeling background, results and discussion

Table 1 Experimental data and characteristic parameters of $G_{on/off}$ gain spatial dynamics in two silica fibers

P_0, mW	***TrueWave RS^{TM} fiber α_p = 0.26 dB/km; α_s = 0.2 dB/km***				
	G_{max}	G_{max}, dB	L_{max}, km	L_0, km	$L_{1/2}$, km
100	1.1	0.4	8	17.5	39.5
300	5.63	7.51	26.5	80	95.5
500	45.1	16.5	35	134	149
800	If $P_s = 76\ mW > P_s^{cr}$ then model is not applicable				

P_0, mW	***G.652 fiber α_p = 0.4 dB/km; α_s = 0.2 dB/km***				
	G_{max}	G_{max}, dB	L_{max}, km	L_0, km	$L_{1/2}$, km
100	1	0	–	–	27
300	1.38	1.41	10.5	25.5	43
500	2.55	4.07	16	46.5	62
800	7.43	8.71	21	75.5	90.5

The calculation parameters: $\lambda_p = 1.425\mu m$, $\lambda_s = 1.52\mu m$

The modeling was performed using the scheme of distributed amplification with direct pumping, where the signal at $\lambda_s = 1.55\ \mu m$ with a power of $P_s = 1\ mW$ propagated along the fiber together with the pump wave at $\lambda_p = 1.425\ \mu m$ of significantly higher power. Both waves propagated in the same direction, and the pump power could be increased, starting from $P_p = 100\ mW$. There are presented data for two model fibers, namely for TrueWave RS^{TM} fibers and for pure silica fibers of the G.652 standard for its comparative analysis purpose.

As modeling results, it has been obtained numerical data for characteristic fiber lengths at the gain coefficients $G_{\max}$, and it are presented in Table 1 for several values of P_0.

It is proved by the Table 1 data the signal power P_s remains significantly below the critical power P_s^{cr} for both fibers and in a fairly wide range of pump powers. Really, the fulfillment of our criterion for the applicability of the weak-signal model is demonstrated at pumping power rise up to 500 mW in both fibers.

Thus, both standard SMFs based on silica glass can be used as active media for distributed Raman amplification of optical waves. With the Raman amplifier, the full transparency length of these transmission fibers can be significantly extended, by several tens or even hundreds of kilometers. Our numerical data clearly indicate applicability of equation (1) for true description of the distributed FRA dynamics the and its design possibilities based on relationships (1).

We illustrate the 2D dynamics of Raman amplification in the C-band transparency window of fibers in Fig. 1. The modeling outcomes of spectral and spatial (2D) dynamics in distributed Raman amplification within standard single-mode fibers are derived using an original analytic model for the nonlinear Raman interaction between a weak optical signal and a strong pumping wave.

It's important to note the presented amplification scenario where a sufficiently strong signal is present at the transmission line's input poses the greatest challenge in terms of model applicability. This is because the model constraints include ensuring that the signal's power does not exceed the critical threshold P_s^{cr}. Therefore, the conditions for model applicability are more strictly fulfilled when considering backward pumping of the signal from the photodetector side, where signals weakened during propagation are amplified.

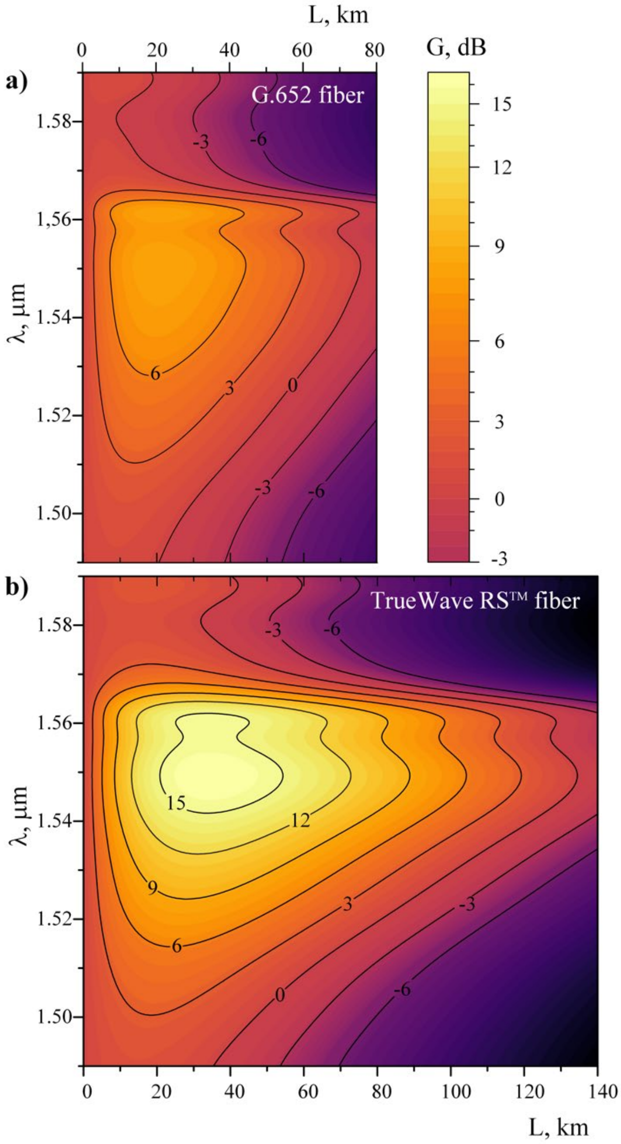

Fig. 1. 2D dynamics of FRA within the transparency window of the fiber with monochromatic pumping at $\lambda_p = 1.425\mu m$: a) G.652 standard SMF at $P_p = 800mW$; b) in TrueWave RS^{TM} fiber at $P_p = 500mW$

Conclusions

Our work establishes the model's suitability for analyzing the gain dynamics of fiber Raman amplifiers implemented in standard single-mode fibers made of silica glass. To describe the typical mode of nonlinear amplification in active fibers, we introduce the critical signal power P_s^{cr}, which enables us to quantitatively express the criterion for signal smallness in the amplifier. The practical application of this criterion for each fiber type determines the limits of both the maximum allowable signal gain and the corresponding pump power.

The nonlinear gain exhibits a uniform distribution within the boundaries of the Raman gain profile $g_R(\omega)$ only under the conditions of meeting the criterion and remains independent of the input signal power across the entire operational frequency range of the amplifier, without competition from nonlinear modes.

The presented numerical data generally support the applicability of our model in describing the dynamics of distributed fiber Raman gain across a wide range of pump power variations in several silica fibers types.

References

[1] I.V. Serdeha, V.I. Grygoruk, G.S. Felinskyi. Spectroscopic features of Raman gain profiles in single-mode fibers based on silica glass // Ukr. J. Phys. 2018. Vol. 63, No. 8, p. 683-700.

[2] A.A. Kononenko, G.S. Felinskyi, M.I Reznikov, S.G. Felinskyi, Spectral and spatial distribution of fiber Raman amplification in telecommunication fibers based on silica glass // Proc. VIII All-Ukrainian Scientific and Practical Conference "Prospective directions of modern electronics, information and of computer systems", MEICS-2023, November 22-24, 2023, Dnipro, Ukraine, p. 166-167.

CONTENTS OF THE CONFERENCE

INVITED LECTURES

1 **MINIATURIZED RAMAN SPECTROSCOPY AND MICROSCOPY** 7

Yaroslav Aulin*, Konstantinos Stergiou, Sofus Boisen, Andrii Kutsyk, Yurii Pilhun, Oleksii Ilchenko
Lightnovo ApS, Blokken 11, 1., Birkerød, Denmark
** e-mail:* ya@ligthnovo.com

2 **LABEL-FREE DETECTION AND ANALYSIS OF BIOMOLECULES USING SOLID-STATE NANOPORES AND NANODIELECTROPHORESIS** 9

Sergii Pud
**University of Twente, Drienerlolaan 5, 7522NB, Enschede, The Netherlands, e-mail:* s.pud@utwente.nl

3 **LIGHT-DRIVEN ULTRAFAST MAGNETISM** 11

Dmytro Afanasiev
Radboud University, Nijmegen, The Netherlands

4 **REMOVAL OF PFAS AND PHARMACEUTICAL RESIDUES FROM WATER WITH A HYPERBOLIC VORTEX PLASMA DISCHARGE** 12

Roman Klymenko*, Elmar C. Fuchs, W.F.L.M. (Wilfred) Hoeben***, Jakob Woisetschlägerilfred****, Luewton L.F. Agostinho*******
** Department of Electrical Engineering, Electrical Energy Systems group, Eindhoven University of Technology, Eindhoven, The Netherlands, e-mail:* r.klymenko@tue.nl
*** Wetsus, European Centre of Excellence for Sustainable Water Technology, Leeuwarden, The Netherlands, e-mail:* elmarchristof.fuchs@wetsus.nl
**** Department of Electrical Engineering, Electrical Energy Systems group, Eindhoven University of Technology, Eindhoven, The Netherlands, e-mail:* w.f.l.m.hoeben@tue.nl
***** Laser Optical Metrology Group, Institute of Thermal Turbomachinery and Machine Dynamics, Graz University of Technology, Graz, Austria, e-mail:* jakob.woisetschlaeger@tugraz.at
****** Water Technology Research Group, NHL Stenden University of Applied Sciences, Leeuwarden, The Netherlands, e-mail:* luewton.agostinho@hvhl.nl

1. LASER PHYSICS AND OPTOELECTRONICS (LPO)

2. POLARIMETRY: THEORY AND APPLICATIONS (PTA)

3. PHYSICS OF MAGNETISM (PM)

4. MATHEMATICAL PROBLEMS OF APPLIED PHYSICS (MAP)

5. SURFACE PHYSICS, NANO- AND MICROELECTRONICS (SP)

4 **THRESHOLD STOICHIOMETRIES FOR FORMATION OF DIFFERENT PHASE COMPOSITIONS OF Si OXYNITRIDE FILMS BY THERMODYNAMIC MODELING** 69

Mariia Babiichuk*, Andrey Sarikov**
**Educational Scientific Institute of High Technologies, Taras Shevchenko National University of Kyiv, 4-g Hlushkova Avenue, 03022 Kyiv, Ukraine, e-mail: mariiababiichuk@knu.ua*
*** V. Lashkaryov Institute of Semiconductor Physics, National Academy of Sciences of Ukraine, 41 Nauky Avenue, 03028 Kyiv, Ukraine, e-mail: sarikov@isp.kiev.ua*

5 **THE IMPACT OF THE DIELECTRIC COATING ON THE REFLECTIVE PROPERTIES OF THE STRUCTURE “UNIAXIAL PLASMONIC METASURFACE-DIELECTRIC-METAL”** 71

Mykola Beletskii, Ivan Popovych
Department of solid-state electronics A.Ya. Usikov Institute for Radiophysics and Electronics National Academy of Sciences of Ukraine, Kharkiv, Ukraine, email: bnnbeletski@gmail.com
Department of solid-state electronics A.Ya. Usikov Institute for Radiophysics and Electronics National Academy of Sciences of Ukraine, Kharkiv, Ukraine,
email: ivdpopovich@protonmail.com

6 **THE THERMOCHROMIC MICROCOMPOSITE WITH A HIGH SENSITIVITY TO IONIZING RADIATION** 73

Andrii Hrytsak*, Volodymyr Kapustianyk, Yurii Chornii*****
** Department of Physics, Ivan Franko National University of Lviv, Dragomanova str. 50, 79005 Lviv, Ukraine, e-mail: grytsak.andrew@gmail.com*
*** Department of Physics, Ivan Franko National University of Lviv, Dragomanova str. 50, 79005 Lviv, Ukraine, e-mail: kapustianyk@yahoo.co.uk*
**** Department of Physics, Ivan Franko National University of Lviv, Dragomanova str. 50, 79005 Lviv, Ukraine, e-mail: ychornii@gmail.com*

7 **PRACTICAL APPLICATIONS OF SCANNING PROBE MICROSCOPY IN THE ELECTROSTRUCTURAL CHARACTERIZATION OF SEMICONDUCTOR STRUCTURES** 75

Petro Lytvyn
V. Lashkaryov Institute of Semiconductor Physics NAS Ukraine,
41, Nauky pr., Kyiv 03028, Ukraine, e-mail: plyt@isp.kiev.ua peter.lytvyn@ccu-semicond.net

8 **MODELING OF THE SCANNING TUNNELING MICROSCOPY IMAGES AND MATERIAL PROPERTIES USING THE DENSITY FUNCTIONAL THEORY** 77

Dmytro Karakuts[1],*
[1]Taras Shevchenko National University of Kyiv, 01601 Kyiv, Ukraine
**email: karakutzdw@gmail.com*

6. PHYSICS OF SEMICONDUCTORS AND DIELECTRICS, SEMICONDUCTOR DEVICES (PS)

7. MEDICAL PHYSICS (MP)

8. PLASMA PHYSICS (PP)

9. COMPUTER TECHNOLOGIES (CT)

10. RADIO ENGINEERING AND COMMUNICATIONS (REC)

5 152

2D RAMAN GAIN DYNAMICS BY SPECTRAL AND DISTANCE DISTRIBUTION IN TELECOMMUNICATION SILICA FIBERS

Kononenko A.A. [*]**, Felinskyi G.S.**[**]**, Felinskyi S.G.**[**].
Taras Shevchenko National University of Kyiv, Kyiv, Ukraine,
[*] *Faculty of Radiophysics, Electronics and Computer Systems e-mail: kononenko@knu.ua*
[**] *Educational and Scientific Institute of High Technologies e-mail: felinskyi.gs@gmail.com, felinskyi.sg@gmail.com*